Library Authorisation

The University of Waikato
Te Whare Wānanga o Waikato

I hereby authorise the Librarian of the University of Waikato to make my thesis, titled

Potential tsunami hazard associated with the Kerepehi Fault, Hauraki Gulf, NZ

available to people wishing to consult it and I agree that after five years, the Librarian, at his or her discretion, may have it copied for Library purposes but not for publication.

Name: Louise Chick ID No: 9418003

Signature: Louise Chick Date: 23/11/99

To Kūaha The Gateway STUDENT REGISTRY

THE BOOKBINDERY
cnr Parau St & Fearon Ave
Mt Roskill, Auckland, NZ
Ph: (09) 620-6747

POTENTIAL TSUNAMI HAZARD
associated with the
KEREPEHI FAULT,
HAURAKI GULF, NEW ZEALAND

A thesis submitted in partial fulfilment of
the requirements for the Degree of

Master of Science

In Earth Sciences
At the University of Waikato University by

Louise Mae Chick

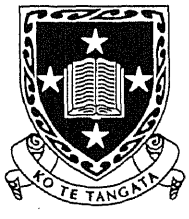

The
University
of Waikato
Te Whare Wānanga
o Waikato

1999

ABSTRACT

A review of 'active' faults in the Auckland region identified the Kerepehi Fault as a potential tsunami source (de Lange and Hull, 1994). The Kerepehi Fault trends NNW, transecting the central region of the inner Hauraki Gulf. A tsunamigenic event along the Kerepehi Fault has not occurred during historical times making this hazard difficult to quantify. Consequently, this study assessed the hazard represented by the Kerepehi Fault using numerical simulation, which required that the locations of offshore segments and behaviour of each segment of the Kerepehi Fault be determined.

Shallow seismic sub-bottom profiles totalling 135 km in length were analysed and used to locate the submarine extension of the Kerepehi Fault. Without core data, only the *relative* timing of movement along the fault could be determined. The seismic data clearly showed that movement has occurred since the last observable reflector/unconformity. Onland evidence indicates that this unconformity corresponds to a surface flooding event which occurred at 6.5 ka; suggesting that the submarine extension of the Kerepehi Fault is still active and potentially tsunamigenic.

Seismic data indicates the offshore Kerepehi Fault trends NNW up the central Firth of Thames and is divided into four segments by three WSW-ENE trending transverse faults. The displacement that is most likely to occur for any given event ranges from 2.1-7.35 m. Tsunami generation and propagation was modelled using a linear, finite element model, 'TSUNAMI'; a finite difference hydrodynamic circulation model, '3DD'; and an empirical set of parametric equations (Abe, 1995). The results indicate:

(i) The greatest risk to Thames township is associated with displacement along an adjacent fault segment, which produces wave heights of the order of 1.8 m.

(ii) The largest shoreline wave heights (~4 m) were generated by displacement in deep water and had the most severe impact upon Pakatoa, Ponui, and Rotorua Islands. The maximum *mainland* wave resulting from displacement along the Kerepehi Fault impacts at Deadmans Point and has a height of the order of 2.8 m.

(iii) The overall tsunami hazard associated with this fault is low.

Comparison of wave heights generated by the three methods indicated that for shallow water source regions, 'TSUNAMI' generally under predicts maximum wave height. This is suggested to occur because 'TSUNAMI' is unable to cope with the highly non-linear wave processes that occur in shallow water.

The behaviour of tsunami waves within the Firth of Thames was further investigated through the simulation of teletsunami (distantly generated tsunami) propagation into the Hauraki Gulf, which was undertaken using the model '3DD'. Wave height time histories for selected regions and amplitude attenuation graphs produced from '3DD' output indicate:

(i) Generally, for wave periods between 10 and 30 minutes, the maximum predicted sea level rise increases as teletsunami wave period becames longer.

(ii) The confined nature of the Firth of Thames acts to focus wave energy resulting in elevated wave heights within this embayment. The maximum amplitude reinforcement occurring in the Firth of Thames is equivalent to 50 % of the amplitude at the open ocean boundary and is considered significant.

(iii) For townships adjacent to the Firth of Thames, the maximum rise above mean sea level caused by teletsunamis of similar magnitude to the 1960 Chilean tsunami was between 0.36 and 0.49 m. The largest of these, 0.49 m, is observed at Tapu.

(iv) A teletsunami of this magnitude, represents a less significant hazard than tsunamis locally generated along the Kerepehi Fault.

Wave heights observed during the 1960 Chilean tsunami and those predicted by model '3DD' are in strong agreement. However, the coarse grid employed by '3DD' (1500 m) limits the number of grid cells per wavelength. Consequently wave propagation in shallow water may not be fully represented, particularly for short period waves. Hence, the above results should be regarded with caution.

The probable extent of tsunami inundation occurring in the Thames region was investigated using the non-linear finite difference model, 'TUNAMI N2'. The results indicate that should a tsunami of at least moderate amplitude (3 m) be generated in the Firth of Thames, 7 metres of vertical run-up is likely to occur between Tararu and Moanataiari, and land adjacent to the Thames aerodrome will be horizontally inundated by up to 450 m.

ACKNOWLEDGEMENTS

Whilst undertaking this thesis I have received support and advice from many people. I would like to take this opportunity to thank them and show my sincere appreciation of the time and effort they have given.

Firstly I'd like to thank Civil Defence for making this project available and providing financial support. Auckland Regional Council has contributed additional funding and resources, which have proven invaluable, particular thanks to Michelle Daly for her assistance in making these resources available.

I'd like to thank my superisors Dr Willem de Lange and Professor Terry Healy. My sincere thanks goes out to Willem for the continued advice and support he has provided over the last year and a half. I would like to thank Terry for initiating this thesis topic, and giving constructive criticism and much encouragement.

I would like to thank Barbara Manighetti (NIWA), Michelle Malcolm (Environment Waikato) and Darryl Gillgren for the provision and manipulation of data required for completion of this thesis.

Many thanks to Brian Ricketts, Karin Bryan, Richard Gorman, Allan Hull, Terry Webb, Bruce Parkinson, Earl Bardsley, Scott Stevens, Haydon Jones and in particular George Crook for their technical assistance and general support.

On a personal note, many, many, thanks to the various people who have given support, shared knowledge and laughs over the last two years. In particular, thanks so much to Tash, Jacqui, and Chris for all the fun times. Your encouragement has been invaluable and your friendship is precious.

Thanks to Troy for his encouragement and for managing to see the light at the end of the tunnel.

To my parents, Bronwyn and Graeme who have always been there for me, and who have given their love and support in so many ways. Thank you so much.

CONTENTS

LIST OF FIGURES

CHAPTER 4

CHAPTER 5

APPENDIX 3

APPENDIX 9

APPENDIX 11

LIST OF TABLES

CHAPTER 7

CHAPTER 8

Chapter One

INTRODUCTION

1.1 INTRODUCTION

The long period (10-30 min.), shallow water waves commonly referred to as tsunami's have more potential than any other coastal natural hazard (save for impact of a large meteorite) to cause widespread, sudden catastrophic damage and risk to life (Pararas-Carayannis, 1988). These impulsively generated sea waves of local or distant origin, result from seafloor fault movement, large-scale slides, or volcanic eruption (de Lange, 1983). The magnitude and geometry of the displacement source determine the amount of energy transferred from the seafloor into the displaced water, and therefore significantly influence the size of the resulting tsunami. Tsunamis have extremely long wavelengths (several hundred kilometres in deep water). The product of wave length and water depth govern the dispersion properties of waves, hence tsunamis always propagate as shallow water waves, regardless of water depth. In deep water they can travel at velocities of about 700 $km.hr^{-1}$ and possess wave heights of less than 0.5 m. On approaching the shoreline, reduced water depth and local bathymetric seabed configuration cause tsunami waves to be subjected to a wide range of shoaling processes which reduce tsunami wave speed and can cause substantial amplification, of up to 30 m. Upon reaching the shoreline, the magnitude of the tsunami wave is further modified by the non-linear dynamics of the breaking wave inundation (Prasetya, 1998).

Compared to other hazards in New Zealand, tsunamis have caused limited damage in the past, with only two reported tsunamis causing loss of life or injury (1868 Aug. 13 & 1952 Nov.4). However, tsunami inundation has the potential to cause significant damage and loss of life (e.g. an estimated 2000 Papua New Guinea people were killed in the 1998 (July 17) tsunami), and this risk is increasing as development along the New Zealand coastline continues. For example, the West Wairarapa tsunami that generated a 9.1 m run-up caused limited damage in 1855. It is expected that future tsunamis in developing coastal regions such as this, will have a much more severe social and economic impact than that of past events (Pararas-Carayannis, 1988).

Prediction of coastal response to long period, tsunami waves is essential for risk mitigation as it aids the planning, design, and protection of near-shore submerged structures, waterfront buildings, and other harbour facilities such as ports and vessels (Street et al., 1970; McKenzie, 1993; Thompson et al., 1995). Near shore tsunami propagation has been investigated using hydraulic scale models, but not only are these expensive to construct (Pararas-Carayannis, 1988) but reflections from the driving wave paddle and tank boundaries can generate bias (Gaillard, 1982). Consequently, numerical models have become the most widely used tool for investigating tsunami generation, propagation and inundation.

This study applies the numerical modelling technique to investigate the potential tsunami hazard associated with the Kerepehi fault, located within the Hauraki Gulf, New Zealand (Figure 1.1).

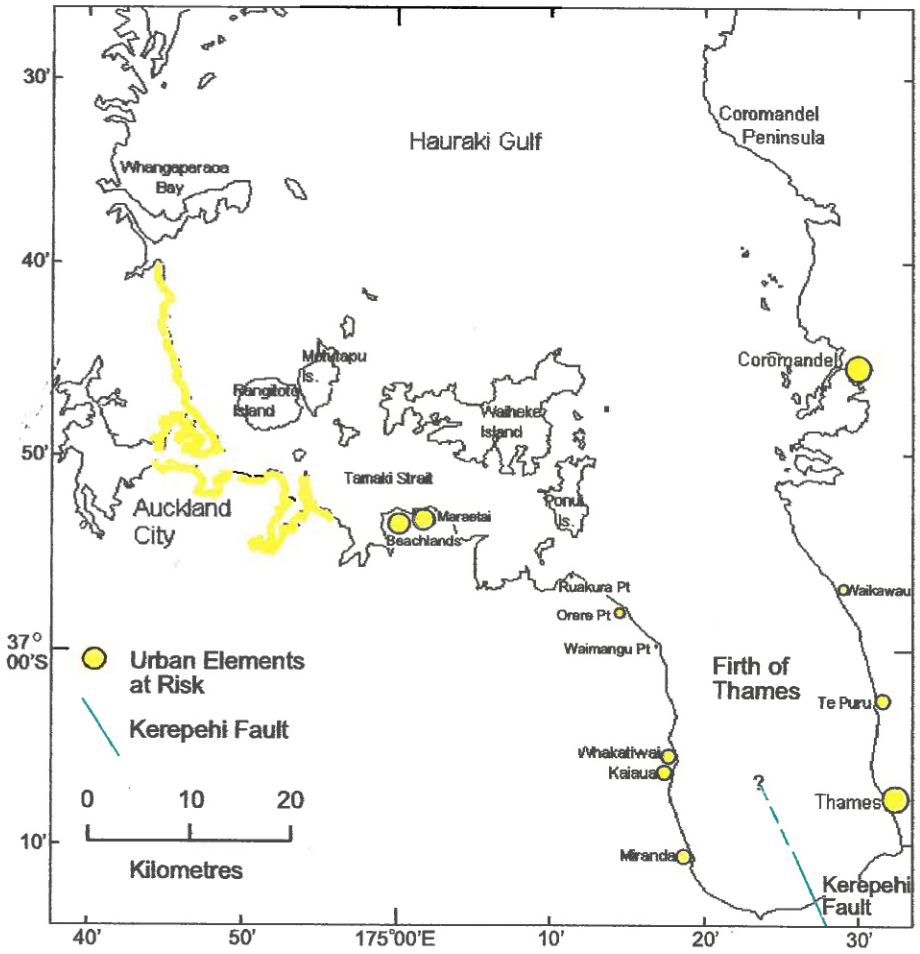

Figure 1.1: The study region: the Hauraki Gulf. Yellow dots and lies represent urban elements at risk (where elements at risk are defined by Varnes (1984) as population, properties, economic activity at risk in a given area).

1.2 STUDY AREA

The Kerepehi Fault trends NNW through the central region of the inner Hauraki Rift, which extends for over 300 km from Whangarei, through the Hauraki Gulf, Firth of Thames (as indicated by the parallel Firth of Thames shorelines) and Hauraki Depression into the Taupo Volcanic Zone (Hochstein et al., 1986; Hochstein and Nixon, 1979). The offshore extension of the Kerepehi Fault begins within the Firth of Thames, in the southern Hauraki Gulf, off the East Coast of New Zealand. The Firth of Thames is a low wave energy, mud-filled, shallow, semi-enclosed marine embayment. This region has been subjected to 12 tsunamis during historic times, all of which have been of pan-Pacific (distantly generated) origin.

Okal (1988) noted that tsunamis may be generated by earthquakes of moment magnitude less than 7.3, the generally accepted threshold for tsunami generation (de Lange, 1983), if rupture occurs in soft sediments and/or within a confined water body where wave energy can be focused. Weaker, more elastic sediments are believed to have a slower moment rate release (Schindele et al., 1995) and as a result increase the maximum sea surface elevation by approximately 30% (Zhdonov, 1991), therefore generating 'tsunami earthquakes' or events which generate disproportionate tsunamis in relation to their standard magnitudes (Schindele et al., 1995). Both of these conditions occur in the Firth of Thames, which contains active segments of the Kerepehi Fault. Therefore the potential for tsunami generation within the Hauraki Gulf exists.

Recently, the Kerepehi Fault has been identified as the most likely local tsunami source for the Auckland-Waitemata region (de Lange & Hull, 1994). Hence this fault presents significant risk for adjacent coastal townships (Figure 1.1) and the large coastal population of Auckland City and associated infrastructure, particularly modern marina installations and ports (Healy & de Lange, (in press)). In addition, there is potential for damage to the low standing (a few metres above sea), northern reach of the intensively farmed Hauraki Lowlands.

1.3 AIMS & OBJECTIVES

The principle aim of this study is to determine the potential tsunami hazard represented by the Kerepehi Fault system. In accordance with the study aim, a number of study objectives have been defined:

1. To characterise the offshore segments of the Kerepehi Fault system in order to reconstruct the recent movement history with regards to location, frequency and magnitude of movement. This will be achieved through compilation and interpretation of seismic data, previously collected from along offshore segments of the Kerepehi Fault.
2. To re-examine the M.C.E. (Most Credible Earthquake) predictions made by de Lange & Hull (1994) in order to ascertain the most probable rupture magnitude.
3. Numerically model tsunami (i) generation from selected sites along the Kerepehi Fault and for selected fault movement scenarios, and (ii) propagation using the 'TSUNAMI' finite element model.
4. Numerically simulate tsunami inundation effects using 'TUNAMI N2' finite difference model.
5. Identify regions most susceptible to the tsunami hazard through interpretation and analysis of model output data.
6. From the modelling results, assess whether movement along the Kerepehi Fault represents a credible threat to the Auckland-Hauraki Gulf region.

1.4 STUDY APPROACH

In order to achieve the objectives outlined above, Chapter 2 reviews the regional tectonic setting and known information about the Kerepehi Fault. Chapter 3 outlines the data collection and analysis methodology. The results of seismic sub-bottom profile analysis and implications for the location and likely magnitude of displacement along the Kerepehi Fault are presented in Chapter 4. These results are used as inputs for 'TSUNAMI' finite element model, which simulates tsunami generation and propagation. Chapter 5 discusses the 'TSUNAMI' model set-up and the results of five fault movement scenarios. These results are then compared with maximum predicted

wave heights generated by two other methods in order to assess the accuracy of the 'TSUNAMI' model. In Chapter 6 the propagation of 0.5 m amplitude teletsunami of varying wave period are simulated. The results are used to investigate how shoaling processes occurring during wave propagation affect tsunami wave height in the Firth of Thames, and in so doing, determine which localities adjacent to the Firth of Thames are likely to be subjected to attenuation or amplification of tsunami waves. In Chapter 7 the probable extent of tsunami inundation occurring in the Thames region is investigated using the non-linear finite difference model 'TUNAMI N2'. Chapter 8 concludes this study by using the modelling results to assess the tsunami hazard associated with displacement along offshore segments of the Kerepehi Fault.

1.5 REFERENCES

de Lange, W.P., 1983. *Tsunami Hazard, an investigation into the potential tsunami hazards of the Bay of Plenty region using numerical models*, M.Sc. Thesis, University of Waikato, Hamilton. 275 p.

de Lange, W.P., and Hull, A.G., 1994. *Tsunami Hazard for the Auckland Region*, Earth Sciences Department, University of Waikato, and Institute of Geological and Nuclear Science Limited. 37 p.

Gaillard, P., 1982. Numerical calculation of Seiche motions in Harbours of arbitrary shape, *Proceedings of the 18th Coastal Engineering Conference*, A.S.C.E. 1: p. 172-191.

Healy, T.R., and de Lange, W.P., Potential tsunami hazard associated with the Kerepehi Fault, Hauraki Gulf, New Zealand (in press), In Braddock, R.K. (ed), *Tsunamis of the Southwest Pacific*, Kluwer Publishers.

Hochstein, M.P., and Nixon, I.M., 1979. Geophysical study of the Hauraki Depression, North Island, New Zealand; *New Zealand Journal of Geology and Geophysics*, Vol. 22, p. 1-19.

Hochstein, M.P., Tearney, K., Rawson, S., Davey, F.J., Davidge, S., Henrys, S., and Backshall, D. 1986. Structure of the Hauraki Rift (New Zealand), In W.I. Reilly and B.E. Harford (eds). *Recent Crustal Movements of the Pacific Region*, Royal Society of New Zealand Bulletin 24. Wellington, The Royal Society of New Zealand, p. 334-348.

McKenzie, D.D.J., 1993. *Numerical Modelling of Tsunamis in the Bay of Plenty*; M.Sc. Thesis, Department of Earth Sciences, The University of Waikato. 60 p.

Okal, E.A., 1988. Seismic parameters controlling far-field tsunami amplitudes: a review. *Natural Hazards*, Vol. 1, p. 67-96.

Pararas-Carayannis, G., 1988. Risk Assessment of the Tsunami Hazard, In M.I. El-Sabh and T.S. Murty (eds). *Natural and Man-made Hazards*, D. Reidel Publishing Company, p. 183-191.

Prasetya, G.S., 1998. *Modelling Volcanic Tsunamis.* MSc Thesis, University of Waikato. 108 p.

Schindele, F., Reymond, D., Gaucher, E., and Okal, E.A., 1995. Analysis and Automatic processing in near-field of eight 1992-1994 Tsunamigenic earthquakes: improvements towards real-time tsunami warning, *Pure and Applied Geophysics*, Vol. 144, No. ¾., p. 381-408.

Street, R.L., Chan, R.K.C., and Fromm, J.E., 1970. The Numerical Simulation of Long Water Waves: Progress on Two Fronts, In: *Tsunamis in the Pacific Ocean*, East-West Center Press, Honolulu, p. 377-398.

Thompson, E.F., and Hadley L.L., 1995. Numerical modeling of harbor response to waves, *Journal of Coastal Research*, Vol. 11, No. 3, p. 746-753.

Varnes, D.J., 1984. *Landslide Hazard Zonation, a review of principles and practice*, Commission on Landslides and other Mass Movements of slopes International Association of Engineering Geology, Paris, UNESCO, p. 6.

Zhdanov, M.A., 1991. An analytical model of tsunamis generated by earthquakes, In S. Tinti (ed), *Tsunamis in the World, fifteenth international tsunami symposium*, p. 77-94.

Chapter Two

REGIONAL TECTONIC SETTING

2.1 THE HAURAKI RIFT

2.1.1 Introduction

The Hauraki Rift is a continental rift with a mean strike of approximately 340° (Figure 2.1) that extends for over 300 km from Whangarei to the Taupo Volcanic Zone (Hochstein et al., 1986; Hochstein and Nixon, 1979). The Hauraki Rift consists of a set of fault angle depressions that lie to the west and east of a median ridge (Figure 2.2). This ridge widens from south to north, but is believed to be poorly developed in the central Firth of Thames.

The north-west trending Kerepehi and Hauraki faults form the eastern margins of the westward and eastern basins. These faults dip west at approximately 35°. However, gravity models indicate that in the northern rift (Hauraki Gulf & upper Firth of Thames), below 0.5 km, the dip can increase to 70°. Dissecting the major normal faults are a series of transverse faults causing up to 3 km of horizontal offset of the major faults (Hochstein et al., 1986).

2.1.2 Is the Hauraki Rift Active?

A literature review investigating the sedimentary and tectonic history of the Hauraki rift was undertaken to ascertain whether the Hauraki rift is considered active or inactive. Such a review provides insight into the likelihood of the Kerepehi Fault being active.

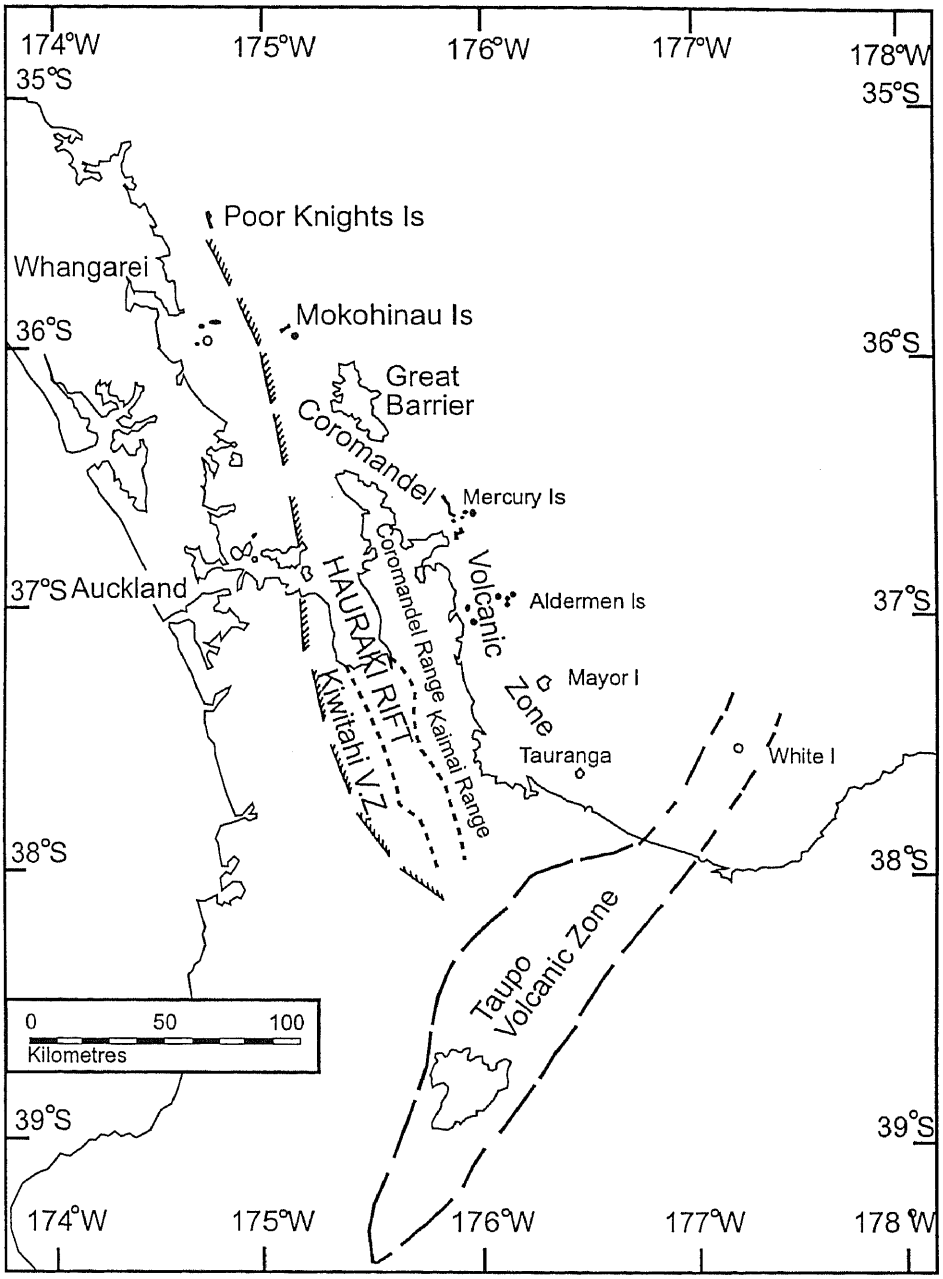

Figure 2.1: Extent of the Hauraki Volcanic Region with its' constituent Kiwitahi and Coromandel Volcanic Zones, and the Hauraki Rift (adapted from Skinner, 1986).

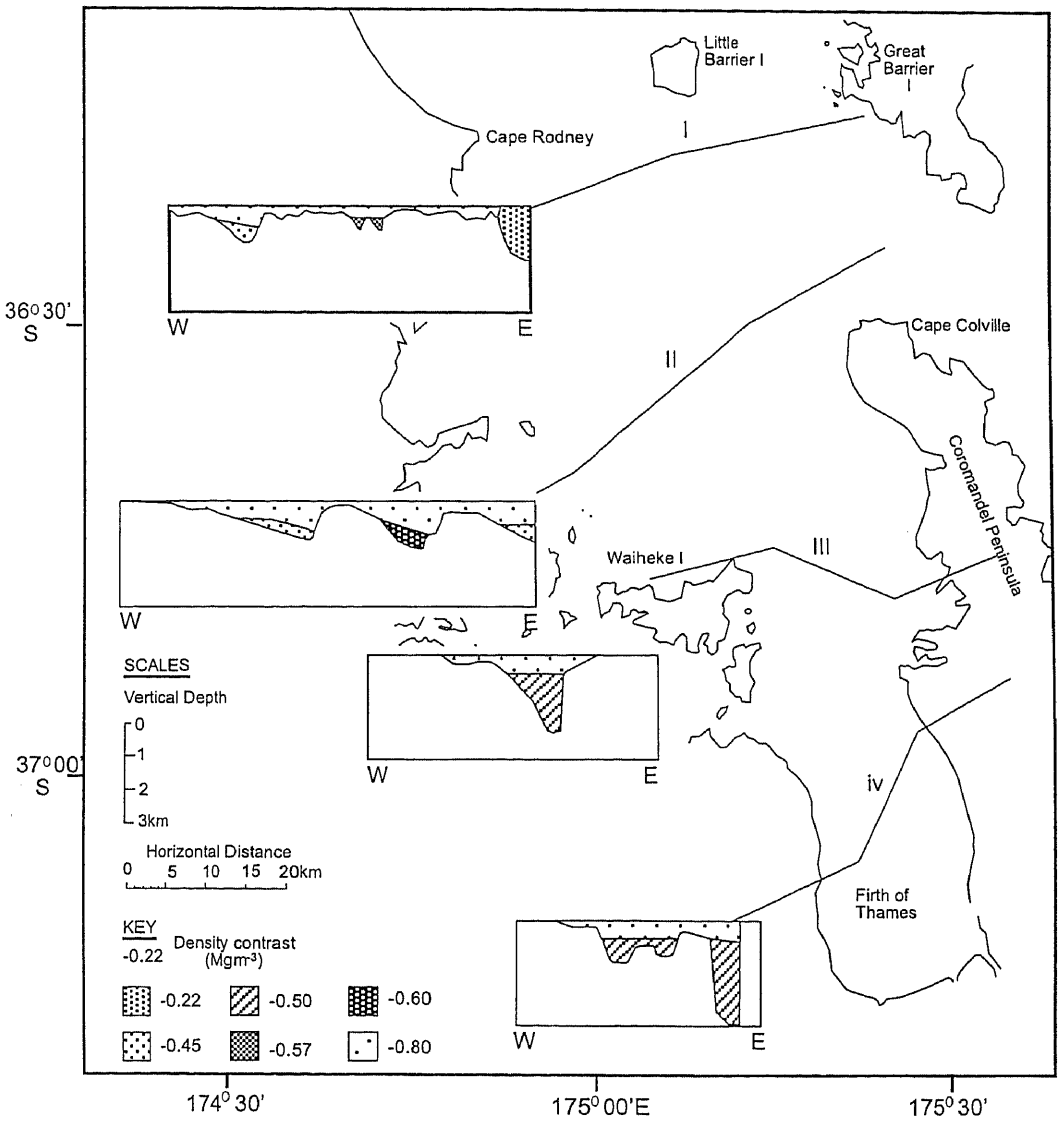

Figure 2.2: Cross-sections of Hauraki Rift (Hauraki Gulf and Firth of Thames) based on interpretation models of residual gravity anomalies and seismic reflection and refraction data (Hochstein et al., 1986).

Echograms recorded in the Hauraki Gulf were analysed by Greig (1982). Several echograms stretching across the northern Firth of Thames show evidence of recent tectonic activity.

Hochstein et al. (1986) reviewed a series of marine geophysical surveys in order to determine the structure or the Hauraki Rift and concluded:

- Tensional tectonism (horizontal tensile stress) has generated 2.5-4 km of subsidence in the narrow, central section enabling sediment deposition in

offshore regions. The velocity structure as determined by seismic profiles is consistent with unconsolidated sediments, suggesting *recent* sedimentation into newly formed grabens and fault angle depressions. An estimated 0.7-1 km of sedimentation has occurred during the Quaternary implying recent subsidence and significant sedimentation.

- A micro earthquake survey conducted near Te Aroha, on the eastern margin of the rift provides additional evidence of active rifting. This survey was conducted near Te Aroha (Figure 2.3) along a 50 km segment of the rift and detected at least one earthquake of magnitude M≥1 every 5 days, with focal depths ranging between 2 and 9 km. The focal mechanism corresponded to movement of normal faults, with a strike close to 335°, similar to that of known active faults and the strike of the rift axis (339°) (Hochstein et al., 1986).

Active subsidence within the Firth of Thames/Hauraki Rift was also suggested by Pillians (1986). Pillians investigated the last interglacial marine terraces, Holocene marine deposits and older Quaternary Marine Deposits in this region. From these data it was suggested the Hauraki Graben (within the Hauraki Rift) is a fault controlled region of subsidence, of at least 1 mm/year.

Gibb (1986) also advocated tectonic instability of the Firth of Thames region. Gibb dated 19 paleosealevels along a 50 km stretch from Kelly's Beach to Miranda, western Firth of Thames. The paleosealevel ages were at variance with the regional eustatic sealevels (Figure 2.4), suggesting tectonic uplift of the Western Firth of Thames coastline (Gibb, 1986) and indirectly implied that the Hauraki Rift is active.

While recognising the Hauraki Rift has been tectonically active in the past (thus generating grabens and fault angle depressions), Thrasher (1986) suggested the Hauraki Gulf and offshore Coromandel region (within the Hauraki Rift) is "currently largely stable" and represents a region of low tectonic activity. He observed no evidence of active seafloor fault expression, but noted that this may be due to high rates of contemporary sedimentation or poor seismic sub-bottom data quality, and

does not necessarily mean that faults within the Hauraki Rift have been inactive in the Quaternary.

More recently there has been direct evidence of the active nature of the Kerepehi Fault. De Lange & Lowe (1990) dated and correlated tephra layers across an onland segment of the Kerepehi Fault, just south of the Firth of Thames in the Kopouatai bog. The radiocarbon dates showed Quaternary movement along the Kerepehi Fault and suggest a mean recurrence interval of 2500 years. In addition, historical movements at the southern end have been observed. The most recent event occurred in the last decade and caused cracking in the vacinity of the Kopouatai Peat Bog (Figure 2.3).

Further south, trenching studies undertaken along the south-east end of the Waitoa segment (Figure 2.3) by de Lange & Hull (1994) suggest that along the Waitoa segment, surface rupture at least 1.8 m occurred between 1800-4800 years ago. The trenching studies also suggest this segment has an average recurrence interval of 4500-9000 years.

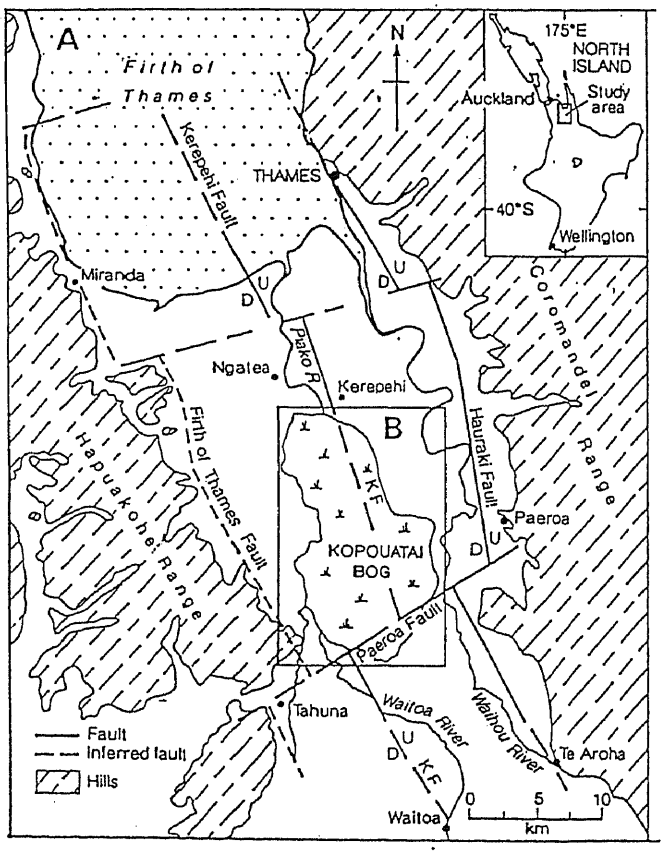

Figure 2.3: Generalised structure of the Hauraki Rift and the location of Kopouatai peat bog in the Hauraki Lowlands (from de Lange & Lowe, 1990).

2.2 WEST & EASTERN MARGINS OF THE HAURAKI RIFT

The Firth of Thames fault, a minor hinge fault, and the Hauraki Fault form the west and eastern boundaries of the Hauraki Rift. Adjacent to the western margin of the Hauraki Rift lies the Kiwitahi Volcanic Zone (Figure 2.1). Within the central region of this zone lies the Hunua-Hapuakohe Ranges, stretching from the Firth of Thames down to the southern end of the Hauraki Depression. They are composed of Jurassic meta-greywackes capped with Plio-Pleistocene andesite lava flows andesite volcanics. The absolute age range of these volcanics as determined by whole rock K/Ar dating is from 11.5-5.58 m.y. (Skinner, 1986).

On the western margin of the Hauraki Rift lies the Coromandel Volcanic Zone, consisting of the Coromandel and Kaimai Ranges. The geology is this region is varied but is composed predominantly of pre-Quaternary volcanic rock and associated intrusives. Late Jurassic marine sedimentary rocks form the basement which is overlain in places by restricted, non-volcanogenic Oligocene coal measures and calcareous marine rocks, minor quantities of volcanogenic conglomerate and marine sandstone and siltstones (early Miocene in age). Overlaying this is a wide variety of igneous rock types, ranging from sub-volcanic hypabyssal & plutonic rock complexes, to basalt and ignimbrite.

2.3 HOLOCENE SEA LEVEL FLUCTUATIONS

Knowledge of sea level changes over the period that sediment was deposited in the upper 80 m (depth of seismic profiles – refer to Chapter 4) of the Firth of Thames provides some indication of sediment age in locations where core data is unavailable for dating. Glacial sealevel lows are observed within the seismic profiles (refer to Chapter 3) as strong unconformities. Providing these unconformities can be identified and correlated some age constraints can be placed upon the last movement observed along the Kerepehi Fault.

Some of the earliest estimates of sea level fluctuations in the Firth of Thames were made by Schofield (1960) through the interpretation of chenier ridge elevations and locations at Miranda. The fluctuations determined by Schofield (1960) were made under the assumption that tectonic movement within this region was negligible, and that each chenier ridge represented a storm tide berm level. Past sea levels were then estimated by radiocarbon dating of shells present on each chenier crest. From these dates Schofield (1960) suggested sealevel from approximately 2.1 m (7ft) between 4000 ka to 2000 ka to the present day level and has remained relatively stable since. In order to determine whether the above results were local or regional, the same technique was applied to beach ridge systems extending 270 km north and 55 km east from Miranda (Schofield, 1973). The results of the second study revealed that post-glacial sea-level changes were consistent over a distance of at least 270 km, and therefore suggest eustatic sea-level has risen a maximum of 2 m above present during post-glacial times.

Greig (1982) researched marine sediments within the Hauraki Gulf and upholds that the sediments in the Hauraki Gulf and Firth of Thames record 2 phases of sea-level rise during the last 14 000 years. The first phase began 14 000 years ago and ended as sea-level stabilised at a few tens of metres below present. The 2nd phase occurred between 7250-6500 years b.p. when sea-level rose rapidly (Gibb, 1979) to present day sea-levels.

Gibb (1986) radiocarbon dated 103 samples thought to represent paleosea-levels from around New Zealand. The results suggested that at approximately 10 ka, eustatic sea-level rose from –33.5±2.5 m below present sea-level with stillstands and associated sea level decreases occurring between 9.2 to 8.4 ka (-24.0 ± 2.9 m) and 7.5 to 7.3 ka (–9.0 ±2.8 m). The current marine transgression then culminated at the present sea level at about 6.5 ± 0.1 ka but has since undergone minor fluctuations involving a maximum increase of 0.5 m at 3.5 ka, and maximum decrease of –0.4 at 4.5 ka (Refer to Figure 2.4 from Gibb, 1986). Radiocarbon dating of in-situ sub-fossil molluscs by Woodroffe et al. (1983) generated a slightly larger maximum transgression of 0.8±0.1 m, peaking at approximately 3.6 ka. Woodroffe et al. (1983) propose that this was

followed by a regressive period which ceased at approximately 1.2 ka at around the present day sea level.

An alternative interpretation was offered by Pillans (1986) after producing an uplift map developed using data from the last interglacial marine terraces, Holocene marine deposits and older Quarternary Marine Deposits. Pillans (1986) suggests that the data presented by Schofield (1960) and Woodroffe (1983) could indicate 0.9 mm/yr and 0.2 mm/yr of uplift assuming sea level has not fluctuated more than 1m in the last 6500 years.

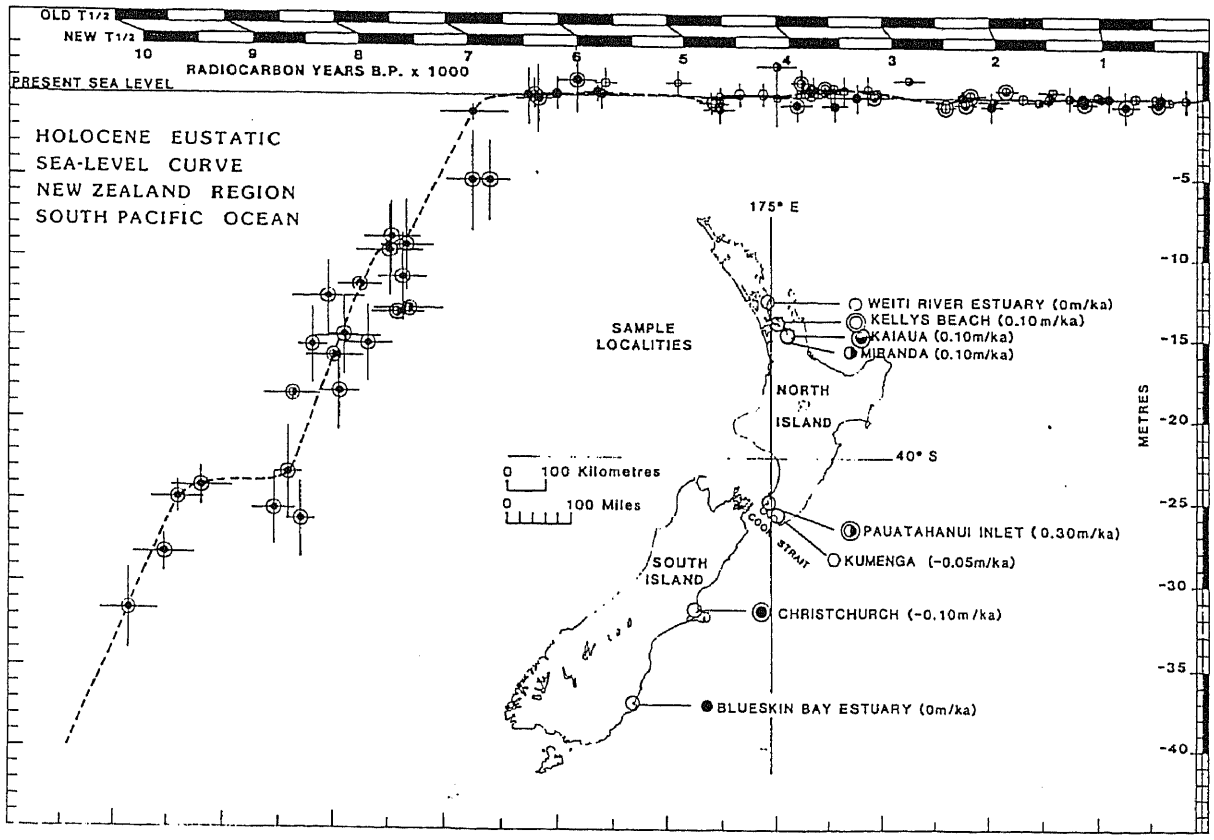

Figure 2.4: New Zealand regional Holocene eustatic sea-level curve relative to the present sealevel. Symbols represent data from each site and bracketed values are tectonic uplift (positive values) and downdrop (negative values) rates in metres per 1000 years (m/ka) (From Gibb, 1986).

2.4 SUMMARY

The Hauraki Rift is bounded to the west and east by the Kiwitahi Volcanic Zone (Hunua-Hapuakohe Ranges) and the Coromandel Volcanic Zone (Coromandel & Kaimai Ranges) respectively. The rift is bisected by the Kerepehi Fault which trends NNW through the central Firth of Thames. Review of the literature suggests the Hauraki Rift is currently subsiding and that the Kerepehi Fault is active, therefore having tsunamigenic potential.

2.5 REFERENCES

de Lange, P.J., and Lowe D.J., 1990. History of vertical displacement of Kerepehi Fault at Kopouatai bog, Hauraki Lowlands, New Zealand, since c. 10 700 years ago., *New Zealand Journal of Geology and Geophysics*, Vol. 33, p. 277-283.

de Lange, W.P., and Hull, A.G., 1994, Tsunami Hazard for the Auckland Region, Unpublished report prepared for the Auckland Regional Council, 37 p.

Gibb, J.G., 1986. A New Zealand regional holocene eustatic sea-level curve and its application to determination of vertical tectonic movements: A contribution to IGCP-Project 200., In W.I. Reilly and B.E. Harford (eds). *Recent Crustal Movements of the Pacific Region*, Royal Society of New Zealand Bulletin 24. Wellington, The Royal Society of New Zealand, p. 377-395.

Gibb, J.G., 1979. *Late Quaternary shoreline movements in New Zealand.* Unpublished Ph.D. thesis, Victoria University of Wellington, 217 p.

Greig, D.A., 1982. *Sediments and recent geological history of the Hauraki Gulf, Firth of Thames & Colville Channel, North Island, New Zealand*, M.Sc. Thesis, University of Auckland, New Zealand.

Hochstein, M.P., and Nixon, I.M., 1979. Geophysical study of the Hauraki Depression, North Island, New Zealand, *New Zealand Journal of Geology and Geophysics*, Vol. 22, p. 1-19.

Hochstein, M.P., Tearney, K., Rawson, S., Davey, F.J., Davidge, S., Henrys, S., and Backshall, D., 1986. Structure of the Hauraki Rift (New Zealand), In W.I. Reilly and B.E. Harford (eds). *Recent Crustal Movements of the Pacific Region*, Royal Society of New Zealand Bulletin 24. Wellington, The Royal Society of New Zealand, p. 334-348.

Pillans, B., 1986. A Late Quaternary uplift map for North Island, New Zealand, In W.I. Reilly and B.E. Harford (eds). *Recent Crustal Movements of the Pacific Region*, Royal Society of New Zealand Bulletin 24, Wellington, The Royal Society of New Zealand, p. 409-417.

Schofield, J.C., 1960. Sea level fluctuations durng the last 4000 years as recorded by a chenier plain, Firth of Thames, *New Zealand Journal of Geology and Geophysics*, Vol. 3, p. 467-485.

Schofield, J.C., 1973. Post-glacial sea levels of Northland and Auckland, *New Zealand Journal of Geology and Geophysics*, Vol. 16, p. 359-366.

Skinner, D.N.B., 1986. Neogene Volcanism of the Hauraki Volcanic Region, In Smith, I.E.M. (ed), *Neogene Volcanism of the Hauraki Volcanic Region*, The Royal Society of New Zealand Bulletin 23, Wellington, The Royal Society of New Zealand, p. 21-47.

Thrasher, G.P., 1986. Casement structure and sediment thickness beneath the continental shelf of the Hauraki Gulf and offshore Coromandel region, New Zealand, *New Zealand Journal of Geology and Geophysics*, Vol. 29, p. 41-50.

Woodroffe, C.D., Curtis, R.J., and McLean, R.F., 1983. Development of a chenier plain, Firth of Thames, New Zealand, *Marine Geology*, Vol. 53, p. 1-22.

Chapter Three

SEISMIC METHODOLOGY

3.1 INTRODUCTION

In order to identify potential tsunami source regions, the location and movement history of offshore segments of the Kerepehi Fault were estimated. This required an understanding of offshore stratigraphy and structure, which was obtained through analysis and interpretation of existing seismic reflection data. This chapter discusses the various data sets available for characterisation of the Kerepehi Fault zone and the method used to analyse the seismic sequence stratigraphy of the sediments represented in these data sets.

3.2 THE DATA SETS

3.2.1 Collection

The Kerepehi Fault is known occur within the Firth of Thames (Hochstein et. al., 1986) and is likely to extend further north into the Hauraki Gulf; the seismic data used for interpretation were collected within these regions. Seismic data from four different sources were examined and used to interpret the location and movement history of the Kerepehi Fault (Table 3.1).

Table 3.1: Table summarising the four data sources used for this study.

Data collected by:	Year collected:	Ship name:
NIWA - cruise 1007	1973	RV Tangaroa
University of Waikato	1990	Asterix
N.Z. Defence Scientific Establishment & University of Waikato	1990	H.M.N.Z.S. Tui
NIWA - cruise 3026	1995	RV Tangaroa

3.2.2 Equipment & System Set-up

Defence Scientific Establishment (D.S.E) & University of Waikato Data:

The University of Waikato collected sub-bottom profiles in conjunction with D.S.E. (or "Defence Operation Technical Support Institution" (D.O.T.S.E.), as it is currently called) during the 25, 26 and 27th of September 1990. A Ferranti Ocean Research Equipment (O.R.E.) sub-bottom profiling system (Figure 3.1) employing the GeoPulse Model 5420A Power Supply, the GeoPulse model 5210A Receiver (Figure 3.2a.), the Model 5813A Acoustic Source upon a Model 5812A Catamaran Tow Vehicle Figure (3.2b) and an 'eel' composed of 10 hydrophones in an oil filled urethane tube were used to collect the data. A Linescan recorder (Raytheon) produced the graphics (Figure 3.2c) (Refer to Appendix 2 for Equipment specifications).

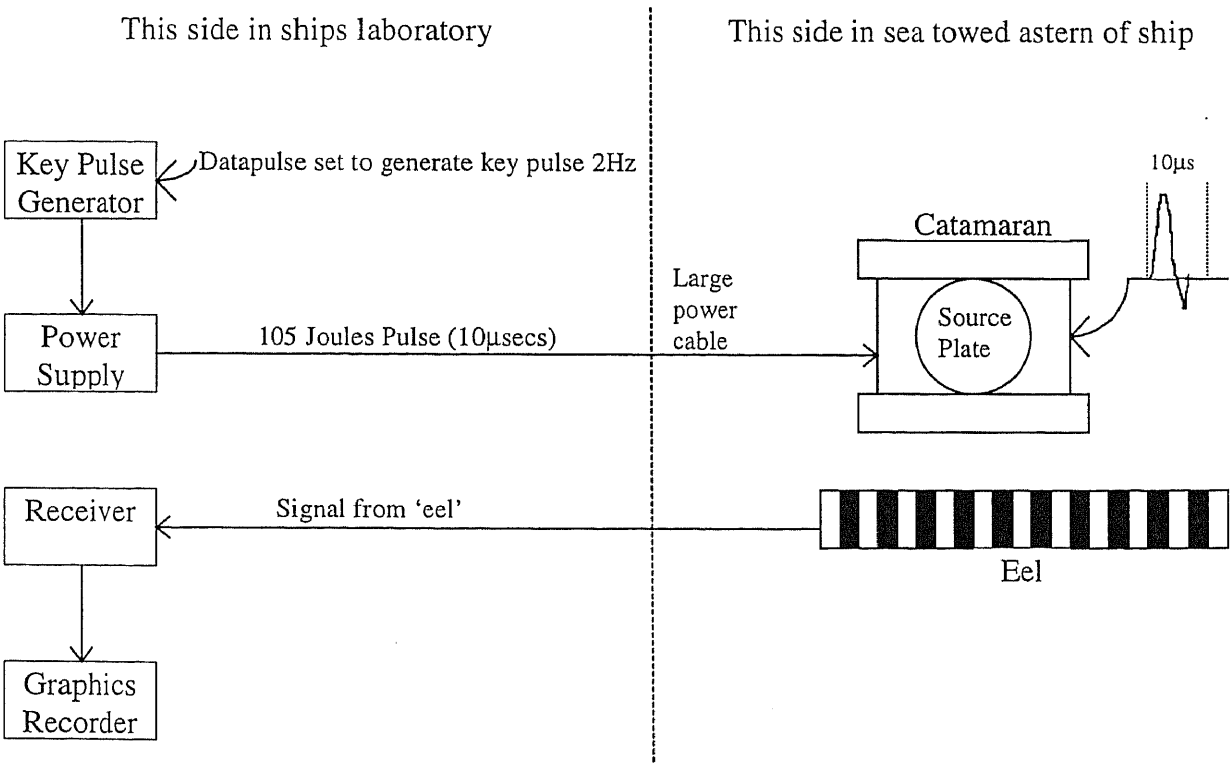

Figure 3.1: Geopulse set-up for data generated 25-27 September 1990, collected by the D.S.E.

Figure 3.2a: Geopulse model 5210A Receiver sitting upon the Geopulse model 5420A Power Supply.

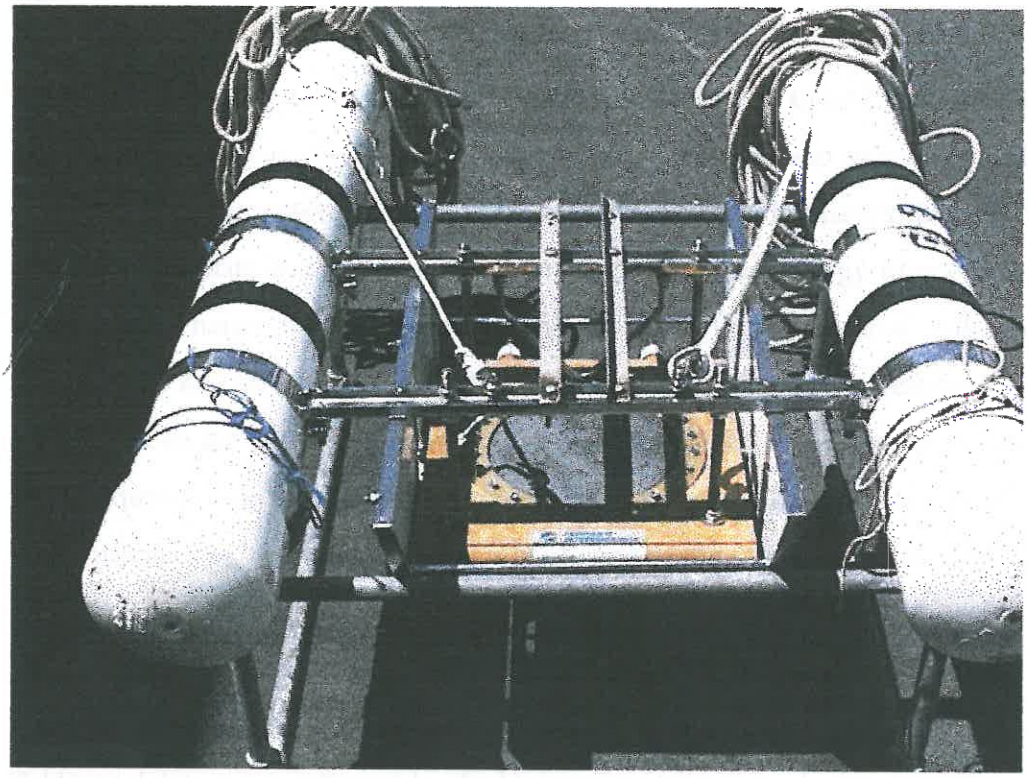

Figure 3.2b: Model 5813A Acoustic Source sitting within the Geopulse model 5812A Catamaran Tow Vehicle.

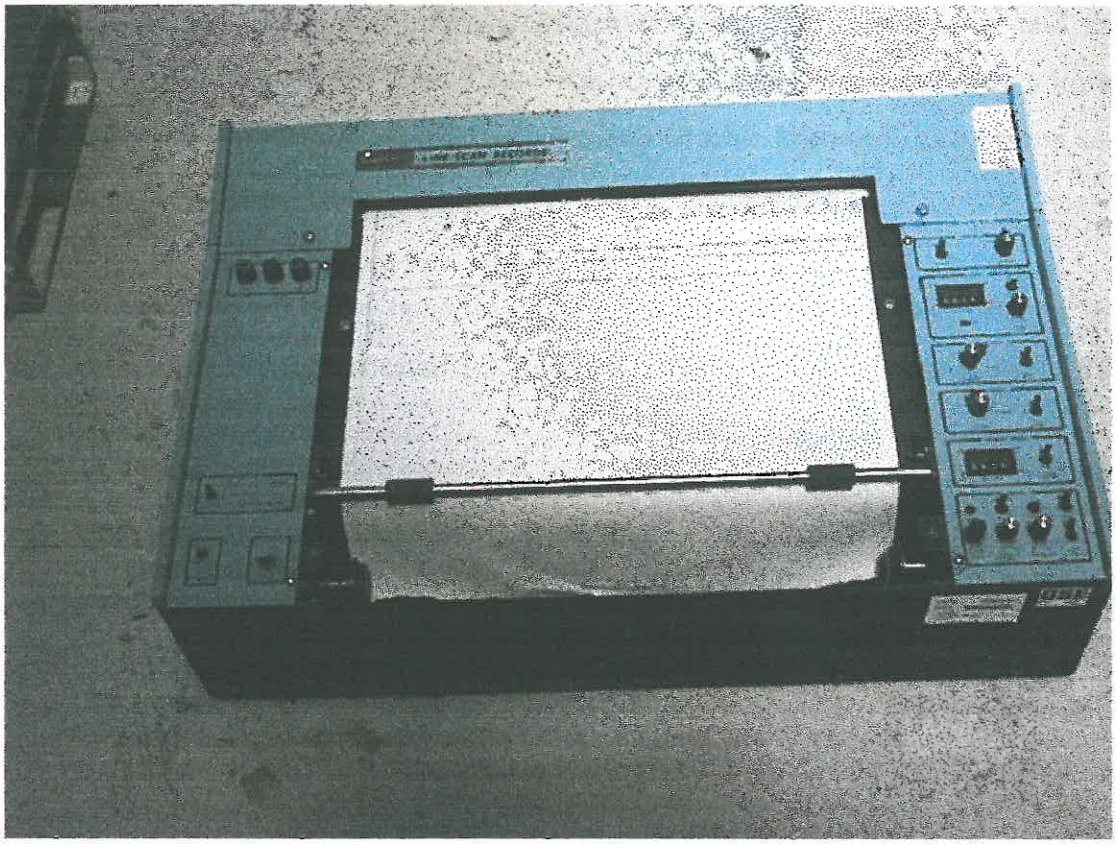

Figure 3.2c: Linescan recorder (Raytheon).

The key pulse generator initiates and transmits a series of 'square' pulses at a rate of 2Hz to the power supply. This triggers the power supply and generates a 105 Joule charge to energise a storage capacitator. The capacitator discharges the stored energy to the source plate in the catamaran, converting electrical energy to acoustic energy. An acoustic energy pulse is generated and travels to the ocean floor and sub-bottom strata where it is reflected. The 'eel' (10 hydrophones) detects the reflected signal and transmits it to the geopulse receiver. The geopulse receiver has the option of filtering high frequencies, low frequencies and swell sea waves. The signal is then transferred to the graphics recorder which prints a hard copy of the seismic profile.

University of Waikato Data:

Additional data were collected by the University of Waikato during the 16th and 17th of November 1990 using a similar system, also employing the Ferranti Ocean Research Equipment (O.R.E.) GeoPulse Sub-bottom profiling system (Figure 3.3). This system comprised of the Model 5420A power supply (Figure 3.2a), Model 5813A geopulse

acoustic source (Figure 3.2b), Model 5110A geopulse hydrophone array and the 5210A Geopulse Receiver (Figure 3.2a). The returned signal was recorded on a lower resolution graphic recorder, the EPC Model 4800 Graphic Recorder. The system set-up is outlined below (Figure 3.3).

This system operated in the same way as the D.S.E equipment (outlined above), but did not employ the sophisticated filtering mechanism, custom developed by D.S.E. (Refer to Section 3.3).

NIWA Data:

Data collected during NIWA cruises 3026 (RV *Tangaroa*, 1995) and 1007 (RV *Tangaroa*, 1973) were also examined. 3.5 kHz profiles, made available courtesy of Barbara Manghetti, NIWA, were obtained using an ORE 16-element, hull-mounted system (Manighetti and Carter, in press). The 1007 cruise employed a 3.5 kHz high resolution seismic system by EDO Western which recorded on a 'wet paper' ocean sonic recorder.

3.2.3 Determination of Data Location

Defence Scientific Establishment (D.S.E.) Data:

The seismic lines gathered by the University of Waikato and the Defence Operational Technical Support Est. (D.S.E.) are archived at the University of Waikato. While collecting the seismic data, the D.S.E. employed a Del Norte Trisponder navigational system. This system is accurate to 3 m. During the seven year period between collection and interpretation, these logged navigational records were unfortunately discarded. Consequently, for this study it was possible only to refer to extracts from the ship's log to estimate seismic track location. As a result, some track locations are inexact (Figure 3.4).

Data collected on the 25-26 September 1990 included:

Tracks: J (W11 - W12)
K (W13 - W14)
F (W20 - W21)
E (W22 - W23)

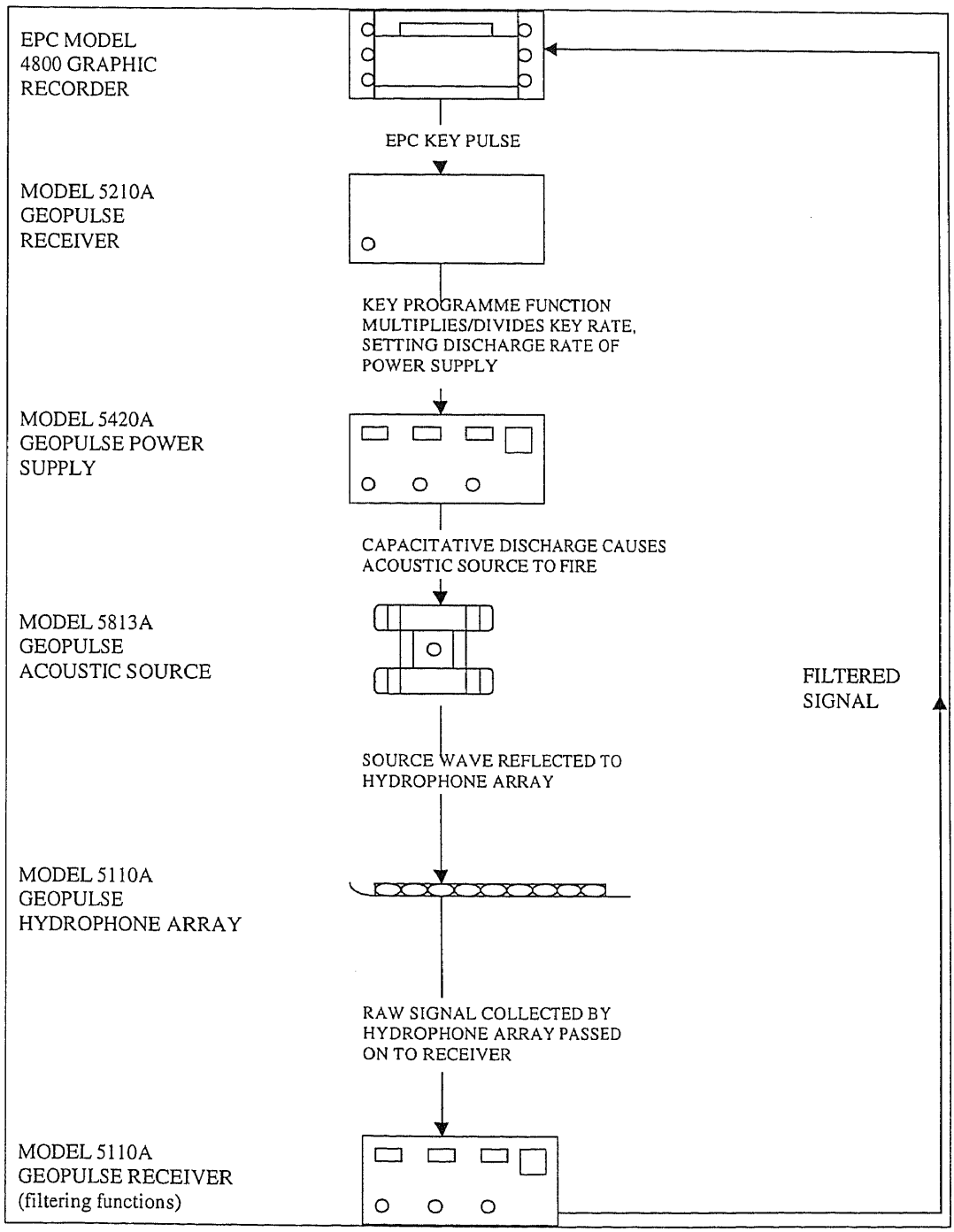

Figure 3.3: Seismic Sub-bottom profiling system set-up (Allan, 1990) for data generated on the 16 & 17 November 1990, collected by the University of Waikato.

An extract from the ship's log containing the track start and finish positions (degrees latitude) was forwarded by George Crook, D.O.T.S.E. The ship was assumed to have moved in a straight line between the track start and finish points.

Data collected on 27 September 1990 included:

Tracks:	H	(1459-1550)
	L	(1554-1630)
	I	(1655-1810)
	G	(1852-1935)
	M	(2130-2225)
	N	(2229-2311)

For data collected on the 27 September 1990, the ship's track during the period of data collection between 14:59 and 23:11 hours was estimated using the ships log (forwarded by George Crook) and the Dead Reckoning method[1].

The ship's position at 1200 & 2000 hrs (in degrees latitude and longitude) was used as the starting point for the Dead Reckoning method. The "Estimated distance run through water (nautical miles)" and "True bearing" were used to interpolate and extrapolate the ship position. Recorded tape positions for 1708-1810 hrs (Track I; forwarded by George Crook) were converted from eastings and northings on the North Island National Metricated Grid to degrees latitude and longitude. These, and the ship's position at 0800, 1200 & 2000 hrs provided the only accurate ship location during 27 September, 1990.

In addition, notes recorded on the seismic lines e.g. EOL (end of line), turning to port etc were used to obtain more accurate temporal estimates (& therefore spatial estimates) of when the boat finished a track, or changed course.

[1] Dead Reckoning Method: Method of calculating boat location, using a known starting point and extrapolating future locations using boat speed and direction of travel. If known, wind and tide data can also be incorporated into the method.

University of Waikato Data:

Data collected on the 16 November 1990 included:

Tracks: A (recorded as line 2 on raw data)

Data collected on the 17 November 9, 1990 included:

Tracks: D (recorded as line 3 on raw data)

C (recorded as line 4 on raw data)

B (recorded as line 5 on raw data)

The track location for data collected by the University of Waikato was mapped using Radar ranging, supplemented by McGellan GPS when satellites were available (W.P. de Lange, pers. comm.), (Figure 3.4).

NIWA data:

Seismic data plus maps illustrating boat track location and collection time were provided by NIWA (Wellington). The track location for data collected on cruise 3026 (1995) was mapped using differential GIS.

The boat track for all analysed data collected in the above cruises is illustrated in Figure 3.4.

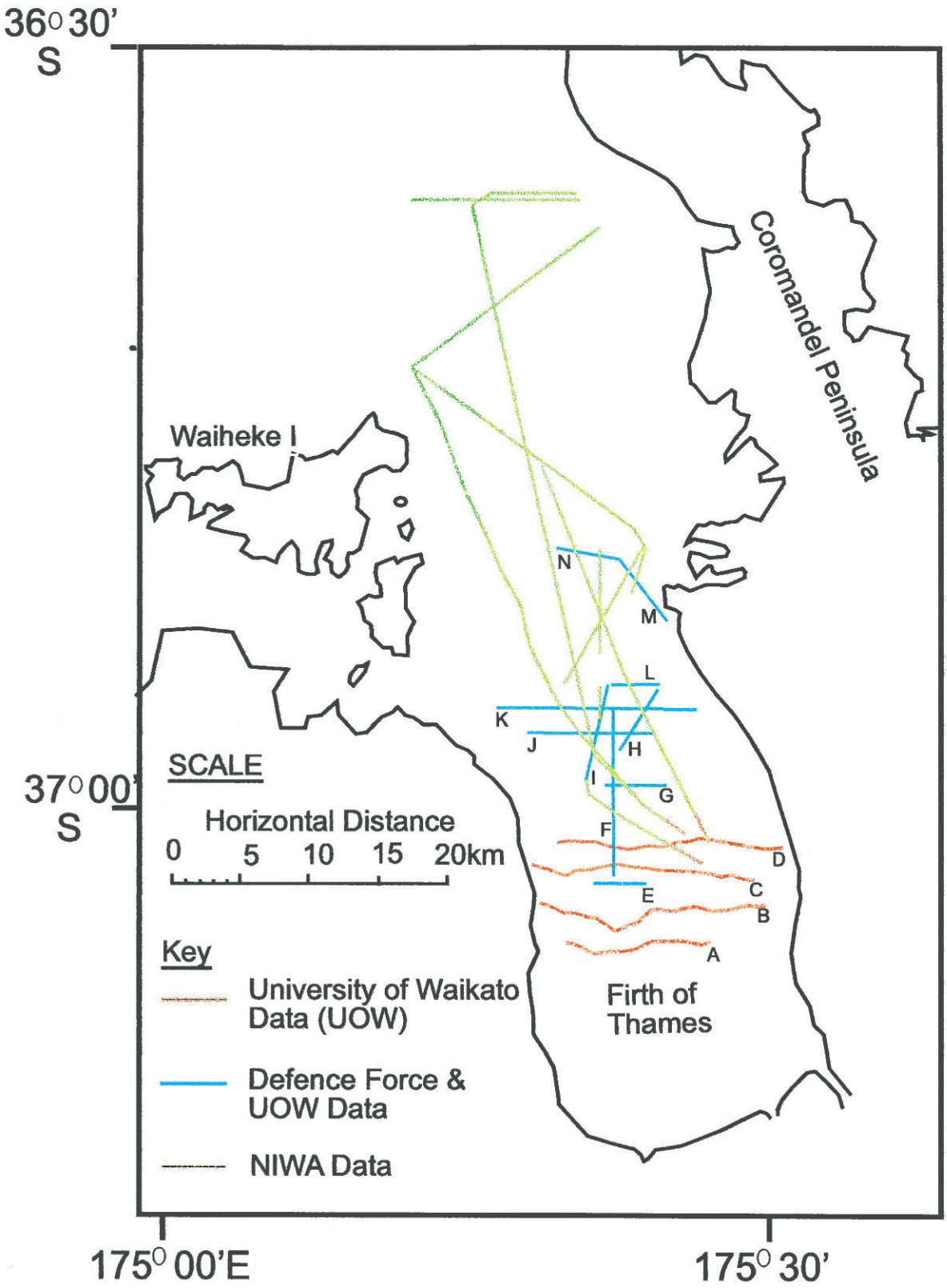

Figure 3.4: Vessel tracks of seismic sub-bottom records from various cruises used in this study.

3.2.4 Determination of Vertical and Horizontal Scale

Defence Scientific Establishment & University of Waikato 1990 Data:

Vertical Scale: The Linescan graphic recorder (Raytheon) employed by the Defence Scientific Establishment produced seismic sub-bottom profiles with 20 divisions, each spaced 5 mS (TWT) apart (Figure 3.5).

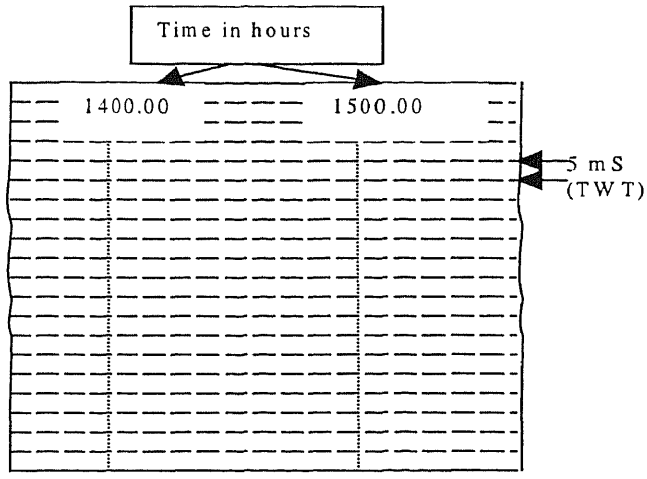

Figure 3.5: An example of graphical output format for data collected by the D.S.E.

Horizontal Scale: The horizontal scale represented on the profiles varied with boat speed. Once the boat track had been plotted (by Dead Reckoning method), the horizontal scale of the profiles could be determined. The boat track provided the track location at a given time of the day. The sub-bottom profile collection time was recorded at the top of the profile. Hence, the actual distance between two times recorded on the profiles was determined and distance (km) was linearly interpolated and recorded on the top of each profile.

University of Waikato 1990 Data:

Vertical Scale: The EPC model 4800 Graphic recorder overlaid the seismic profile with 25 dashed lines, breaking the profile into 25 divisions (Figure 3.6). The span (m) that the profile covered is printed at regular intervals at the top of the seismic profile. This span ranged from 25 - 40 metres and was calculated assuming a sound velocity of 1460ms^{-1} (EPC model 4800 Graphic Recorder instruction manual). The two way

travel time per division was then calculated e.g. given 40 m span with 25 divisions, each division corresponds to a distance of 1.6 m. This was then converted to two-way-travel time by dividing by $1460ms^{-1}$: $1.6m/1460ms^{-1} = 1.1$ msec.

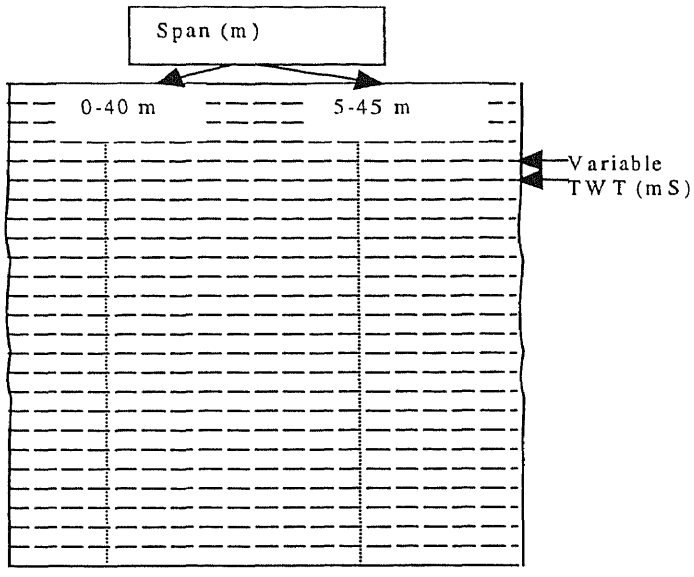

Figure 3.6: Figure illustrating format of graphical output for data collected by University of Waikato.

Horizontal Scale: The original map showing the boat track location also illustrated position fix number along side the boat track. This position fix number was also recorded on the raw profiles and consequently could be used to determine the horizontal scale of the seismic sub-bottom profiles.

NIWA 1995 Data:

Vertical scale: Water depth and sediment depth scales were provided by Barbara Manighetti, Wellington NIWA. These were generated assuming a sound velocity of 1500 $m.s^{-1}$ in water and $1600m.s^{-1}$ in sediment.

Horizontal scale: Maps accurately illustrating boat track location and collection times were provided by NIWA (Wellington). The collection time was recorded at regularly spaced intervals on the raw data (seismic sub-bottom profiles) and was consequently used to determine the horizontal scale.

3.2.5 Impact of Data Quality

Data quality and availability determined how thoroughly the data were analysed and the extent to which they could be used to draw conclusions. The seismic sub-bottom profile data provided by NIWA were used to obtain a rough estimate of fault location. Detailed analysis was not possible, as only photocopied data were available.

The data collected by the University of Waikato and the D.S.E are of higher quality, allowing the seismic stratigraphy to be determined. Seismic stratigraphy interpretation relies on a variety of reflector geometry's that are inferred to represent onlap, toplap, downlap of strata (Figure 3.8). Not all seismic lines showed evidence of these features and consequently were not developed into profiles e.g. line 6. Other lines show intense noise interference (e.g. line 1) making identification of discernible reflectors an impossibility. In addition, line 1, being the first of all 6 lines collected by the University contained numerous changes of filters, boat speed, Time Varying Gain (TVG) and delay system adjustments and changes in the Acoustic Source frequency. Consequently this line had very few, intermittent patches of clear readable seismic signal and was not analysed.

The criteria used to identify reflectors and determine the seismic stratigraphy is outlined below.

3.3 SEISMIC STRATIGRAPHY ANALYSIS METHOD

3.3.1 Introduction

Primary seismic reflections are usually generated from physical surfaces within the rock, such as: (i) stratal (bedding) surfaces & (ii) unconformities with velocity/density constrasts. A seismic reflection is inferred to represent an isochronous surface *except* where the reflection surface is an unconformity identified by toplap, baselap, onlap or truncation (Brown et al., 1980). i.e. seismic sections represent "chronostratigraphic

(time-stratigraphic) depositional and structural patterns and not a record of the time-transgressive lithostratigraphy (rock-stratigraphy)" (Vail et al., 1977) (Refer to Figure 3.7).

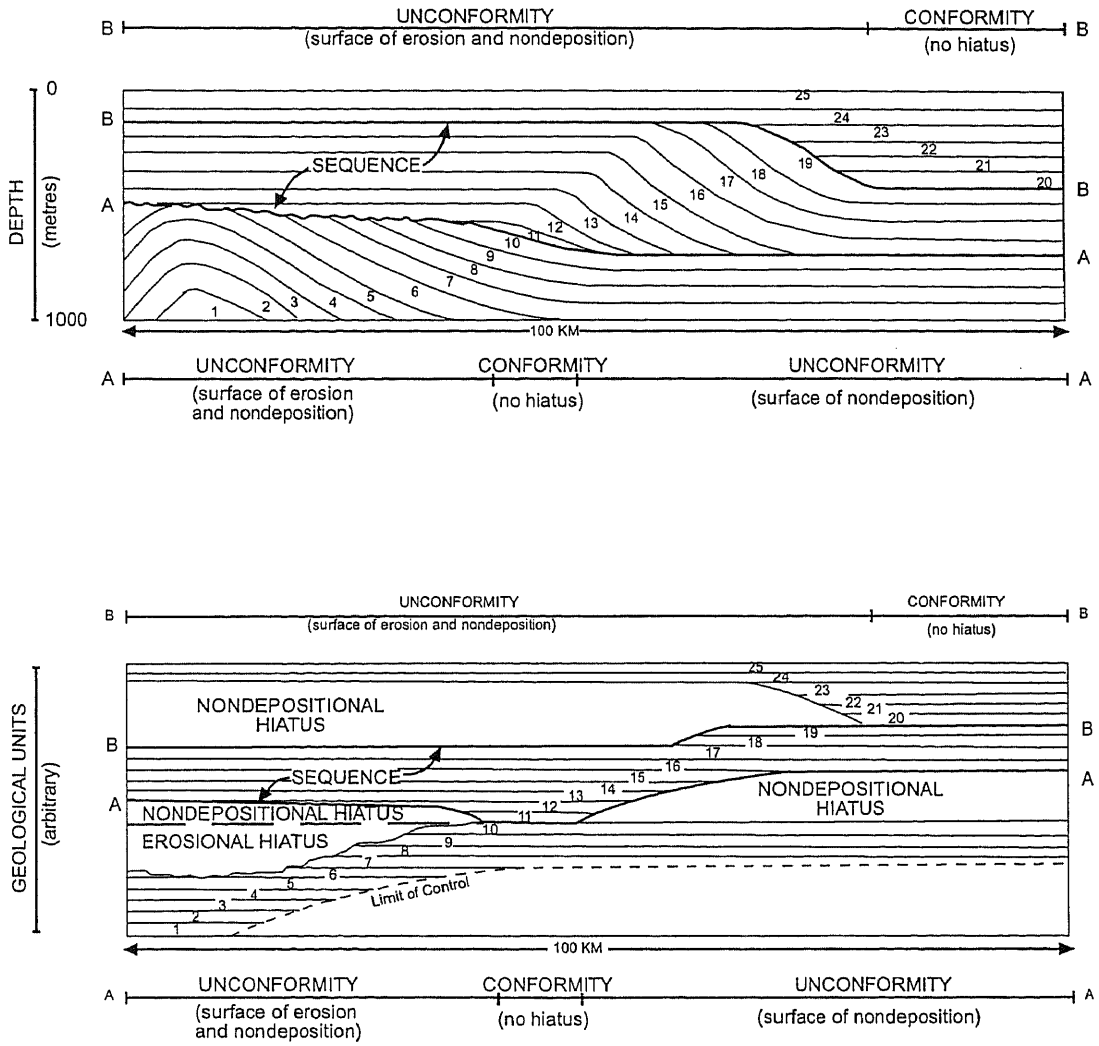

Figure 3.7: Figure illustrating that seismic reflection occurs along stratal boundaries (chronostratigraphic units) as opposed to lithostratigraphic units which have gradational boundaries unless an unconformity is present. A) Generalised stratigraphic section of a sequence. B) Generalised chronostratigaraphic section of a sequence (from Mitchem et al., 1977).

With the aid of chronostratigraphy, seismic reflections have the potential to determine (i) geologic correlation, (ii) definition of genetic depositional units, (iii) thickness and depositional environment of genetic units, (iv) paleobathymetry, (v) burial history, relief & topography on unconformities, and (vii) paleogeography and geologic history when combined with other geologic data (Vail & Mitchum, 1977). However, the objectives of this study only require the postdepositional and/or syndepositional

structural deformation to be determined. Hence the seismic sections from the Firth of Thames were analysed only to estimate the location and displacement along the Kerepehi Fault. This was achieved through the identification of displacement of depositional sequences and sequence boundaries.

3.3.2 Limitations

In order to make stratigraphic conclusions from seismic data, high quality recording and processing is recommended so that seismic noise may be removed (Sheriff, 1977; Refer to Appendix 3). This provides a seismic section where wave shape variations essentially represent variations in subsurface rather than changes in noise (Sheriff, 1977). As only unprocessed, raw data was available for this study, the noise (e.g. multiples and diffraction umbrellas) and horizontal travel paths have not been removed (has not been migrated), and therefore the reflections have not been repositioned before being interpreted. In addition, no well log data is available to supplement seismic sections, hence the seismic profiles should not be considered to quantitatively reflect the geometry of a geological cross-section.

3.3.3 Criteria for Identifying Boundaries

Depositional Sequences:

The results of the seismic sequence analysis were summarised on simplified profiles that illustrate the stratigraphic relationship between depositional sequences. A depositional sequence is a stratigraphic unit composed of a relatively conformable succession of chronostratigraphically constrained, genetically related strata and bounded at it's top and base by unconformities or their correlative conformities (Mitchum, et al., 1977; Vail, 1987) (Figure 3.7).

The strata within a depositional sequence may have concordant or discordant relations to the sequence boundary. "Discordance is the main physical criterion used in the determination of sequence boundaries. The type of discordant relation is the best

indicator of whether an unconformity results from erosion or non-deposition." (Mitchum et al., 1977). Onlap, downlap and toplap are indicators of non-depositional hiatus (Figure 3.8). Truncation of reflectors defines an erosional hiatus unless the truncation is a result of structural disruption (Refer to Appendix 5). All possible geometric relations of strata to boundaries of depositional sequences are outlined in Figure 3.8.

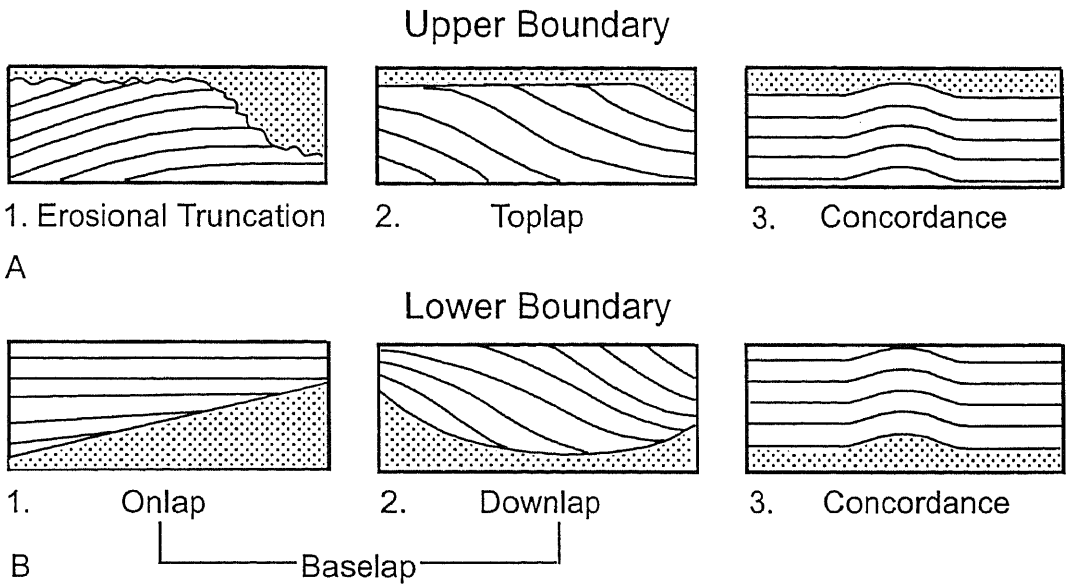

Figure 3.8: Relations of strata to boundaries of depositional sequences (From Mitchum et al., 1977):

- **A.** Relations of strata to upper boundary of a sequence. **A1.** Erosional truncation: strata at top of given sequence terminate against upper boundary mainly as result of erosion (e.g., tilted strata terminating against overlying horizontal erosion surface or horizontal strata terminating against later channel surface). **A2.** Toplap: initially inclined strata at top of given sequence terminate against upper boundary mainly as result of nondeposition (e.g., foreset strata terminating against overlying horizontal surface at base-level equilibrium where no erosion or deposition took place). **A3.** Top-concordance: relation in which strata at top of given sequence do not terminate against upper boundary.
- **B.** Relations of strata to lower boundary surface of a sequence. **B1.** Onlap: at base of sequence initially horizontal strata terminate progressively against initially inclined surface, or initially inclined strata terminate updip progressively against surface of greater initial inclination. **B2.** Downlap: at base of sequence initially incline strata terminate down dip progressively against horizontal or inclined surface (e.g., initially incline strata terminating against underlying initially horizontal surface). **B3.** Base-concordance: strata at base of sequence do not terminate against lower boundary.

Seismic System Tracts:

Depositional sequences can be further divided into a predictable succession of systems tracts (Figure 3.9, from Vail, 1987; Posamentier & Vail, 1988). A systems tract is a linkage of contemporaneous depositional systems and is a function of the interaction between eustasy, sediment supply and tectonics (Van Wagoner et al, 1988). Four types of system tract are recognised: lowstand, transgressive, highstand and shelf-margin. Sequences commonly consist of a well developed low stand systems tract, followed by a transgressive system tract ending with a truncated high stands systems tract (Bradshaw, 1991). A lowstand systems tract develops when eustatic sea level fall is greater than subsidence of the depositional-shoreline break (uppershore face) giving rise to subaerial exposure of sediments and valley incision. As sea level rises, incised valleys are infilled and a marine flooding (transgressive) surface develops. Landward of the low stand systems tract the marine flooding (transgressive) surface truncates the underlying strata and coincides with the lower sequence boundary. As sea level rises, transgressive system tract sediment onlaps the underlying marine flooding surface. As increasingly younger sediment is deposited the transgressive system tract is progressively emplaced landward causing the upper surface to backstep in a landward direction. The transgressive systems tract is upwardly bound by a maximum flooding surface upon which prograding highstand coastal and shelf sediment downlaps (Van Wagoner, 1990).

Application of the above Criteria:

The seismic sub-bottom profiles collected by the Waikato University and the New Zealand Defence force were carefully scrutinised in order to identify any of the above stratal relationships (Figure 3.8). The sequence boundaries within seismic profiles were usually identified as unconformities, where a discordant relation between strata occurs. However, some boundaries are concordant with the underlying/overlying stata. In this case the strength of the reflection was used to identify the boundary. i.e. Concordant but incongruously strong reflectors were correlated with discordant boundaries and hence assumed to be a sequence boundaries. Each sequence boundary was labelled with a colour (Figure 3.10) and traced along the length of each seismic profile.

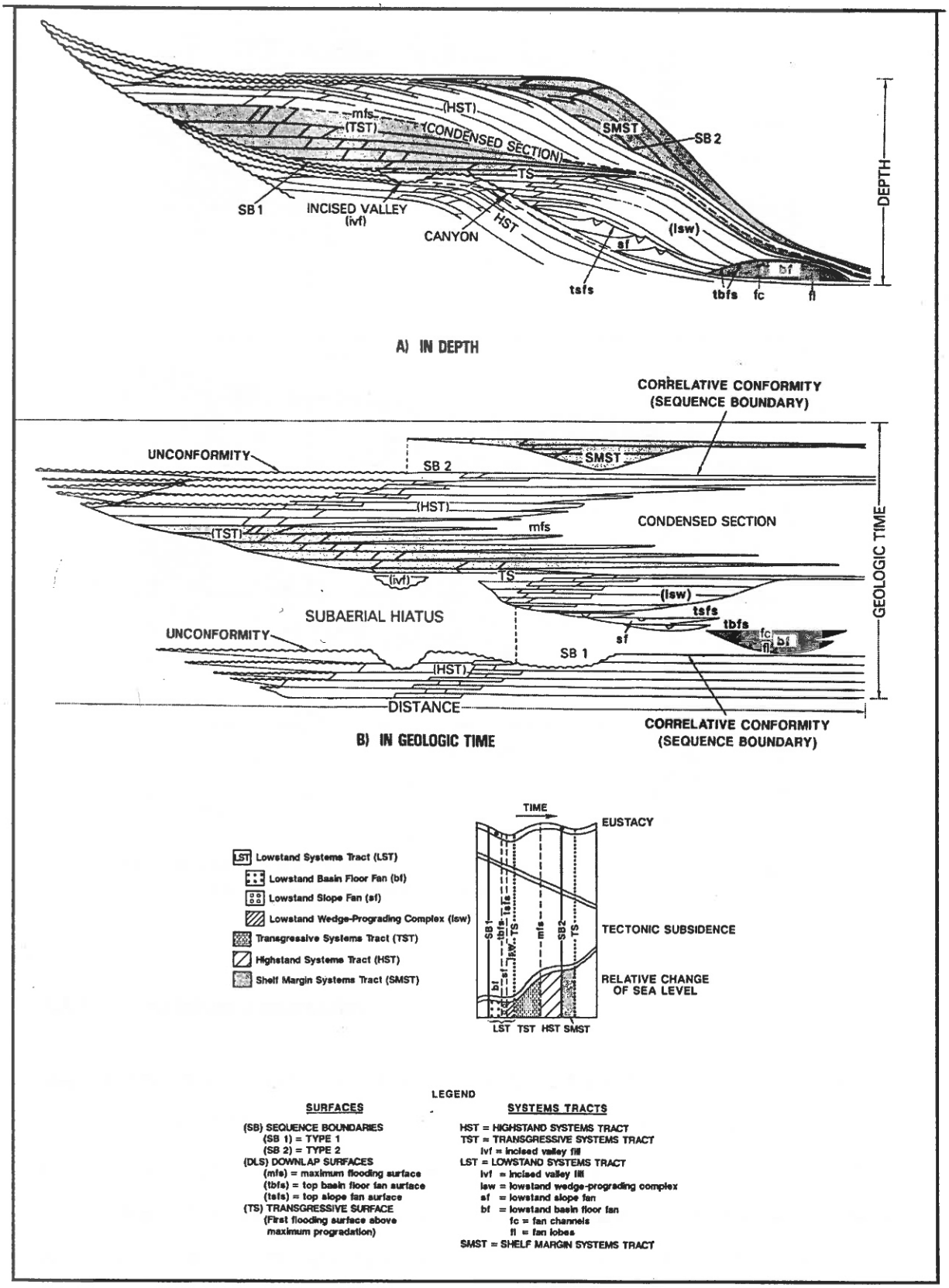

Figure 3.9: Sequence stratigraphy diagrammatic section showing sequences and systems tracts in depth and geologic time (From Vail, 1987).

Figure 3.9: Sequence stratigraphy diagrammatic section showing sequences and systems tracts in depth and geologic time (From Vail, 1987).

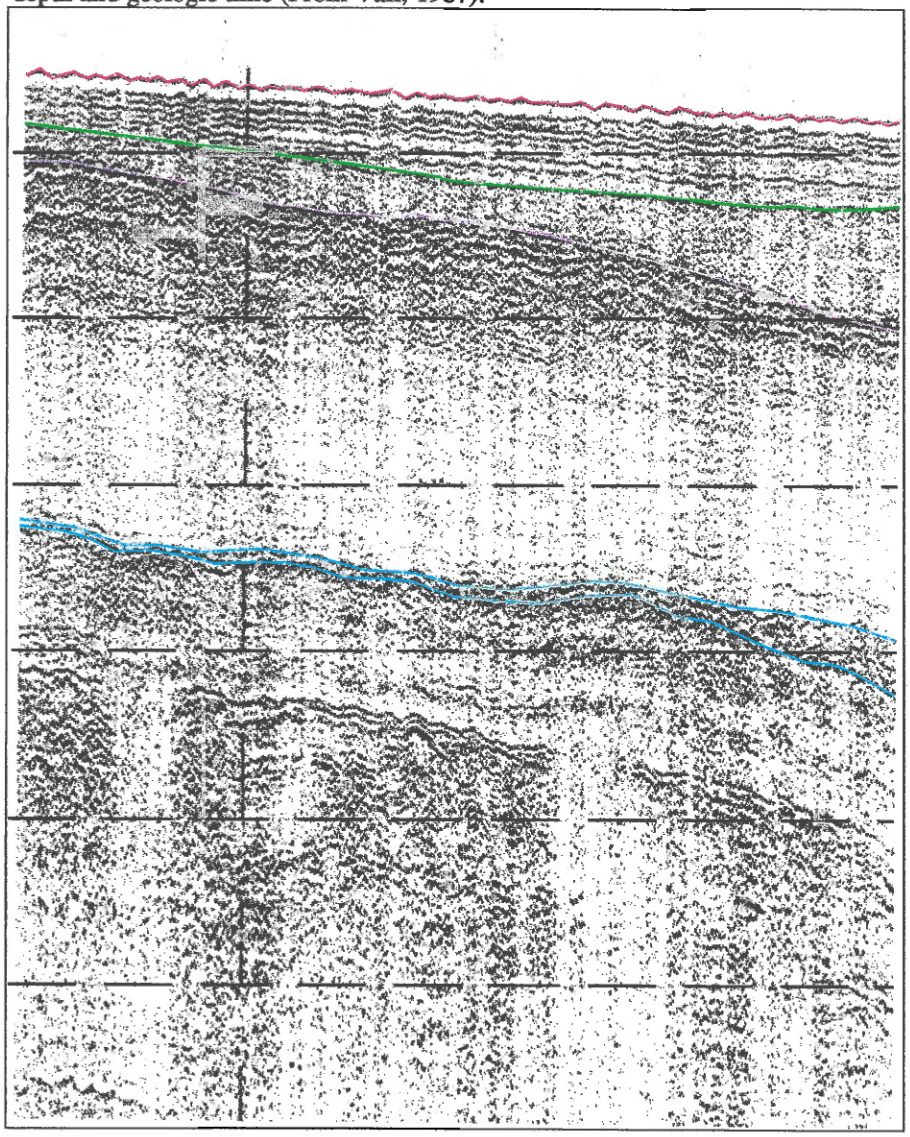

Figure 3.10: Scanned segment of seismic profile Profile F (Track W20-W21 (5-6 km)) illustrating how key reflectors were labelled with colour.

3.3.4 Correlating Boundaries

Sequence boundaries (key reflectors) were correlated across discontinuities created by (i) noise (Figure 3.11), and (ii) fault zones. Correlation is based on reflector character i.e. amplitude, spacing and dip and how a sequence fitted in relation to the depths of surrounding reflectors. Spatial variations in stratal reflector and sequence boundary amplitude, geometry, and spacing made correlation difficult. In order to confirm that the reflectors had been correlated correctly, regions where the boat track overlapped were checked to ensure that a given sequence boundary occurred at the same depth on

of a given sequence boundary did not always correspond. Consequently those reflector labels (colours) were altered.

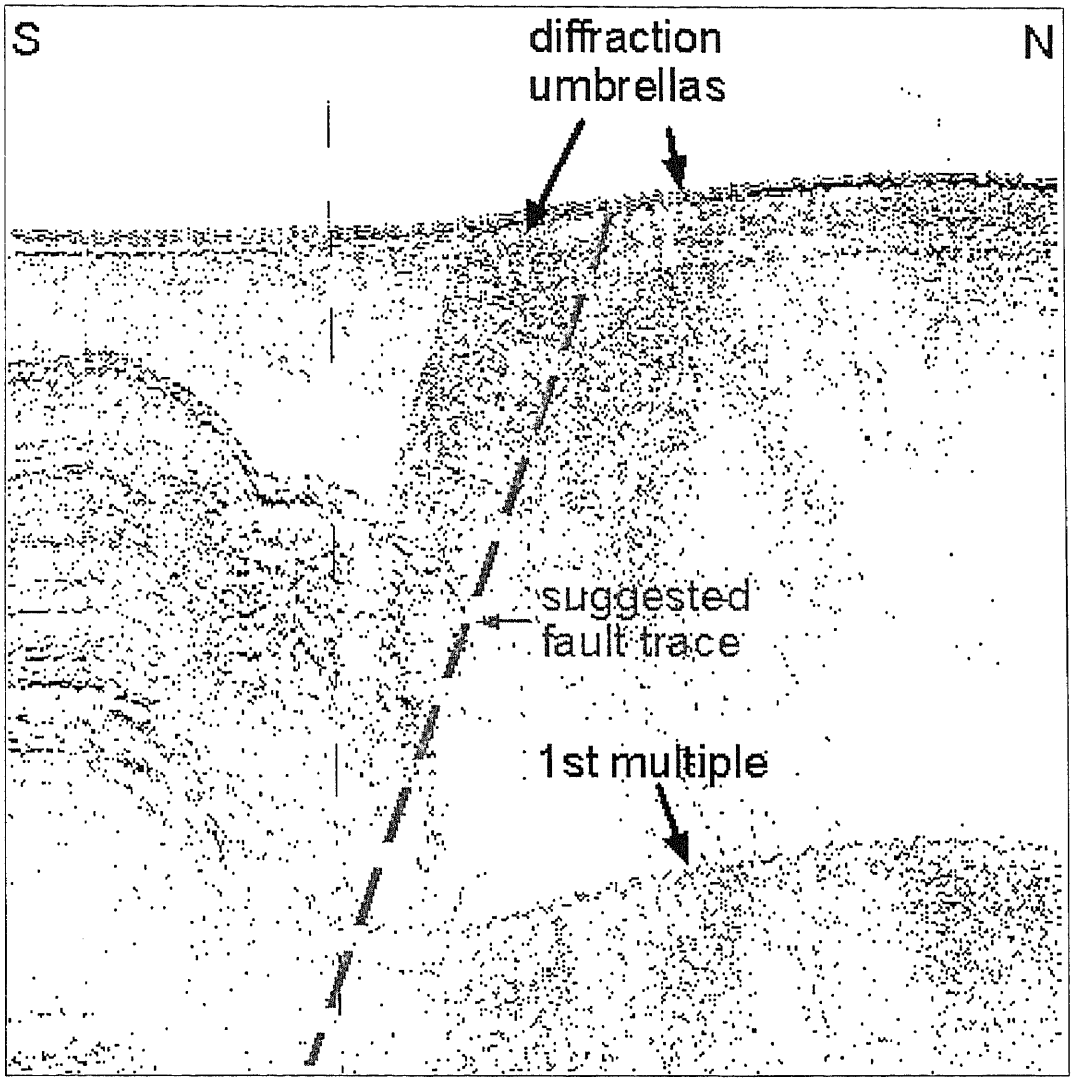

Figure 3.11: Section of seismic sub-bottom profile (scanned from track 1655-1810 (at 4-5 km north)) illustrating a discontinuity generated by noise associated with the Kerepehi Fault.

An additional problem was encountered where the depth to the seafloor at some overlap points, was different. As no interpretation is required to distinguish the seafloor, these inconsistencies must have occurred because the boat track, and hence the location of the profiles had been incorrectly mapped. This is highly possible given that the 'Tui' boat track for the 27 September 1990 was calculated using the Dead reckoning method. Consequently one of the boat track locations for this day, was adjusted (namely track H (1459-1550)) and as a result the seafloor depth and depth of reflectors at overlap points, corresponded more accurately.

Once the sequence boundaries have been correlated, they were summarised on simplified profiles (Figure 4.3- Figure 4.16) that were used to estimate the location and amount of displacement along the Kerepehi Fault.

Note: Because the data has not been completely processed, the simplified profiles presented in Figures 4.3 - Figure 4.16 (refer to Chapter 4) should not be considered to quantitatively reflect the geometry of a depth display or geological cross-section.

3.4 SUMMARY

The location, and vertical and horizontal scale of data collected by the University of Waikato, the Defence Scientific Establishment and NIWA were presented. The logged navigational records and therefore data location for data collected on the 27 September 1990 by the D.S.E. were accidentally discarded in the seven year period between collection and interpretation. As a consequence the location of profiles collected on this date was estimated using the Dead Reckoning method. The vertical scale (mS) for profiles collected by the University of Waikato was calculated assuming a sound velocity of 1460 $m.s^{-1}$ (Instruction Manual for Model 4800 Graphic Recorder). The vertical scale (mS) of data collected by NIWA and D.S.E. were provided with the data. The horizontal scale of profiles collected by the D.S.E. and NIWA was determined by matching collection time on the profiles, with collection time presented on boat track maps. The University of Waikato data matched position fix numbers presented on a hydrographic chart with fix numbers printed on the seismic sub-bottom profiles. Seismic sequence boundaries were determined by identifying discordant relationships between stratal reflectors, following a method first postulated by Mitchum et al. (1977). Reflector character was used to correlate seismic sequences across discontinuities generated by seismic noise.

3.5 REFERENCES

Allan, T.M.H., 1990. *A High Resolution Seismic Study of the offshore extension of the Waihemo Fault System*, Unpublished M.Sc. Thesis, University of Otago, Otago, New Zealand.

Bradshaw, B.E., 1991. *Nearshore and Inner shelf Sedimentation on the East Coromandel Coast, New Zealand.* Unpublished M.Sc. Thesis, University of Waikato, New Zealand.

Brown, L.F., and Fisher, W.L., 1979. Principles of Seismic Stratigraphic Interpretation: Interpretation of Depositional Systems and lithofacies from Seismic Data. In Brown, L.F., and Fisher, W.L. (eds), *Seismic Stratigraphic Interpretation and Petroleum Exploration*, Texas, University of Texas at Austin, Continuing Education Course Note Series No. 16, 1-125 p.

De Lange, W.P., 1998. Scientist at the University of Waikato, written commumication, 29 August.

Hochstein, M.P., Tearney, K., Rawson, S., Davey, F.J., Davidge, S., Henrys, S., and Backshall, D., 1986. Structure of the Hauraki Rift (New Zealand). In W.I. Reilly and B.E. Harford (eds). *Recent Crustal Movements of the Pacific Region*, Royal Society of New Zealand Bulletin 24. Wellington, The Royal Society of New Zealand. p.333-348.

Manighetti, B. & Carter, L. in print; Across Shelf Sediment Dispersal, Hauraki Gulf, New Zealand.

Mitchum, R.M., Vail, P.R., and Thompson, S., 1977. Seismic Stratigraphy & Global changes in sea level, Part 2: The Depositional Sequence as a Basic Unit for Stratigraphic Analysis. In C.E. Payton. (ed), *Seismic Stratigraphy – applications to hydrocarbon exploration.* Tulsa, Oklahoma, U.S.A., American Association of Petroleum Geologists Memoir 26. p. 53-62.

Posamentier, H.W. & Vail, P.R., 1988. Eustatic controls on clastic deposition II – Sequence and System Tract Models. In C.K. Wilgus, B. Hastings, C.G.St.C. Kendall, H.W. Posamantier, C.A. Ross, and J.C. Van Wagoner (eds), *Sea Level Changes: An Integrated Approach.* Society of Economic Paleontologists and Mineralogists, Special Publication, 42, p. 187-202.

Sheriff, R.E., 1977. Limitations on Resolution of Seismic Reflections and Geologic Detail Derivable from Them. In C.E. Payton (ed), *Seismic Stratigraphy – applications to hydrocarbon exploration.* Tulsa, Oklahoma, U.S.A., American Association of Petroleum Geologists Memoir 26. p. 3-14.

Vail, P.R., and Mitchum, R.M., 1977. Seismic Stratigraphy & Global changes in sea level, Part 1: Overview. In C.E. Payton (ed). *Seismic Stratigraphy – applications to hydrocarbon exploration.* Tulsa, Oklahoma, U.S.A., American Association of Petroleum Geologists Memoir 26, p. 51-52.

Vail, P.R., Todd, R.G., and Sangree, J.B., 1977. Seismic Stratigraphy & Global changes in sea level, Part 5: Chronostratigraphic Significance of Seismic Reflections. In C.E. Payton (ed), *Seismic Stratigraphy – applications to hydrocarbon exploration.* Tulsa, Oklahoma, U.S.A., American Association of Petroleum Geologists Memoir 26, p. 99-116.

Vail, P. R., 1987. Seismic Stratigraphy Interpretation using Sequence Stratigraphy. Part 1: Seismic Stratigraphy Interpretation Procedure. In A.W. Bally (ed), *Atlas of Seismic Stratigraphy.* American Association of Petroleum Geologists Studies in Geology, Vol. 27 p. 1-10.

Van Wagoner, J.C., Posamentier, H.W., Mitchum, R.M., Vail, P.R., Sarg, J.F., Loutit, T.S., and Hardenbol, J., 1988. An Overview of the Fundamentals of Sequence Stratigraphy and Key Definitions. In C.K. Wilgus, B. Hastings, C.G.St.C. Kendall, H.W. Posamantier, C.A. Ross, and J.C. Van Wagoner (eds), *Sea Level Changes: An Integrated Approach.* Society of Economic Paleontologists and Mineralogists, Special Publication, 42, p. 39-45.

Van Wagoner, J.C., Mitchum, R.M., Campion, K.M., and Rahmanian, V.D., 1990. *Siliclastic Sequence Stratigraphy in well logs, cores, and outcrops: Concepts for high resolution of time and facies.* American Society of Petroleum Geologists. AAPG Methods Exploration Series, No. 7, 55 p.

Chapter Four

RESULTS OF SEISMIC SEQUENCE ANALYSIS AND INTERPRETATION

4.1 INTRODUCTION

The character of stratal reflectors and sequence boundary reflectors is fundamental for a) identifying individual seismic sequences and b) correlating sequences across discontinuities. This chapter summarises the character of seismic sequences and sequence boundaries within seismic sub-bottom profiles collected by the Defence Scientific Establishment (D.S.E.) and the University of Waikato. Following this the location of offshore segments of the Kerepehi Fault and the most credible magnitude of displacement along these segments is presented.

4.2 SEISMIC SEQUENCE ANALYSIS RESULTS

Analysis of the seismic sequence data and investigation of the character of reflectors in these profiles, resulted in the identification of 5 definite sequences, which for the purposes of this study were labelled 'Red', 'Green', 'Purple', 'Turquoise', and 'Dark Blue'. The following briefly describes the character of observed seismic sequences and seismic sequence boundaries.

4.2.1 Limitations of the Seismic Data

Limited data processing during the collection of the seismic profiles created a wide range of data quality making it difficult to define the seismic character for a given sequence. Poor quality data are observed as an over abundance of noise (e.g.

diffraction umbrellas (Figure 4.11 Profile I, track '1810-1655') and mottled seismic signal (Figure 4.1)). Noise has been generated by (i) structures with abrupt boundaries e.g. fault margins, abrupt lithology changes, boulders, (ii) the equipment employed, (iii) gas within the sediment e.g. 'mottled' segments, and (iv) convolution (Refer to Appendix 4).

Also, reflectors appear weak or indistinct in a number of profiles, making individual strata difficult to distinguish (Figure 4.11 – Profile I, '1810-1655'). This may be a real effect due to poorly defined stratification, providing no acoustic impedance contrast, or may be a result of inadequate 'gain' control. i.e. the Model 5210A Geopulse Receiver did not adequately enhance the amplitudes of the deeper reflectors in order to compensate for the natural absorption of seismic energy.

In addition, the most southern profiles, collected by the University of Waikato, were generated by a slightly different seismic system to those collected by the New Zealand Defence Force (D.S.E.) (northern profiles). The seismic sequence and reflector character (discussed below), is the character of seismically unmigrated data (Refer to Appendix 3), incorporating a variety of seismic noise e.g. diffraction, collected by two different systems. Consequently, it is unknown whether the observed variations in seismic character are due to variation in the output of the two different systems, or spatial changes in noise, or real spatial changes in character. This made correlation of sequence and reflectors difficult, and means that lithological interpretations were not deduced from these data.

In some locations a sequence was observed but it was impossible to identify which seismic unit it belonged to e.g. whether it was part of the 'Purple' sequence, part of the 'Turquoise' sequence or a new sequence. In this circumstance, the sequence boundary in question was labelled black. Hence, 'Black' reflectors and associated sequences have variable character, which are briefly described at the end of the Seismic Sequence section.

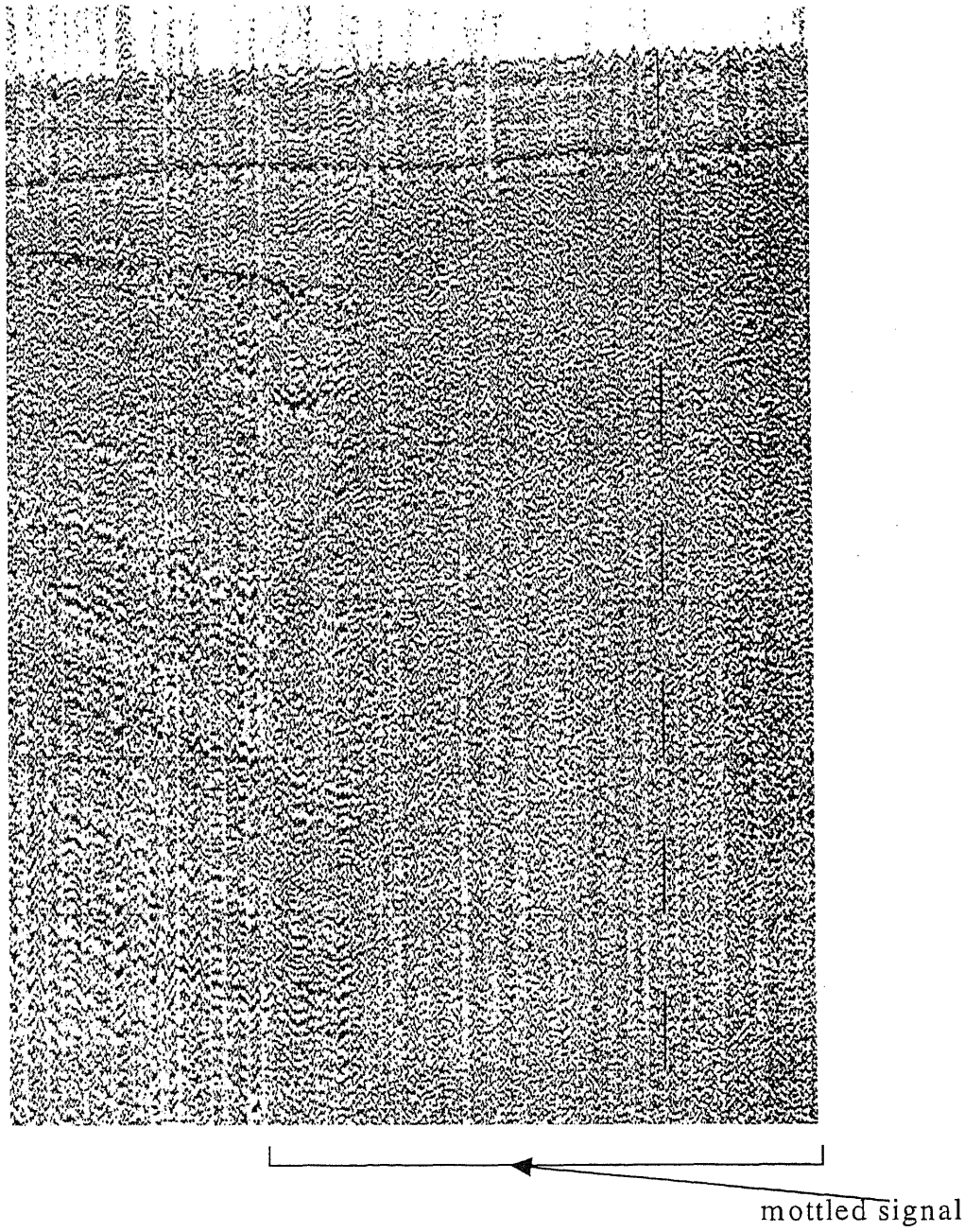

Figure 4.1: Scanned section from Profile J (Track 'W11-W12', @~8 km) (Refer to Figure 3.4) illustrating noise that has been referred to as 'mottling' or 'mottled' section. 'Mottling' may occur in response gas charged sediments.

4.2.2 Key Seismic Sequence Reflectors

Red

The Red reflector represents the sea floor and as recognised as the first seismic signal.

It has a moderate-high amplitude seismic signal.

Orange

The 'Orange' reflector has moderate to high amplitude with limited relief and sub-horizontal geometry. It shows very similar character to reflectors above and below it. Apparent truncation is evident at some locations along this reflector e.g. Profile C. The Orange reflector is believed to represent a marine flooding surface, which separates two components of the Red Sequence: the Highstand Systems Tract (red) from the Lowstand Systems Tract (orange) (Refer to Figure 3.9).

Yellow

This reflector is observed in the central Firth of Thames directly above uplifted units which form a 'high block'. It has variable amplitude, overlies and truncates steeply dipping stratal reflectors, and is overlain by sub-horizontal reflectors (usually only two) which drape over the 'high'. Diffraction umbrellas associated with fault zones bounding the uplifted 'high' mask the terminations of this reflector.

Green

This moderate to high amplitude reflector of horizontal to sub-horizontal geometry has limited relief but does illustrate heightened relief in some of the southern profiles e.g. western end of Profile D. It is evident in all locations except above regions of uplifted sediment in the central Firth of Thames (from where it is believed to have been eroded). The 'Green' reflector is shallowest at the landward margins of the Firth of Thames (shallow water depths) and adjacent to the central Firth of Thames region where faulting has caused uplift. It is usually easily distinguished, as onlap of overlying reflectors and truncation of underlying reflectors is common, which also suggests this is an erosional unconformity. However, in some locations where stratal relations are conformable and/or noise is significant this reflector can lose its' distinctive signature making identification speculative e.g. Profile D (in the east); Profile K (in the west).

The Green reflector has been displaced by faulting in all profiles, except Profiles N, C, G, E and B.

Purple

The 'Purple' sequence boundary represents a moderate to high amplitude reflector that is consistently present in most northern profiles, except for profile Profile N ('2229-2311') where excessive folding and diffraction umbrellas (thought to be caused by slumping) makes the 'Purple' reflector unidentifiable. It is not visible in locations where the signal is masked by mottled reflections or broken by diffraction umbrellas (e.g.Profiles I, (Figure 4.11, '1655-1810'), Profile G (Figure 4.9, '1852-1935'), Profile F (Figure 4.8, 'W20-W21')). Laterally, it is not very extensive and is usually only present in depressions (low-lying regions) and is never present over highs.

In many locations identification of the Purple reflector was speculative (e.g. Profiles L (Figure 4.14, '1630-1554'), K (Figure 4.13, 'W13-W14'), H (Figure 4.10, '1500-1550'), M (Figure 4.15, '2130-2225'), G (Figure 4.9, '1852-1935')). In these locations where seismic character was either too variable or not distinct enough to identify this reflector, comparison with reflectors within neighbouring profiles was undertaken to determine the presence and location of the Purple reflector.

Turquoise

The Turquoise reflector has moderate to high amplitude and often displays considerable relief (e.g. Profile F, (Figure 4.8, 'W20-W21'))). This reflector is commonly masked by diffraction umbrellas or mottled seismic signals and consequently becomes indistinct or intermittent (Profile G (track N), despite it's high amplitude signal. On occasion, the Turquoise reflector has similar character to surrounding reflectors making identification difficult (e.g. Profile J, 'W11-W12' (Figure 4.12), Profile K, 'W13-W14' (Figure 4.13)) i.e. hard to tell if reflector represents 'Turquoise', 'Purple' or some other unknown (black) reflector.

Dark Blue

This moderate to very high amplitude reflector often has irregular geometry (high relief and folded in some regions e.g. Figure F ('W20-W21')).

The 'Blue' reflector is hard to distinguish from surrounding reflectors at times, a task made more difficult by the presence of multiples and diffraction umbrellas caused by faulting. Where seismic character wasn't enough, comparison with the depths of Blue reflectors within surrounding profiles was used to identify this reflector. It is often present in uplifted blocks where it displays dipping reflections and underlies the Red sequence. The uplifted blocks are believed to represent an axial ridge possibly basement material (Greig, 1982) composed of Jurassic greywackes (Hochstein et al., 1986).

4.2.3 Seismic Sequences

Red

The Red sequence is present in all seismic profiles but in places, the reflectors become indistinct as a result of 'mottling', making individual strata difficult to identify. However, visible reflectors are typically of moderate amplitude, sub-horizontal and closely spaced. The red sequence unconformably drapes underlying sequences. Above regions of uplifted sediment (highs), the red sequence thins over and laps onto underlying units.

In Profiles B, C, and D a component of the Red sequence, the Transgressive Systems Tract (Refer to Figure 3.9) has been identified and labelled Orange. This Transgressive Systems Tract contains moderate to high amplitude reflectors of sub-horizontal geometry and limited relief.

There are two profiles that exhibit significantly different seismic character within the Red sequence. The southern most track (Figure 4.3 ('Track 2')) contains low amplitude strata within a seismically bland signal (limited, weak reflections). Profile N (Figure 4.16) exhibits abundant folding and is partially obscured by diffraction umbrellas, particularly within the Red and Green units. This structure may be due to faulting or earthquake generated slumping.

Green

The character of the 'Green' sequence varies considerably between profiles collected in the south, by the University of Waikato and those collected in the north, by the D.S.E.

In the south (U.O.W.) stratal reflectors within the 'Green' sequence have higher amplitudes e.g. Profiles A and C, which are often masked or disrupted by (i) multiple reflectors e.g. observed deeper than 7.6 mS on Profile A ('Track 2'), deeper than 18 mS from 0-4 km on profile D ('Track 3') and within Profiles C ('Track 4'); and (ii) folding and faulting. Very disturbed stratal reflectors with variable dip are also present between 4 and 7.5 km along Profile D ('Track 3'). On the western and eastern flanks of the Firth of Thames, reflectors dip strongly to the east and west respectively.

In the north, stratal reflectors have low-moderate amplitude and have sub-horizontal geometry e.g. Profile E. Some locations are mottled and indistinct making the reflectors imprecise. e.g. Profile G, southern Profile F, western Profile K.

Generally, it is similar in appearance to the Red sequence (e.g. Profile H, '1500-1550'), except that strata show slightly more relief (i.e. are more wavey). The Green sequence has a weaker seismic response than the Turquoise sequence, which occasionally underlies it (e.g. Figure 4.5 – Profile C ('Track 4')). The stratal reflections in the Green sequence appear to have been truncated, suggesting the upper boundary of the Green sequence is an unconformity (e.g. Figure 4.11 – Profile I (1810–1655)).

This unit is commonly truncated by faulting (e.g. faults bounding the uplifted, underlying units (Profiles I, K., Profile F ('W20-W21')): 3 and 9.25 km) limiting its lateral extent.

In the western margin of Profile M ('2130-2225') (Figure 4.15), the Green unit shows anomalous, bland character with no reflectors at all.

Purple

The Purple sequence is observed in profiles collected by the D.S.E. It is not observed within profiles collected by Waikato University. This may be due to shallower penetration or poorer resolution associated with the data set. Alternatively, the Purple sequence may not be present in the southern Firth of Thames.

The reflections within the Purple sequence display a variety of amplitudes, even within the same profile (e.g. Profile M, '2130-2225' (Figure 4.15)). Reflector amplitude ranges from moderately high (Profile G, '1852-1935' (Figure 4.9); profile M, 2130-2225 (Figure 4.15)) to low, to reflector free (seismically bland) (Profile H, '1500-1550' (Figure 4.10); Profile K, 'W13-W14' (Figure 4.13)).

The Purple sequence has been faulted in many places (e.g. Profile F, 'W20-W21'): @ 7km) and contains multiple diffraction umbrellas near faulted regions. In some locations faulting truncates the sequence causing it to be laterally discontinuous e.g. (Figure 4.13, Profile K ('W13-W14')).

The variations observed in reflector amplitude and data quality in some profiles render it difficult to differentiate between the 'Purple' and 'Turquoise' sequences. In such situations, the depth to the 'Purple' sequence was identified by comparison with the depth of the 'Purple' sequence on an adjacent profile, at a location where the two profiles intersect.

Turquoise

The Turquoise sequence contains low-frequency, moderate amplitude, and closely spaced reflectors. These have the same apparent dip angle as the upper boundary. Strata are commonly wavy in appearance i.e have high relief (~± 2mS) and masked by mottled segments making strata indistinct. Sudden changes in dip are also common and are probably due to faulting. Diffraction umbrellas are associated with most faults and in many cases completely mask the reflectors.

Dark Blue

Although not always distinguishable, the Blue sequence is believed to be present under all seismic sections. Reflectors are often indistinct at depth primarily because the lower section is masked by multiples, but also be because the greater portion of seismic energy has been absorbed before it reaches these depths.

This sequence contains high relief, high amplitude reflectors with variable dip, and in places extensive faulting and folding. Mottling (possibly in response to gas) and diffraction umbrellas (created by faulting) frequently make the seismic signal within this unit indistinct and hard to decipher. Apparent dip beneath the observed high is typically to the north or east (depending upon the direction the profile is trending i.e. n/s or e/w respectively).

Black

The 'Black' sequence has been used to illustrate the presence of an unidentifiable sequence or a new sequence of very limited lateral extent. The 'Black' reflector often occurs as a moderate amplitude reflector between the 'Purple' and 'Turquoise'. Within Profile H (Figure 4.10, '1500-1550') the 'Black' sequence has very limited extent and displays wavy internal structure of the same appearance as mega ripples. Within Profile K ('W13-W14') it represents a sequence which is present between the 'Purple' and 'Turquoise' sequences of almost identical seismic character to the 'Purple' sequence. It was identified as a separate sequence by the truncation of the strata within the 'Turquoise' sequence.

The sequence is frequently unidentifiable because of unusual seismic character, often resulting from poor data quality. In western margin of Profile F and K (0-9 km) mottled signal make stratal reflectors indistinguishable and is therefore included in the 'Black' sequence. Small patches (~5%) of Profile F 'Black' sequence is unmottled and reveals that at this location the sequence is moderate to high in amplitude with closely spaced reflectors, similar to those observed in the 'Turquoise' sequence.

4.2.4 Supplementary Interpretation

Without core data or extensive seismic-stratigraphic interpretation of the observed deposition systems (beyond the scope of this thesis) exact age constraints can not be placed upon any of the observed sequences. However the following points represent a brief summary of ideas and possible interpretations of observations made while analysing the seismic data.

- Green
  - ⇒ Likely to represent sediments laid down during the Pleistocene.
  - ⇒ Profile M (2130-2225): Seismically bland signal: May represent paleochannel comprised of Pleistocene sands.

- Purple
  - ⇒ The 'Purple' sequence is not evident within the seismic sub-bottom profiles collected in the southern Firth of Thames. There are two possible reasons for this: (i) the seismic sub-bottom profile system employed by the University of Waikato had resolution too low to detect the 'Purple' sequence; or (ii) the 'Purple' sequence is not be present in the southern Firth of Thames, possibly as a result of uplift and erosion by the transverse fault (most southern fault) observed on Profile F (W21-W22).
  - ⇒ Reflections generally have the same inclination as the upper boundary of this sequence (i.e. the purple reflector), suggesting it was deposited in a tectonically stable environment.

4.2.5 Summary Stratigraphy

The character of the identified sequences and sequence boundaries were used to help correlate sequences across discontinuities generated by (i) noise, and (ii) fault zones. The results of identification and correlation of seismic sequences are presented on simplified profiles that summarise the suggested stratigraphy of each seismic sub-bottom profile analysed (Figure 4.3-Figure 4.16). These profiles were then used to identify the fault margins belonging to the Kerepehi Fault system.

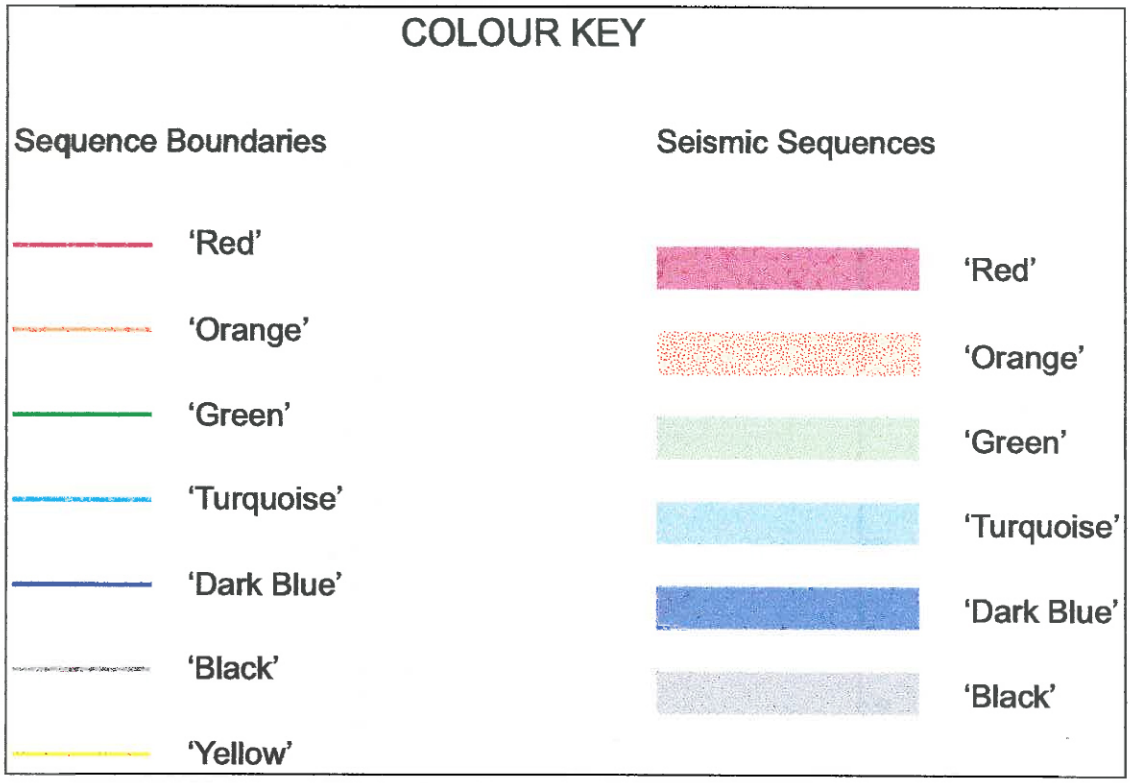

Figure 4.2: Colour key identifying colours used in Profiles A-N to describe seismic sequences and sequence boundaries.

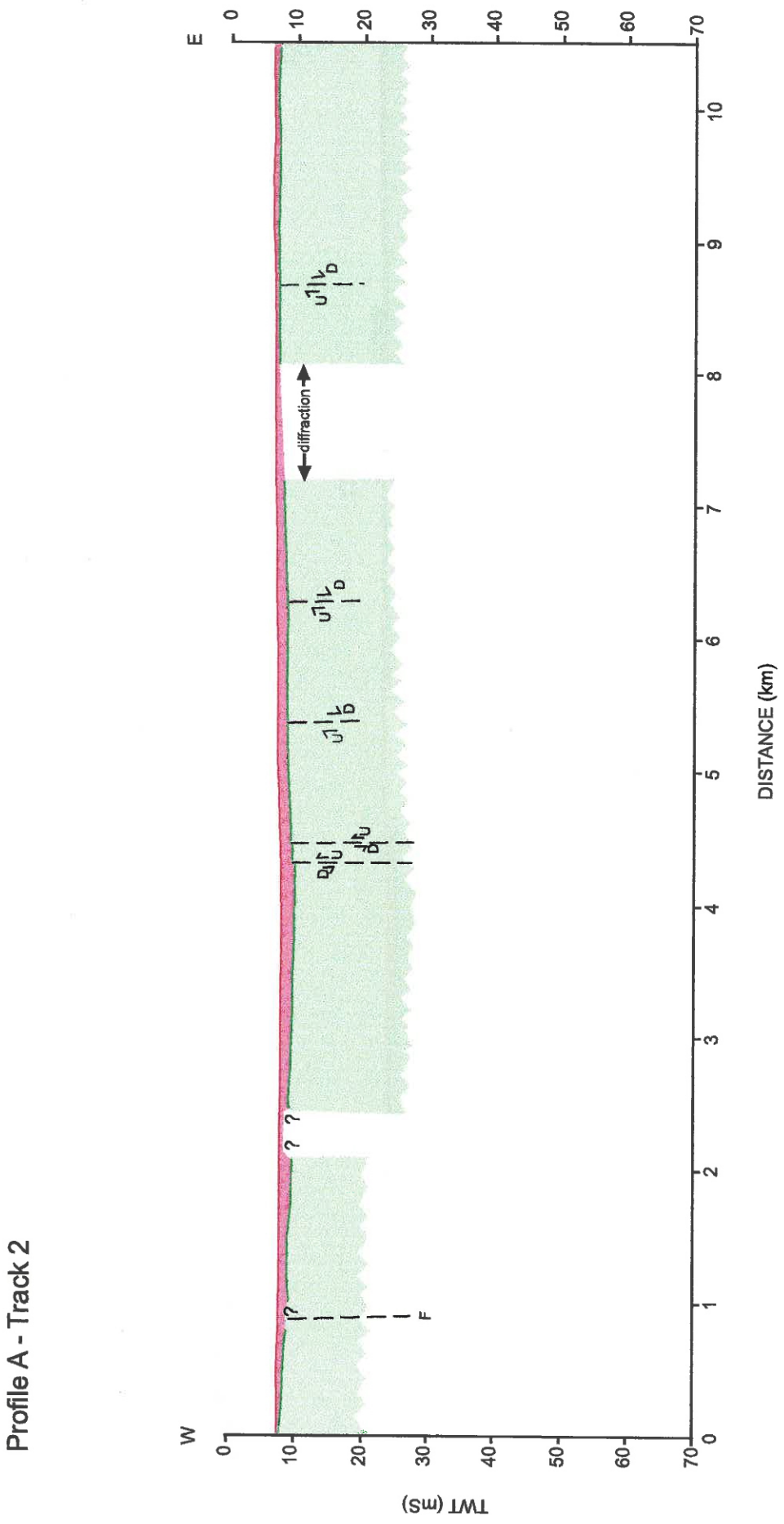

Figure 4.3: Profile A: summary startigraphy determined from seismic bottom profile collected on Track 2.

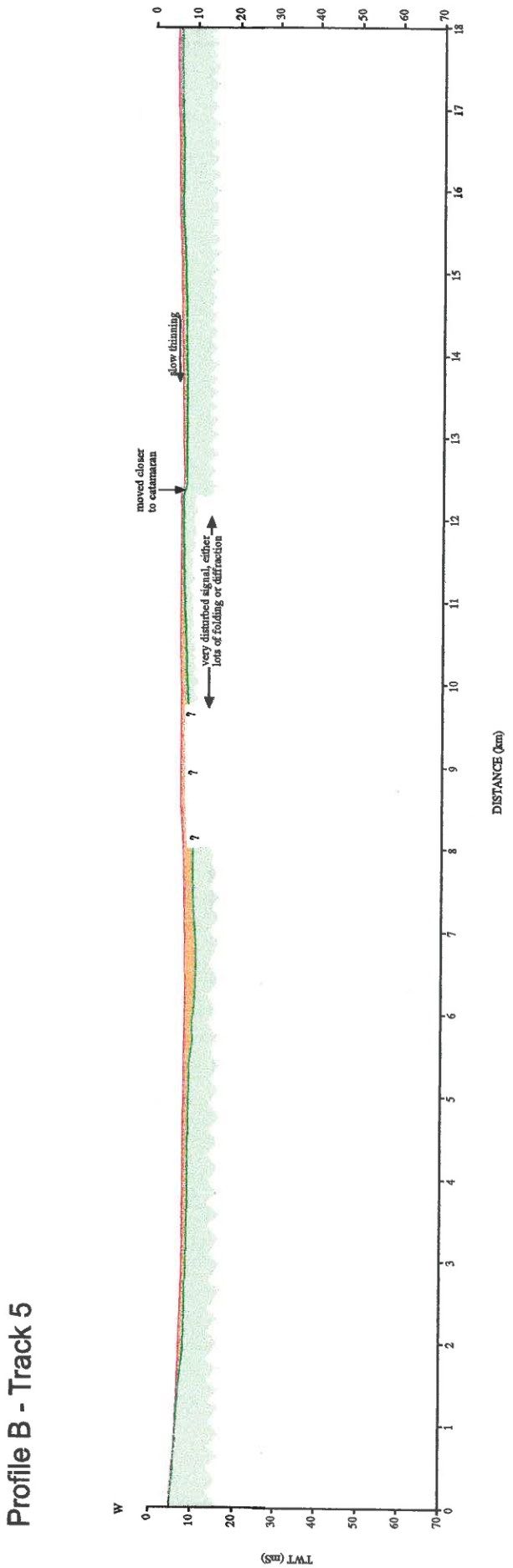

Figure 4.4: Profile B: summary startigraphy determined from seismic bottom profile collected on Track 5.

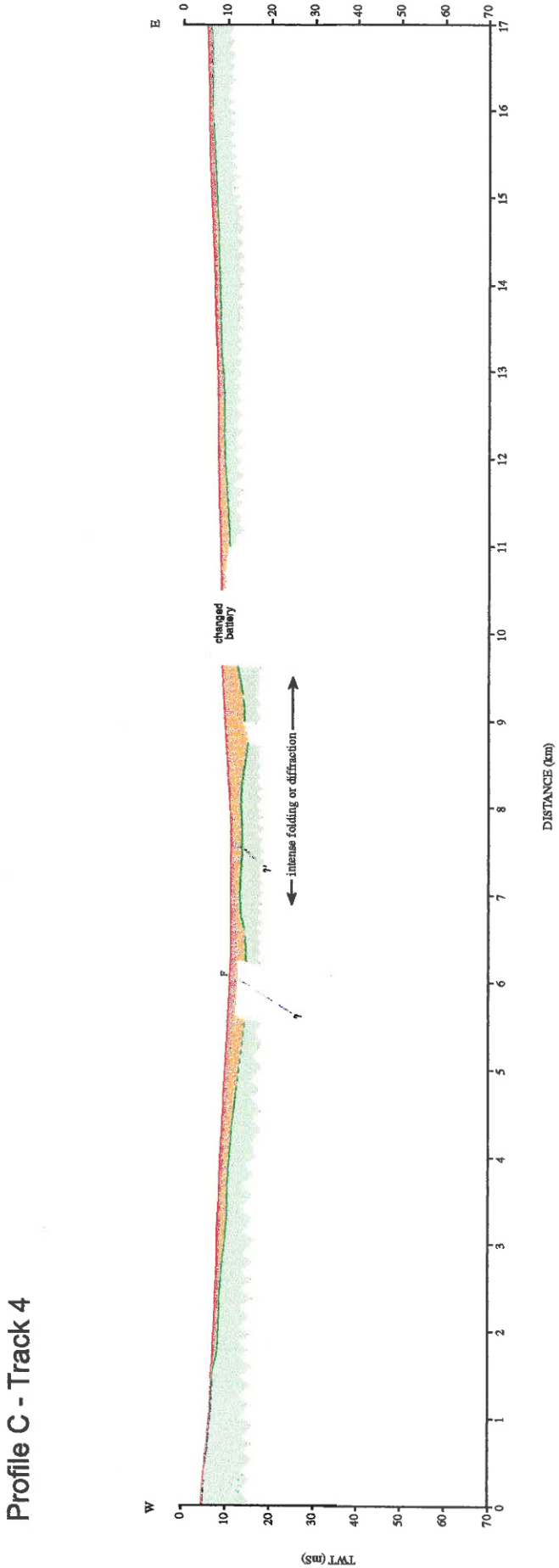

Figure 4.5: Profile C: summary startigraphy determined from seismic bottom profile collected on Track 4.

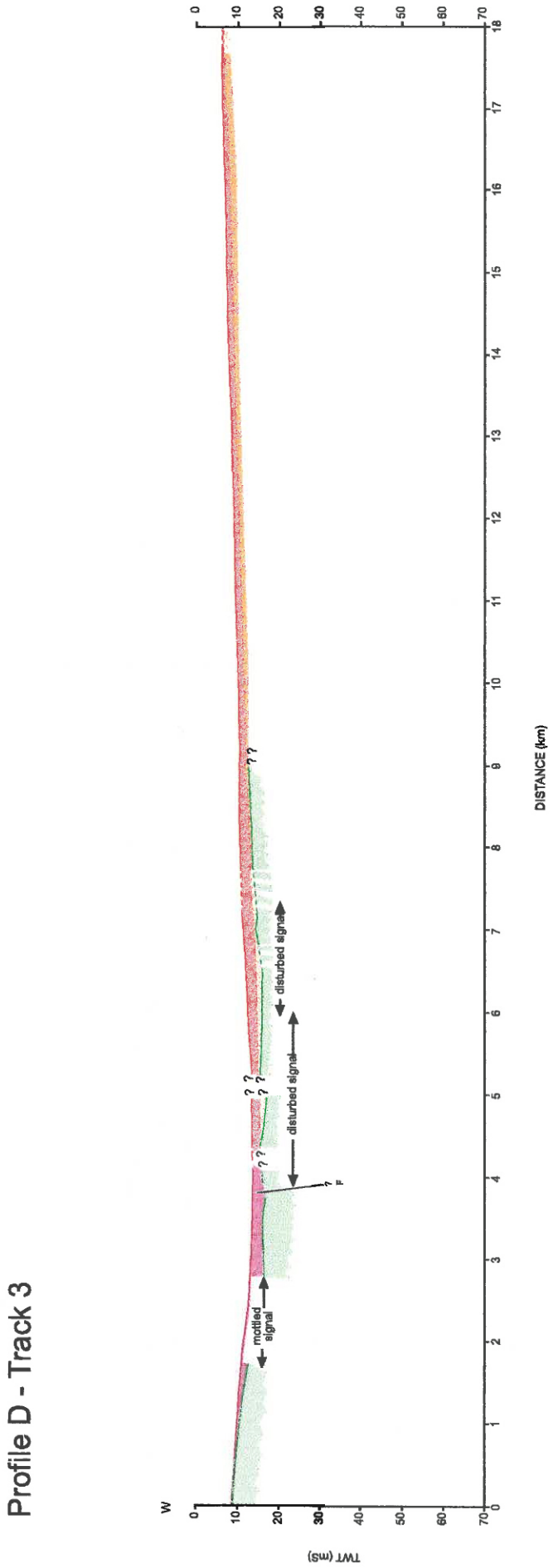

Figure 4.6: Profile D: summary startigraphy determined from seismic bottom profile collected on Track 3.

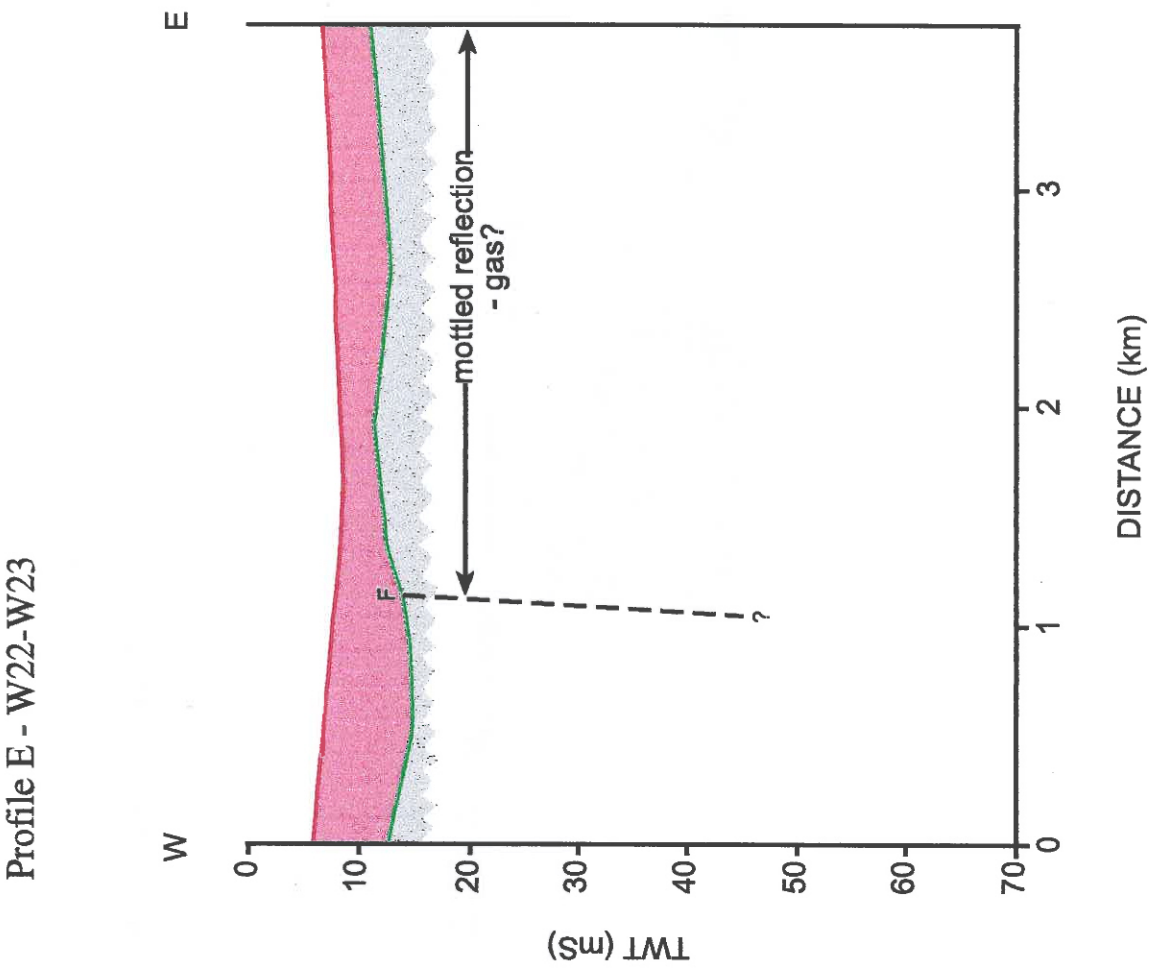

Figure 4.7: Profile E: summary startigraphy determined from seismic bottom profile collected on Track W22-W23.

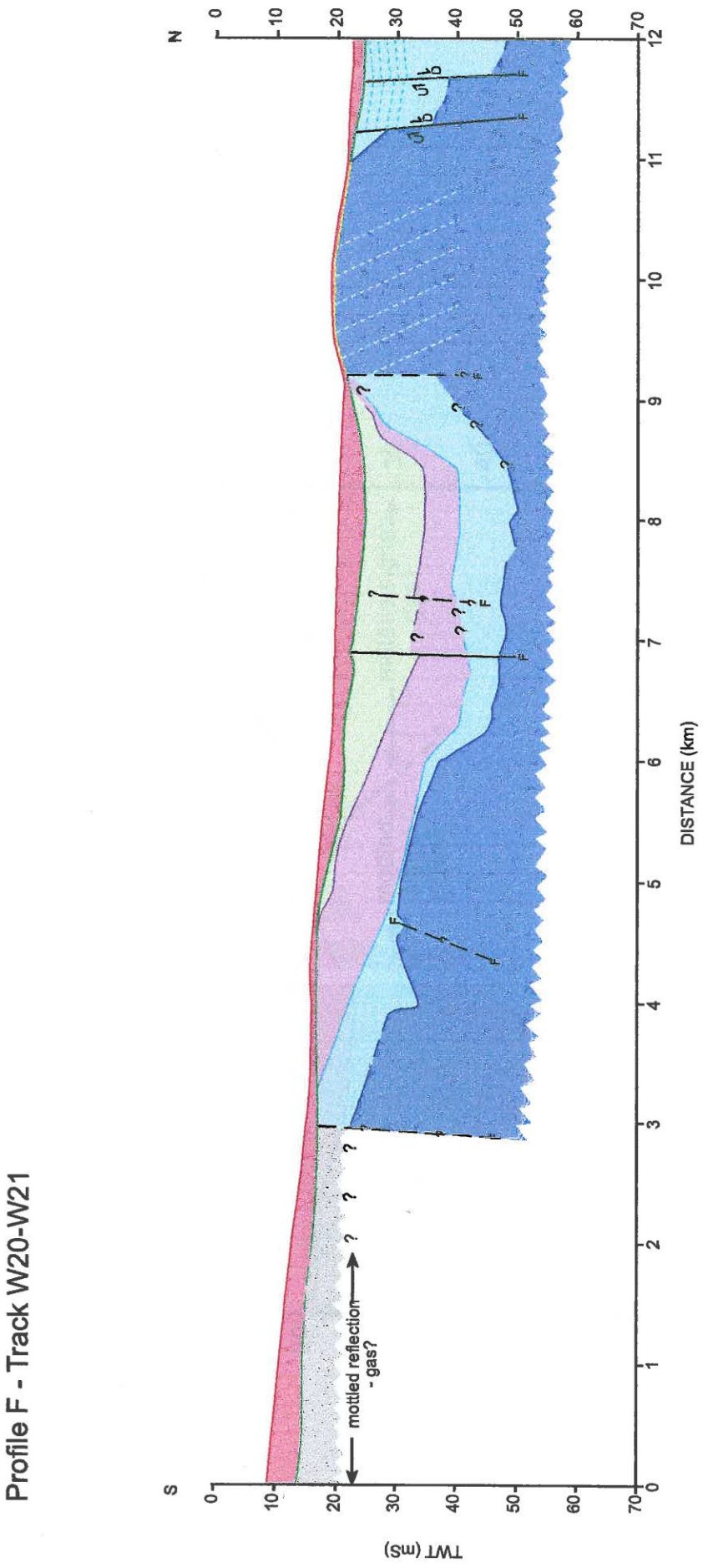

Figure 4.7: Profile F: summary startigraphy determined from seismic bottom profile collected on Track W20-W21.

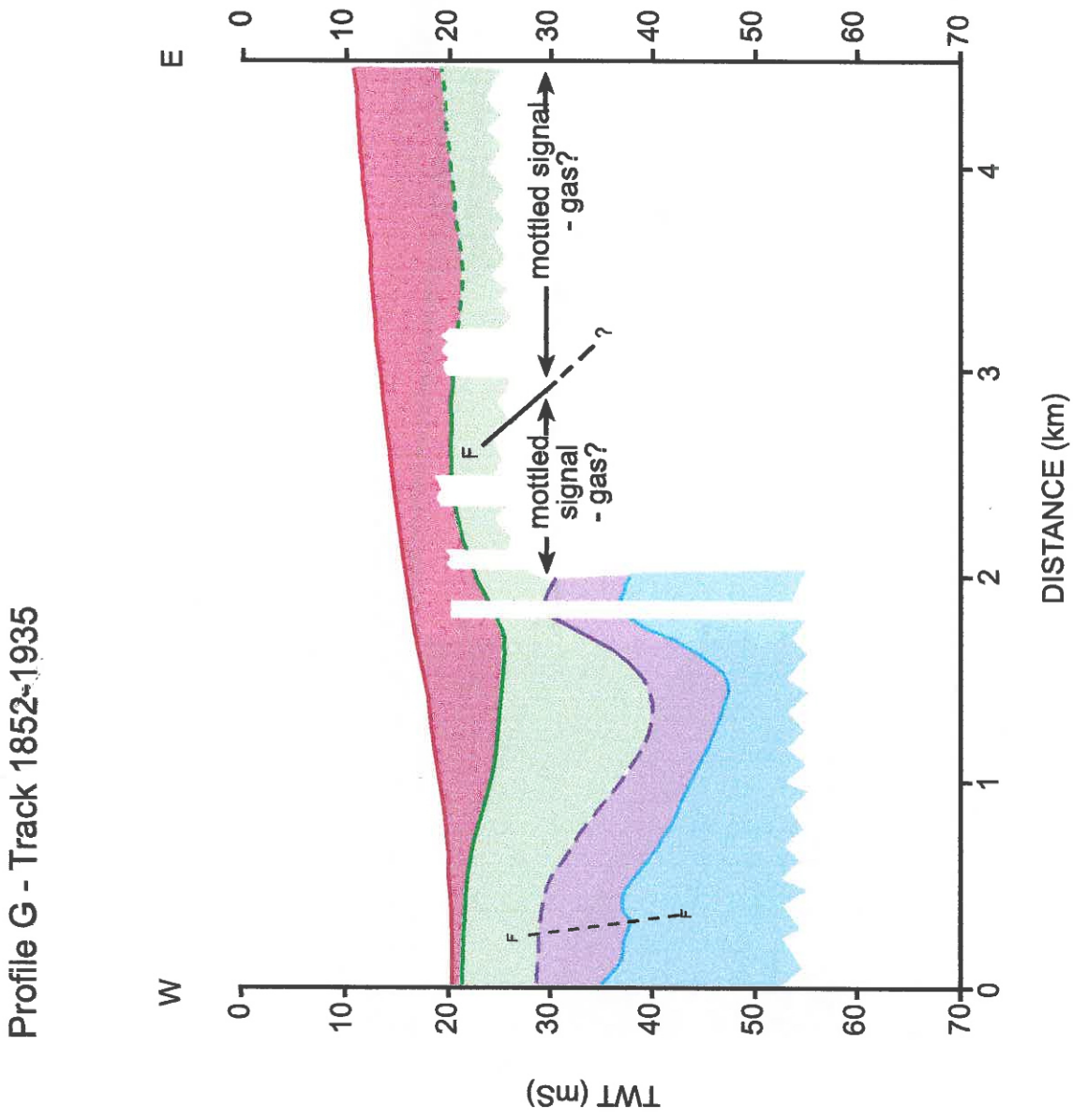

Figure 4.9: Profile G: summary startigraphy determined from seismic bottom profile collected on Track 1852-1935.

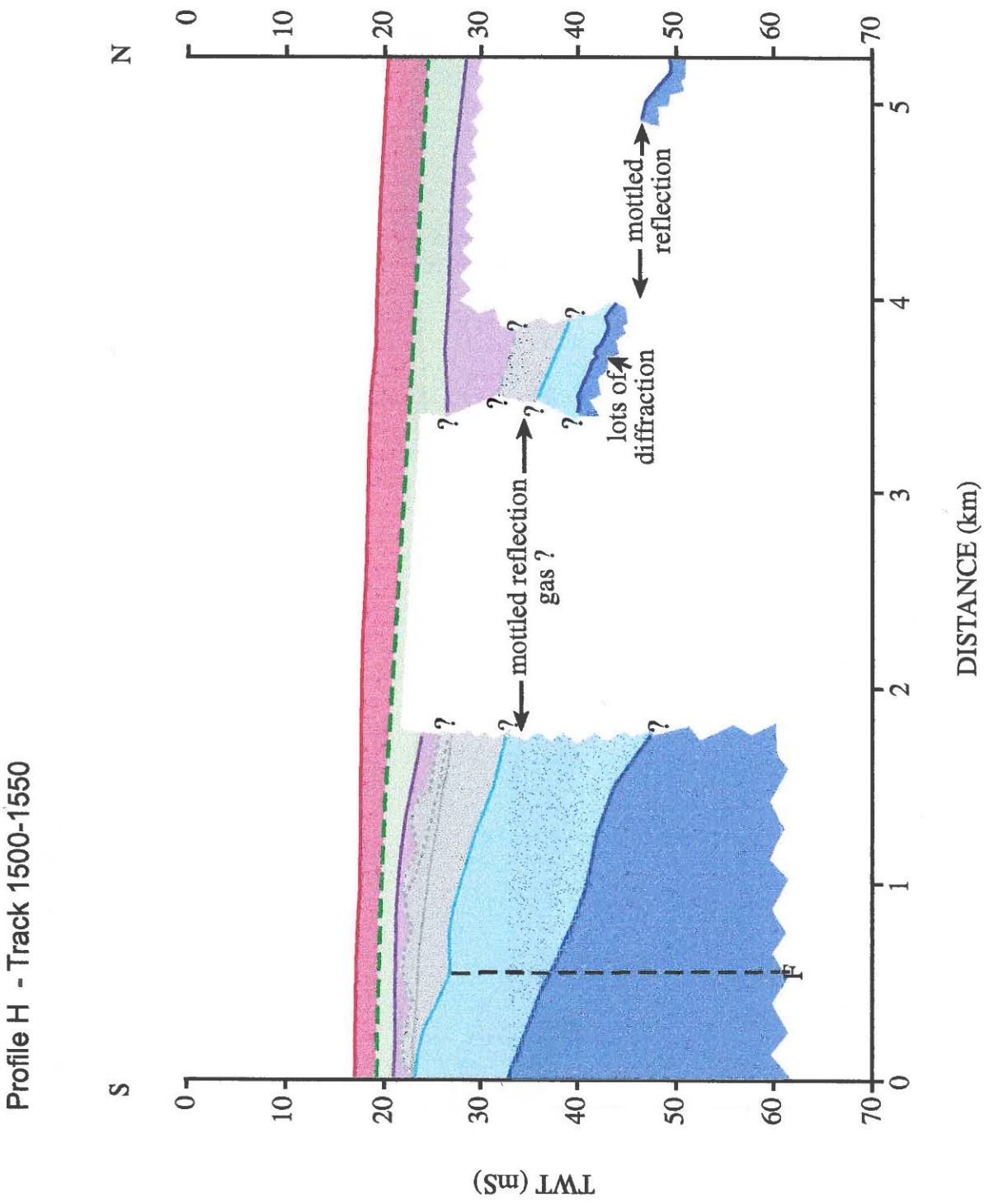

Figure 4.10: Profile H: summary startigraphy determined from seismic bottom profile collected on Track 1500-1550.

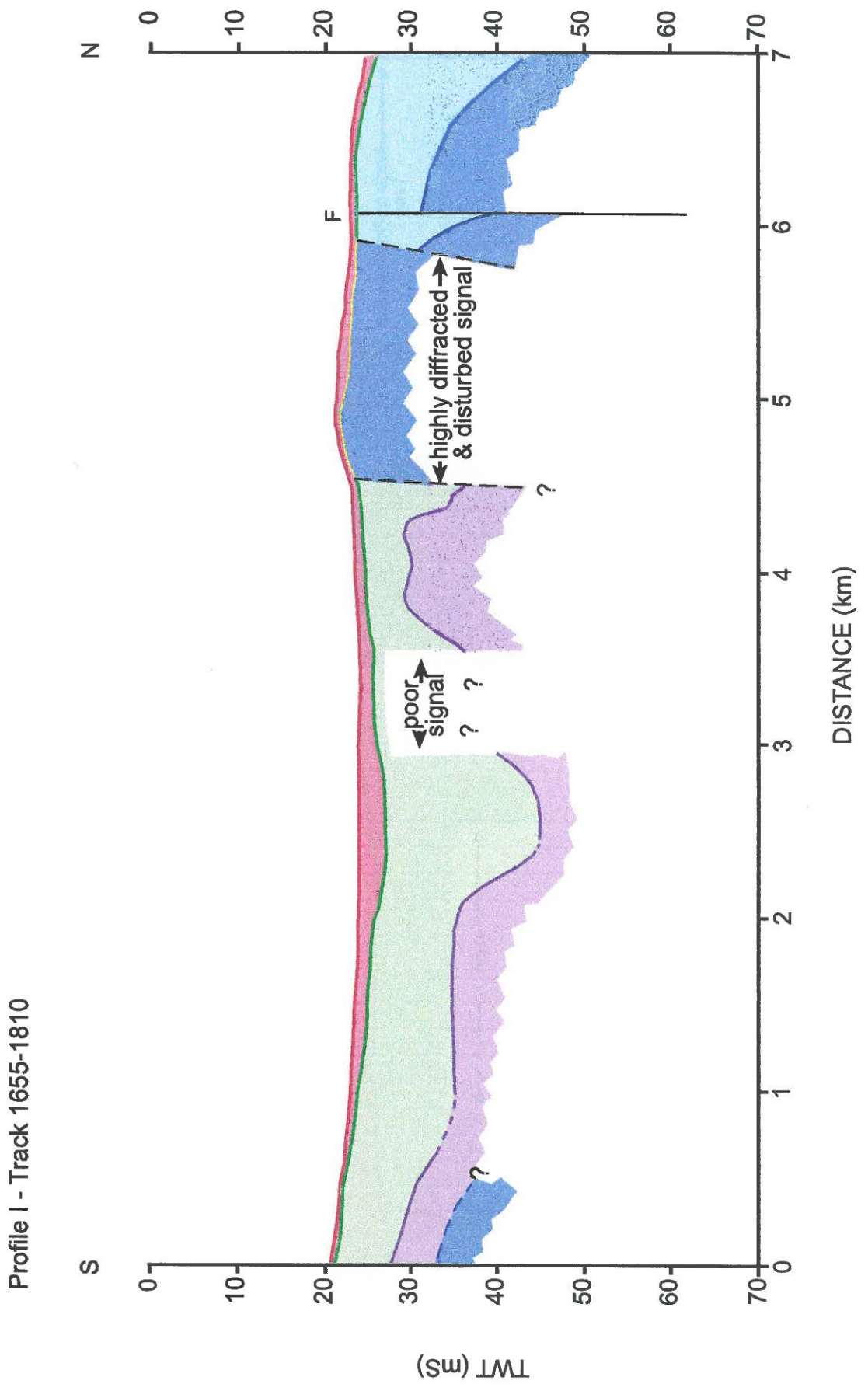

Figure 4.11: Profile I: summary startigraphy determined from seismic bottom profile collected on Track 1655-1810.

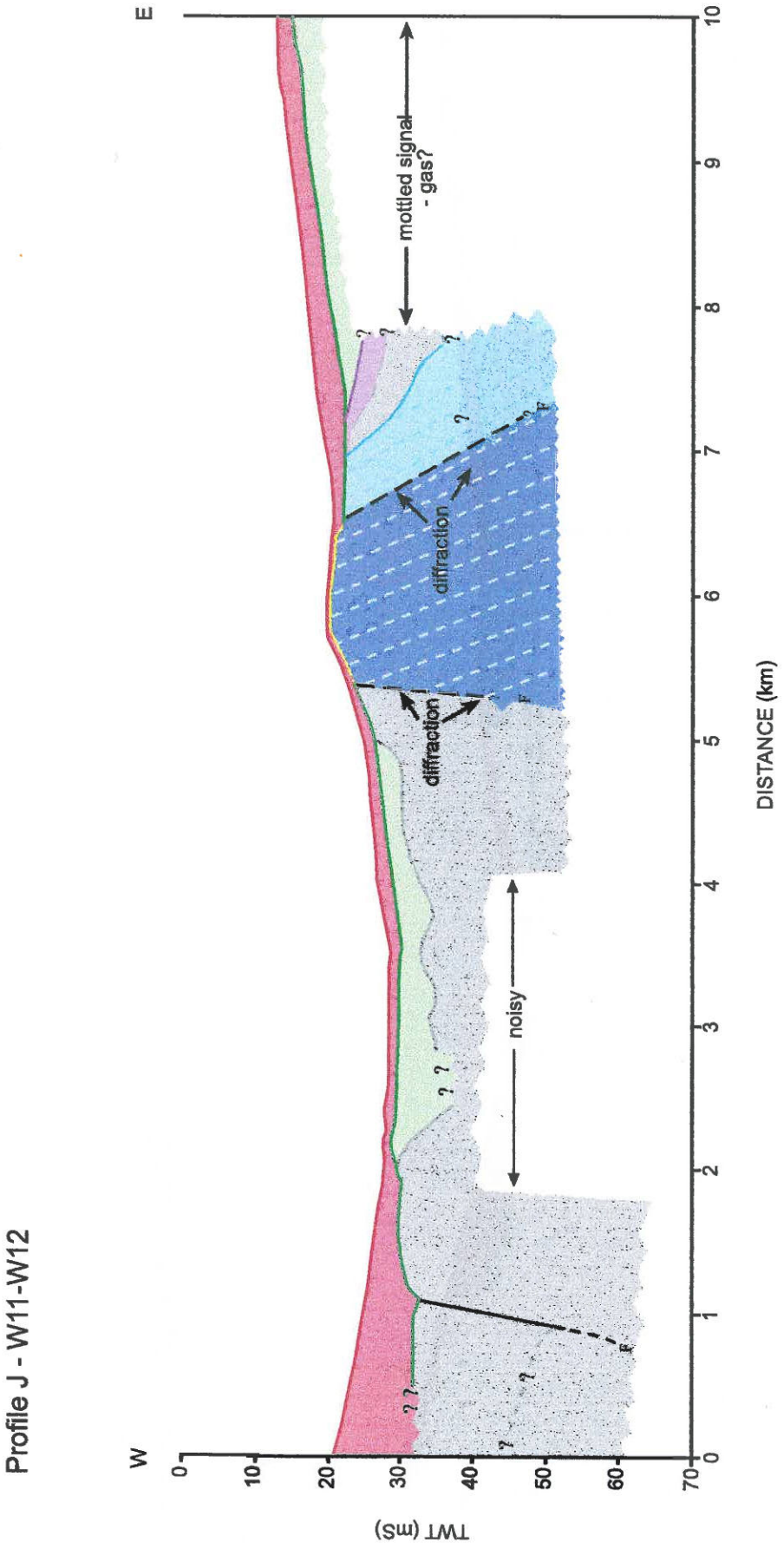

Figure 4.12: Profile J: summary startigraphy determined from seismic bottom profile collected on Track W11-W12.

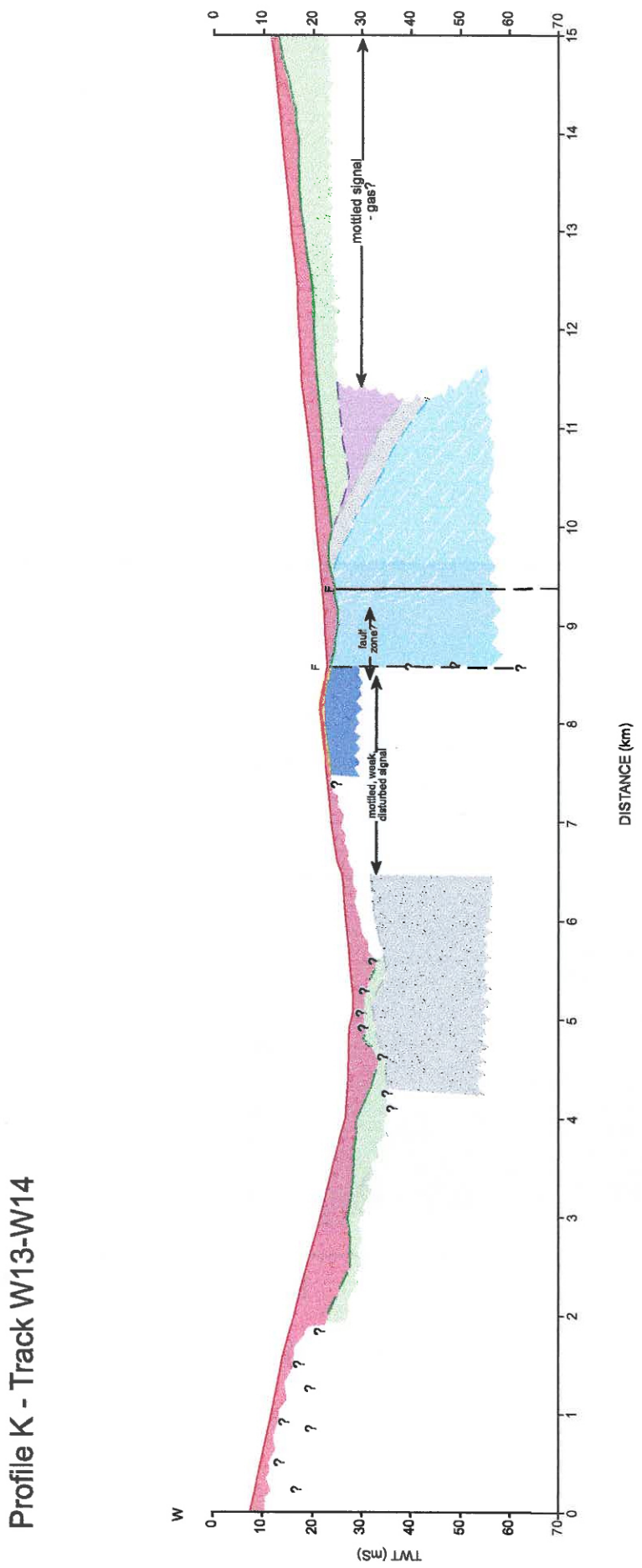

Figure 4.13: Profile K: summary startigraphy determined from seismic bottom profile collected on Track W13-W14.

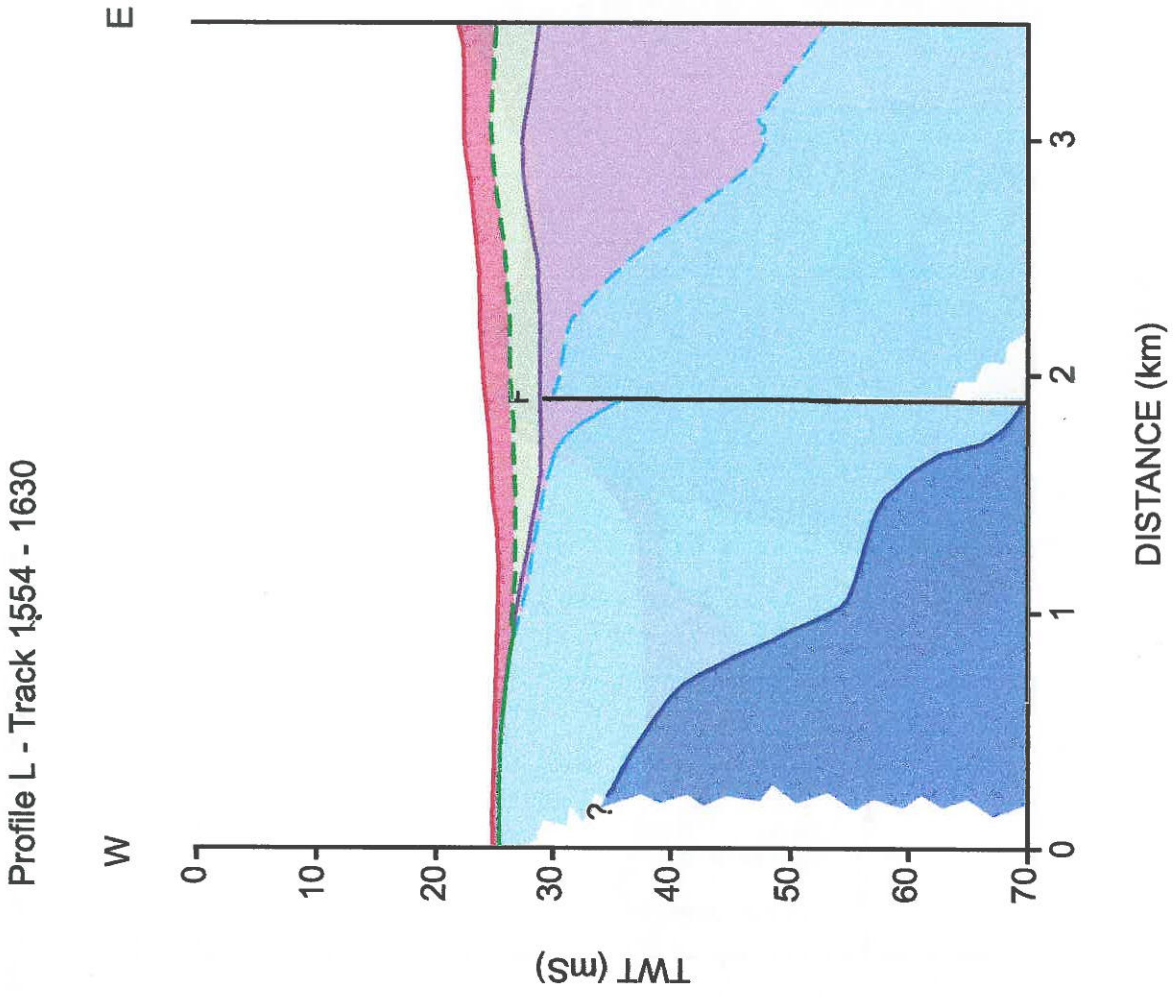

Figure 4.14: Profile L: summary startigraphy determined from seismic bottom profile collected on Track 1554-1630.

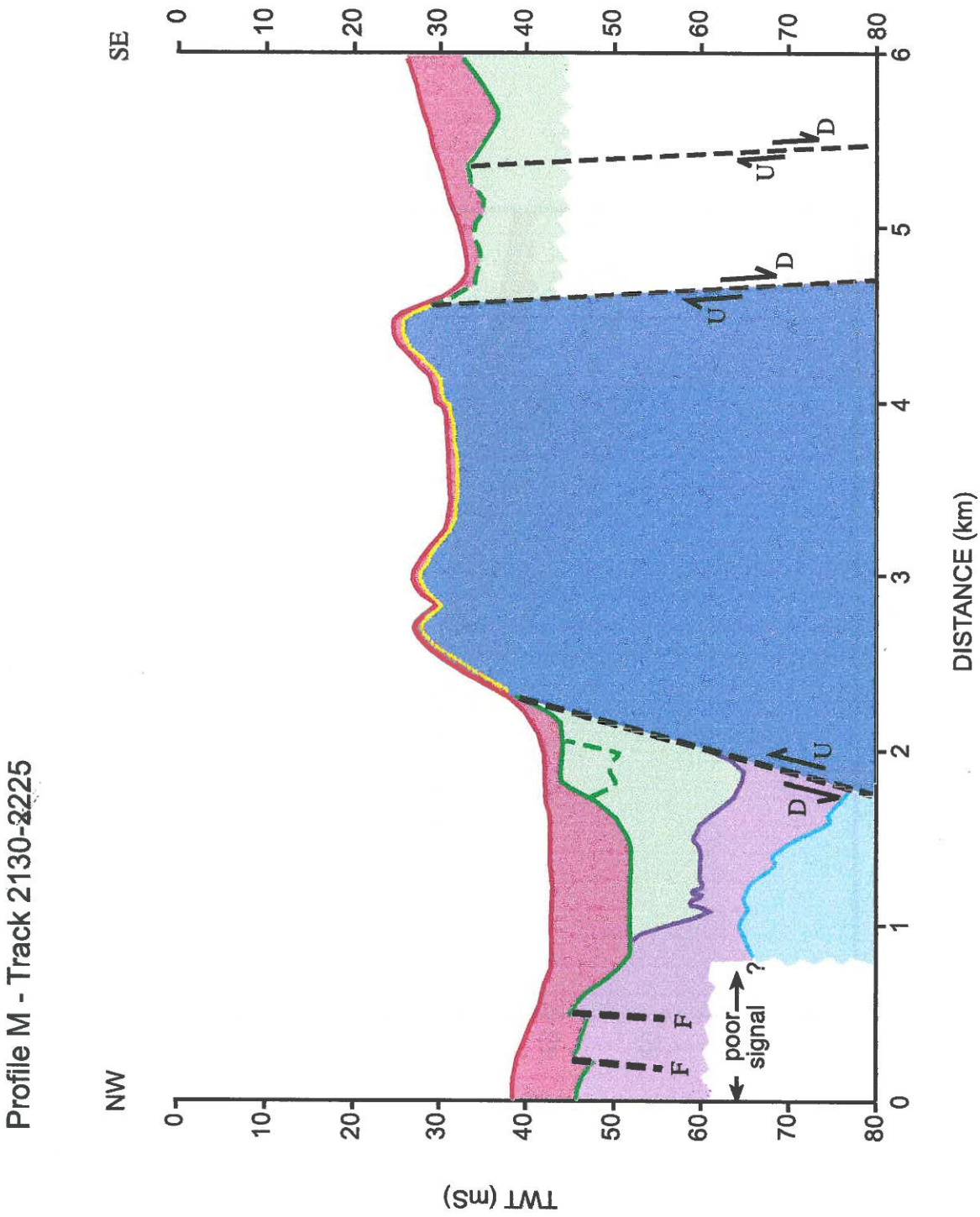

Figure 4.15: Profile M: summary startigraphy determined from seismic bottom profile collected on Track 2130-2225.

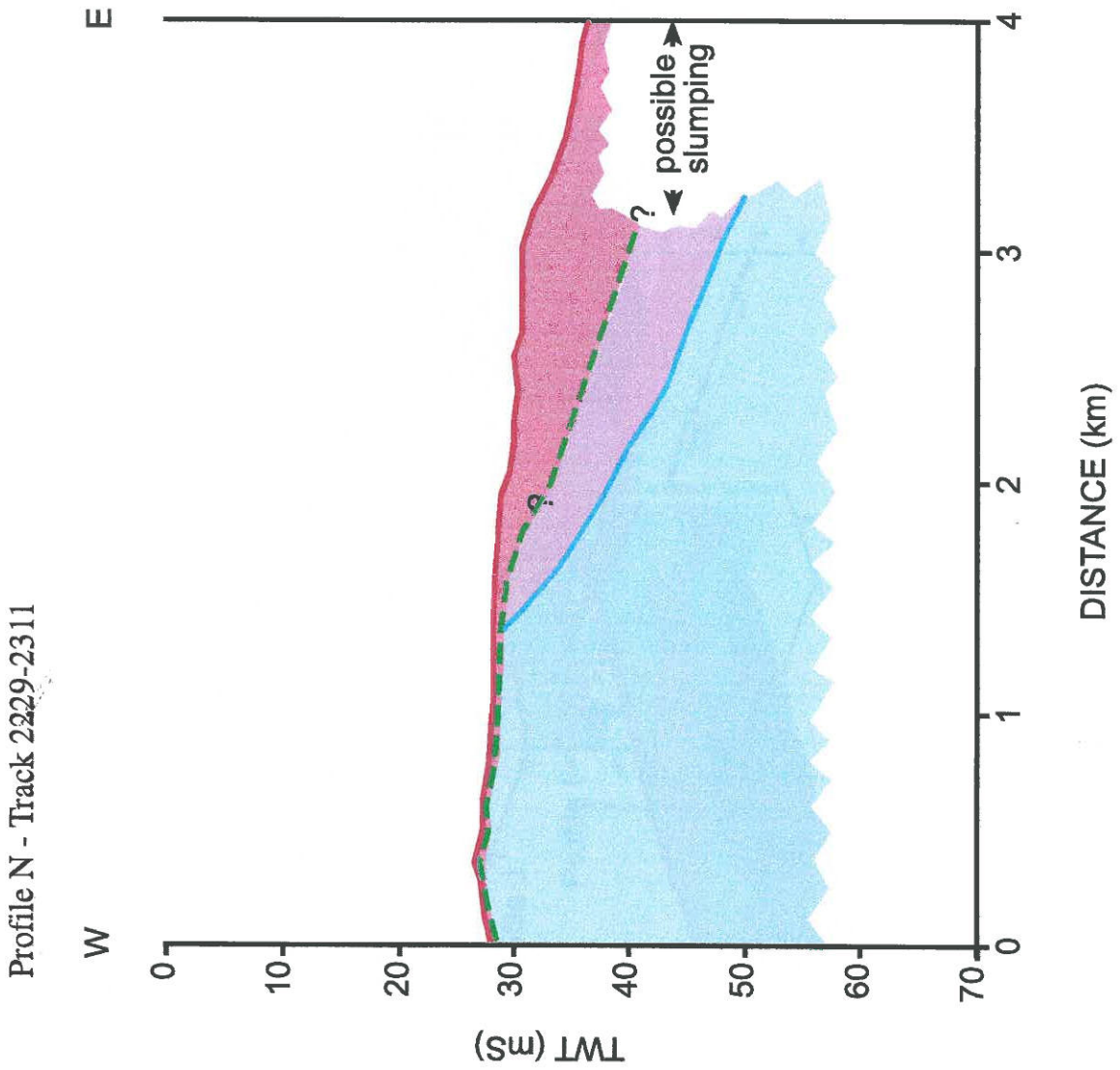

Figure 4.16: Profile N: summary startigraphy determined from seismic bottom profile collected on Track 2229-2311.

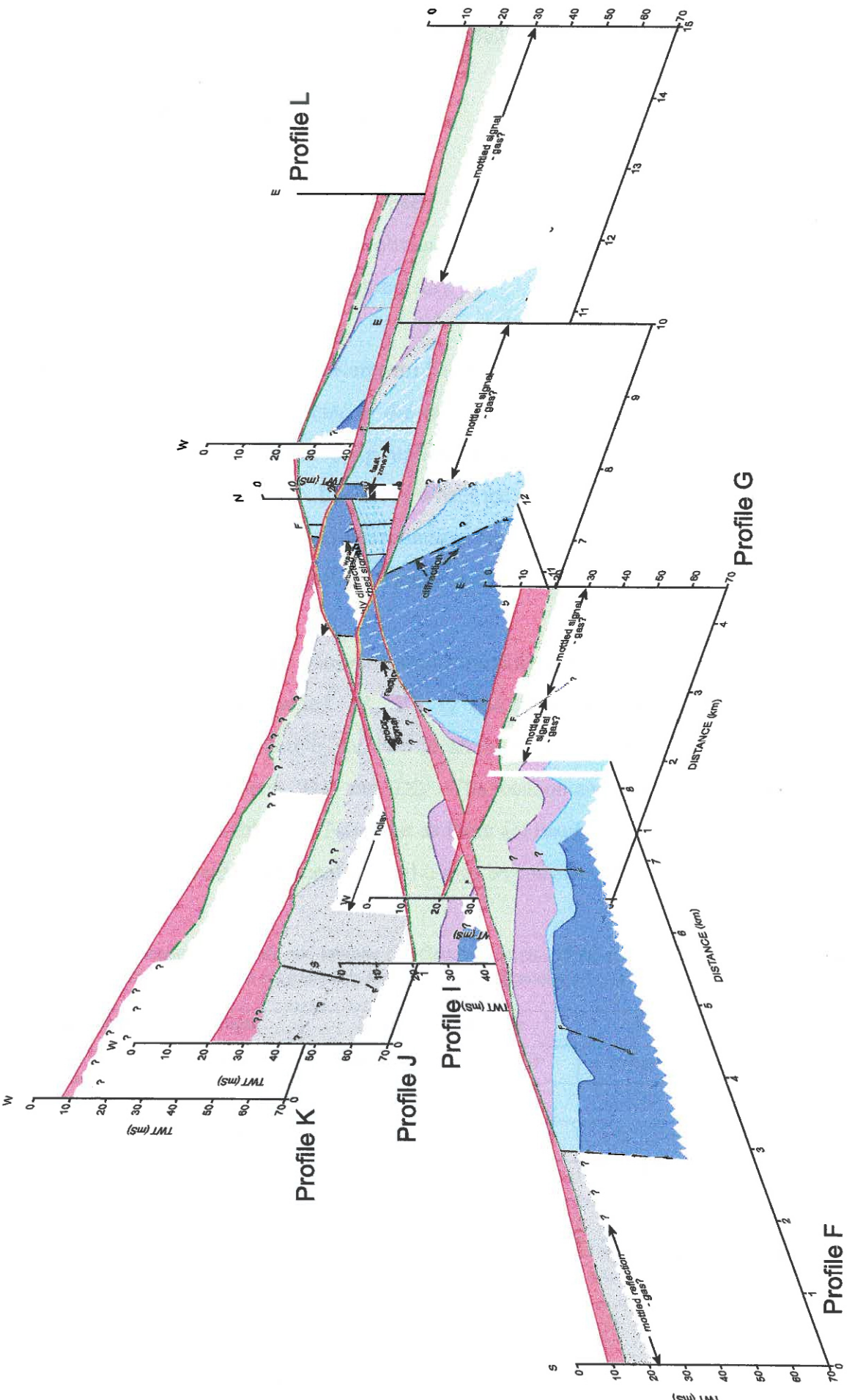

Figure 4.17: Perspective view of Profiles F, G and I-L illustrating summarised stratigraphy.

4.3 INTERPRETATION OF SEISMIC SEQUENCE ANALYSIS RESULTS

4.3.1 Location of the Kerepehi Fault

Once the sequence boundaries had been identified, correlated, and summarised on profiles, fault margins, regions of obvious uplift and heavily diffracted zones were mapped on plan view (Refer to Figure 4.18).

Fault margins belonging to the Kerepehi Fault system were identified by investigating (i) where possible, the character of the fault e.g. dip, location with regards to other geologically significant features e.g. uplifted highs; and (ii) the location of the fault zone (Refer to Appendix 6). Locations where the Kerepehi Fault crossed the seismic profiles were then mapped and interpolation between profiles was undertaken. The results are summarised in Figure 4.19 and Table 4.1.

Within the field area, three transverse faults trending WSW-ENE divide the Kerepehi Fault into 4 segments, labelled 'A', 'B', 'C' and 'D' (Figure 4.19). The location of segments B and D is tentative, and two locations are proposed for segment D, which are referred to as segments 'D1' and 'D2'. The location and length of these segments are summarised in Table 4.1. Note that as there are insufficient data to determine the most northern extent of Segment D1 and it may be considerably longer than stated.

Table 4.1: Location (longitude and latitude NZ Geodetic datum, 1949) and length of four segments of Kerepehi Fault as suggested by analysis and interpretation of seismic sub-bottom profiles.

Segment	Length	Southern End Point		Northern End Point	
	(km)	Long (E)	Lat (S)	Long (E)	Lat (S)
A	15	175°27'53"	37°12'32"	175°25'15"	37°04'41"
B	8.8	175°25'51"	37°04'31"	175°21'30"	37°01'19"
C	13.5	175°23'47"	37°01'09"	175°19'55"	36°54'32"
D1	22.5	175°20'35"	36°54'15"	175°15'38"	36°42'50"
D2	19	175°21'03"	36°54'01"	175°11'36"	36°46'48"

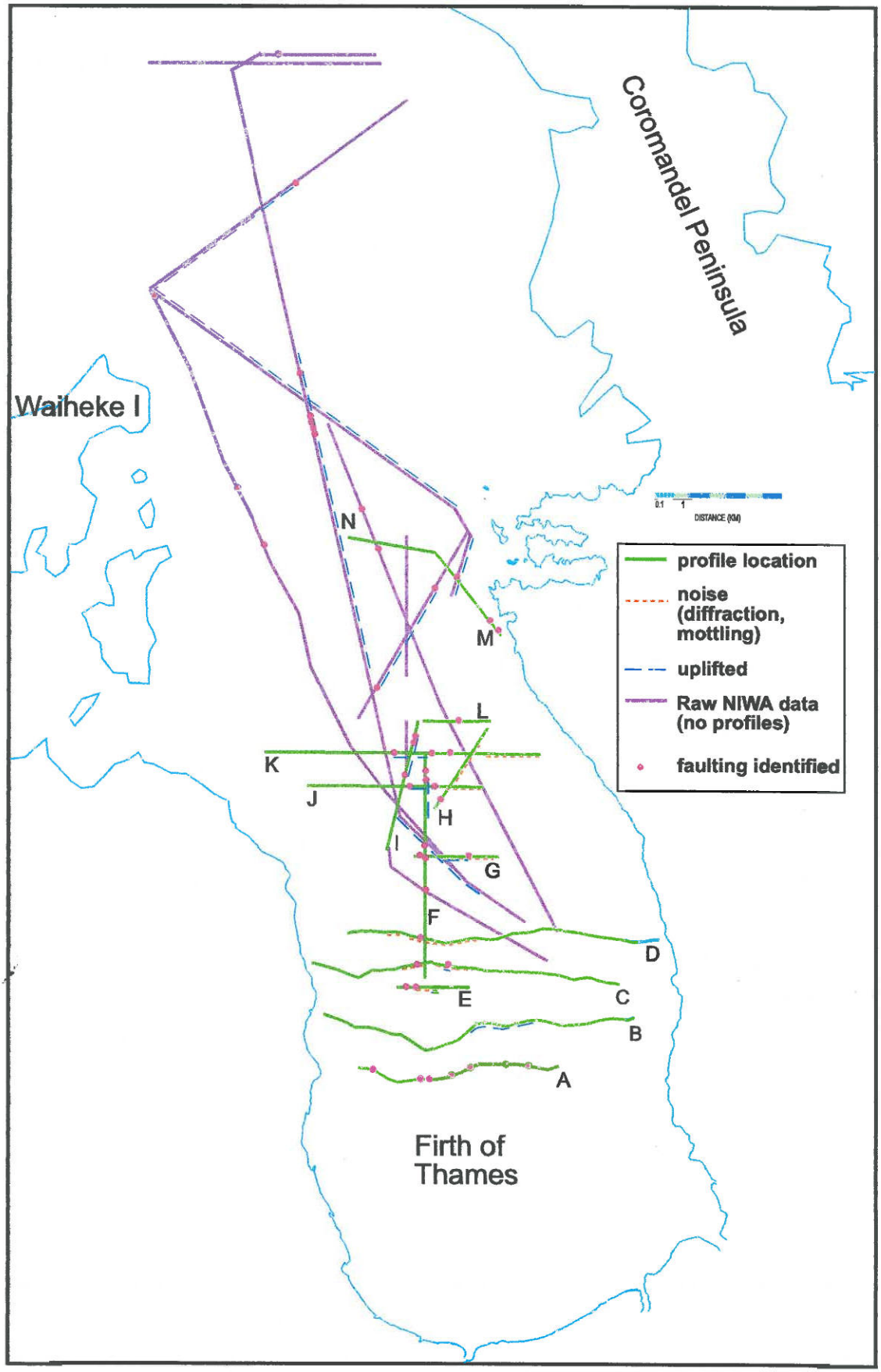

Figure 4.18: Profile locations showing regions of faulting, obvious uplift and extensive diffraction.

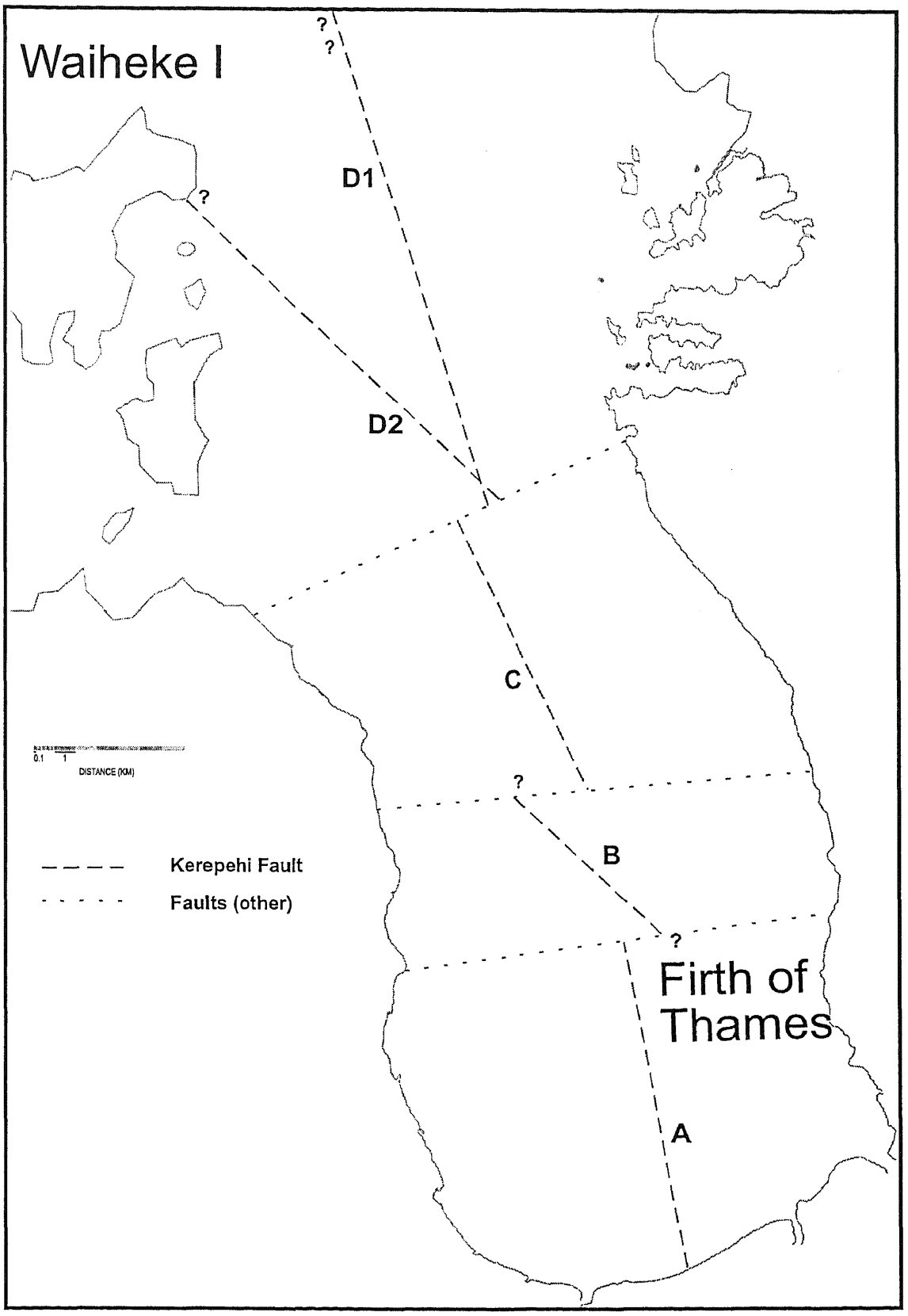

Figure 4.19: Figure illustrating the proposed location for four offshore segments of the Kerepehi Fault based on the results of analysis and interpretation of seismic sub-bottom profiles in this study.

4.3.2 Displacement along the Kerepehi Fault

Profiles generated by seismic sequence analysis provided depths (TWT) for seismic sequences and boundaries. Correlating key reflectors (e.g. sequence boundaries) across the fault margin and calculating the difference in vertical distance between them enables the determination of total historical fault movement, since the generation of that reflector. To accurately determine the time frame over which the fault displacement occurred, and therefore the rupture magnitude likely for any given event, sequence boundary age must be constrained. Absolute age of sequence boundaries can be determined through (i) dating of core sediments, and (ii) stratigraphic modelling which requires comprehensive seismic processing (Neidell, 1977).

In this study, the determination of the amount of displacement is limited by (i) lack of sufficiently deep cores in this region, and (ii) degree of data processing. Hence the suggested displacement rates, derived from seismic sequence analysis and interpretation of relevant literature, represent estimates. However, previous research undertaken in the Bay of Plenty and Gisborne illustrates a linear relationship between observed tsunami wave heights and fault displacement for any given tsunami source region (de Lange and Healy, 1997). Consequently, should any future research suggest a larger or smaller displacement is more likely, the wave heights determined from simulations in this study may be scaled accordingly.

The various stratigraphic units (summarised in Figures 4.3 - 4.16) were most easily recognised in profiles generated from seismic data collected by the D.S.E. (Figures 4.7 – 4.16, Profiles E-N). However, only three of these (Figure 4.8, 4.11, 4.12, Profiles F, I and J) are transected by the Kerepehi Fault *and* illustrate insignificant noise levels in the vicinity of the Kerepehi Fault margin, enabling sequence boundaries to be identified. In each of these profiles the 'Green' reflector, the first sub-surface sequence boundary, is not observed immediately north or east of the Kerepehi Fault. It is hypothesised that displacement along the Kerepehi Fault upthrust sediment immediately north or east of the Kerepehi Fault thus creating an 'uplifted sediment high block' from which the 'Green' reflector has since been eroded. Thus the height above the present seabed that the 'Green' reflector was upthrust can not be accurately

However, assuming the 'Green' reflector was once present above the now, uplifted regions, the minimum distance it may have been uplifted corresponds to 5.3 milliseconds of TWT time (Figure 4.20).

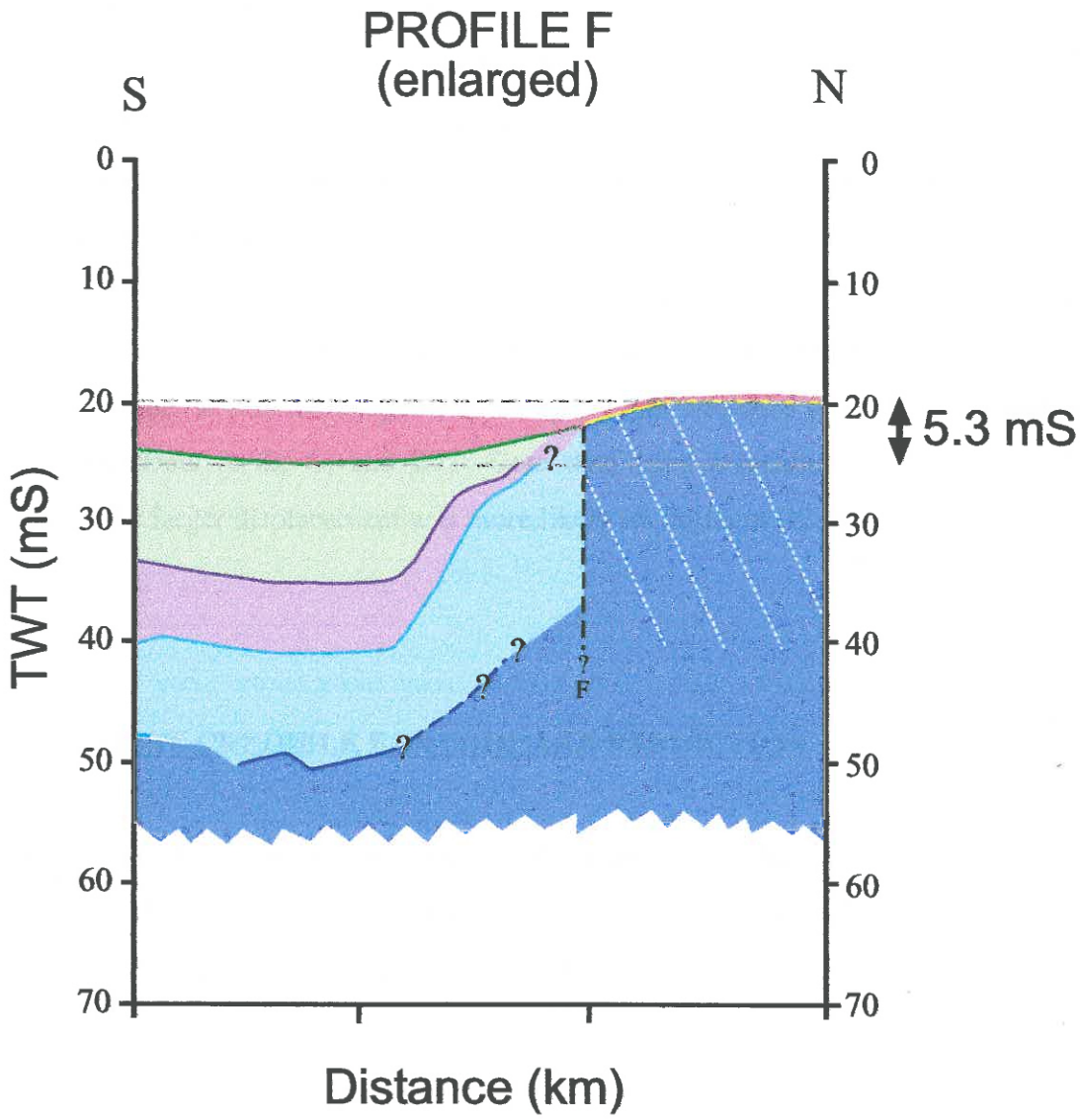

Figure 4.20: Enlarged section of Profile F illustrating minimum magnitude of displacement having occurred since development of the 'Green' reflector.

The 'Green' reflector, the first sequence boundary, is inferred to represent a post-glacial transgressive basal erosion surface that probably formed during the post-glacial Holocene marine transgression that culminated at the present day sea level 6000-6500 years ago. This is consistent with the findings from seismic sub-bottom profiles collected off the east coast of the Coromandel Peninsula (Bradshaw, 1991).

Assuming the compressional velocity of sound in unconsolidated marine sediment is approximately 1600 m/s (Hamilton, 1979), this equates to 4.26 m of displacement occurring over the 6500 year period or 0.7 $mm.year^{-1}$.

De Lange and Lowe (1990) dated and correlated tephra layers across an onland segment of the Kerepehi Fault, just South of the Firth of Thames in the Kopouatai bog. Step functions, fitted to the age versus offset data indicated a mean recurrence interval of 2500 years (lower bound confidence limit given in Appendix 7). Assuming recurrence intervals along the offshore segments are similar to the onland segments, the estimated minimum displacement of 4.26m has probably occurred over two displacement events. Hence, approximately 2.1 m of vertical movement occurs during a given event. It was this magnitude of rupture that was used to model displacement along segments A, B, C, and D1. Core data from a location along segment D2 suggested a larger displacement was more likely for segment D2 (Refer to Chapter 5).

4.4 MOST CREDIBLE EARTHQUAKE PREDICTION

The results of the seismic sequence analysis and palynology information obtained from core 80/20 (Refer to Chapter 5) were used to re-evaluate the Most Credible Earthquake prediction made by de Lange and Hull (1994).

De Lange and Hull (1994) recommended an M.C.E. of M_w=6.9 based on results of trenching studies undertaken on the south-eastern end of the onland, Waitoa segment of the Kerepehi Fault (Figure 2.3). This moment magnitude corresponds to a surface rupture length of approximately 25 km, an average fault slip of 2.5 m, a focal depth of 10 km and a fault dip of 60°W.

The seismic sub-bottom profile data analysed in this study indicated a slightly smaller fault slip[2], 2.4 m is most likely for segments A, B, C and D1. Palynology data from core 80/20 suggest a fault slip along segment D2 could be as large as 8.5 m. The suggested surface rupture length of offshore segments of the Kerepehi Fault range from 9-23 km. The seismic data provides no evidence to indicate focal depth and fault dip are different to those suggested by de Lange and Hull (1994). Applying the same technique as de Lange and Hull (1994) to the revised fault slips and surface rupture lengths produces a range of M.C.E. predictions for offshore segments of the Kerepehi Fault (Refer to Table 4.2). The method required the seismic moment M_0 to be calculated and then converted to M_w. This ensured earthquake source strength was characterised by a magnitude scale that is *not* associated with narrow-band time domain amplitude measurements, and is therefore a scale that does *not* become saturated at large magnitudes. This was undertaken by employing the same method as de Lange and Hull (A. Hull, pers. comm.), a method first outlined in Hanks and Kanamori (1979) (Refer to Appendix 8).

Table 4.2: Most Credible Earthquake predictions for offshore segments of the Kerepehi Fault, in terms of Moment Magnitude, M_w. The fault parameters used to calculate M_w are included in the table.

Segment	M_w	Surface Rupture Length (km)	Fault Slip (m)	Fault Dip (°)	Focal Depth (km)
A	6.7	15	2.4	60	10
B	6.5	8.8	2.4	60	10
C	6.7	13.5	2.4	60	10
D1	6.8	22.5	2.4	60	10
D2	7.1	16	8.5	60	10

[2] Fault slip accounts for both vertical and horizontal components of fault movement. Consequently a 2.1 m vertical displacement results in 2.4 m of fault slip, given a fault dip angle of 60°.

4.5 CONCLUSIONS

This chapter discusses the character of five depositional sequences identified within 135 km of seismic sub-bottom profiles collected by D.S.E and the University of Waikato. Seismic sequence character was used to help correlate seismic sequences across discontinuities in the data and identify regions of displacement (fault zones). Seismic sequences and fault zones were summarised in a series of profiles.

It is proposed that the offshore Kerepehi Fault trends NNW up the central Firth of Thames and is divided into four segments by three WSW-ENE trending transverse faults. The full extent and the exact location of the most northern segment, segment D could not be determined and two locations were proposed. The seismic sub-bottom profiles suggest a minimum displacement of 4.2 m over the last 6500 years is most likely. Interpretation of relevant literature suggests the Kerepehi Fault has an average displacement recurrence interval of 2500 years, hence a 2.1 m displacement is most likely for any given event along segments A, B, C, and D1. This displacement magnitude compares well with a conservative displacement estimate of 2.25 m/displacement event, calculated for the Waitoa segment of the Kerepehi Fault (average vertical separation rate ~0.5/1000 years, most frequent recurrence interval = 4500 years (de Lange and Hull, 1994)).

Fault parameters determined from the analysis of seismic sub-bottom profiles were used to calculate Most Credible Earthquake (M.C.E.) predictions for each segment of the Kerepehi Fault. M.C.E. predictions, presented in terms of M_w (Hanks and Kanamori, 1979), are similar to that calculated from onshore fault parameters (de Lange and Hull, 1994). Displacement along onshore segments has been accurately determined by radiocarbon dating (de Lange and Lowe, 1990) and trenching studies (de Lange and Hull, 1994). The similarities observed between the M.C.E. predictions for onshore and offshore segments provide confidence in the assumptions used to predict fault displacements along offshore segments of the Kerepehi Fault.

4.6 REFERENCES

de Lange, W.P., and Healy, T.R., 1997. Numerical modelling of tsunamis associated with marl diapirism off Poverty Bay, New Zealand, In *Proceedings of Pacific Coasts and Ports: 13th Australasian Coastal and Ocean Engineering Conference and 6th Australasian Port and Harbour Conference, 7-11 September, Christchurch, New Zealand*, Vol. 2, p.1043-1047.

de Lange, W.P., and Hull, A.G., 1994. *Tsunami Hazard for the Auckland Region*, Earth Sciences Department, University of Waikato, and Institute of Geological and Nuclear Science Limited, p. 37.

de Lange, P.J., and Lowe D.J., 1990, History of vertical displacement of Kerepehi Fault at Kopouatai bog, Hauraki Lowlands, New Zealand, since c. 10 700 years ago., *New Zealand Journal of Geology and Geophysics*, Vol. 33, p. 277-283.

Bradshaw, B.E., 1991. *Nearshore and Inner Shelf Sedimentation on the East Coromandel Coast, New Zealand.* M.Sc. Thesis, University of Waikato, Hamilton, New Zealand, 565 p.

Greig, D.A., 1982. *Sediments and recent geological history of the Hauraki Gulf, Firth of Thames and Colville Channel, North Island, New Zealand*, M.Sc. Thesis, University of Auckland, New Zealand.

Hamilton, E.L. 1979. Sound Velocity Gradients in Marine Sediments; *Journal Acoustical Society of America*, Vol. 65, p. 909-922.

Hanks, T.C., and Kanamori, H., 1979. A Moment Magnitude Scale, *Journal of Geophysical Research*, Vol. 84, No. B5, p. 2348-2350.

Hochstein, M.P., Tearney, K., Rawson, S., Davey, F.J., Davidge, S., Henrys, S., and Backshall, D., 1986. Structure of the Hauraki Rift (New Zealand), In W.I.

Reilly and B.E. Harford (eds). *Recent Crustal Movements of the Pacific Region*, Royal Society of New Zealand Bulletin 24. Wellington, The Royal Society of New Zealand.

Hull, A., 1998, email to author, 27 November.

Neidell, N.S., Poggiagliolmi, E., 1977. Stratigraphic Modelling and Interpretation-Geophysical Principles and Techniques. Section 3: Stratigraphic Models from Seismic Data. In C.E. Payton (ed), *Seismic Stratigraphy – applications to hydrocarbon exploration.* Tulsa, Oklahoma, U.S.A., American Association of Petroleum Geologists Memoir 26, p. 389-416.

Chapter 5

NUMERICAL MODELLING OF SEISMOGENIC TSUNAMI GENERATION & PROPAGATION

5.1 INTRODUCTION

Analysis of seismic sub-bottom profiles (Refer to Chapter 4) identified four potentially tsunamigenic segments of the Kerepehi Fault. In order to evaluate the potential tsunami hazard associated with displacement along any of these segments, numerical simulations were undertaken using the 'TSUNAMI' model. The outputs of the simulations undertaken by 'TSUNAMI' were then tested against wave height predictions made by (i) a set of empirical, parametric equations, and (ii) a hydrodynamic circulation model, '3DD'. Finally the results and consequent conclusions derived from comparison of the three prediction methods are presented, and the potential tsunami hazard represented by the Kerepehi Fault is assessed.

The 'TSUNAMI' model is a finite element, deep water generation-propagation and shallow water propagation model that is composed of two computer programs 'TSUGRID' and 'TSUNAMI'. Details regarding the wave theory used to this model, or the finite element method and numerical techniques driving the 'TSUNAMI' model can be found in Prasetya (1998)[3]

The set of parametric equations can be applied to estimate the height of regional tsunami at a particular site as a function of propagation distance. The derivation of these equations is presented in Abe (1995).

'3DD' is a finite difference, circulation and transport numerical model that can be readily applied in shallow water environments. The momentum and continuity equations that drive '3DD' and other details are presented in Appendix 10.

[3] Since submission of Prasetya (1998) the 'TSUNAMI' model has been adapted to allow for different time steps in the generation and propagation phases. Consequently no longer requires a hot start between these two phases.

5.2 MODEL SET-UP

5.2.1 Finite Element Grid

Prasetya (1998) developed the original, finite element grid of the Hauraki Gulf region stretching from 175°36'36"E, 37°15'S to 174°38'E, 36°25'42"S (NZ Geodetic Datum 1949). This grid was developed using bathymetric information from the most detailed Royal New Zealand Navy Hydrographic chart available (de Lange, pers. comm.) in such a way that ensured that rapid changes in bathymetric contours were approximated by fine element resolution (Prasetya, 1998), (Figure 5.1).

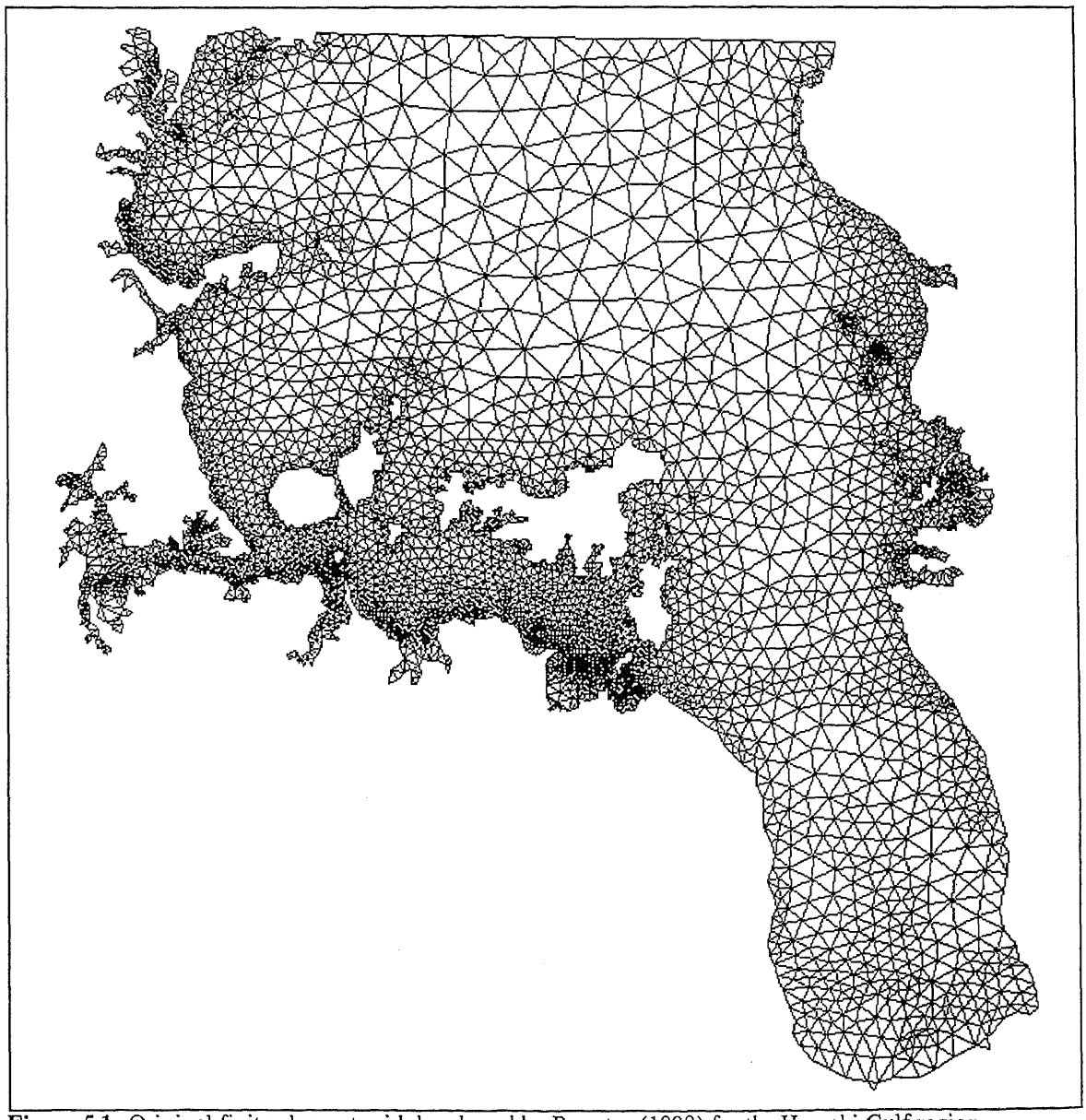

Figure 5.1: Original finite element grid developed by Prasetya (1998) for the Hauraki Gulf region.

The original finite element grid was then further refined in regions where fault displacement were to be modelled, in order to allow the displacement geometry required to drive tsunami simulations, to more closely approximate the geometry of the uplifted high observed in the seismic sub-bottom profiles.

For example, the Kerepehi Fault forms the western margin of a median basement ridge (Hochstein et al., 1986); the surface expression of this ridge, as observed in the seismic sub-bottom profiles analysed in this study, suggests this ridge is approximately 1.25 km wide (Figure 5.2). Refining the element resolution along the fault zone, enabled a displacement zone of approximately the same width to be generated.

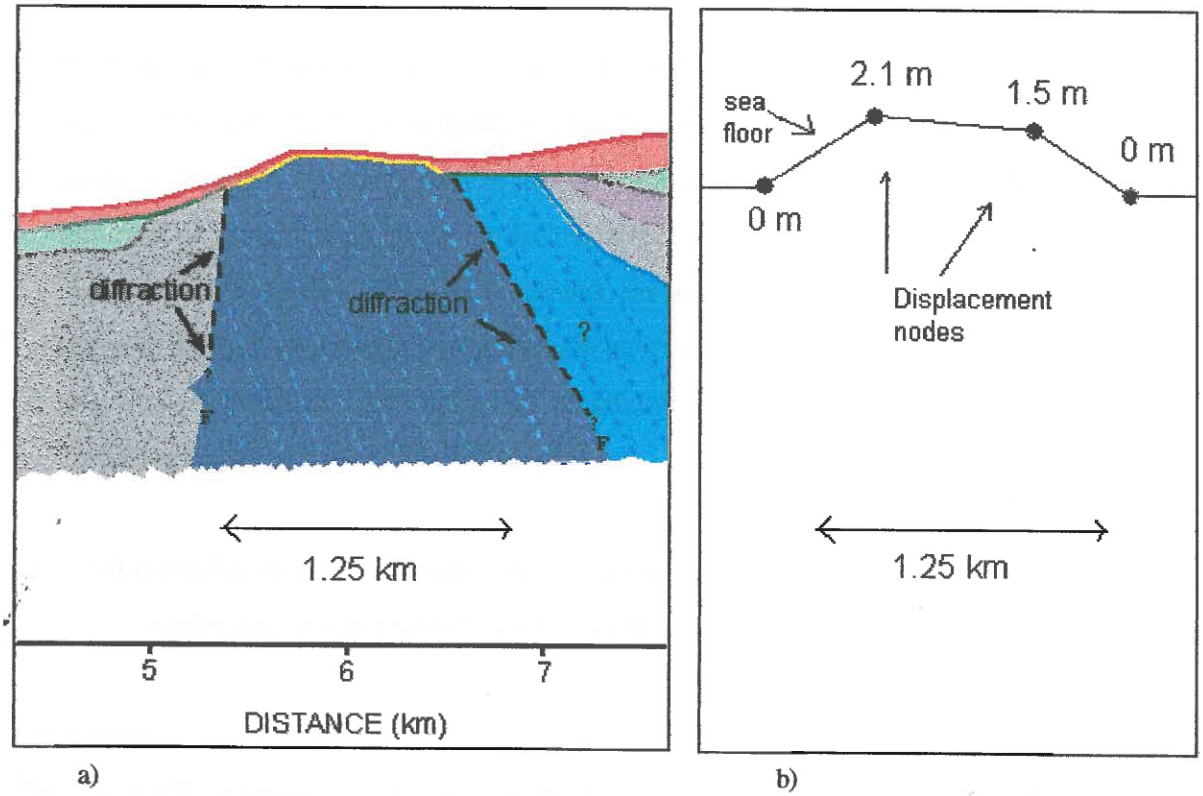

Figure 5.2: a) Enlargement of Profile J (W11-W12) illustrating geometry and width of median ridge at the surface. **b)** displacement geometry used for scenarios 1-4. Note the geometry is similar to that of a).

The refining of the model grid was undertaken using the EDITOR program that is part of the TRIGRID software package. The grid design package TRIGRID, comprises of 16 fundamental programs used to carry out five main functions (Walters and Henry, 1995):

TRIGRID software achieves:

i. Verification and adjustment of coastline and bathymetric data;
ii. Preparation of an irregular triangular depth grid covering the domain to be modelled;
iii. Production of a preliminary irregular triangular model grid with nodes suitably positioned for accurate and efficient numerical modelling;
iv. Interactive checking and editing, including trimming and joining, of model grid;
v. Display and plotting of model output.

Within this study only functions iv. and v. were required, thus only 2 or the 16 TRIGRID programs were employed: EDITOR and DISPLOT.

- **EDITOR** software allows examination and modification of the existing grid. The region to be modified can be specified by clicking on selected vertices in order to create a polygon. Vertices within this polygon can then be added or deleted and removed or merged thus allowing the triangle shape to be adjusted. This program incorporates a 'testing' function to check the integrity of vertice, triangle, node edges or boundary triangle properties (Walters and Henry, 1995). The resulting grid and triangle lists are output as neighbour (*.ngh) and triangle (*.tri) files. These are required by the TSUGRID program.

- **DISPLOT** software displays and plots (i) various geometry files, and (ii) scalar and vector model output variables (Walters and Henry, 1995).

TSUGRID:

The TSUGRID program uses the output files (*.ngh and *.tri) from the EDITOR program to convert the grid into the format required by TSUNAMI. i.e. x and y distances are converted from kilometres into metres. In addition, the program generates interpolating functions for each element, assigning the same interpolating function to elements with similar dimensions i.e. dimensions within a user specified error range are given the same function (de Lange, 1997).

The outputs are then summarised in 3 files:

i. Binary file (*.bin) containing the reformatted grid, interpolating functions and grid constants in a format that can be read by TSUNAMI.
ii. ASCII text file (*.out) containing a summary of the contents of the binary file which enables the user to check for problems in the binary file.
iii. ASCII log file containing a summary of problems identified by TSUGRID and the program's actions (de Lange, 1997).

5.2.2 Boundary Conditions

In order to simulate tsunamis, the TSUNAMI model requires the above mentioned **.bin* file plus up to 5 input files, one of which must include additional boundary condition information (provided by user). There are three types of boundary conditions that may be stipulated in this file:

i. Specified x and y velocities: These may be fixed at specified nodes and applies for the whole simulation. This is useful for specifying river flow.
ii. Specified elevations: Defines nodes to which fixed forcing period and amplitudes should be applied. e.g. open sea boundaries.
iii. Displacement condition: The nodes where seafloor displacement is to occur and the velocities of vertical displacement are specified. These nodes are responsible for generation of the tsunami (de Lange, 1997).

Once the grid is in the correct format and boundary conditions specified, tsunami simulations can be undertaken using the TSUNAMI model. The following figure (Figure 5.3) summarises the steps required to refine the original grid (generated by Prasetya, (1998)) and prepare the TSUNAMI model for simulation.

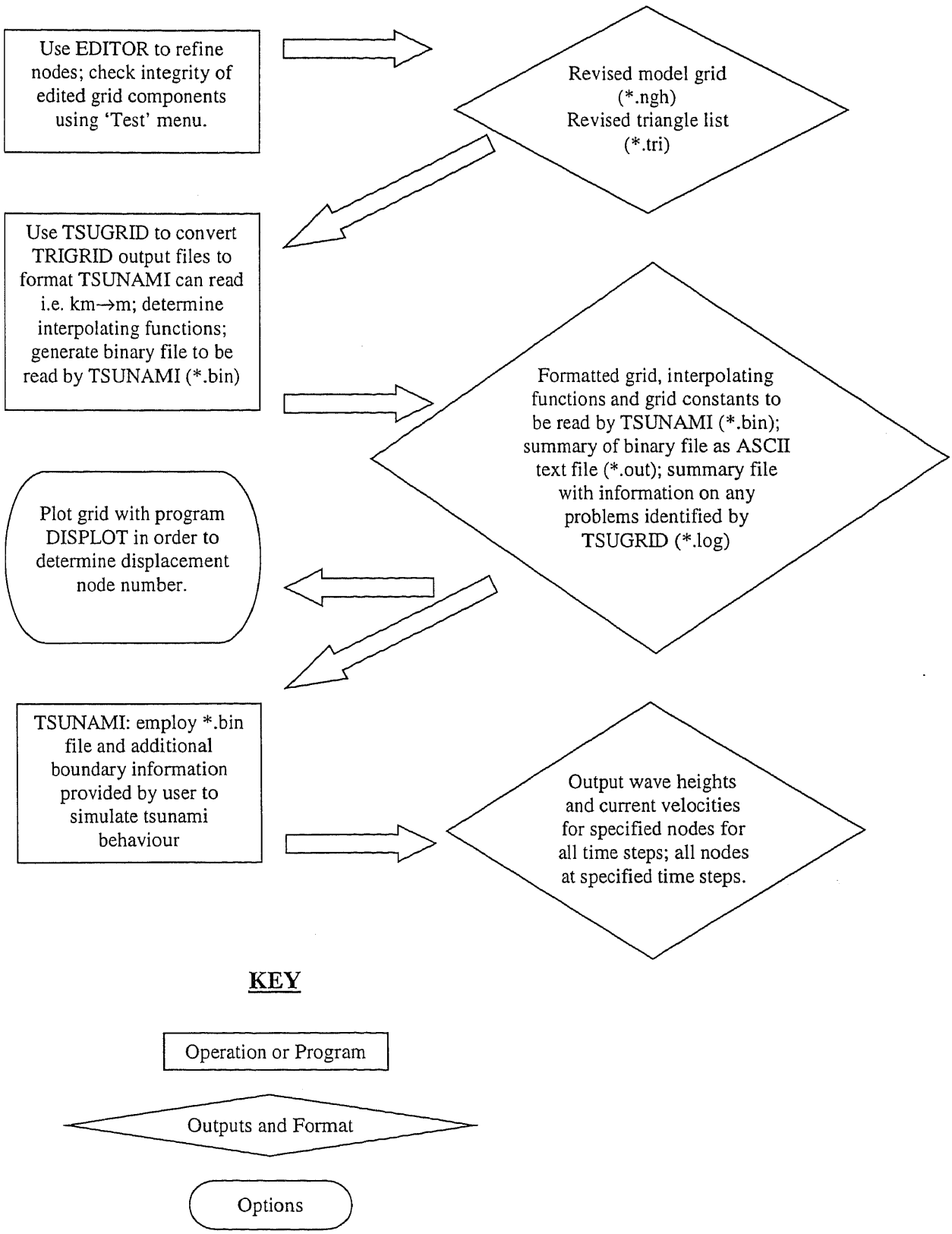

Figure 5.3: Flow chart summarising the steps taken to prepare the files required by the TSUNAMI model.

5.3 EVENTS SIMULATED

A total of five fault displacement events were simulated using 'TSUNAMI'. These involved displacement along Segments A, B, C, D1 and D2 of the Kerepehi Fault. The generation parameters are summarised in Table 5.1. These parameters are specified within the boundary condition file for the 'TSUNAMI' software by defining:

- 'x' number of displacement nodes,
- displacement start time,
- vertical displacement velocity,
- displacement stop time.

Table 5.1: Generation parameters of the five simulations undertaken using the 'TSUNAMI' software.

Scenario	Segment		Displacement		
	Name	Length (km)	Magnitude (m)	Duration (s)	Volume (m^3)
1	A	15	2.1	2	$3.94x10^7$
2	B	8.8	2.1	2	$2.31x10^7$
3	C	13.5	2.1	2	$3.54x10^7$
4	D1	22.5	2.1	2	$5.91x10^7$
5	D2	19	7.35	2	$1.75x10^8$

The displacement locations (segment length and position) were determined through analysis of seismic sub-bottom profiles (Refer to Chapter 4).

As no displacement events have occurred during human recorded time along the Kerepehi Fault, there was no precedent for displacement duration. However, the displacement resulting from the 1987 Edgecumbe earthquake has a number of similarities with displacement along the Kerepehi Fault. Like the Kerepehi Fault, the Edgecumbe earthquake occurred in a rifting environment and was associated with normal faulting. The Edgecumbe earthquake had had a maximum vertical offset of 2 m and magnitudes of M_L = 6.3 (Smith, 1989), M_b =5.9, M_s = 6.6 (Priestley, 1989), M_w = 6.3, similar to the displacement magnitudes expected along the Kerepehi Fault (M.C.E: M_w = 6.5-7.1). Consequently the displacement duration (slip duration) of the Edgecumbe earthquake was used to simulate displacement along the Kerepehi Fault.

Displacement duration theoretically corresponds to the dislocation rise time (duration of slip at a given point), which was in the order of 2 seconds for the Edgecumbe earthquake (T. Webb, pers. comm.).

In addition, deterministic modelling of strong motion and teleseismic waveforms by Heaton (1990) suggest that, on average, the dislocation rise time is only 16% of the overall rupture duration (total duration of rupture for Edgecumbe earthquake was 8 seconds). However, of the data presented by Heaton (1990), earthquakes of magnitudes (M~6.5) (similar to that expected along the Kerepehi Fault) have average dislocation rise times that are 24% of the overall rupture duration. This corresponds to approximately 2 seconds for the Edgecumbe earthquake.

The displacement magnitude of Segments A, B, C and D1 were determined using the results of the seismic sub-bottom profile analysis and average rupture recurrence interval (de Lange and Lowe, 1990), (Chapter 4).

The magnitude of displacement occurring along Segment D2 was determined using conclusions drawn from a paper (Pocknall et al. 1989) discussing the palynology (study of pollen, spores and microfossils) of Core 80/20, as discussed below.

Determination of Displacement Magnitude from core 80/20

Core 80/20 is a shallow (~ 1.4 m deep) core drilled at 35 m water depth at location NZMS260 S11/126 820; (175° 16' 01"E, 36° 50' 33" S, NZ Geodetic Datum, 1949). Peaty mud sediment deposited in a marginal marine environment and observed between 0.5-1.4 m core depth were dated at 11.9-14 ka. This suggests that sea level was at 35 m below present between 11.9 –14 ka. However, it is commonly accepted that sea level in New Zealand at this time was 55-70 m below present. Thus the core exhibits a sea level anomaly of 20-35 m. There are two possible explanations for this:

- rapidly rising post-glacial sea levels, that would account for *some* of observed anomaly.
- Local and aberrant tectonic uplift within the longer term subsidence of the Hauraki Rift (Pocknall et al., 1989).

The second explanation is acceptable if we consider that core 80/20 may be situated on a tectonic high generated by uplift along eastern margin of Segment D2 of the Kerepehi Fault (Figure 5.4). Therefore, Segment D2 of the Kerepehi Fault may be considered to have an average uplift rate of 1.4 – 2.9 mm.yr^{-1} (i.e. between of 20 –35 m of uplift over 11 900 – 14000 years), (Figure 5.5).

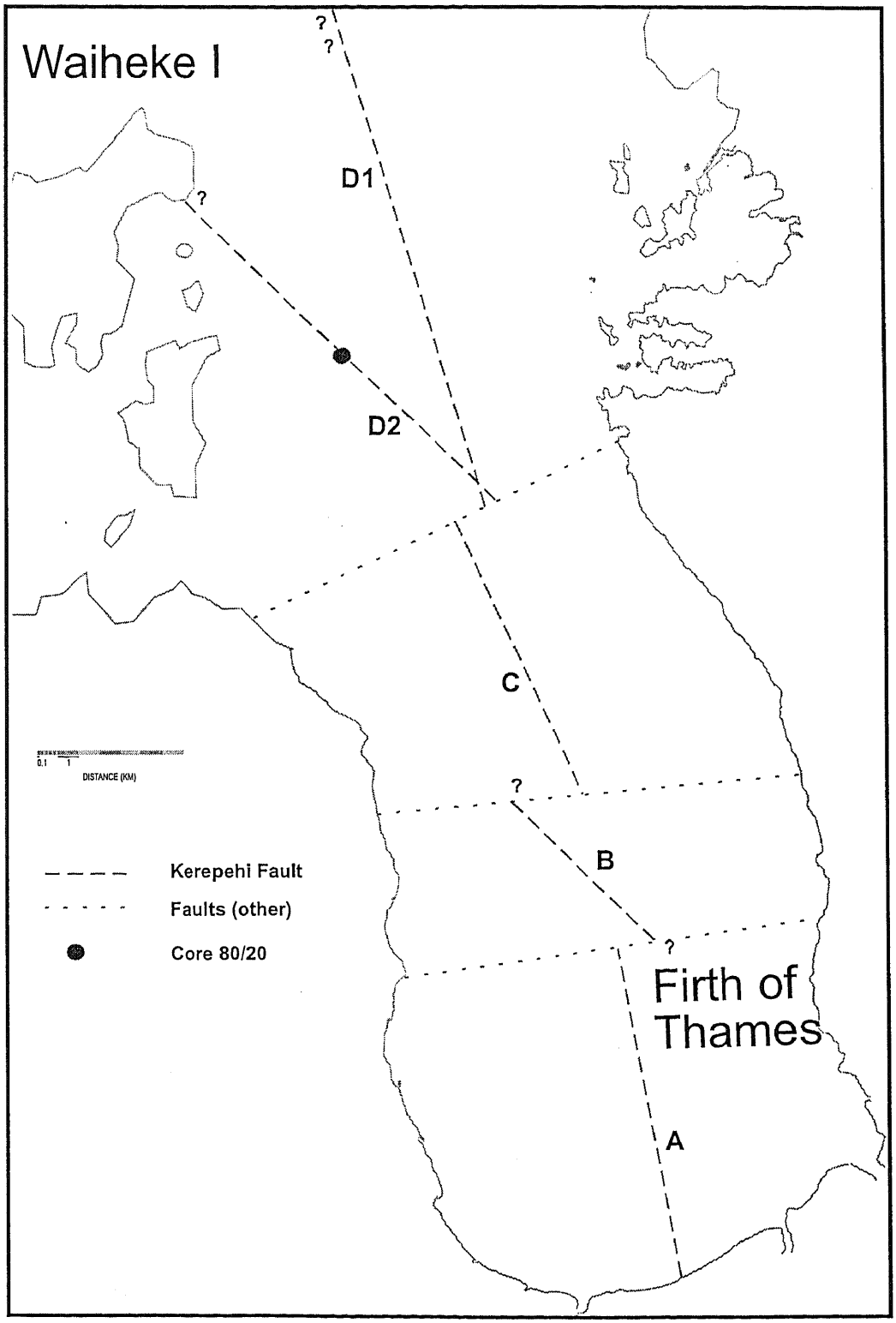

Figure 5.4: Location of core 80/20 in relation to the Kerepehi Fault.

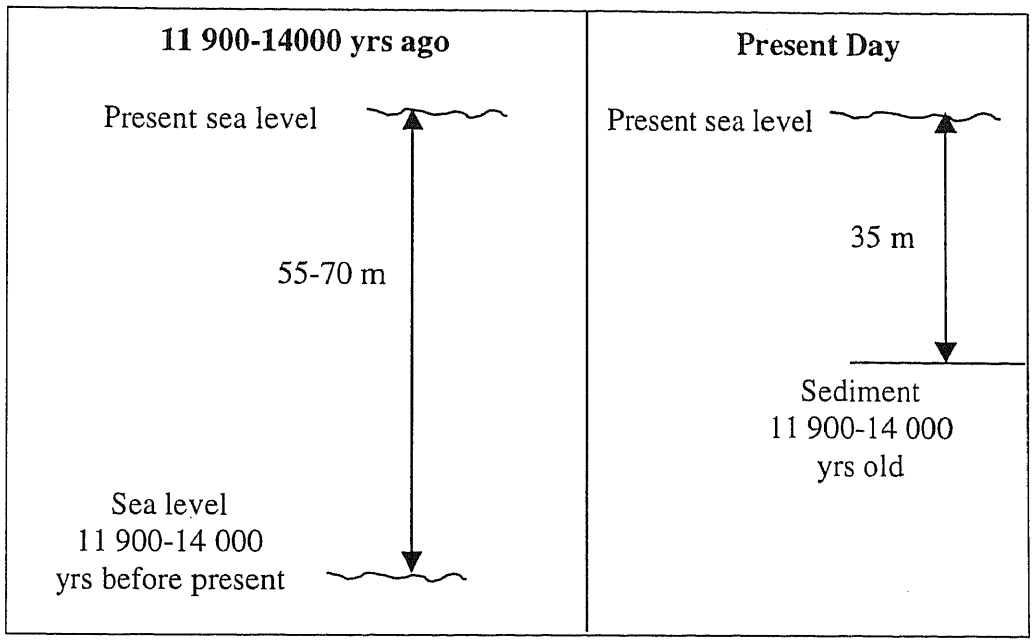

a) b)

Figure 5.5: a) In New Zealand, sea level 11 900-14000 years ago is commonly accepted to be 55-70 m below present day sea level; **b)** At the location of core 80/20 marginal marine sediment 11 900-14 000 years old only lies 35 m below present day sea level. The anomaly between sea level in a) and b) is believed to be due to tectonic uplift of 20-35 m occurring over the last 11 900-14 000 years.

Assuming the recurrence interval of onland segments determined by de Lange and Lowe (1990) hold for Segment D2, displacement is expected once every 2500 years (on average) which provides an expected rupture for any given event of:

- minimum rupture = 3.55 m,
- maximum rupture = 7.35 m.

5.4 RESULTS

5.4.1 Scenario 1: Displacement along Segment A

Scenario 1 involved 2.1 m of displacement along 15 km long Segment A. The initial water depth along the displacement zone ranged from 0.6-9.5 m. The displacement occurred over a 2 second period with an average rupture velocity of 1.05 $m.s^{-1}$.

Waves

The largest water displacement generated by this wave occurred directly above the generating area at the end of the displacement, and was approximately 0.8 m. At this time (i.e. 2 s after displacement began) the maximum shoreline wave height was experienced and occurred at the base of the Firth of Thames with wave heights of 0.64 m.

Within 10 seconds the wave has propagated further onshore, reaching the base of the Fifth of Thames with maximum wave heights reduced to 18.5 cm (Appendix 9, Figure A9.2). By 3.5 minutes the wave impacts on the eastern margin of the Firth with a wave height of 3 cm occurring just north of Tararu, at Windy Point (Appendix 9, Figure A9.4). The maximum onshore wave height at this time (14 cm) still occurs at the base of the Firth of Thames, just west of Pipiroa. By 5 minutes, 10 seconds the majority of coastline in the southern Firth of Thames has been impacted by a wave of between 1 and 2.5 cm although a 13 cm maximum is still observed at the base (Appendix 9, Figure A9.6). At 6 min, 50 sec wave height continues to decay at the shoreline, the maximum still only 12 cm high (Appendix 9, Figure A9.8). It continues to propagate out from the base of the Firth of Thames. The majority of the Firth is impacted by a 1-2.5 cm wave, and the largest waves are still concentrated at the base of the Firth of Thames. By 17 minutes all wave heights are under 10 cm high.

Table 5.2: Scenario 1: Arrival time and magnitude of maximum observed wave heights for a variety of locations around the Firth of Thames after 2.1 m displacement along Segment A.

Location	Max Wave Height (cm)	Time of Max Height (hrs, min, sec)
Between Piako and Waihou Rivers	7.74	0, 16, 10
Te Puru	3.85	0, 17, 0
Kaiaua	4.21	0, 17, 50
Tararu	6.7	0, 21,10
Moanataiari (Thames)	7.05	0, 22, 10
Offshore Miranda	6.84	0, 22, 30
Waihou River Mouth	7.1	0, 23, 10
S of Wilson's Bay	1.67	0, 41, 20
Waimangu Pt	1.72	0, 41, 30

Currents

Between 0.5 and 1 minute after displacement, current velocities have increased to approximately 0.05 $m.s^{-1}$. Initially currents radiate out from the generation area in predominantly WSW and ENE directions (Appendix 9, Figure A9.3, A9.5). Some time between 13 min. 30s and 21 min. 50 s the main direction of propagation changes to a northerly direction (Appendix 9, Figure A9.10-A9.11).

The presence of land at the southern end of the generation area prevents water from flowing southwards and is the likely cause of wave focussing occurring at Miranda and between Tararu and Thames during the early phases of tsunami propagation i.e. at around 6 min (Figure A9.7 and A9.9). Despite the focussing, wave heights are still small i.e. between 1 and 5 cm. The focussing is no longer evident at Miranda at 6 min 50 sec or Thames, 21 min 50 sec after displacement. After one hour all currents are less than 0.05 $m.s^{-1}$. These current velocities are depth averaged results and are considerably smaller than tidal currents.

5.4.2 Scenario 2: Displacement along Segment B

Scenario 2 involved 2.1 m of displacement along 8.8 km long Segment B. The initial water depth along the displacement zone ranged from 8.5-17.3m. The displacement occurred over a 2 second period with an average rupture velocity of 1.05 $m.s^{-1}$.

Waves

The maximum wave height of 0.8 m occurred above the displacement region at the end of displacement i.e. at 2 s. The maximum onshore wave height occurred just north of Wharekawa (175°18'6" E; 37°3'24" S) 9 min. 20 s after the initial displacement began, but was only 5 cm high (Table 5.3). The wave does not disperse evenly from the generation area, but is inclined to propagate in a predominantly southward direction (Appendix 9, Figure A9.12-A9.21). The wave is greatest in the

shallowest water depth (i.e. at the shoreline) which is expected as a result of shoaling. This wave front propagates southwards into the Firth of Thames and peaks at the base 57 minutes after generation began with a maximum wave height of 2.7 cm. Wave height versus time graphs for a variety of locations, each with increasing distance from the base of the Firth of Thames, show plateau's in the graph slope that occur at longer times after initial displacement, as distance from the base of the Firth of Thames increases (Table 5.4; Figure 5.6). This suggests the wave is reflected from the base of the Firth of Thames and forced to propagate northward, back out of the Firth of Thames.

Note: at 55 minutes elevated water levels occur adjacent to the eastern margin of Ponui Island. This anomalous result may occur in response to wave focusing at this region.

Table 5.3: Scenario 2: Maximum wave height and associated arrival times for a variety of locations after 2.1 m displacement along Segment B.

Location	**Max. Wave Height (cm)**	**Time of Max. Height (hr, min, s)**
Wharekawa	4.98	0, 9, 20
Kaiaua	4.35	0, 17, 10
Base of Firth of Thames (FOT)	2.72	0, 57, 20
Tararu	2.70	0, 50, 50
Miranda	2.66	0, 50, 0
Between Piako R. & Waihou R.	2.40	0, 57, 0
Waihou R. mouth	2.29	0, 58, 0
S. of Wilson Bay	2.28	0, 17, 10
Moanataiari	2.27	0, 56, 50
Waimnagu Pt	1.87	0, 11, 20
E. of Ponui Is.	1.40	0, 40, 20
Rangipukea Is.	0.81	0, 31, 0
E of Waiheke	0.65	0, 42, 20
Kawakawa Bay	0.47	1, 13, 40
Tamaki St.	0.04	2, 29, 40
Musick Pt (Half Moon Bay)	0.00	N/A
Water front, Auckland City	0.00	N/A

At no point during the simulation do waves reach onshore heights as large as 10 cm.

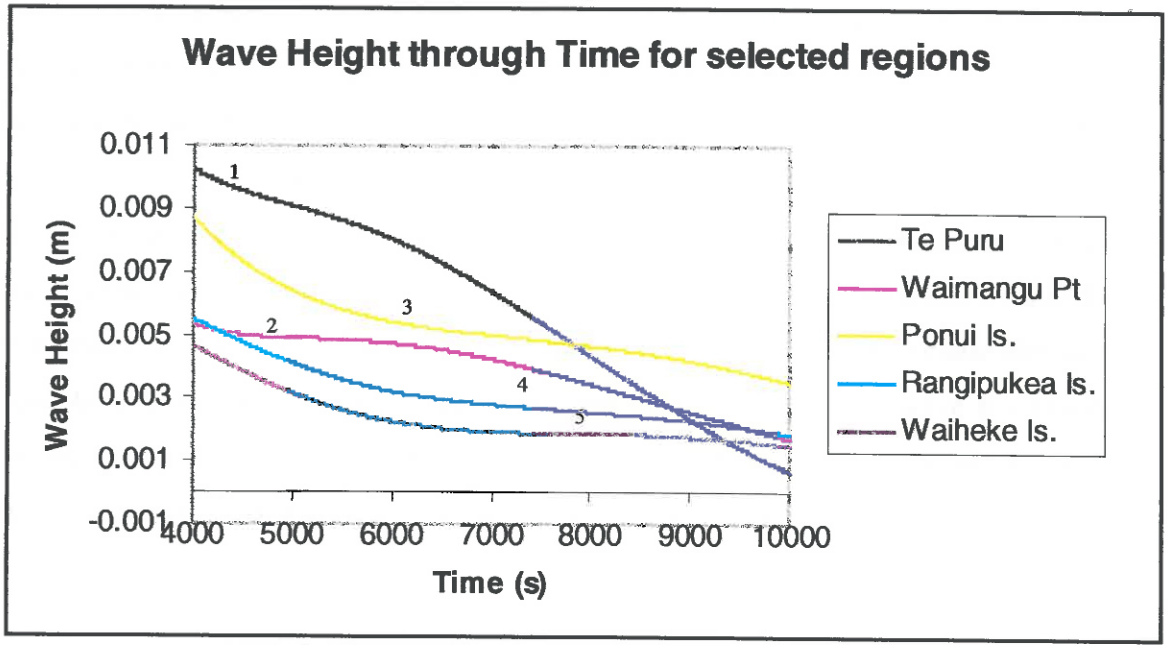

Figure 5.6: Scenario 2: Figure illustrating five peaks/plateaus in the Wave Height (m) through Time (s) graph slope generated from passage of the wave reflected from the base of the Firth of Thames. The values 1, 2, 3, 4, 5 denote the approximate peak of the reflected wave for Te Puru, Waimangu Point, Ponui Island, Rangipukea Is and Waiheke Island respectively.

Table 5.4: Scenario 2: Arrival time of reflected waves at locations situated increasingly north of the base of the Firth of Thames, after a 2.1 m displacement along Segment B.

Location	**Arrival time of Plateau/2nd Peak (hrs, min, s)**
Te Puru	1, 24, 20
Waimangu Pt	1, 25, 40
E of Ponui Is.	1, 53, 40
Rangipukea Is.	2, 1, 40
E of Waiheke	2, 8, 40

Currents

Throughout this simulation currents remained insignificant (Appendix A9.13-A9.21). The maximum current velocity occurred approximately 5 minutes after the initial displacement and had a magnitude of only 0.06 $m.s^{-1}$.

Immediately after displacement, currents were non-existent but by 3 min. 30 s were observed radiating from above the generation area in predominantly NE and SW directions. Currents propagating in a SW direction appear to be larger. This is believed to be due to steeper wave height gradients generated in response to the

displacement geometry (i.e. the fault scarp on the SW edge is steeper than the land on the NE edge). As a consequence, the wave appears to propagate as a front travelling southwards into the Firth of Thames. Currents radiate out from directly behind this region (north of the zone showing the largest wave heights), and the strongest of these propagate southwards (Figure A9.20, A9.21). The presence of land causes current convergence at the base of the Firth of Thames. This is evident between 27 and 55 min., however, the magnitudes of these currents are too insignificant to cause elevated wave heights at this location. After 55 minutes the reflection of the wave front from the base of the Firth of Thames changes the predominant current direction from southwards to northwards. Current magnitudes are still negligible.

5.4.3 Scenario 3: Displacement along Segment C

Scenario 3 involved 2.1 m of displacement along 13.5 km long Segment C. The initial water depth along the displacement zone ranged from 17.1-26.9 m. The displacement occurred over a 2 second period with an average rupture velocity of 1.05 $m.s^{-1}$.

Waves

The maximum wave height (0.81 m), is observed at the end of displacement (i.e. at 2 s) above the north western displacement zone. The largest onshore wave height for this simulation, 0.075 m, occurs at Waimangu Point 8 min. after displacement began. The maximum wave heights and time of impact for several locations around the Firth of Thames are summarised in Table 5.5.

Immediately after the displacement, the tsunami wave is elongated NWN-SES and radiates away from the displacement zone. By 7 minutes the segments of the wave closest to the shore are shoaling, increasing in wave height and causing the wave to be elongated W-E (Figure A9.27, A9.29). By 13 min 30 s the wave has separated into two elevated zones occurring at the western and eastern shorelines of the Firth of Thames, at Waimangu Pt and Waikawau respectively (Figure A9.31). These zones of elevated wave height then propagate southward (Figure A9.32) and reach the base of

the Firth of Thames by 55 minutes. Graphs of wave height through time suggest the wave is then reflected from the base of the Firth of Thames and propagates northwards (Figure 5.7). Table 5.6 lists the arrival times of 2nd and 3rd peaks[4] observed at locations around the Firth of Thames. The last peak observed within the Wave Height through Time graphs is believed to be associated with reflection of the wave from the base of the Firth of Thames. The Wave Height through Time graphs for Deadmans Point, Rangipukea Island, Wilsons Bay, Ruthe Passage and Ponui Island show an additional peak occurring between that generated by the initial displacement and the generated from reflection from the base of the Firth of Thames. These peaks most likely occur in response to reflection of wave energy from (i) Ponui Island, and (ii) the land adjacent to and west of the displacement zone.

Table 5.5: Scenario 3 (2.1 m displacement along Segment C): Maximum wave height and associated arrival times for a variety of locations near the displacement region.

Location	**Magnitude (cm)**	**Time (hrs, min, s)**
Base of Firth of Thames	2.9	1, 6, 30
Deadmans Pt	3.8	0, 8, 50
Kaiaua	2.9	0, 32,50
Miranda	2.9	1, 3, 40
Moanataiari	2.5	0, 53, 20
Orere Pt	5.4	0, 11, 20
Pakihi Is.	1.2	0, 37, 0
Ponui Is	2.9	0, 23, 0
Rangipukea Is (S tip)	2.1	0, 12, 10
Ruakura Pt	1.5	0, 26, 20
Ruthe Passage	1.3	0, 23, 30
Tapu	4.7	0, 16, 20
Te Puru	3.4	0, 27, 50
Waiheke Is.	0.7	0, 37, 10
Waimangu Pt	7.5	0, 8, 0
Waikawau	0.1	0, 14, 0
Whakakaiwhara Pt	0.1	1, 32, 0
Wharekawa	4.1	0, 12, 40
Wilsons Bay	7.4	0, 8, 50

[4] Note that the 2nd crest is often masked behind the initial wave form, making it difficult to identify. However, the sharp decrease in slope observed in the initial peak (e.g. Figure 5.7, 4900 s at TePuru,) generates a plateau, representing the second, masked peak believed to be generated from a reflected wave (Table 5.6).

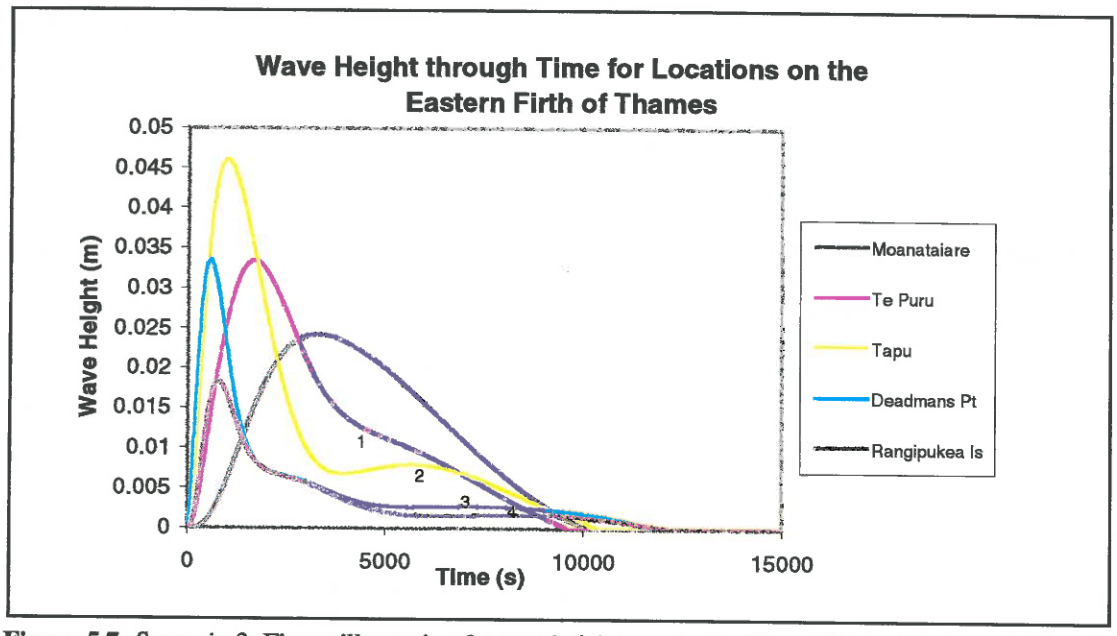

Figure 5.7: Scenario 3: Figure illustrating four peaks/plateaus in the Wave Height (m) through Time (s) graph slope generated from passage of the wave reflected from the base of the Firth of Thames. The values 1, 2, 3, 4 denote the approximate peak of the reflected wave for Te Puru, Tapu, Deadmans Pt and Rangipukea Is respectively.

Table 5.6: Scenario 3: Table illustrating the magnitude and arrival time of 2nd and 3rd* peaks (or plateaus♣) generated as a result of reflection after a 2.1 m displacement along Segment C.

Location	Time (hrs, min, s)	Magnitude (cm)
S. tip of Rangipukea Is.	♣0, 39, 50	0.65
Deadmans Pt	♣0, 42, 30	0.64
Wilsons Bay	0, 53, 50	0.52
Ruthe Passage	♣1, 7, 0	0.31
Ponui Is	♣1, 12, 10	0.43
Orere Pt	♣1, 20, 40	0.35
Waimangu Pt	1, 24, 0	0.47
Wharekawa	♣1, 24, 20	0.86
*Ruthe Passage	1, 25, 40	1.09
Te Puru	♣1, 26, 00	0.21
Tapu	1, 34, 20	0.79
Waikawau	1, 42, 10	0.67
*Wilsons Bay	1, 46, 40	0.52
*Deadmans Pt	1, 58, 30	0.27
*S. tip of Rangipukea Is	2, 17, 10	0.17
*Ponui Is.	2, 20, 30	0.39
Ruakura Pt	2, 23, 50	0.23
Waiheke Is.	2, 28, 30	0.14
Pakihi Is.	2, 30, 20	0.21

♣ Represents a plateau in graph slope as opposed to a peak, * Identifies 3rd peak to impact on location.

Currents

Currents (Appendix 9, A9.24-A9.32) start becoming obvious by 3 min. 30 s and are observed to radiate in all directions from around the displacement zone. The maximum current velocity, 0.035 $m.s^{-1}$ occurs at approximately 10 min. by which time the strongest currents propagate predominantly north and south of the displacement zone. Comparatively strong, westward currents are also observed east of Ruakura Pt. After 10 min. current magnitudes begin to decline and by 25 minutes are too small to be significant.

Current divergence: Initially current divergence occurs from around the displacement zone, radiating in all directions. Divergence from above the displacement zone remains the major current pattern until 16 minutes at which time wave height gradients associated with elevated wave heights on the east side of the Firth of Thames generate divergence from the coastline near Waikawau. Between 16 – 40 minutes both divergence zones (i.e. Figure 5.8: (A) over displacement zone, (B) north of elevated wave heights on eastern margin of Firth of Thames) are evident. By 27 minutes these divergence zone begin to shift southwards, in the same direction of wave propagation, but appear to 'lag' behind the wave crest (Figure 5.8). By 40 minutes the divergence associated with the displacement zone is negligible and only divergence from behind the wave front is significant.

Current convergence: Convergence is evident at two localities: (i) between Ruakura Pt and Ponui Island, and (ii) at the base of the Firth of Thames. Convergence between Ruakura Pt and Ponui Island is first observed at 3 min. 30 s and continues for the duration of the simulation. Convergence at the base of the Firth of Thames is not evident until 23 minutes into the simulation but does also continue throughout the simulation but without having any apparent impact of wave height at this location.

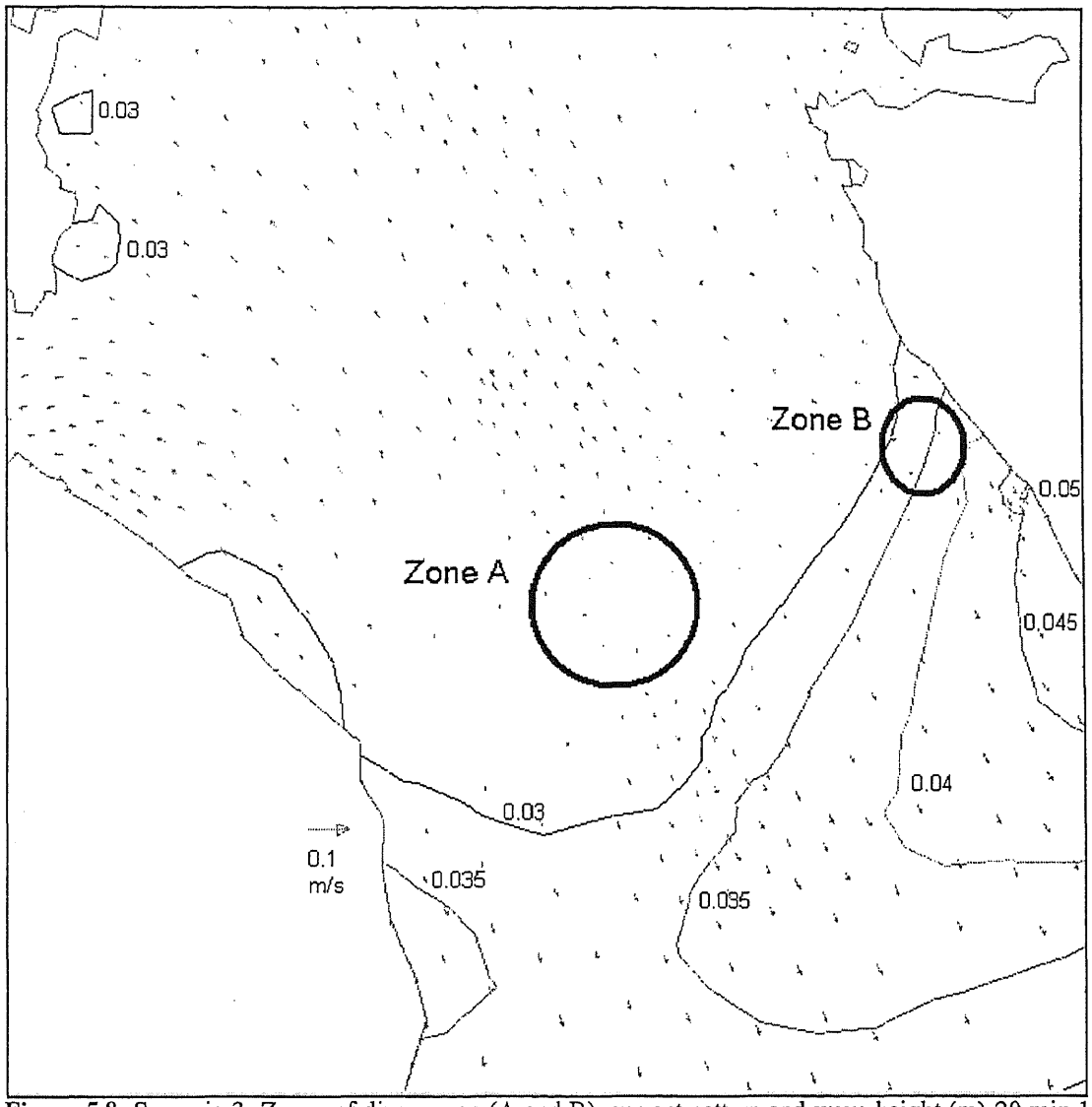

Figure 5.8: Scenario 3: Zones of divergence (A and B), current pattern and wave height (m) 20 min 10 s after 2.1 m displacement along Segment C.

5.4.4 Scenario 4: Displacement along Segment D1

Scenario 4 involved 2.1 m of displacement along 22.5 km long Segment D1. The initial water depth along the displacement zone ranged from 24.9-37.8 m. The displacement occurred over a 2 s period with an average rupture velocity of 1.05 $m.s^{-1}$.

Waves

The maximum wave height (0.89 m), is observed at the end of displacement (i.e. at 2 s) above the central displacement zone. The largest onshore wave height for this

simulation, 0.093 m, occurs at the western tip of Whanganui Island 11 minutes after displacement began. The maximum wave heights and time of impact for several locations around the Firth of Thames are summarised in Table 5.7.

Table 5.7: Scenario 4 (2.1m displacement along Segment D1): Arrival time of first wave height peak and associated magnitude for a variety of locations within the Hauraki Gulf.

Location	Arrival Time (hrs, min, sec)	Magnitude (cm)
N. of Te Kawau Pt	0, 23, 55	2.48
*Rakino Is.	0, 26, 45	0.52
Waiheke Is.	0, 8, 25	3.95
S. of Man O War Bay	0, 22, 5	2.81
Motuoruhi Is.	0, 9, 15	8.96
Moturua Is.	0, 14, 20	3.81
W. tip of Wanganui Is.	0, 11, 10	9.32
*Coromandel Whalf	1, 12, 15	0.88
Rangipukea Is.	0, 9, 15	8.37
Deadmans Point	0, 6, 15	7.47
Rotorua Is.	0, 13, 5	8.40
Ruthe Passage	0, 12, 55	7.54
Browns Bay	0, 54, 20	0.38
Waiheke channel (northern end)	0, 11, 10	5.35
*Mania Harbour	0, 52, 10	1.63
Ruakura Pt.	0, 31, 25	3.07
Orere Pt.	0, 28, 0	5.34
Waimangu Pt.	0, 31, 0	4.35
*Base of Firth of Thames	1, 45, 30	2.91
*Moanataiari	1, 38, 30	2.61

* locations where only the initial peak is observed.

Immediately after displacement wave heights and current velocities indicate the wave propagates away from the generation area, dispersing in all directions (Appendix 9, Figure A9.38). However, by 5 min. it is clear that the majority of wave energy is dispersing perpendicular to the longest displacement axis i.e. westward and eastward directions (Appendix 9, Figure A9.40). The wave then essentially breaks into two wave fronts causing the largest wave heights to be observed at two zones, (i) between Rotorua and Ponui Islands, and (ii) near the entrance to the Coromandel Harbour, namely from Rangipukea Is. north up to Motuoruhi Island (Appendix 9, Figure

A9.42). Following this the largest wave heights are observed (i) in the entrance to Manaia Harbour, and (ii) propagating southward, along the western margin of the Firth of Thames from Ponui Island to Orere Point to Waimangu Point etc (Appendix 9, Figure A9.43, A9.44).

By 1 hour 36 minutes, 40 seconds (Appendix 9, Figure A9.46) the southward propagating wave peaks at the base of the Firth of Thames with a maximum wave height of ~2.9 cm. The majority of wave energy appears to linger and eventually decay (Appendix 9, Figure A9.48) at this location. Wave height time series graphs (Appendix 9, Figure 5.9) indicate a small portion of this energy is reflected and observed as a final peak propagating northwards up the Firth of Thames (Refer to '*Reflections*').

Reflections:

Wave height time series graphs indicate between 1 and 3 peaks are evident at locations surrounding the generation area. Locations with only 1 peak observed within the time series graphs (asterisked values in Table 5.7) appear to occur (i) near the *base* of the Firth of Thames, and (ii) East of the islands surrounding the Coromandel Harbour. The first peak is associated with the initial wave propagating away from the displacement zone. The wave heights and arrival times associated with this initial wave are summarised in Table 5.7.

The second peak, partially masked by the initial peak, appears as a change of slope in the wave height time series graphs. It is evident at locations directly west and east of the generation area i.e. off the eastern side of Ponui Is, Waiheke Is and islands in this vicinity; islands occurring near the entrance to the Coromandel Harbour e.g. Rangipukea Is. and Whanganui Is. and the mainland on the Eastern margin of the Firth of Thames, adjacent to the generation area e.g. Deadmans Point.

Time series graphs along a transect from the Northern tip of Rotorua Is to the western tip of Whanganui Island indicate the arrival time of the second 'peak' increases as we move from west to east (Appendix 9, Figure 5.10, 5.11). Moturoruhi Island and Deadmans Point are the most northern and southern locations respectively (of those

specified in Table 5.7) to show evidence of this second peak. It is suggested that this second 'peak' is generated from reflection off Ponui and Waiheke Islands. It is believed that this reflection is significantly attenuated during its passage between the islands surrounding the Coromandel Harbour, to the extent where it is completely masked by the first peak and consequently is not evident at mainland locations east of these islands e.g. east of Rangipukea, Whanganui and Motuoruhi Islands.

The final peak (2^{nd} or 3^{rd} peak at locations that respectively were not and were impacted by reflection off Ponui and Waiheke Islands) is believed to be generated as a result of reflection of the initial wave (1^{st} peak) from the *base* of the Firth of Thames. It is evident at all locations (even as distant as Browns Bay) except at the base of the Firth of Thames, Rakino Island and locations where the wave is significantly attenuated e.g. Coromandel Whalf and Mania Harbour (Note that the later two locations have long tails suggesting slow decay of the wave).

The arrival time of the final peak increases with distance from the base of the Firth of Thames (Table 5.8) except for 2 locations that show anomalous 'late' arrival times i.e. Man O War Bay and Rurakura Point.

Table 5.8: Scenario 4 (2.1 m displacement along Segment D1): Arrival time and magnitude of the wave height peak associated with reflection from the base of the Firth of Thames (last peak).

Location	**Arrival Time (hrs, min, sec)**	**Magnitude (cm)**
Waimangu Pt.	2, 29, 50	0.29
Deadmans Pt.	2, 48, 10	0.30
Orere Pt.	2, 49, 5	0.24
Rangipukea Is.	2, 54, 35	0.22
Wanganui Is.	2, 58,45	0.22
Ruthe Passage	2, 58,45	0.22
Moturoruhi Is.	2, 59, 25	0.22
Rotorua Is.	3, 0, 5	0.22
Moturua Is	3, 5, 15	0.12
Ruakura Pt.	3, 6, 10	0.28
Waiheke Channel	3, 6, 55	0.19
Man O War Bay	3, 20, 10	0.17
Browns Bay	3, 53, 20	0.01

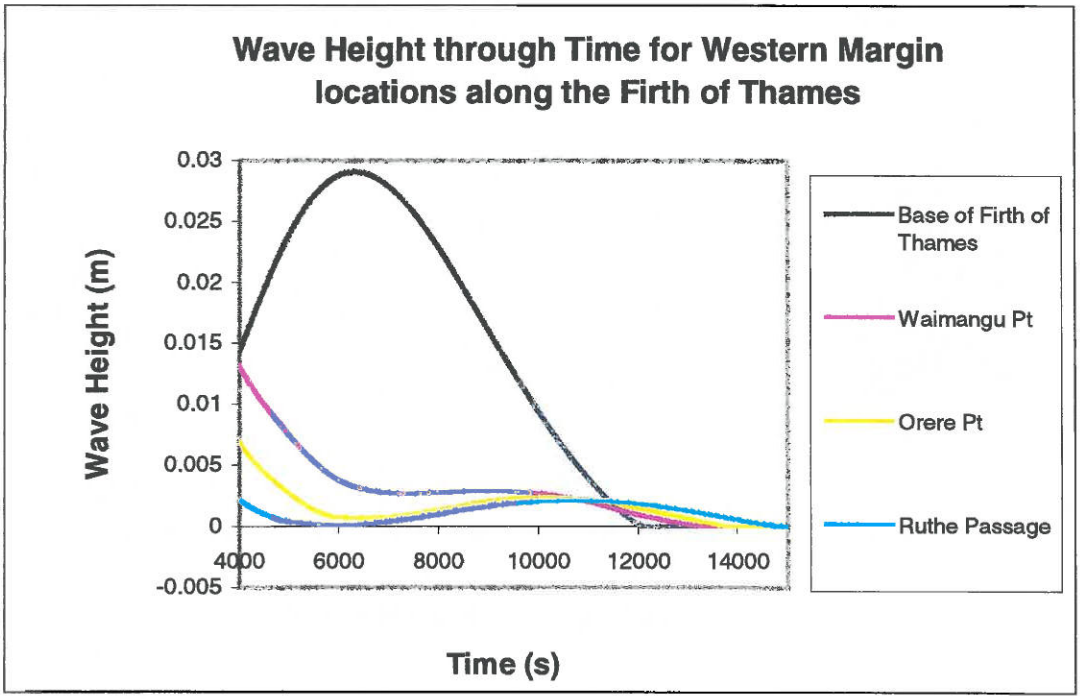

Figure 5.9: Wave Height through Time for selected regions on the western margin of the Firth of Thames. This figure illustrates how the arrival time of the final wave peak increases with increasing distance from the base of the Firth of Thames. This suggests the final peak is generated by reflection of wave energy from the base of the Firth of Thames.

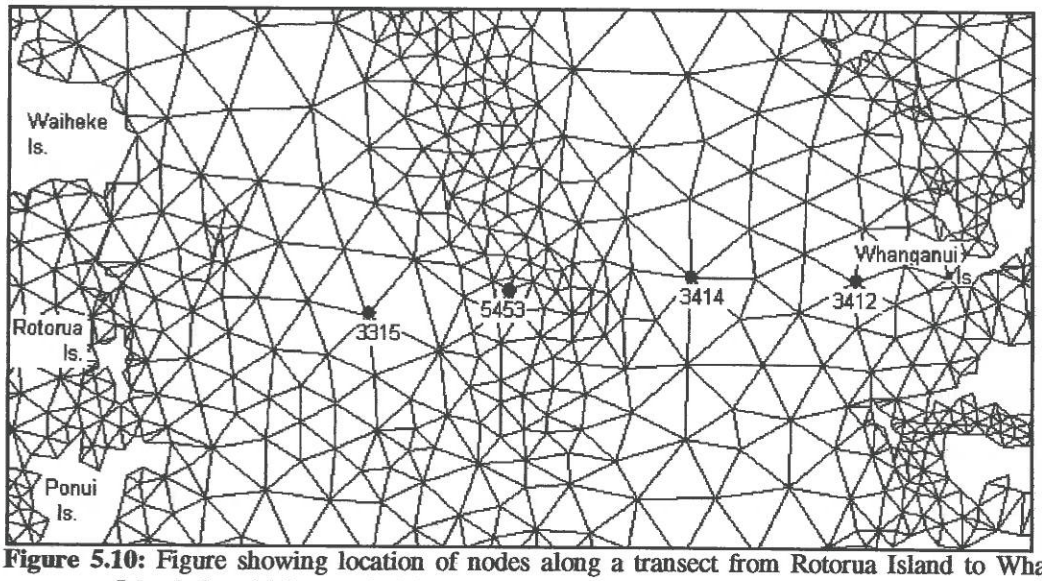

Figure 5.10: Figure showing location of nodes along a transect from Rotorua Island to Whanganui Island, for which wave height was recorded for the duration of the simulation.

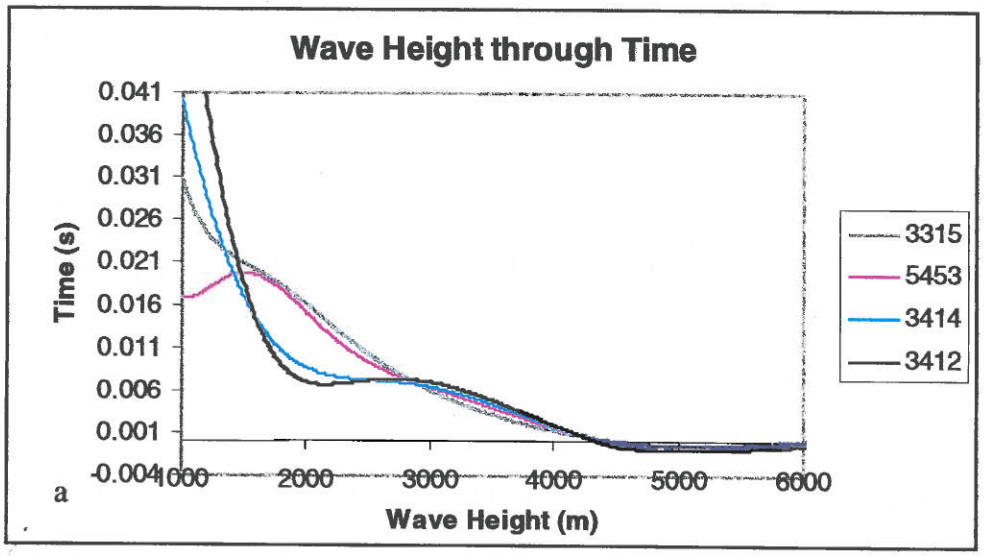

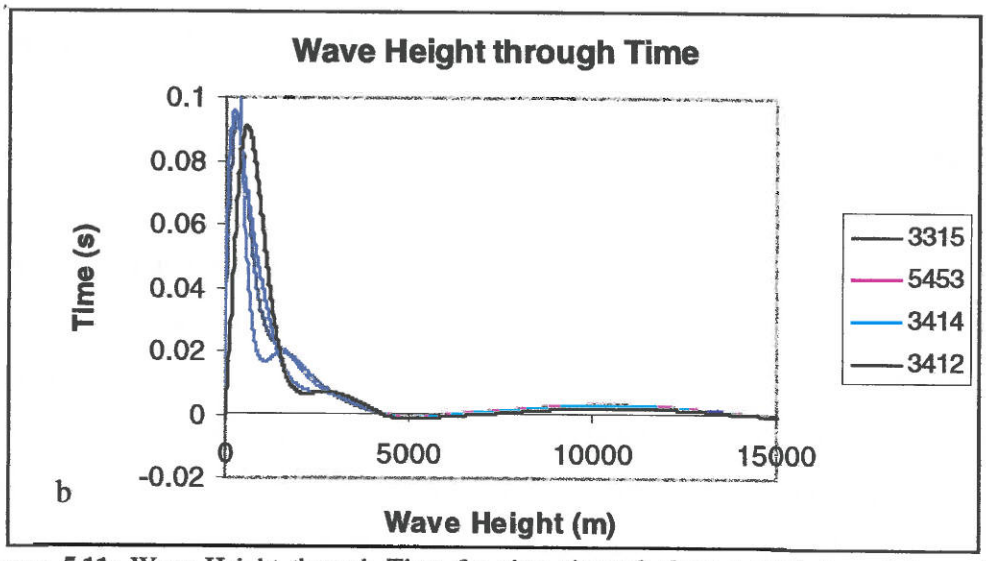

Figure 5.11: Wave Height through Time for sites situated along a west to east transect between Rotorua Island and Whanganui Islands. (a) Graph for 0-15000 seconds; (b) enlarged segment of (a) highlighting that the arrival time of the second peak/pleateau increases from west to east, suggesting this peak is generated from reflection from Ponui Island.

Currents:

By 3 min. 30 s currents reached velocities of ~0.04 $m.s^{-1}$ and radiate away from the displacement zone in all directions (Appendix 9, Figure A9.39). The maximum current velocity, 0.05 $m.s^{-1}$ occurs at approximately 7 min. and propagates predominantly east-north-east and west-south-west away from the displacement zone (Appendix 9, Figure A9.41). After this time current magnitudes begin to decline. The strongest currents, observed at 17 minutes occur south of the generation area, propagating into the Firth of Thames. At 23 minutes 30 seconds a zone of comparatively strong current velocitites is also observed west of Ruakura Point. By 1 hour these no longer exist but comparatively large currents continue to be observed in the central Firth of Thames until currents are so diminished they are no longer observable.

Current divergence and convergence:

Initially current divergence occurs from around the displacement zone, radiating in all directions. Divergence from above the displacement zone remains the major current pattern until 20 minutes at which time wave height gradients associated with elevated wave heights off Rotorua Island and Coromandel Harbour entrance cause divergence from these regions. This forces currents to propagate westward and eastward respectively resulting in current convergence near the centre of the displacement zone which ultimately forced currents to propagate both northwards and southwards away from this area (Appendix 9, Figure A9.43).

As the wave front (elevated wave heights) propagates southwards, the zone of divergence associated with this also moves southwards, to Ponui Is, to Orere Point and continues down the western margin of the Firth of Thames, but remains slightly behind the region of maximum wave height. Current divergence in Coromandel and Manaia Harbours continues until approximately 45 minutes when wave heights have reduced in these locations. As the wave propagates southward, the water level at the base of the Firth of Thames increases and currents begin to converge in this region. Convergence is evident at this location from approximately 30 min. till 1 hr and 45 min.

Currents diverge around islands and converge on the lee side of islands.

From 30-50 minutes current convergence is evident just west of Ruakura Point as a result of water being compressed into the channel between Ruakura Point and Ponui Island.

5.4.5 Scenario 5: Displacement along Segment D2

Scenario 5 involved 7.35 m of displacement along 19 km long Segment D2. The initial water depth along the displacement zone ranged from 10.7-30.1 m. The displacement occurred over a 2 second period with an average rupture velocity of 3.675 $m.s^{-1}$.

Waves

The maximum wave height (2.8 m) is observed at the end of the displacement (i.e. at 2 s) in the south-eastern end of the displacement zone. 3 seconds after displacement the largest waves to impact on land reach Pakatoa Island and are approximately 2.18 m in elevation. The maximum mainland wave height is 0.20 m high and occurs at Deadmans Pt after 9.5 minutes. By 38 minutes the wave is less than 0.1 m at all locations. The maximum wave heights and time of impact for several locations impacted by displacement along Segment D2 are summarised in Table 5.9.

Immediately after displacement waves propagate away from the generation area, dispersing in all directions causing 1.24 m waves impact on Pakatoa Is. and 0.613-0.926 m wave reach Tarahiki Island (Appendix 9, Figure A9.50). At 3 seconds, Tarahiki Island is impacted by waves of max. height of 1.5 m. Waikeke Island suffers waves somewhere between 0.613-0.926 metre elevation. The spatial distribution of the wave is such that at least 0.1 m high waves impact on the following land masses: Waiheke, Pakatoa, Ponui and Tarahiki Islands. By four seconds Tarahiki Island is completely surrounded by waves between 0.1 and 1.1 m high. Waiheke and Pakatoa Islands are impacted by up to 0.57 and 1.3 m waves respectively. By 5 seconds waves

of 0.1 m are just offshore of Deadmans Point (Coromandel Peninsula) and Ponui Island. The maximum on land wave heights are: Pakatoa = 1.14 m; Tarahiki Is. = 1.0 m; Waiheke Is. = 0.54 m; Ponui Is.= 0.35 m.

Table 5.9: Scenario 5 (7.35 m displacement along Segment D2): Arrival time and magnitude of maximum observed wave heights for a variety of locations around the generation area.

Location	Max Wave Height (cm)	Time of Max Height (hr, min, sec)	Last Peak (cm)	Last Peak Arrival Time (hr, min, sec)
Pakatoa Island	218.0	0, 0, 3	0.32	2, 49, 00
Ruthe Passage	42.3	0, 2, 40	0.6	2, 43, 0
Deadmans Point	25.1	0, 6, 20	0.9	2, 33, 50
Man O War Bay	21	0, 7, 10	0.4	2, 57, 5
E. side of Ponui Is.	29	0, 7, 20	1.3	2, 37, 50
S. of Wilsons Bay	19.6	0, 9, 30	0.9	2, 17, 0
Rangipukea Island	13.3	0, 11, 00	0.5	2, 44, 50
Motuoruhi Island	16.9	0, 13, 10	0.8	2, 43, 5
Whanganui Island	16.1	0, 13, 40	0.5	2, 47, 5
E. of Orere Point	16.4	0, 17, 40	0.6	2, 38, 0
Waimangu Point	14.9	0, 19, 10	0.8*	2, 11, ??
Ruakura Point	9.45	0, 21, 25	0.9	2, 48, 30
Waikawau	12.1	0, 22, 20	2.5*	1, 23, ??
Waiheke Channel	9.8	0, 22,50	0.37*	1, 66, ??
Sandspit passage	2.65	0, 27, 20	0.6	2, 24, ??
Tapu	8.3	0, 37, 5	4*	1, 20, ??
Wharekawa	8.6	0, 39, 30	N/A	N/A
Kawakawa Bay	4.8	0, 43, 20	0.72	3, 04, 5
Te Kouma	3.44	0, 47, 40	1.1	2, 44, 10
Te Puru	8.4	0, 50, 50	N/A	N/A
Kaiaua	8.48	0, 55, 0	N/A	N/A
Windy pt	8.04	0, 55, 30	N/A	N/A
Coromandel Wharf	2.89	1, 10, 10	1.2*	2, 46, ??
Tararu	7.6	1, 11, 5	N/A	N/A
Moanataiari	7.8	1, 11, 20	N/A	N/A
Miranda	8.47	1, 24, 50	N/A	N/A
Base of Firth of Thames	8.36	1, 30, 10	N/A	N/A
Auckland Water Front	0.03	2, 7, 20	0.01	4, 14, 40

*observed as change of slope (plateau) in graph, therefore arrival time and magnitude are approximate.

By 10 seconds Pakatoa Island is also completely surrounded by waves between 0.1 and 0.825 m high. Pakatoa (max. = 0.825 m), Rotorua (max. = 0.58 m), Tarahiki (max. = 0.68) and Ponui (max. = 0.32 m) Islands still remain the only land to be impacted by waves any bigger than 0.1 m. 30 seconds after displacement, 0.1 m waves have also reached Deadmans Point and wave heights have declined to: Pakatoa Is.= 0.74 m; Tarahiki Is.= 0.64 m; Waiheke Is. = 0.45 m; Ponui Is.= 0.35 m; Rotorua= 0.63 m.

Wave heights continue to decline (except for Ponui which has a 4 cm increase in maximum wave height) and at 1 minute after displacement began, the following islands are still the only land to be impacted by waves larger than 0.1 m: Pakatoa = 0.67 m; Tarahiki Is.= 0.57 m; Waiheke Is. = 0.43 m; Ponui Is.= 0.39 m; Rotorua= 0.62 m.

At 2 minutes wave heights at Ponui Island have increased to 0.43 m but all other Islands show decreases in their maximum observed wave height.

At 3.5 minutes it becomes evident that the zone of highest elevation waves is propagating southwards and hence the highest waves are now observed at Rotorua Island.

By 10 minutes, 10 seconds time (Appendix 9, Figure A9.60) the main wave body has clearly broken into two main zones of elevated wave height, one travelling SSW toward Ponui Island and the other eastward toward Deadmans Point. This trend had become slightly evident at 6 min. 50 sec. A third zone of elevated wave heights lingered near Man O War Bay, Waiheke Is. The region between Deadmans Point and Rangipukea Island was impacted by 0.2 m waves. The maximum wave heights at Ponui and Rotorua Islands are 0.31 and 0.29 m respectively.

By 20 minutes, 10 seconds zones of maximum wave height have further divided into four main groups. Two of these propagate southwards along the western and eastern margins of the Firth of Thames respectively. The third propagates NE toward the Coromandel Harbour and the fourth lingers with a zone of high setup occurring at the

Man O War Bay. The maximum onshore wave height at 20 minutes 10 seconds is approximately 0.17 m and occurs at Orere Point. The other three zones have maximum waves heights of: north of Waikawau Bay= 0.15 m; Man O War Bay = 0.15 m; Coromandel Harbour entrance = 0.14 m.

At 30 minutes 20 seconds much the same pattern as that observed at 20 min. 10 sec. But wave fronts i), ii) and iv) have propagated further south. Zone iii) (Coromandel harour) has attenuated more than the others. The maximum onshore wave height is ~0.12 m and occurs between Waimangu and Orere Points.

By 38 minutes and 40 seconds all wave heights are less than 10 cm. There remains only one main wave body which propagated southwards into central Firth of Thames. However there are some lingering larger wave heights against the eastern margin of Waiheke Channel (next to Rotorua Is.) and Waikawau Bay.

At 1 hr, 20 min. and 20 seconds the largest wave heights occur at the base of the Firth of Thames and are in the order of 0.085 m (Appendix A9, Figure A9.65).

Elevated water levels linger around Rotorua Island and Waimangu Point, possibly in response to wave focussing.

Reflections:

Wave height time series graphs indicate between 1 and 3 peaks are evident at locations surrounding the generation area. Locations with only 1 peak observed within the time series graphs occur near the *base* of the Firth of Thames. The first peak is associated with the initial wave propagating away from the displacement zone. The wave heights and arrival times associated with this initial wave are summarised in Table 5.9.

The second peak is only observed at 3 locations: Pakatoa Island, Ruthe Passage and east of Ponui Island (Refer to Table 5.10; Figure 5.12). The 2nd 'peak' at Pakatoa Island is partially masked by the initial peak and appears as a change of slope in the wave height time series graphs (Figure 5.12, 5.13). The arrival time of this second

peak increases with distance from Man O War Bay suggesting it is generated by reflection of wave energy from this location.

It is believed that this reflection is significantly attenuated during its passage between the islands adjacent to Man O War Bay (Waiheke Island), to the extent where it is not evident beyond these islands.

The final peak (2nd or 3rd peak at locations that respectively were not and were impacted by reflection off Waiheke Island) is believed to be generated as a result of reflection of the initial wave (1st peak) from the *base* of the Firth of Thames. It is evident at all locations (even as distant as central Auckland City water front) except those close to the base of the Firth of Thames (Figure 5.14, 5.15). Generally the arrival time of the final peak increases with distance from the base of the Firth of Thames (Table 5.9).

Table 5.10: Scenario 5 (7.35 m displacement along Segment D2): Arrival time and magnitude of the middle peak/plateau observed as 3 locations. This peak is believed to be generated by wave reflection from Man O War Bay, Waiheke Island.

Location	Height of Peak (cm)	Arrival Time of Peak (hr, min, sec)
Pakatoa Island*	5.13	0, 24, 20
Ruthe Passage	4.5	0, 35, 00
E. side of Ponui Island	3.6	0, 37, 50

*observed as change of slope (plateau) in graph, therefore arrival time and magnitude are approximate.

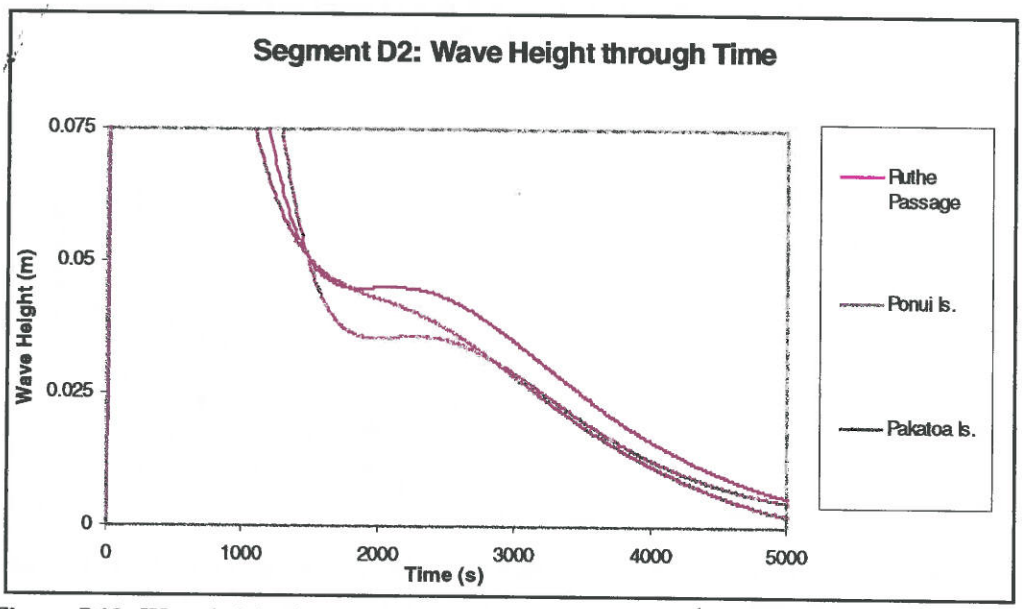

Figure 5.12: Wave height through time graph illustrating the 2nd 'peak' observed at Pakatoa Is., Ruthe Passage and Ponui Island.

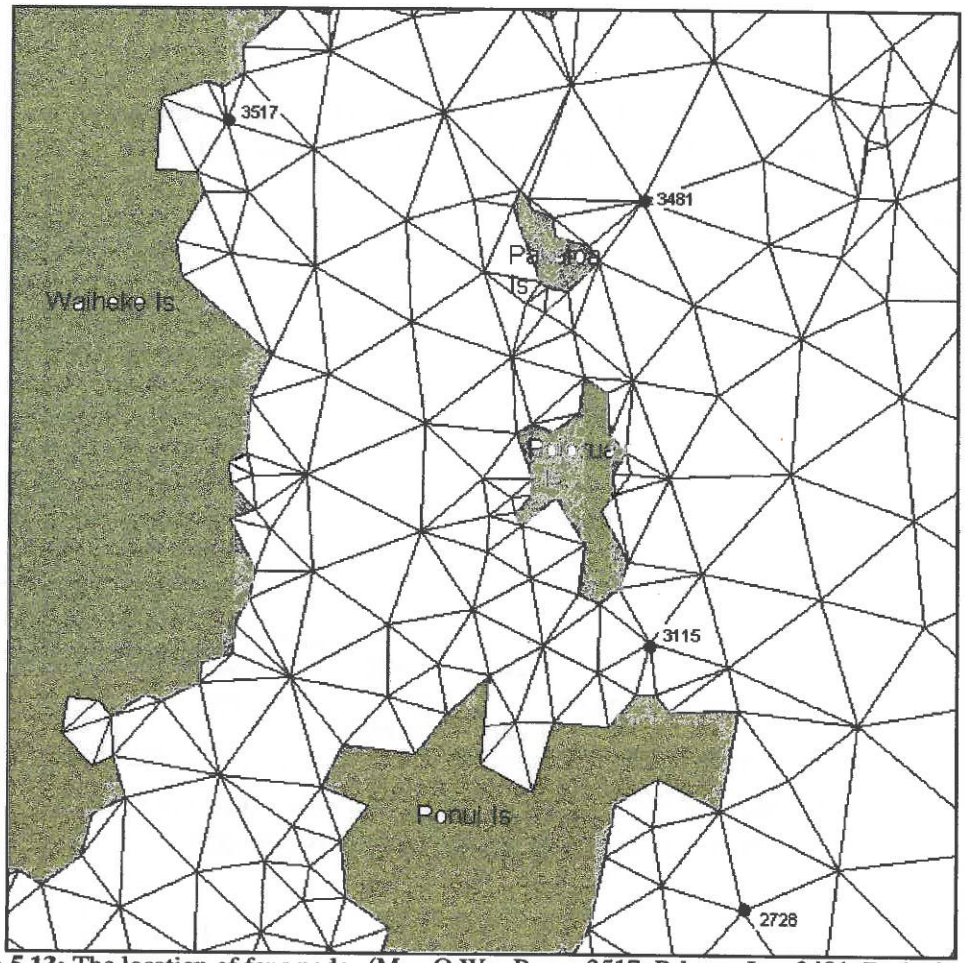

Figure 5.13: The location of four nodes (Man O War Bay = 3517, Pakatoa Is = 3481, Ruthe Passage = 3115, Ponui Island = 2728) discussed in Figure 5.12. These were stipulated to record wave height for the duration of the simulation.

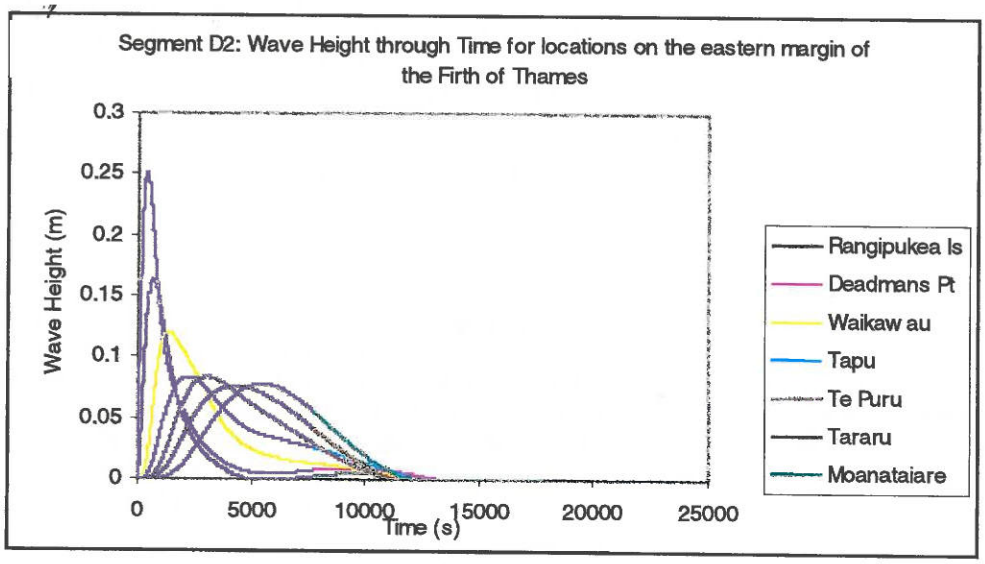

Figure 5.14: Wave Height through time for locations situated along the eastern margin of the Firth of Thames. This figure illustrates that the arrival time of the last wave height peak observed at these locations increases with distance from the base of the Firth of Thames, suggesting it was generated by reflection from the base of the Firth of Thames

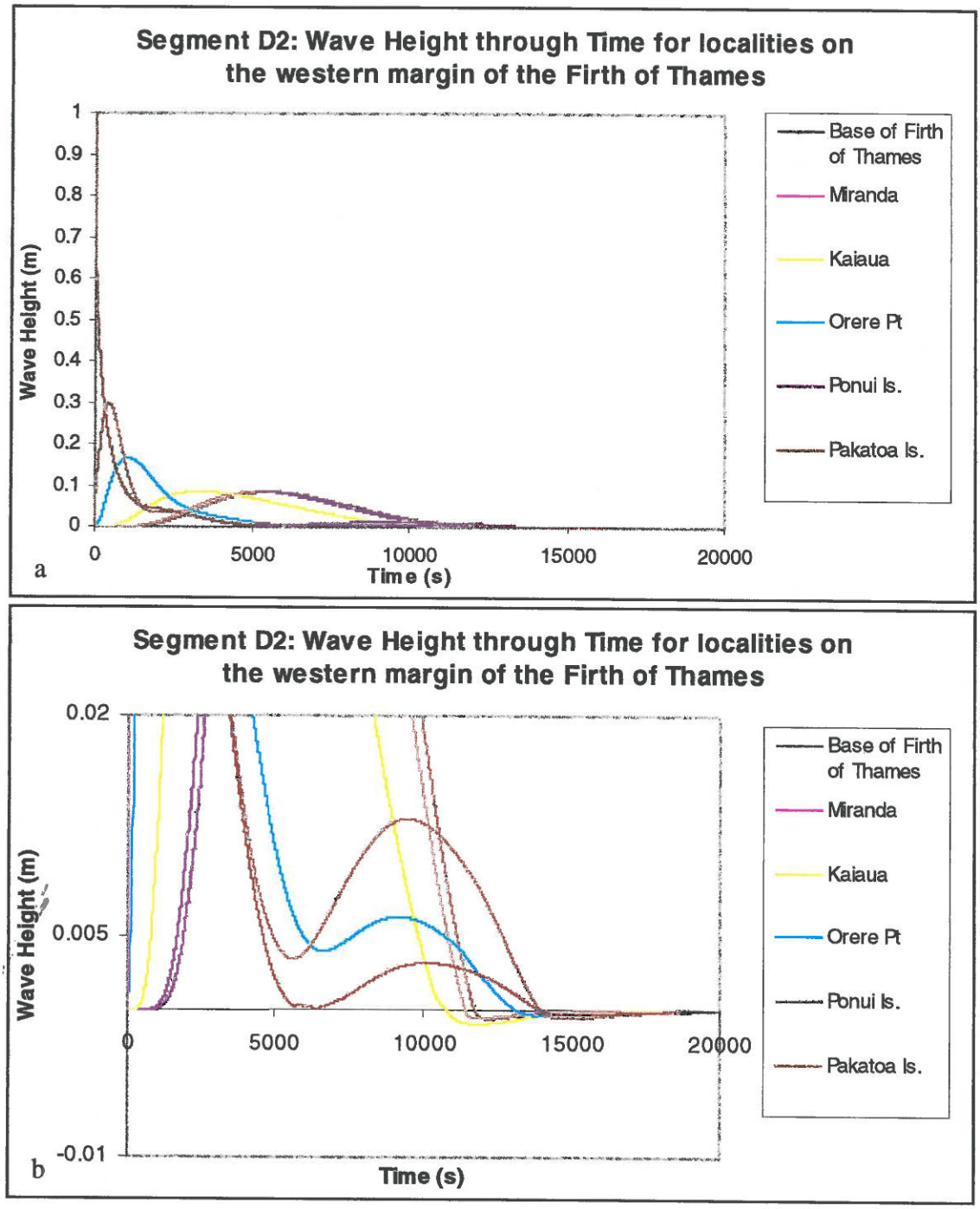

Figure 5.15: Scenario 5: Wave Height through time for locations situated along the western margin of the Firth of Thames. A) Graph for 0-2000 seconds; b) enlarged segment of a) highlighting that the arrival time of the last wave height peak observed at these locations increases with distance from the base of the Firth of Thames, suggesting it was generated by reflection from the base of the Firth of Thames.

Currents

Currents begin to develop immediately after displacement and continue to grow in strength until approximately 2 minutes at which time the maximum current velocity (0.13 $m.s^{-1}$) is observed within channels between islands that lie adjacent to the displacement zone (i.e. Pakoatoa, Tarahiki, Rotorua, Waiheke and Ponui Islands).

Current maximums, divergence and convergence:
By the end of the displacement (at 2 sec) currents are observed radiating out from above the generation area. Current velocities increase through time but are still below 0.05 $m.s^{-1}$ after 10 seconds. 30 seconds after displacement the fastest occur around the islands adjacent to the northern generation area, but still only reach a maximum of 0.07 $m.s^{-1}$. The lee side of Rotorua and Pakatoa Islands are sheltered from strong currents. At 1 minute, currents are fastest in the channels around Pakatoa, Tarahiki, Rotorua, Waiheke and Ponui Islands (maximum of 0.12 $m.s^{-1}$) and on the edge of the displacement zone where wave height gradients are largest. Currents are significantly reduced in the lee of islands and show convergence just east of Man O War Bay (Waikeke Island) and West of Rotorua Is. At 2 minutes, the above trends (illustrated @ 1 min.) still apply but currents have reached a maximum value of 0.13 $m.s^{-1}$ (Appendix 9, Figure A9.53) but are commonly around 0.1 $m.s^{-1}$. 3 minutes after displacement began the maximum observed current velocity has declined to approximately 0.1 $m.s^{-1}$, but *comparatively* strong currents appear to be becoming more wide spread. At Man O War bay convergence is evidence and generates a maximum elevation of 0.28 m.

The strongest currents at 10 minutes 10 seconds after initial displacement are observed in the Waiheke Channel east of Ponui Island, south of Wilsons Bay and near Pakatoa and Rotorua Islands. Currents are propagating much further south and the zone of current divergence (previously situated over the generation area) has migrated southwards.

20 minutes 10 s (Appendix 9, Figure A9.61) after displacement the strongest currents are observed between Pakihi Island and Ruakura Point (NE of Kawakawa Bay) (~0.09

$m.s^{-1}$) and at Waikawau Bay (~0.1 $m.s^{-1}$). As the wave propagates preferentially in a southward direction, current speeds towards the north are not as great.

By 30 minutes, 20 seconds Man O War Bay is no longer the centre of current divergence. The propagation of high wave height zone southwards has also propagated the divergence zone southwards. The maximum current speeds have diminished to ~ 0.08 $m.s^{-1}$ (between Kawakawa Bay and Pakihi Island) and 0.09 $m.s^{-1}$ (at Waikawau Bay). Currents around 0.07 $m.s^{-1}$ are present through most of the central Firth of Thames. The majority of currents move in the same direction the wave front is propagating (i.e. southward) but some currents on the trailing edge propagate in the opposite direction, away from the elevated water levels e.g. currents NE of Ruakura Pt. (Appendix 9, Figure A9.63).

At 38 minutes, 40 seconds the maximum currents are only ~ 0.06 $m.s^{-1}$ and are observed in Kawakawa Bay and the central Firth of Thames. In Kawakawa Bay these current velocities may occur in response to convergence that is evident in this locality.

By 1 hr, 20 minutes currents are significantly reduced in all regions (Appendix 9, Figure A9.65).

5.5 DISCUSSION

The numerical simulations above generate wave height distributions and current velocities, that indicate displacement along any segment results in the following trends:

- Current convergence is consistently evident at the base of the Firth of Thames.
- Refraction around Orere Point augments convergence between Ponui Island and Ruakura Point (mainland) and is believed to enhance current velocities.
- *Comparatively* strong current velocities are consistently observed east of Ruakura Point.
- Shallow water depths in the Firth of Thames cause a reduction in wave speed.

- Maximum predicted current velocity due to the tsunami, 0.13 $m.s^{-1}$, is depth averaged result and is deemed insignificant for sediment transport.
- Maximum wave heights observed in all simulations are small i.e maximum predicted *mainland* wave height is only 0.64 m.

Simulated current velocities are depth-averaged results. The maximum simulated current velocity, 0.13 $m.s^{-1}$, falls in the lower third of the current velocity range resulting from tides (0.05-0.45 $m.s^{-1}$ (Hydrographic Chart NZ 532)). Current velocities of this magnitude are unlikely to entrain sediment and are deemed insignificant.

With regards to the final point, the actual wave heights resulting from potential future displacement along the Kerepehi Fault may be larger than those predicted because of limitations associated with the numerical model employed. 'TSUNAMI' is a linear deepwater generation model being applied for tsunami generation in shallow water. This model may not be entirely appropriate for simulating tsunami generation in such shallow waters and does not account for natural processes that may amplify the wave: (i) effect of soft sediments; and (ii) non-linear processes such as resonance.

If a significant proportion of the displacement (> 10%) occurs in soft sediments, the seismic energy is released very slowly and tsunamis much larger than those expected from their seismic waves may be generated (Okal, 1988; Kanamori and Kikuchi, 1993). Zhadanov (1991) suggest source displacement in soft sediments may increase the value of maximum sea surface elevation by approximately 30%. Therefore it is expected that the actual waves resulting from the above displacements would be larger than those indicated by the simulation results generated from 'TSUNAMI'. However, the same relative wave height distribution is expected. i.e. should the non-linear processes and effects of soft sediments be able to be accounted for, the regions of comparatively worst impact (and least impact) would remain the same.

Results of physical modelling studies (Praysetya, 1988) indicate that a sequence of small, multiple displacement events is more efficient at generating devastating tsunami waves than a single, large displacement event. This suggests that waves

generated in this study by single, large displacement events along Segments A, B, C, D are likely to be smaller than those potentially generated by non-linear multiple seismic displacements (earthquake shaking) during actual seismic events. It is the understanding of the author that at the time of submission, a non-linear, shallow water generation model did not exist.

Despite these considerations, the wave heights predicted from the above simulations appear small for vertical displacements in order of 2.1 m and 7.35 m. Abe (1995) suggests local sub-marine earthquakes of moment magnitudes 6.5-7.1 should produce wave heights considerably larger than those predicted by 'TSUNAMI'. The following equations (Equations 5.1, 5.2, 5.3) can be applied to estimate the height of regional tsunami at a particular site as a function of propagation distance (Abe, 1995):

$$\log H_t = M_w - \log R - 5.55 + C \qquad \textbf{5.1}$$

where H_t is the tsunami height in meters,
R is the distance in km,
C = 0.0 for tsunamis in the fore arc, and
C = 0.2 for tsunamis in the back arc.

Note that for sites close to the source this equation gives an unreasonably large estimate of tsunami height. Hence Equation 5.3 should be applied in order to provide a limiting value on tsunami height for locations within a distance R_0 from the source origin, where R_0 is taken as the radius of a circular fault having an area S.

$$\log R_0 = 0.5M_w - 2.25 \qquad \textbf{5.2}$$

The relationship between R_0 (km) and M_w can be given from the empirical scaling relation of earthquake fault parameters (Equation 5.2):

$$\log H_r = 0.5M_w - 3.30 + C \qquad \textbf{5.3}$$

The integrity of the above height prediction method was tested by comparing height estimates against local maximum heights observed

during six major, locally generated, tsunami events[5] (Abe, 1995). The comparison reveals that on average the above method over predicts local maximum wave height. Consequently it is concluded this method is associated with a factor of uncertainty in the order of 1.5. Hence Abe (1995) warns the application of the formula for evaluating the maximum height should be undertaken with caution.

Applying the above equations for Scenario 1 (2.1 m displacement along Segment A, M_w = 6.7) suggests a tsunami run-up height of 1.78 m would be expected at Thames (8 km from source). This is significantly larger than wave heights predicted by 'TSUNAMI' at this location (7 cm). In an attempt to further understand whether 'TSUNAMI' is predicting wave heights in the right order of magnitude, further simulations involving increased width of surface displacement were undertaken. These results will be used to help determine if increasing the fault width produces tsunami heights more consistent with results predicted using Equation 5.1, 5.2 and 5.3.

5.6 INCREASED FAULT WIDTH SIMULATIONS

5.6.1 Determining New Fault Width

The focal depth and angle of fault dip used to calculate M_w (10 km and 60° respectively) suggest the width of surface displacement along the Kerepehi Fault could be as large as 5.8 km (Refer to Figure 5.16).

The focal depth and fault dip used to calculate this width are estimates based on fault parameters employed in modelling investigations previously undertaken by de Lange and Hull (1994). The focal depth estimate was based on current seismicity depths which are all around 5 km or shallower. This suggests that a large earthquake would have a shallow source, of depth similar to the 1987 Edgecumbe earthquake (M_L=6.3), 8 km (A. Hull, pers. comm.). In addition, a micro earthquake study conducted near

[5] The six major tsunamigenic events used for comparison against Equations 5.1, 5.2 and 5.3 are: 1983 Akita-Oki (M_w=7.9), 1968 Tokachi-Oki (M_w=8.2), 1952 Tokachi-Oki (M_w=8.1), 1946 Nankaido (M_w=8.1), 1944 Tonankai (M_w=8.1) and the 1933 Sanriku-Oki (M_w=8.4) events.

Te Aroha measured focal depths between 2 and 9 km depth, and the 9 Jan 1972 Te Aroha earthquake (M_L=5.1), had a focal depth of approximately 12 km (Adams et al., 1972). Hence a focal depth of 10 km seems appropriate.

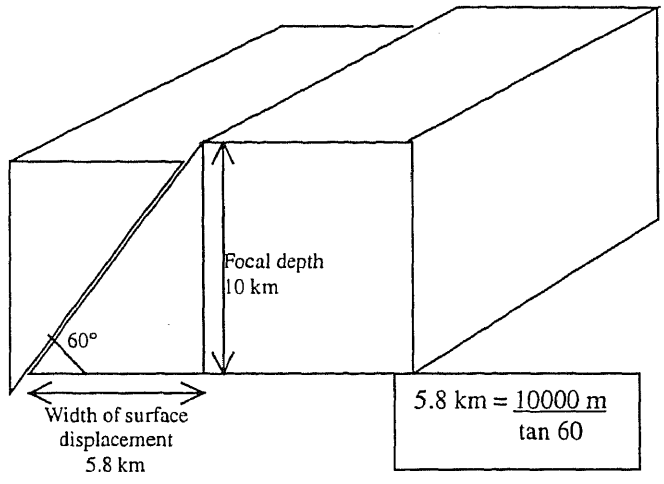

Figure 5.16: Diagram illustrating the relationship between focal depth, fault dip and the width of surface displacement.

Fault dip could not be determined from the seismic sub-bottom profiles employed in this study, as seismic noise, in the form of diffraction umbrellas (Refer to Chapter 3), masked the seismic signal in the region of the Kerepehi Fault. Consequently the fault dip used in this study is the same as that employed by de Lange and Hull (1994). As the Kerepehi Fault is normal, de Lange and Hull (1994) employed a standard 60° (A. Hull, pers. comm.). Future modelling investigations may be better suited to calculate surface displacement using a lesser dip of 35°, like that suggested by Hochstein et al. (1986).

5.6.2 Results

The following (Tables 1-5) represent the results obtained from 5 simulations involving increased surface displacement width, undertaken using 'TSUNAMI'. The model set-up and the events simulated are the same as those outlined in Sections 5.2 and 5.3 with the exception that the width of the seabed displacement region, stipulated as the displacement condition in the boundary file Kere.dat, has increased to approximately

5.8 km from 1.25 km. This increased the displacement volume by approximately 460 % for Segments A, B, C, and D1 and 400 % for Segment D2.

Table 5.11: Maximum Wave Heights and associated arrival times predicted for displacement along Segment A as a result of approximately a 460 % increase in the volume of water displaced.

Location	Maximum Wave Height (m)	Arrival Time of Max. Height (hours, min, sec)	% of Max H from original (1.25 km) fault width
Base of the Firth of Thames (Displacement Node)	0.783	0, 0, 2	817
Waihou River Mouth	0.330	0, 23, 20	465
Moanataiare	0.328	0, 22, 40	465
Between Piako & Waihou Rivers	0.362	0, 15, 10	468
Miranda	0.345	0, 20, 20	504
Kaiaua	0.204	0, 15, 10	484
Wilson Bay	0.081	0, 42, 50	486
Kawakawa Bay	0.037	1, 52, 30	486
Sully Reef, Ponui Is.	0.088	1, 16, 0	483
E. of Waiheke Is.	0.044	1, 19, 20	482
Water front, Auckland City	0.000	3, 23, 0	643
Musick Point	0.002	3, 29, 10	565
Tamaki Strait	0.003	3, 0, 10	505
Coromandel Whalf	0.020	2, 37, 20	497
Central Hauraki Gulf	0.007	1, 23, 10	480
Te Puru	0.170	0, 21, 0	442
Waimangu Pt.	0.080	0, 46, 0	468
Rangipukea Is.	0.055	0, 77, 0	482
Tararu	0.313	0, 21, 30	465

Table 5.12: Maximum Wave Heights and associated arrival times predicted for displacement along Segment B as a result of approximately a 460 % increase in the volume of water displaced.

Location	Maximum Wave Height (m)	Arrival Time of Max. Height (hours, min, sec)	% of Max H from original (1.25 km) fault width
Base of Firth of Thames	0.122	0, 55, 20	449
Waihou River Mouth	0.105	0, 55, 20	458
Moanataiare	0.104	0, 54, 40	458
Between Piako & Waihou R.	0.110	0, 54, 40	456
Miranda	0.119	0, 47, 20	446
Kaiaua	0.197	0, 15, 20	453
S. of Wilsons Bay	0.095	0, 18, 0	418
Kawakawa Bay	0.022	1, 15, 10	458
Scully Reef, Ponui Is.	0.063	0, 41, 0	450
Waiheke Is.	0.030	0, 43, 40	453
Water Front, Auckland City	0.000	2, 55, 10	464
Musick Pt.	0.001	2, 58, 40	468
Tamaki Strait	0.002	2, 30, 30	462
Coromandel Whalf	0.010	2, 2, 0	462
Te Puru	0.181	0, 13, 20	439
Waimangu Pt.	0.082	0, 11, 20	436
Rangipukea Is.	0.036	0, 32, 50	449
Tararu	0.100	0, 48, 50	459

Table 5.13: Maximum Wave Heights and associated arrival times predicted for displacement along Segment C as a result of approximately a 460 % increase in the volume of water displaced.

Location	Maximum Wave Height (m)	Arrival Time of Max. Height (hours, min, sec)	% of Max H from original (1.25 km) fault width
Kaiaua	0.136	0, 32, 0	466
Waimangu Pt	0.329	0, 7, 0	441
Deadmans Pt.	0.134	0, 10, 30	356
Wilson Bay	0.282	0, 9, 0	382
Miranda	0.132	1, 3, 10	461
Base of Firth of Thames	0.133	1, 6, 20	462
Moanataiare	0.116	0, 53, 0	460
Te Puru	0.161	0, 26, 10	468
Ponui Is.	0.124	0, 25, 40	422
Pakihi Is.	0.048	0, 40, 50	414
Ruakura Pt.	0.059	0, 28, 50	403
Orere Pt.	0.219	0, 10, 50	410
Wharekawa Pt.	0.194	0, 12, 0	472
Rangipukea Is.	0.075	0, 14, 10	360
Waiheke Is.	0.029	0, 40, 0	428
Tapu	0.225	0, 15, 0	480
Wakakaiwhara Pt.	0.003	1, 37, 10	430
Ruthe Passage	0.054	0, 25, 50	426
Waikawau	0.278	0, 12, 40	454

Table 5.14: Maximum Wave Heights and associated arrival times predicted for displacement along Segment D1 as a result of approximately a 460 % increase in the volume of water displaced.

Location	Maximum Wave Height (m)	Arrival Time of Max. Height (hours, min, sec)	% of Max H from original (1.25 km) fault width
Te Kawau Pt	0.110	0, 24, 30	444
Rakino Is.	0.023	0, 26, 30	444
Waiheke Is.	0.158	0, 7, 20	400
Man O War Bay, Waiheke	0.130	0, 22, 0	461
Motuoruhi Is.	0.364	0, 9, 20	406
Moturua Is.	0.159	0, 15, 0	418
Whanganui Is.	0.410	0, 11, 20	440
Coromandel Whalf	0.042	1, 13, 0	479
Rangipukea Is.	0.396	0, 9, 30	473
Deadmans Pt.	0.374	0, 6, 50	500
Rotorua Is.	0.372	0, 12, 30	442
Ruthe Passage	0.338	0, 12, 10	448
Browns Bay	0.017	0, 54, 20	457
Waiheke Channel	0.232	0, 10, 50	434
Mania Harbour	0.079	0, 52, 50	484
Ruakura Pt.	0.147	0, 29, 50	479
Orere Pt.	0.249	0, 26, 20	467
Waimangu Pt.	0.206	0, 29, 40	473
Base of Firth of Thames	0.145	1, 43, 20	500
Moanataiare	0.131	1, 36, 40	501

Table 5.15: Maximum Wave Heights and associated arrival times predicted for displacement along Segment D2 as a result of approximately a 404 % increase in the volume of water displaced.

Location	Maximum Wave Height (m)	Arrival Time of Max. Height (hours, min, sec)	% of Max H of original (1.25 km) fault width
Pakatoa Is (displacement node)	3.19	0, 0, 2	146
Kaiaua	0.302	0, 55, 50	356
Moanataiare	0.282	1, 31, 10	359
Coromandel Whalf	0.103	1, 10, 30	357
Howick/Half Moon Bay	0.007	2, 21, 30	309
Kawakawa Bay	0.179	0, 42, 40	374
Wilson Bay	0.648	0, 10, 30	331
Orere Pt.	0.597	0, 17, 50	364
Waiheke Channel	0.224	0, 24, 30	229
Sandspit Passage	0.094	0, 26, 0	355
Tamaki Strait	0.023	1, 12, 50	278
Miranda	0.304	1, 25, 50	358
Wind Pt.	0.288	0, 56, 30	358
Ponui Is.	1.180	0, 5, 50	397
Ruthe Passage	1.674	0, 1, 0	396
Base of Firth of Thames	0.300	1, 30, 40	359
Te Kouma	0.124	0, 48, 10	361
Auckland Water Front	0.001	2, 6, 30	354
Man O War Bay, Waiheke Is.	0.425	0, 10, 30	203
Rangipukea Is.	0.590	0, 11, 40	362
Deadmans Pt.	0.842	0, 6, 50	336
Waikawau	0.428	0, 24, 0	355
Tapu	0.301	0, 37, 20	362
Te Puru	0.300	0, 50, 30	359
Tararu	0.271	1, 10, 10	357
Ruakura Pt.	0.353	0, 20, 30	374
Waimangu Pt.	0.534	0, 19, 40	359
Wharekawa	0.306	0, 39, 40	356

5.6.3 Discussion

The above results indicate that increasing the surface rupture displacement width and therefore the volume of displaced material increases the maximum predicted wave height. More specifically, the "TSUNAMI' model predicts a linear relationship between the volume displaced and the maximum wave height predicted.

Once wave height maximums at localities (i) within 1 km of the source region, and (ii) localities not at the shoreline e.g. Waiheke Channel and Tamaki Strait, had been removed, the average percentage increase in maximum wave height for each segment

(i.e. average of column four of each of the above tables) was within 10% of the increase of displacement volume (%). Some of the discrepancy between the volume increase and the increase in maximum predicted wave height occurs because the exact volume of water displaced during model simulations was not calculated; only an estimate based on the fault parameters was determined.

The above relationship has previously been suggested by wave heights predicted by de Lange and Healy (1997) during numerical modelling of tsunamis in the Gisborne region. Hence, should future research suggest larger vertical displacement or wider surface displacement is more likely, the wave heights determined from the above simulations may be scaled accordingly.

The above results were compared with wave height predictions made by Equations 5.1-5.3 in order to assess if the wave height predictions made by the 'TSUNAMI' model are of the correct magnitude (Table 5.16 and 5.17). The results indicate that although larger than wave heights generated from surface rupture displacements of smaller width (1.25 km), the above wave heights are still significantly smaller than those predicted by Equations 5.1-5.3.

For the five locations selected, the method outlined in Abe (1995) predicts heights that are between 239 and 1475 % larger and 735 % larger on average, than those predicted by 'TSUNAMI'. The closest correlation between the two prediction methods occurs for waves generated by displacement along Segment D2, (the segment with the largest earthquake magnitude) which still illustrates a discrepancy greater than 1.5 times. This suggests that the 'TSUNAMI' model under predicts wave height for the shallow water scenarios outlined above.

Table 5.16: Predicted Run-up Heights for selected sites calculated using Equations 5.1, 5.2, and 5.3. Columns 2-6 present the approximate distance between the center of the fault segment (source) and the location in Column 1.

Location	Distance from Middle of Source (km)					Predicted Run-up Heights (m)				
	A	B	C	D1	D2	A	B	C	D1	D2
Thames	8	16	23	41	39	1.78	0.94	0.97	0.69	1.44
Te Puru	<13	11	17	32	31	1.78	1.28	1.40	0.88	1.76
Waimangu Pt.	22.5	12	8	20	16	1.02	1.18	1.78	1.41	2.82
Ponui Is.	40	28.5	20	10	4	0.56	0.50	1.12	2.00	2.82
Wilson Bay	27.5	17	10	15	15	0.81	0.81	1.78	1.88	2.82

Table 5.17: Summary of maximum predicted wave height (for increased width of surface displacement) presented within Tables 5.1- 5.5 and ratio of heights predicted by Equations 5.1, 5.2, and 5.3 to heights predicted by predicted by 'TSUNAMI'.

Location	Wave Heights Predicted by Tsunami					Equation Prediction/Tsunami Prediction				
	A	B	C	D1	D2	A	B	C	D1	D2
Thames	0.33	0.10	0.12	0.13	0.28	5.39	9.40	8.08	5.31	5.14
Te Puru	0.17	0.18	0.16	-	0.3	10.47	7.11	8.75		5.87
Waimangu Pt.	0.08	0.08	0.33	0.21	0.53	12.75	14.75	5.39	6.71	5.32
Ponui Is.	0.09	0.06	0.12	-	1.18	6.22	8.33	9.33		2.39
Wilsons Bay	0.08	0.10	0.28	-	0.65	10.13	8.10	6.36		4.34

5.7 TSUNAMI SIMULATION IN 1 DIMENSION USING MODEL '3DD'

The discrepancy between wave heights predictions made by 'TSUNAMI' and the formula presented in Abe (1995) and the limitations associated with applying a linear, deep water generation model in shallow water, prompted simulations employing the finite difference hydrodynamic circulation model, '3DD' in 1 dimension (Refer to Appendix 10). This was undertaken to provide further comparison with the wave height results predicted by simulations undertaken using the 'TSUNAMI' model.

5.7.1. Model Set-up

The bathymetry of the grid used for the 1-dimensional simulation was arbitrarily extracted from a 1500 m by 1500 m grid previously generated for the Hauraki Gulf region (Black et al, 1996; Figure 5.16). The region selected trends W-E across the Firth of Thames and is located along grid cell j=10 of the original grid (Figure 5.16). Hence the simulation was undertaken along a profile located approximately 13.5 km from the base of the Firth of Thames that transected the upper reach of Segment A of the Kerepehi Fault.

Empirical parameters such as resistance length and eddy viscosity remained fixed at 0.003 and 10 $m^2.s^{-1}$ for all '3DD' simulations undertaken in this study.

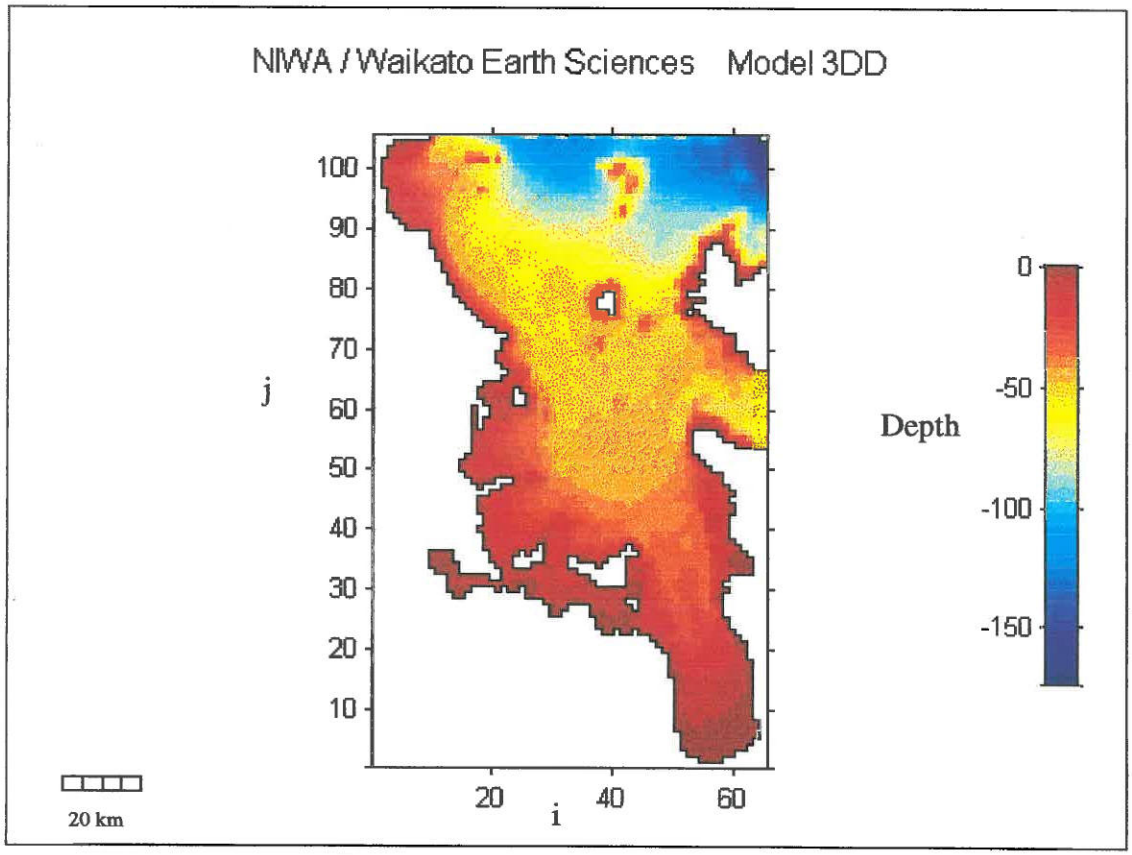

Figure 5.16: Original 2-dimensional grid of the Hauraki Gulf Region from which the bathymetry for the 1-dimensional grid was extracted.

Model Grid

Once the bathymetic data was extracted from the original 1500 m by 1500m grid, the grid resolution was enhanced by interpolating the bathymetric data between the original 1500 m cells, thus allowing the generation of a finer 200 m by 200m grid to

be used for the 1-dimensional simulation. The refined grid is 98 cells by 5 cells and is therefore 19.6 km long (in westward direction) and 1 km wide (in northern direction). Note however, the most northern and southern grid rows (i.e. j=1 and j=5) are boundary cells. The bathymetry of this grid, (as observed from i=1, j=3 to i=98, j=3) is presented in Figure 5.17.

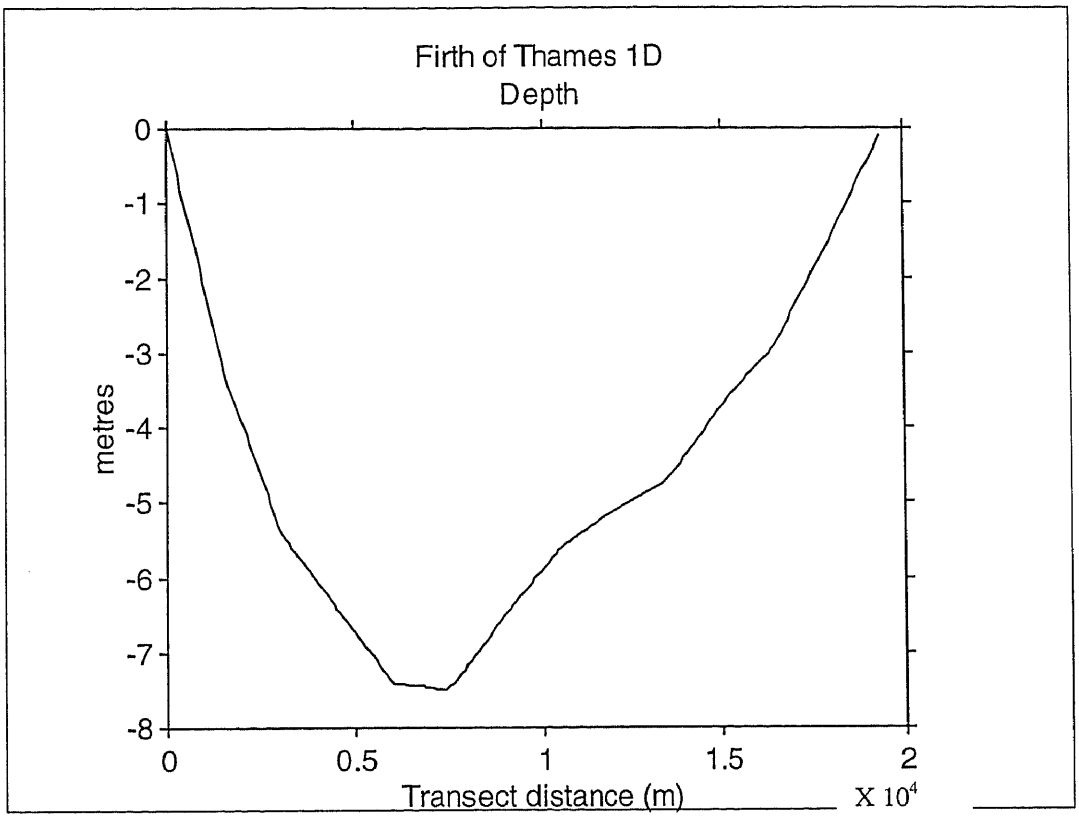

Figure 5.17: Bathymetry of the refined 200 m by 200 m grid as observed along a west to east transect located approximately 13.5 km north of the base of the Firth of Thames.

Boundary Conditions

The model was run using a transmission with sponge boundary (type 2 boundary) along the western and eastern boundaries of the model grid. The sponge boundaries were 10 cells wide (2 km wide) i.e. stretched from i=1 to i=10 and i=88 to 98, j=1 to 5. The inclusion of sponge cells within the boundary reduces the amount of wave reflection occurring at these boundaries thus allowing a more realistic simulation.

Once the boundaries had been defined, a hot start file was generated. This file set the initial sea level to be elevated by 2.1 m above mean sea level (0.67 m) with a geometry similar to that used in simulations undertaken using the 'TSUNAMI' model (Refer to Figure 5.18).

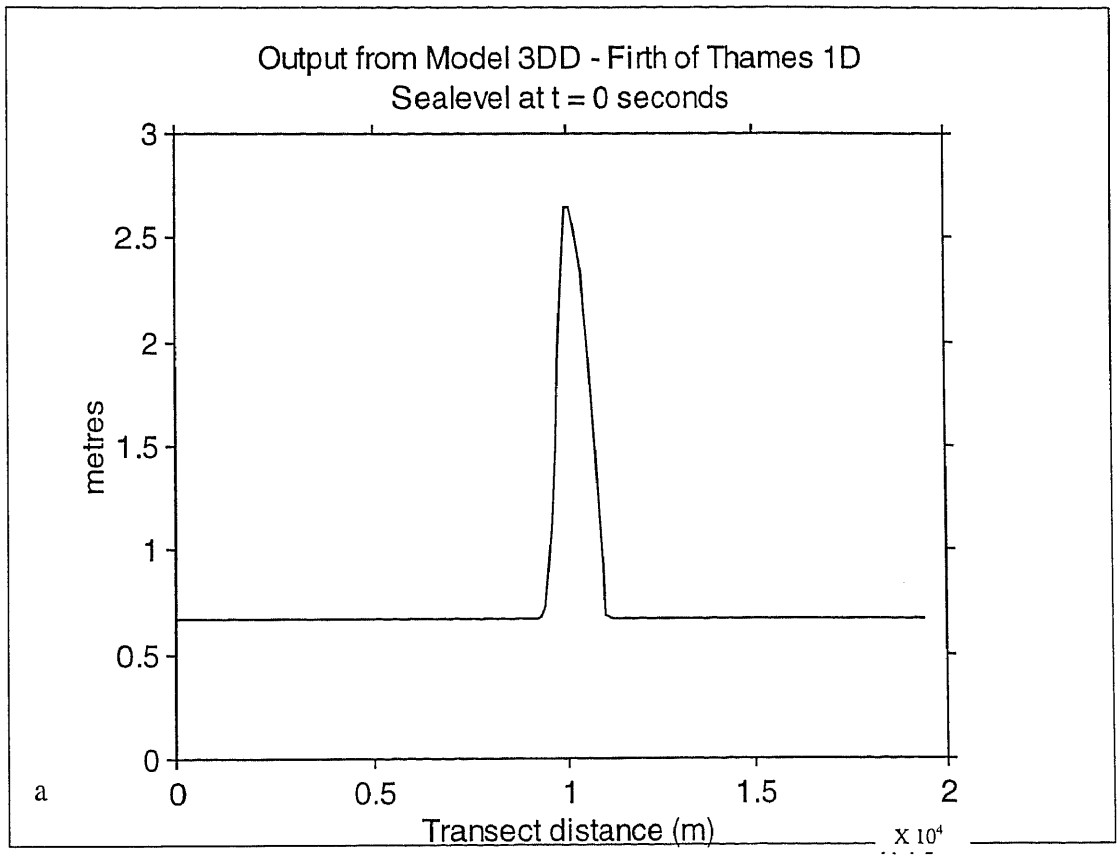

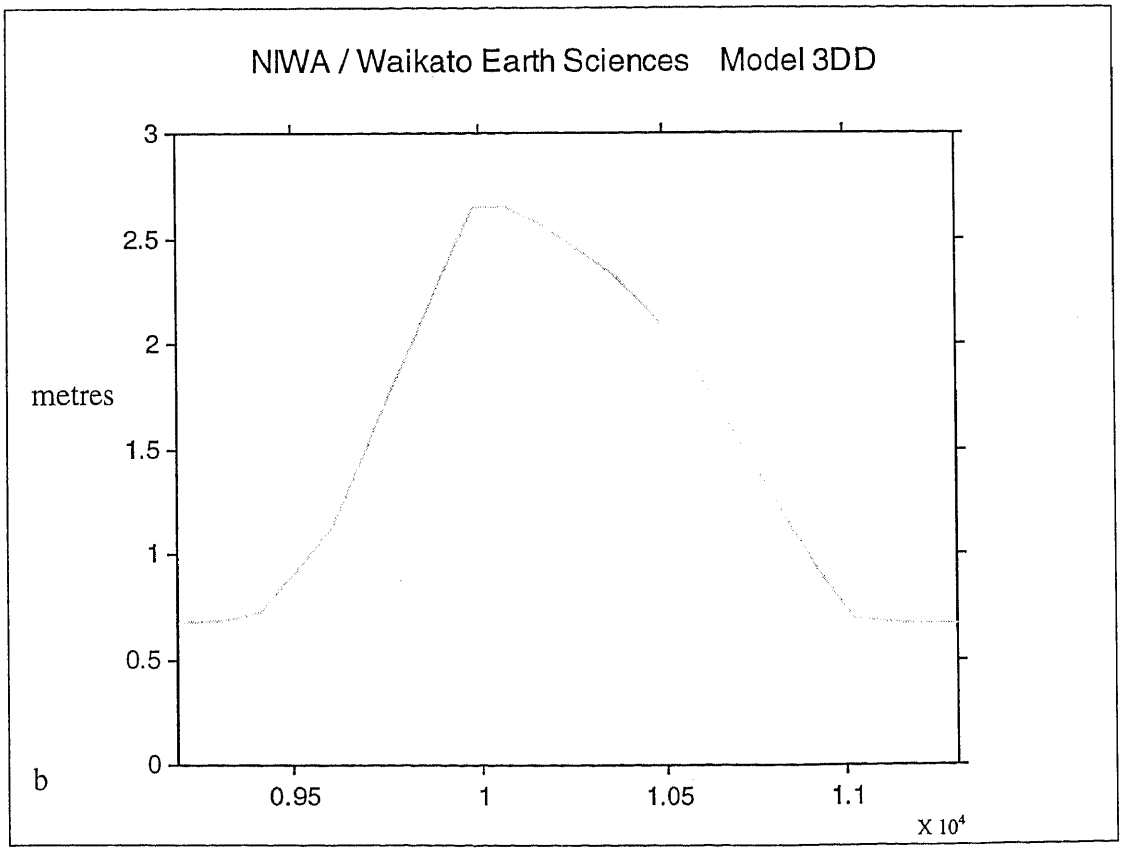

Figure 5.18: a) Initial sea level used for hot start in model '3DD'; **b)** enlargement of a) illustrating the geometry of the initial sea level.

5.7.2. Results

The results of this simulation are summarised as a series of wave height through time profiles (Refer to Figure 5.19).

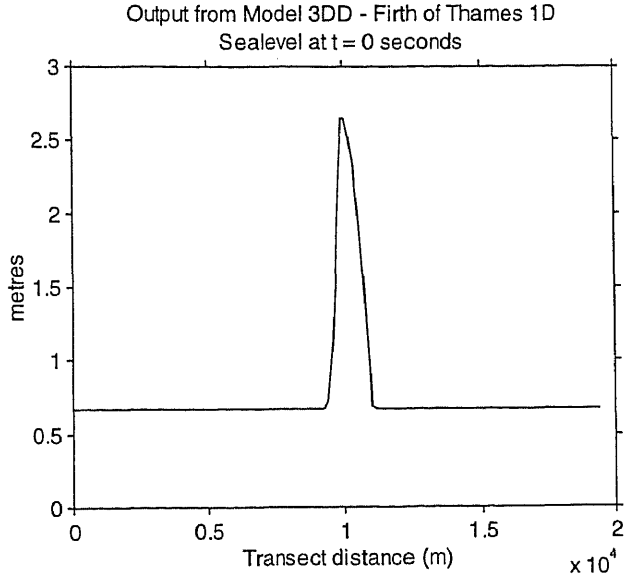

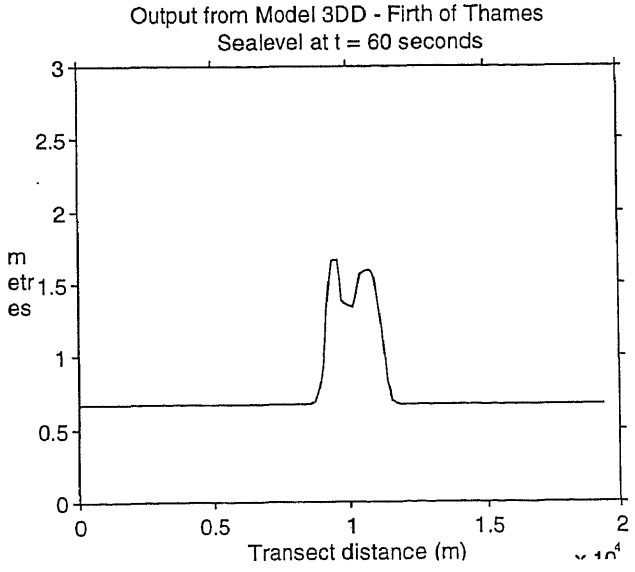

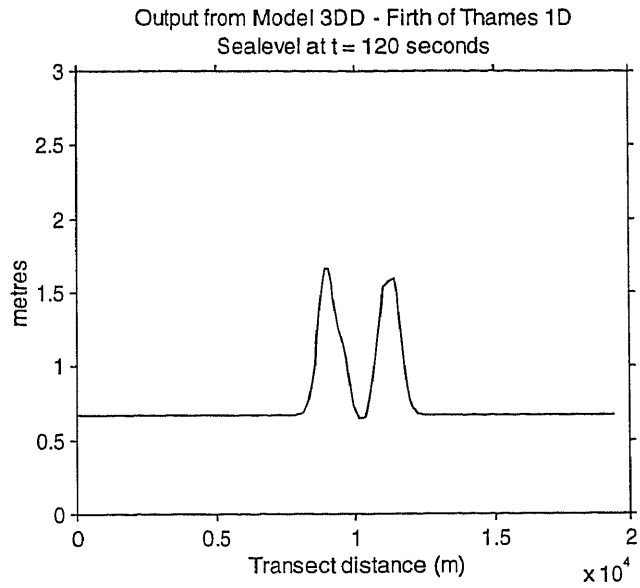
Output from Model 3DD - Firth of Thames 1D
Sealevel at t = 120 seconds
metres
Transect distance (m)
x 10^4

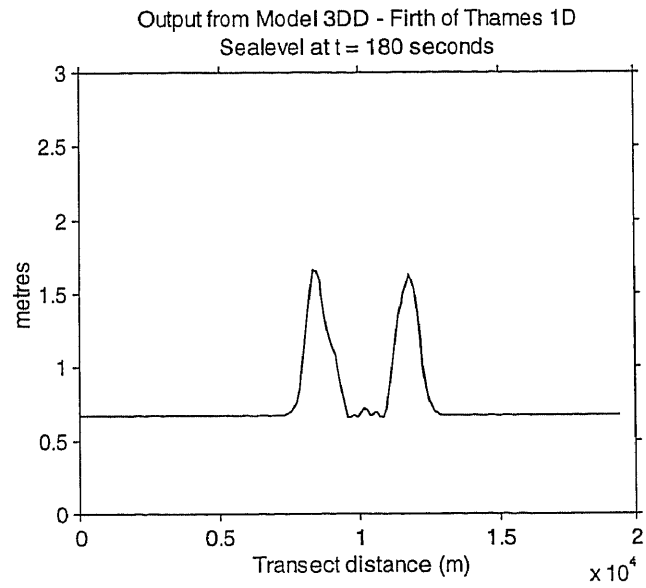
Output from Model 3DD - Firth of Thames 1D
Sealevel at t = 180 seconds
metres
Transect distance (m)
x 10^4

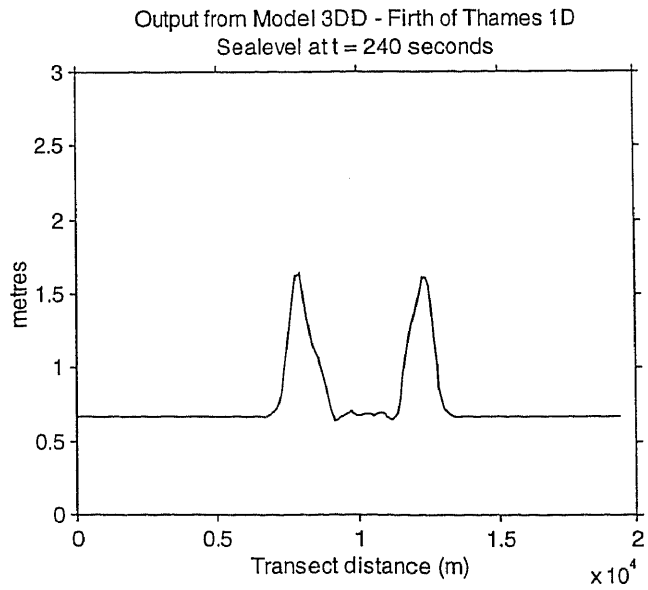
Output from Model 3DD - Firth of Thames 1D
Sealevel at t = 240 seconds
metres
Transect distance (m)
x 10^4

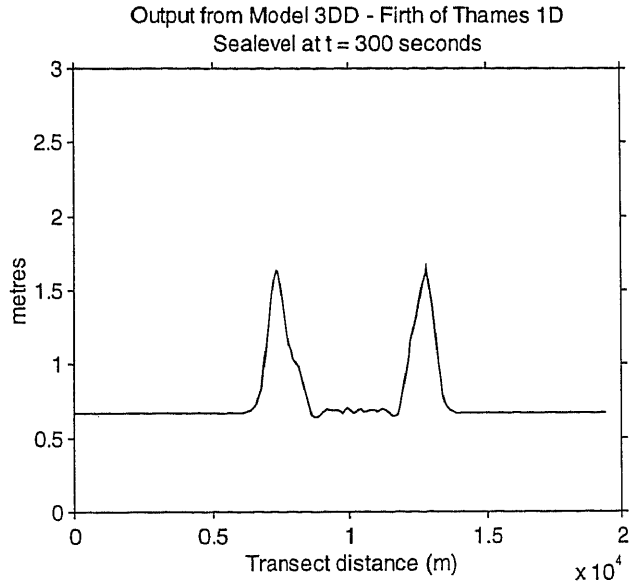
Output from Model 3DD - Firth of Thames 1D
Sealevel at t = 300 seconds
metres
Transect distance (m)
x 10^4

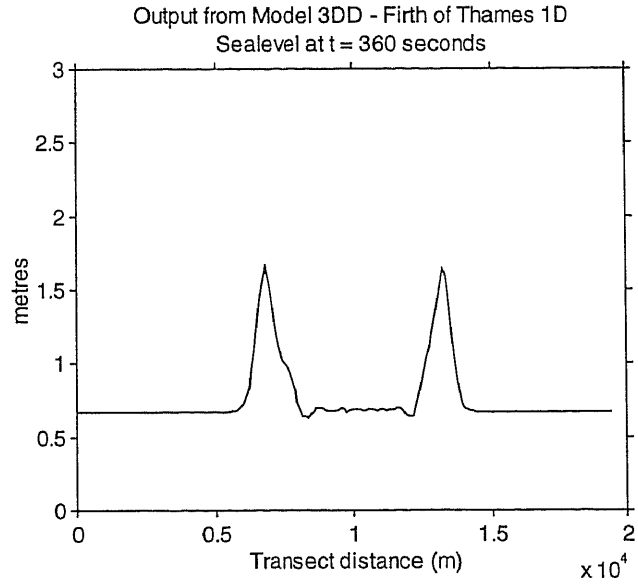
Output from Model 3DD - Firth of Thames 1D
Sealevel at t = 360 seconds
metres
Transect distance (m)
x 10^4

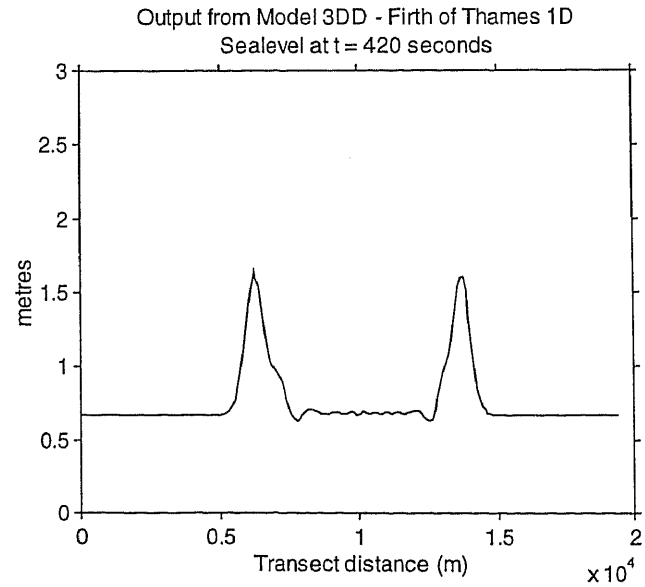
Output from Model 3DD - Firth of Thames 1D
Sealevel at t = 420 seconds
metres
Transect distance (m)
x 10^4

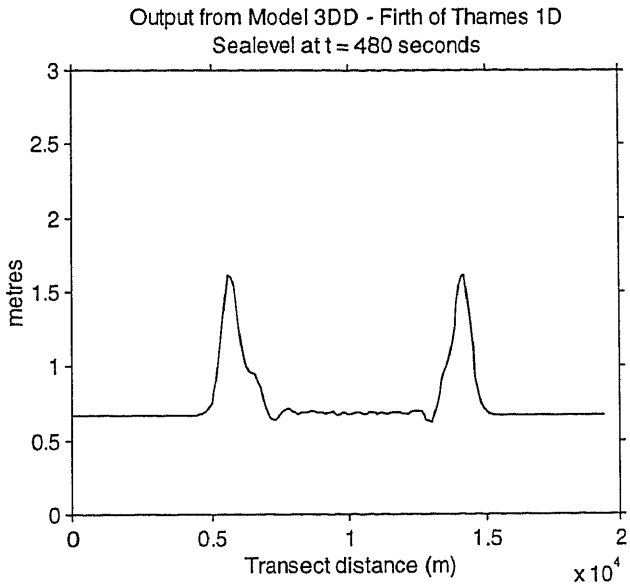
Output from Model 3DD - Firth of Thames 1D
Sealevel at t = 480 seconds
metres
Transect distance (m)
x 10^4

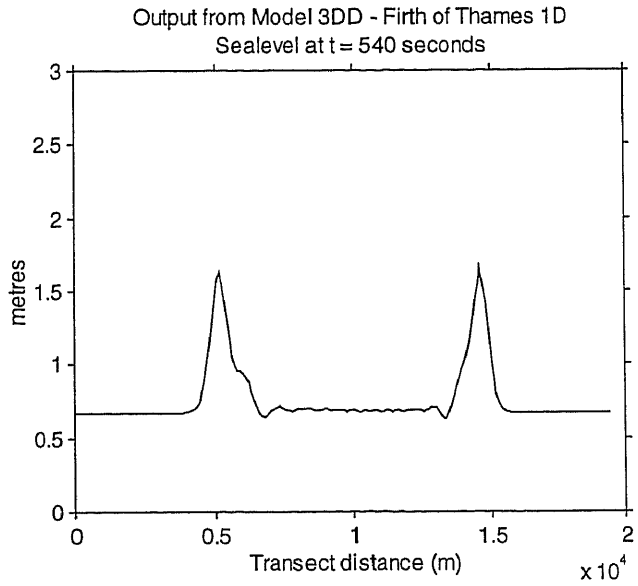
Output from Model 3DD - Firth of Thames 1D
Sealevel at t = 540 seconds
metres
Transect distance (m)
x 10^4

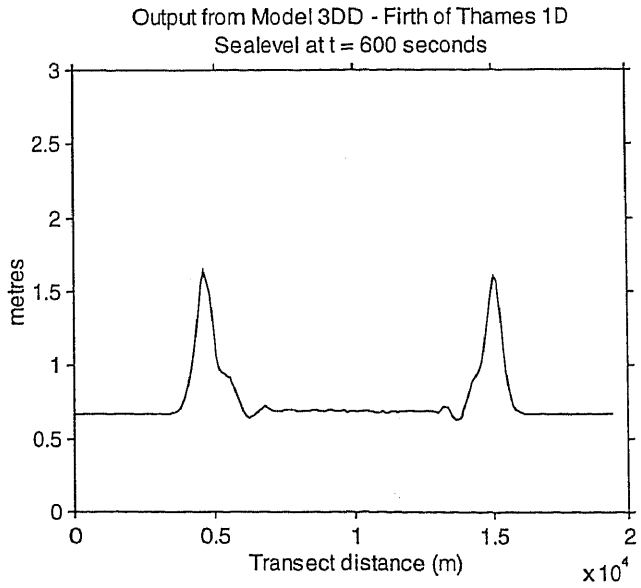
Output from Model 3DD - Firth of Thames 1D
Sealevel at t = 600 seconds
metres
Transect distance (m)
x 10^4

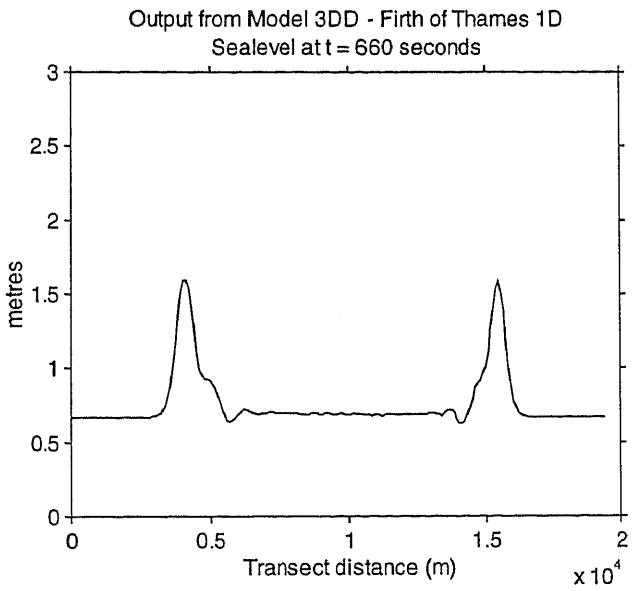
Output from Model 3DD - Firth of Thames 1D
Sealevel at t = 660 seconds
metres
Transect distance (m)
x 10^4

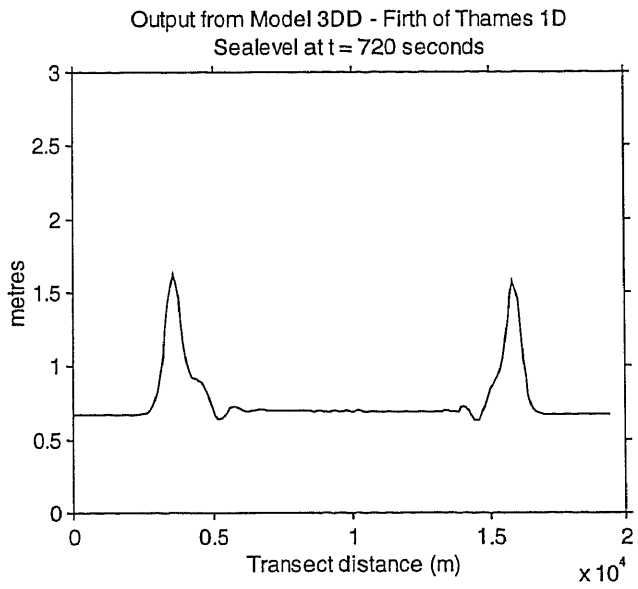
Output from Model 3DD - Firth of Thames 1D
Sealevel at t = 720 seconds
metres
Transect distance (m)
x 10^4

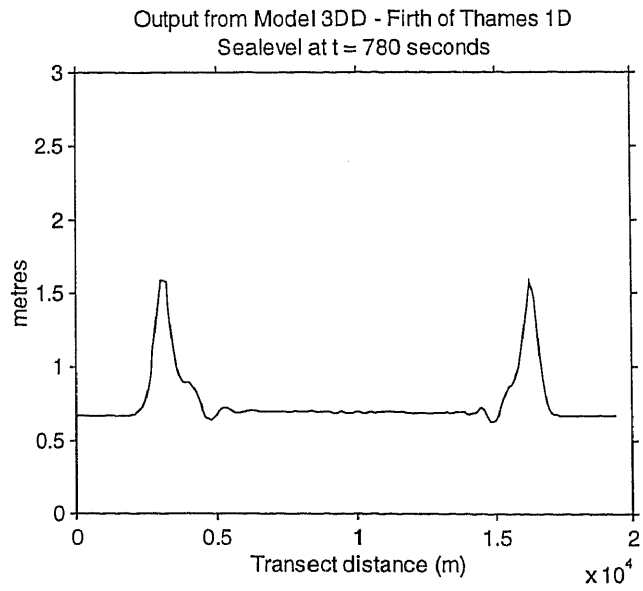
Output from Model 3DD - Firth of Thames 1D
Sealevel at t = 780 seconds
metres
Transect distance (m)
x 10^4

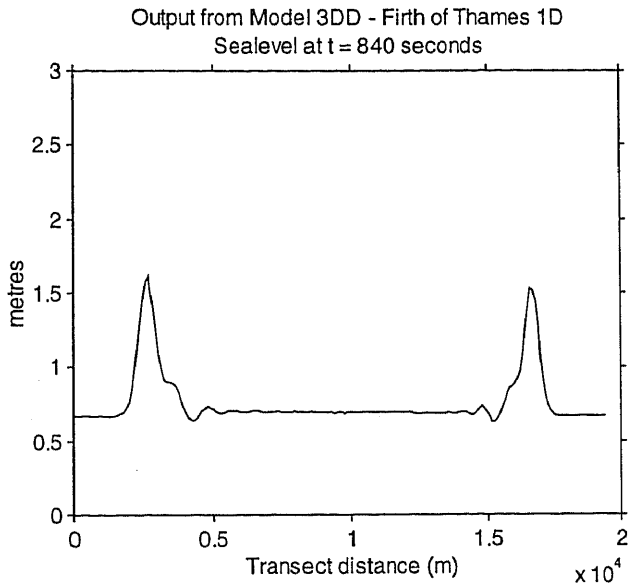
Output from Model 3DD - Firth of Thames 1D
Sealevel at t = 840 seconds
metres
Transect distance (m)
x 10^4

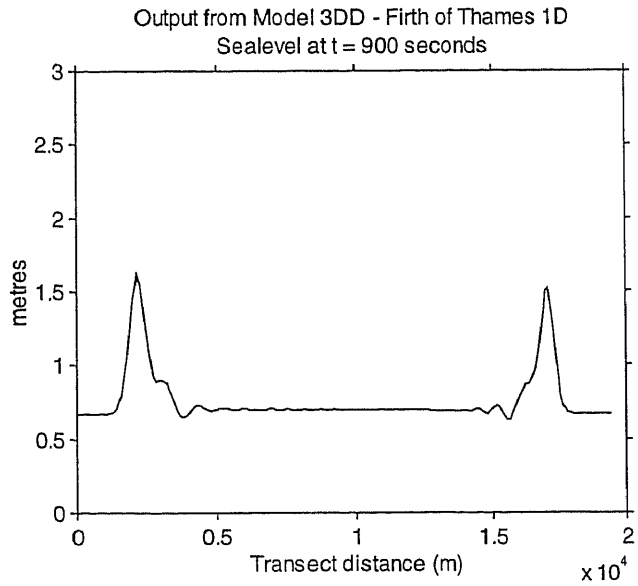
Output from Model 3DD - Firth of Thames 1D
Sealevel at t = 900 seconds
metres
Transect distance (m)
x 10^4

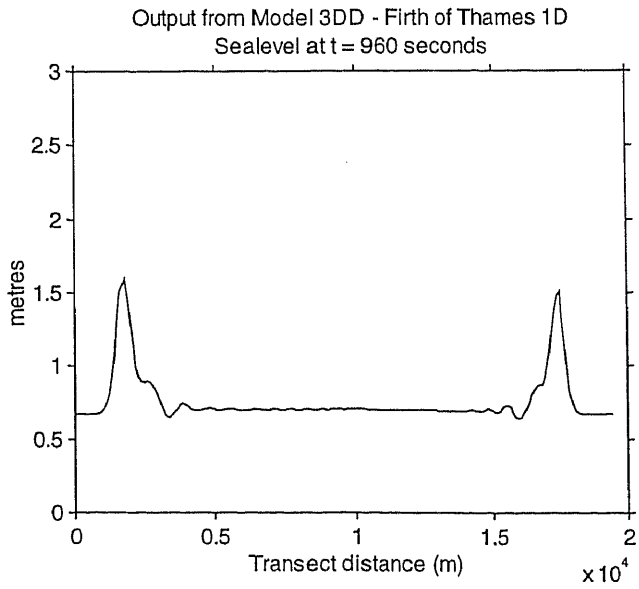
Output from Model 3DD - Firth of Thames 1D
Sealevel at t = 960 seconds
metres
Transect distance (m)
x 10^4

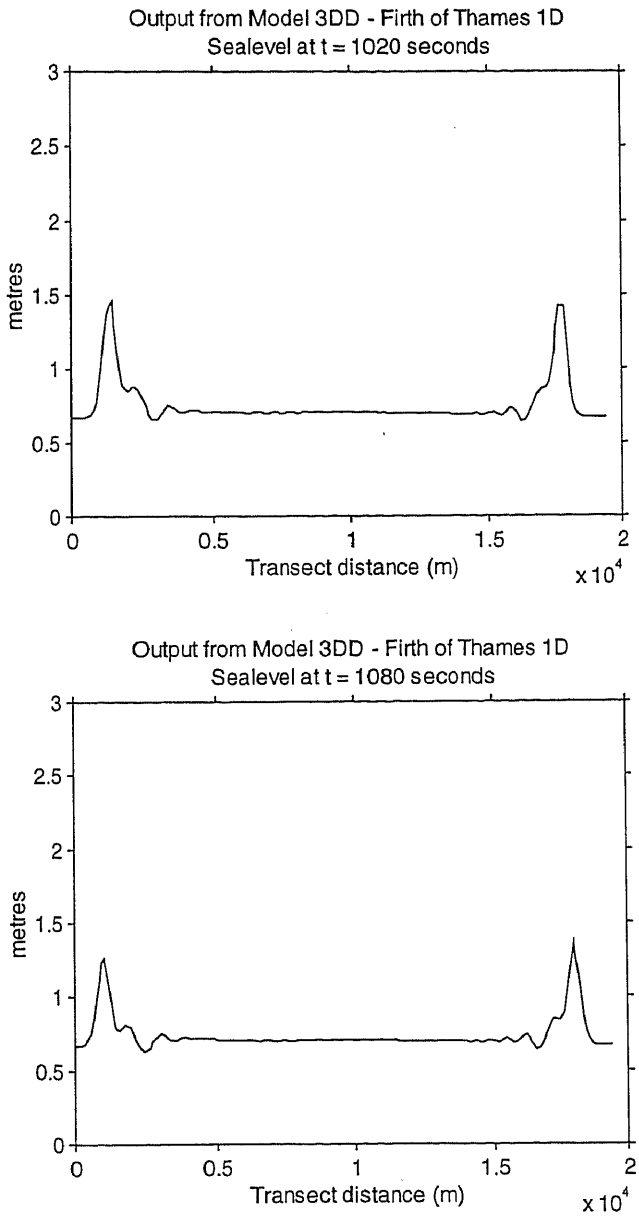

Figure 5.19: Results of 1 Dimensional Modelling using '3DD': Wave height at a) 0 s; b) 60 s; c) 120 s; d) 180 s; e) 240 s; f) 300 s; g) 360 s; h) 420 s; i) 480 s; j) 540 s; k) 600 s, l) 660 s; m) 720 s; n) 780s; o) 840 s; p) 900 s; q) 960 s; r) 1020 s; s) 1080 s.

The results indicate that the maximum wave height decays by approximately 50% during the first 60 seconds. This is most likely due to the dispersion of wave energy into two separate wave fronts that propagate west and east towards the shoreline. Following this both wave fronts maintain wave heights of 1 m until approximately 17 minutes (1020 s) by which time the wave fronts have propagated into the sponge boundary and consequently begin to decay. Hence, results beyond this time are not presented.

Wave speed is greatest during the initial phases of simulation, while it is propagating in the deepest water. i.e. wave initially propagates at around 12.5 $m.s^{-1}$ but slows to about 6.5 $m.s^{-1}$ in shallower water during the later phases (1020 –1080 s).

5.7.3 Comparison with Results predicted by 'TSUNAMI'

Maximum wave height and wave propagation velocities from the above simulation ('3DD') were compared with maximum wave heights and wave velocities generated using 'TSUNAMI', for the same location.

Results and Discussion

Figure 5.20 illustrates the location of nodes (black dots) for which wave height through time data was extracted from simulation results involving 2.1 m of seafloor displacement along Segment A (Scenario 1) employing the 'TSUNAMI' model. Profiles of wave height across a west-east transect located approximately 14 km from the base of the Firth of Thames are presented in Figure 5.21 and results summarised in Table 5.18.

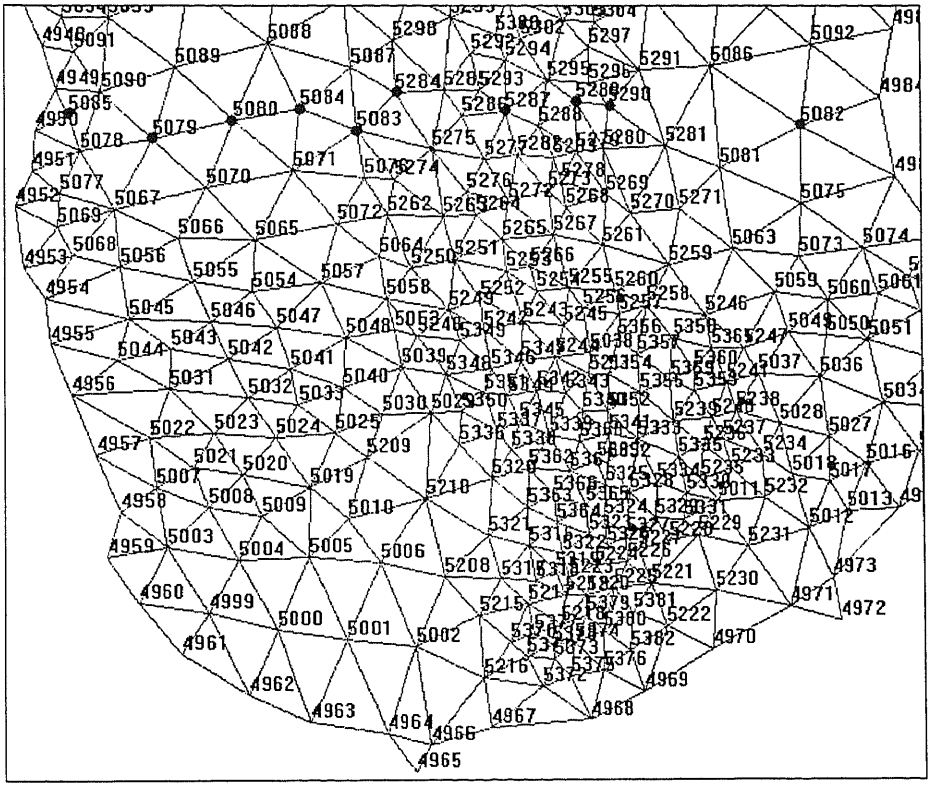

Figure 5.20: Location of nodes for which wave height through time data was extracted from Scenario 1 (2.1 m of displacement along Segment A) employing the 'TSUNAMI' model.

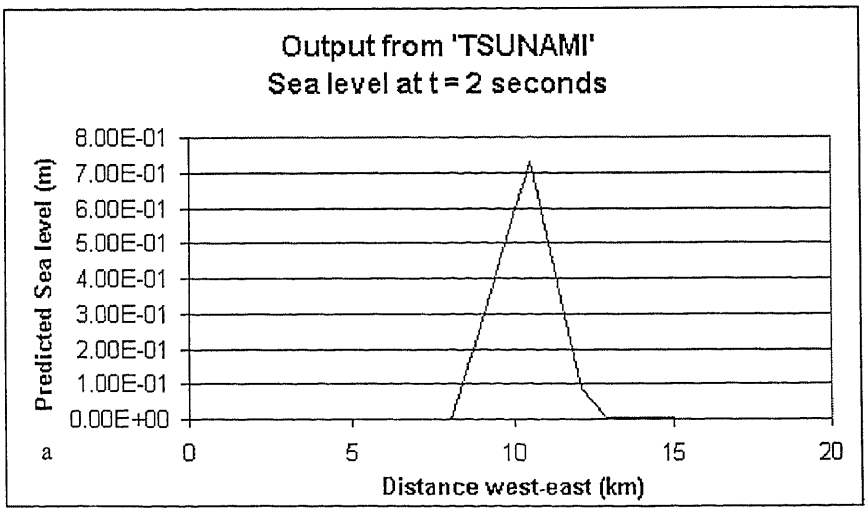

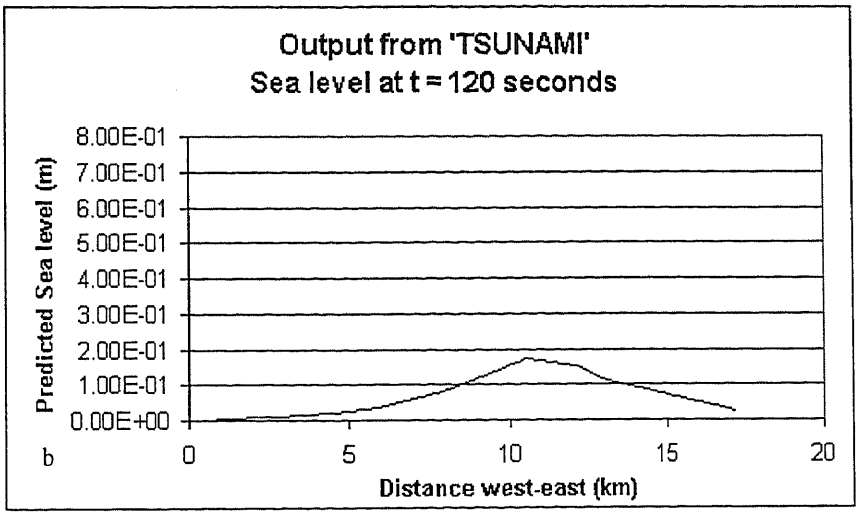
Output from 'TSUNAMI'
Sea level at t = 120 seconds
Predicted Sea level (m)
8.00E-01
7.00E-01
6.00E-01
5.00E-01
4.00E-01
3.00E-01
2.00E-01
1.00E-01
0.00E+00
0
5
10
15
20
Distance west-east (km)

b

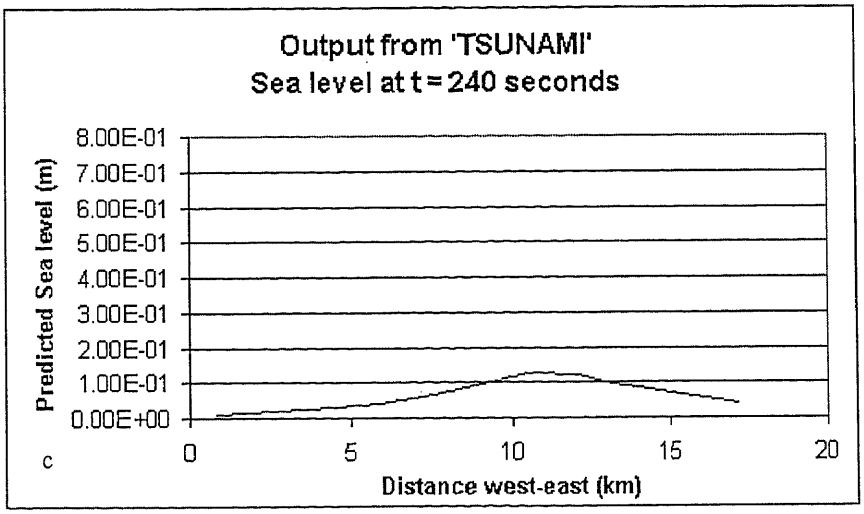
Output from 'TSUNAMI'
Sea level at t = 240 seconds
Predicted Sea level (m)
8.00E-01
7.00E-01
6.00E-01
5.00E-01
4.00E-01
3.00E-01
2.00E-01
1.00E-01
0.00E+00
0
5
10
15
20
Distance west-east (km)

c

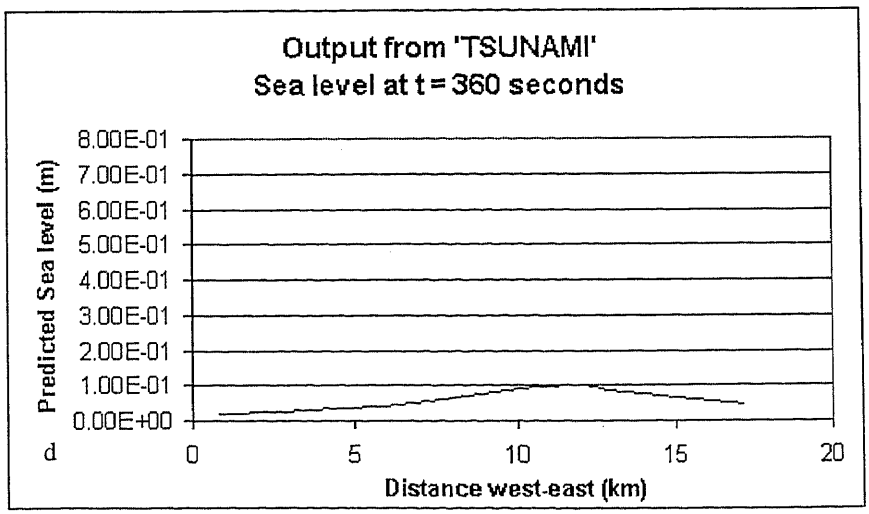
Output from 'TSUNAMI'
Sea level at t = 360 seconds
Predicted Sea level (m)
8.00E-01
7.00E-01
6.00E-01
5.00E-01
4.00E-01
3.00E-01
2.00E-01
1.00E-01
0.00E+00
0
5
10
15
20
Distance west-east (km)

d

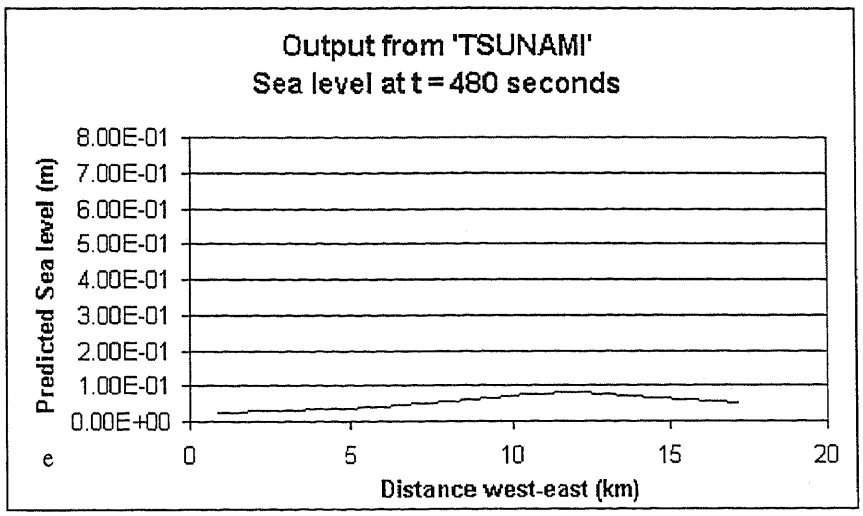
Output from 'TSUNAMI'
Sea level at t = 480 seconds
Predicted Sea level (m)
8.00E-01
7.00E-01
6.00E-01
5.00E-01
4.00E-01
3.00E-01
2.00E-01
1.00E-01
0.00E+00
0
5
10
15
20
Distance west-east (km)

e

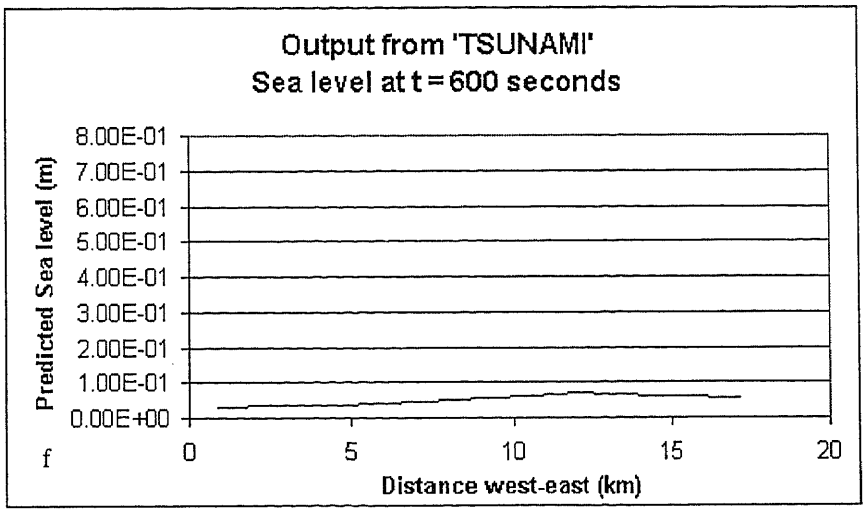
Output from 'TSUNAMI'
Sea level at t = 600 seconds
Predicted Sea level (m)
8.00E-01
7.00E-01
6.00E-01
5.00E-01
4.00E-01
3.00E-01
2.00E-01
1.00E-01
0.00E+00
0
5
10
15
20
Distance west-east (km)

f

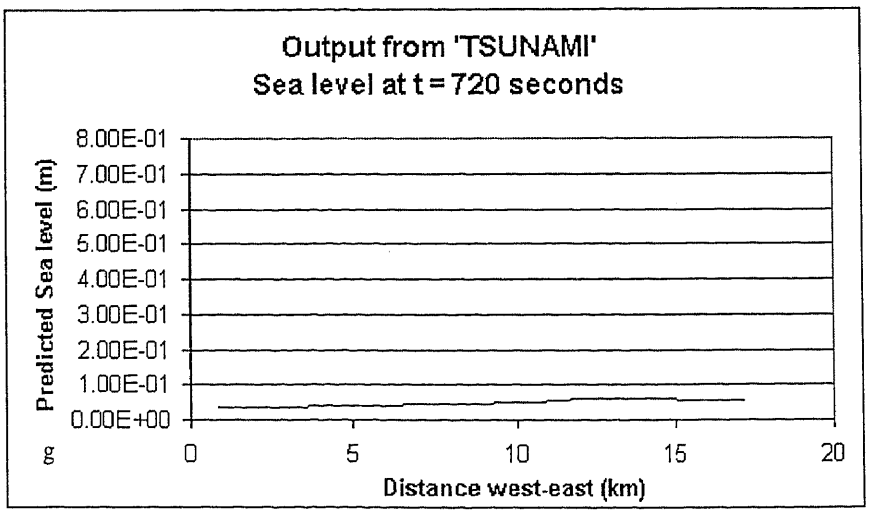
Output from 'TSUNAMI'
Sea level at t = 720 seconds
Predicted Sea level (m)
8.00E-01
7.00E-01
6.00E-01
5.00E-01
4.00E-01
3.00E-01
2.00E-01
1.00E-01
0.00E+00
0
5
10
15
20
Distance west-east (km)

g

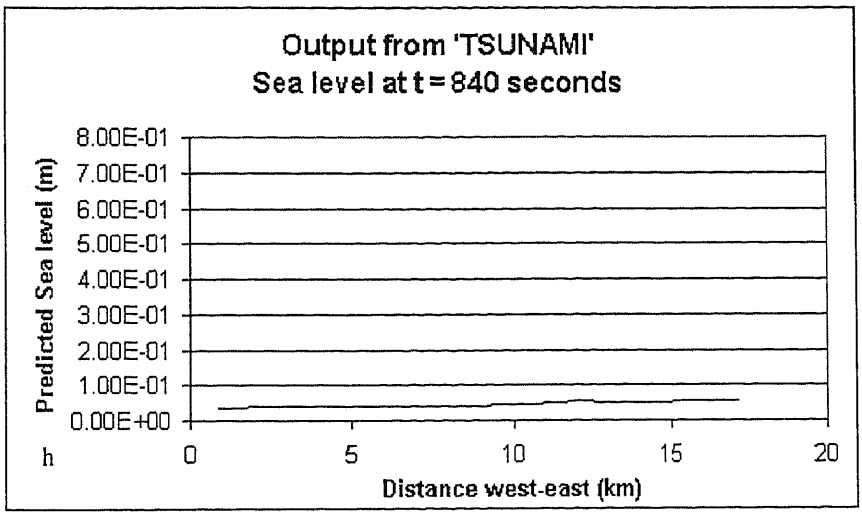

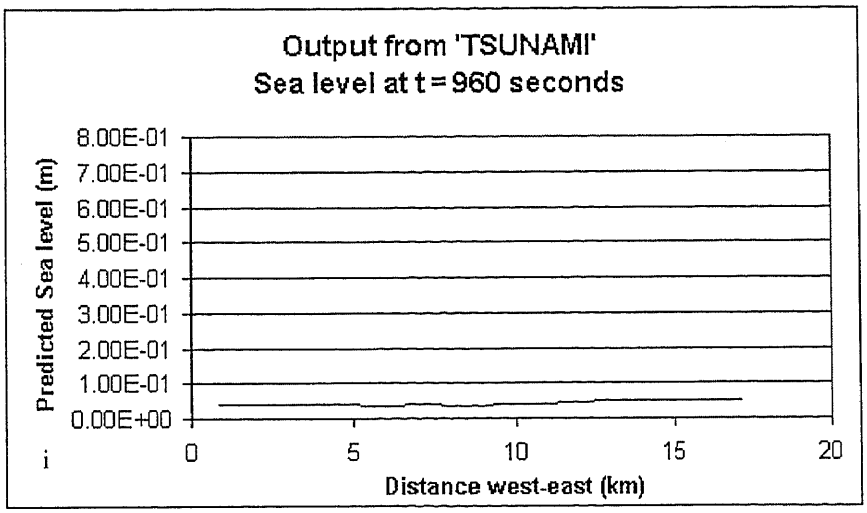

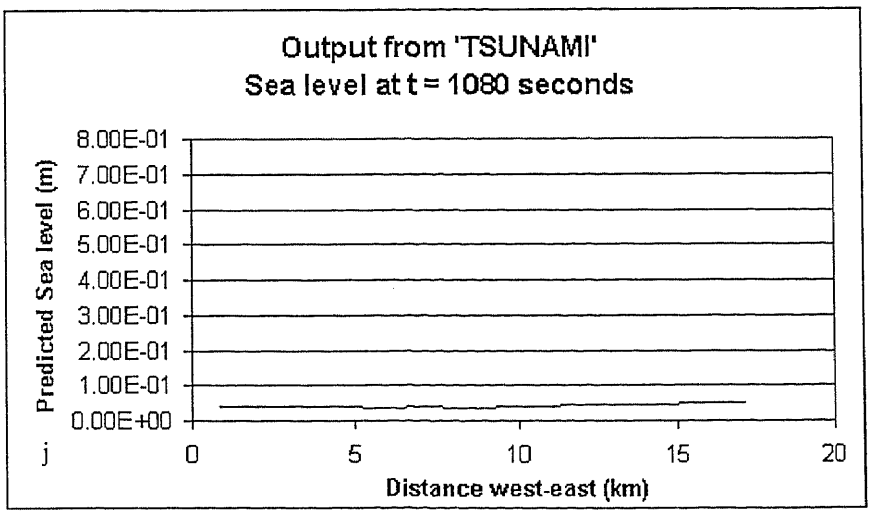

Figure 5.21: Sea level profiles transecting west to east across the Firth of Thames. The profiles were extracted from simulation results generated by the 'TSUNAMI' model for 2.1 m of displacement along Segment A; at times of **a)** 2 s; **b)** 120 s; **c)** 240 s; **d)** 360 s, **e)** 480 s, **f)** 600 s, **g)** 720 s, **h)** 840 s, **i)** 960 s, **j)** 1080 s. The transect is located approximately 14 km above the base of the Firth of Thames.

Table 5.18: Table summarising the results of the simulation undertaken using 'TSUNAMI' for 2.1 m of displacement along Segment A and surface rupture width of 1.25 km.

Node	Distance From Source (km)	Maximum Wave Height (m)	Arrival Time of Max. H. (min, sec)	Wave velocity at Node x ($m.s^{-1}$)
5287	0	0.73	0, 2	n/a
*5289	1.6	0.18	0, 7	228
5284	2.0	0.09	0, 30	67
*5290	2.2	0.11	1, 10	31
5083	2.9	0.07	2, 0	24
5084	4.1	0.04	5, 40	12
5080	5.5	0.04	13, 40	7
*5082	6.3	0.05	11, 20	9
5079	7.2	0.04	16, 20	7
5085	8.8	0.04	17, 10	9

* represents nodes lying to the east of the displacement zone. Unmarked nodes lie to the west of the displacement zone.

1. Maximum wave height above the displacement node (0.73 m) is significantly less than the displacement on the seafloor (only 35% of 2.1 m). This can be partially accounted for as the generation phase occurs over four time steps, each 0.5 s long. Consequently, water moves away from the displacement zone at each time step, and before the seafloor has been displaced by the entire 2.1 m. Note however that it is unlikely that 2/3 of the displaced water moves away from the displacement zone during 2 seconds.
2. Maximum predicted wave height decays rapidly as distance from the source increases. For example, node 5289, located approximately 1.6 km eastward of the displacement zone has a maximum predicted wave height only 25% of that predicted at the source; node 5284, located approximately 2.0 km westward of the displacement zone has a maximum predicted wave height that is only 12% of that predicted at the source.
3. Initial wave propagation velocity is very large. For example, 'TSUNAMI' predicts the peak wave height travels eastward, in approximately 7 m water depth, a distance of 1.6 km during approximately 7 seconds. This equates to a velocity of

228 $m.s^{-1}$. Shallow water theory [$C = \sqrt{g.h}$ where g=9.81 $m.s^{-2}$, h= water depth], predicts the wave propagation velocity for such depths (~7 m) should be in the order of 8 $m.s^{-1}$.

4. Figure 5.21 indicates that at any one time the maximum predicted wave height is observed immediately above the displacement zone. This suggests 'TSUNAMI' may not be simulating propagation of a wave front or peak, as it is observed in the simulation undertaken using '3DD' (Figure 5.19).

The large rate of wave height decay predicted by 'TSUNAMI' and the disparity in the form of wave propagation observed between the 'TSUNAMI' and '3DD' models suggest (i) large diffusion (high mixing) is occurring in the 'TSUNAMI' model and may possibly be responsible for small predicted wave heights. Therefore it is suggested that '3DD' may be modelling wave height more accurately and hence the results predicted by '3DD' would appear most realistic, at least for the shallow water scenario investigated here (displacement along Segment A). This conclusion is supported by run-up height estimates predicted by Equations 5.1 to 5.3 (Abe, 1995).

However, the results from the simulation undertaken using the model '3DD' are limited by three factors: (i) '3DD' is not capable of modelling the generation phase, hence the maximum elevated sea level above the displacement zone employed for the hot start may be larger than would be observed in reality, (ii) the simulation employing '3DD' was undertaken in only 1 dimension whereas 'TSUNAMI' disperses wave energy in 2 dimensions, and (iii) the bathymetric data used for the '3DD' simulation was interpolated from low resolution data (one bathymetric data point every 1500 m) and is consequently not as accurate as that employed in the 'TSUNAMI' model.

Unrealistic wave velocities, such as those discussed in Point 3 above, can be predicted by the 'TSUNAMI' model if numerical diffusion is significant and the time step is small (de Lange, 1997). If manual calculation of tsunami travel times implies unrealistic propagation velocities, the model time step should be increased. Hence, the time step for the generation phase was increased from 0.5 s to 10 s and the model

re-run for displacement along Segment A. Wave propagation velocities were re-calculated and are summarised in Table 5.19.

Table 5.19: Table summarising the results of the simulation undertaken using 'TSUNAMI' for 10 second generation phase time step involving 2.1 m of displacement along Segment A.

Node	Distance From Source (km)	Maximum Wave Height (m)	Arrival Time of Max. H. (min, sec)	Wave velocity at Node x ($m.s^{-1}$)
5287	0	1.05	0, 10	n/a
*5289	1.6	0.17	1, 50	15
5284	2.0	0.09	3, 0	11
*5290	2.2	0.12	3, 40	10
5083	2.9	0.06	4, 20	11
5084	4.1	0.04	7, 0	10
5080	5.5	0.04	16, 20	6
*5082	6.3	0.05	12, 30	8
5079	7.2	0.04	18, 30	7
5085	8.8	0.04	18, 50	8

Increasing the time step for the generation phase has significantly reduced initial wave propagation velocities, producing results more consistent with shallow water wave theory.

In order to further investigate the unlikely occurrence that 2/3 of the water has propagated away from the displacement zone during 2 seconds (Point 1 above), a simulation where all sea floor displacement occurs during 1 numerical iteration was undertaken. The results indicate that an error in the numerical code of the 'TSUNAMI' model meant that only half of the stipulated vertical displacement (2.1 m for Segments A, B, C, and D1 and 7.35 m for Segment D2) was being employed. Hence the wave heights presented for *all* the above numerical displacements simulated using 'TSUNAMI' represent wave heights resulting from 1.05 m and 3.675 m of vertical displacement. Consequently, the 'TSUNAMI' model was re-run for Scenarios 1-5 using an adjusted set of generation conditions.

5.8 SIMULATIONS EMPLOYING CORRECTED VERSION OF 'TSUNAMI'

5.8.1 Events Simulated

The adjusted set of 'TSUNAMI' generation conditions, which essentially double the magnitude of vertical displacement, were employed to re-simulate tsunamis generated by Scenarios 1-5 (Refer to Table 5.1). However, displacement duration was increased from four, 0.5 s time steps (employed in the original simulations) to a single 10 s time step. Displacement occurred for a surface rupture width of 5.8 km.

5.8.2 Results and Discussion

Simulations involving 2.1 m of vertical displacement along Segments A, B, C and D1 and 7.35 m of displacement along Segment D2 generated the following maximum wave height predictions (Refer to Tables 5.20-5.25, corrected 'TSUNAMI' version).

Table 5.20: Arrival time and magnitude of maximum predicted wave height for simulations involving: (a) 2.1 m of displacement along Segment A, (b) a surface rupture width of 5.8 km, and (c) 10 s time step during generation phase.

Location	Maximum Wave Height (m)	Arrival Time of Max. H (hours, min., sec.)
Displacement Node	2.1	0, 0, 10
Base of the Firth of Thames (displacement node)	2.1	0, 0, 10
Waihou River Mouth	0.635	0, 25, 30
Moanataiare	0.630	0, 24, 40
Between Piako & Waihou Rivers	0.704	0, 19, 0
Miranda	0.691	0, 22, 10
Kaiaua	0.399	0, 16, 10
Wilson Bay	0.160	0, 41, 30
Kawakawa Bay	0.071	1, 49, 0
Sully Reef, Ponui Is.	0.171	1, 14, 40
Waiheke Is.	0.085	1, 17, 30
Water Front, Auckland City	0.000	n/a
Musick Point, Half Moon Bay	0.003	3, 23, 0
Tamaki Strait	0.006	2, 82, 50
Coromandel Wharf	0.037	2, 31, 30
Te Puru	0.332	0, 20, 20
Waimangu Pt.	0.156	0, 44, 30
Rangipukea Is.	0.106	1, 14, 50
Tararu	0.594	0, 23, 20

Table 5.21: Arrival time and magnitude of maximum predicted wave height for simulations involving: (a) 2.1 m of displacement along Segment B, (b) a surface rupture width of 5.8 km, and (c) 10 s time step during generation phase.

Location	Maximum Wave Height (m)	Arrival Time of Max H. (hours, min., sec.)
Displacement node	2.1	0, 0, 10
Base of the Firth of Thames	0.254	0, 55, 20
Waihou River Mouth	0.214	0, 57, 20
Moanataiare	0.212	0, 56, 30
Between Piako and Waihou Rivers	0.225	0, 56, 0
Miranda	0.247	0, 47, 0
Kaiaua	0.419	0, 16, 10
Wilson Bay	0.201	0, 18, 40
Kawakawa Bay	0.043	1, 15, 0
Sully Reef, Ponui Is.	0.128	0, 41, 40
Waiheke Is.	0.060	0, 43, 40
Water Front, Auckland City	0.000	n/a
Musick Point, Half Moon Bay	0.002	2, 59, 30
Tamaki Strait	0.003	2, 31, 10
Coromandel Wharf	0.021	2, 1, 40
Central Hauraki Gulf	0.011	0, 57, 0
Te Puru	0.369	0, 14, 20
Waimangu Pt.	0.159	0, 12, 30
Rangipukea Is.	0.073	0, 32, 40
Tararu	0.203	0, 51, 20

Table 5.22: Arrival time and magnitude of maximum predicted wave height for simulations involving: (a) 2.1 m of displacement along Segment C, (b) a surface rupture width of 5.8 km, and (c) 10 s time step during generation phase.

Location	Maximum Wave Height (m)	Arrival Time of Max. H. (hours, min., sec.)
Displacement node	2.1	0, 0, 10
Kaiaua	0.273	0, 31, 10
Waimangu Pt.	0.699	0, 8, 0
Deadmans Pt.	0.284	0, 11, 0
Wilson Bay	0.600	0, 9, 40
Miranda	0.264	1, 3, 10
Base of Firth of Thames	0.267	1, 6, 10
Moanataiari	0.233	0, 53, 0
Te Puru	0.326	0, 26, 20
Ponui Is.	0.255	0, 26, 0
Pakihi Is.	0.097	0, 40, 40
Ruakura Pt.	0.119	0, 28, 40
Orere Pt.	0.463	0, 11, 40
Wharekawa Pt.	0.404	0, 12, 40
Rangipukea Is.	0.156	0, 14, 40
Man O War Bay, Waiheke Is.	0.059	0, 39, 40
Tapu	0.464	0, 15, 40
Whakakaiwhara Pt.	0.006	1, 36, 20
Ruthe Passage	0.110	0, 26, 10
Waikawau	0.580	0, 13, 30

Table 5.23: Arrival time and magnitude of maximum predicted wave height for simulations involving: (a) 2.1 m of displacement along Segment D1, (b) a surface rupture width of 5.8 km, and (c) 10 s time step during generation phase.

Location	Maximum Wave Height (m)	Arrival Time of Max. H. (hours, min., sec.)
Te Kawau Pt.	0.226	0, 24, 40
Rakino Is.	0.047	0, 26, 10
Waiheke Is.	0.353	0, 7, 50
Man O War Bay, Waiheke Is.	0.266	0, 21, 50
Motuoruhi Is.	0.812	0, 9, 30
Moturua Is.	0.337	0, 15, 0
Whanganui Is.	0.901	0, 11, 30
Coromandel Wharf	0.086	1, 10, 40
Rangipukea Is.	0.853	0, 9, 40
Deadmans Point	0.808	0, 6, 50
Rotorua Is.	0.810	0, 12, 50
Ruthe Passage	0.736	0, 12, 30
Browns Bay	0.035	0, 54, 20
Northern Waiheke Channel	0.502	0, 10, 50
Mania Harbour	0.160	0, 52, 10
Ruakura Pt.	0.300	0, 29, 40
Orere Pt.	0.507	0, 26, 40
Waimangu Pt.	0.418	0, 30, 0
Base of Firth of Thames	0.295	1, 43, 10
Moanataiare	0.265	1, 36, 50

Doubling the displacement magnitude has resulted in a doubling of the predicted maximum wave heights (Tables 5.25). The average percentage increase in predicted maximum wave height for all extracted *shoreline* wave heights presented in the above tables (doubled vertical displacement) is 203 %. This supports the conclusion that there is a linear relationship between the volume of displaced material and the maximum wave heights predicted by the 'TSUNAMI' model.

Table 5.24: Arrival time and magnitude of maximum predicted wave height for simulations involving: (a) 7.35 m of displacement along Segment D2, (b) a surface rupture width of 5.8 km, and (c) 10 s time step during generation phase.

Location	Maximum Wave Height (m)	Arrival Time of Max. H. (hours, min., sec.)
Kaiaua	0.615	0, 56, 0
Moanataiari	0.588	1, 30, 50
Coromandel Wharf	0.215	1, 10, 20
Howick/Half Moon Bay	0.013	2, 23, 0
Kawakawa Bay	0.389	0, 41, 50
Wilson Bay	1.375	0, 10, 40
Orere Pt.	1.242	0, 17, 40
displacement node (near Pakatoa Is.)	7.350	0, 0, 10
Waiheke Channel	0.384	0, 26, 10
Sandspit passage	0.195	0, 25, 40
Tamaki Strait	0.044	1, 15, 30
Miranda	0.630	1, 25, 40
Wind Pt.	0.591	0, 56, 20
Ponui Is.	2.407	0, 6, 40
Ruthe Passage	3.377	0, 3, 10
Base of Firth of Thames	0.626	1, 30, 10
Te Kouma	0.259	0, 47, 50
Displacement node	7.350	0, 0, 10
Auckland City water front	0.002	2, 7, 45
Man O War Bay, Waiheke Is.	0.688	0, 12, 10
Rangipukea Is.	1.273	0, 11, 30
Deadmans Pt.	1.846	0, 7, 20
Waikawau	0.888	0, 23, 40
Tapu	0.618	0, 37, 20
Te Puru	0.616	0, 50, 30
Tararu	0.557	1, 10, 30
Ruakura Pt.	0.766	0, 20, 30
Waimangu Pt.	1.091	0, 19, 40
Wharekawa Pt.	0.623	0, 39, 40

Table 5.25: The average % increase in maximum predicted wave height resulting from a doubling of vertical displacement. Column 2 represents the average percentage increase for all shoreline sites for which sea level time histories were extracted.

Location	Average % increased
A	196
B	201
C	205
D1	210
D2	204

In order to assess the accuracy of the above maximum wave height predictions, they were compared with estimates generated using Equations 5.1-5.3 (Refer to Tables

5.26-5.30). Non-shoreline locations and displacement node locations were not included in the comparison.

Table 5.26: Comparison of Maximum wave height predicted by Tsunami and Equations 5.1-5.3 for 2.1 m displacement along Segment A. The wave heights predicted by 'TSUNAMI' were generated from doubling of the vertical displacement, and extending the generation time step length from 0.5 s to 10 s.

Location	Distance from Source (km)	Max H. prediction from Equations (m)	Max H. prediction from 'TSUNAMI' (m)	Equation/ Tsunami prediction
Waihou River Mouth	< 13	1.78	0.64	2.80
Moanataiare	< 13	1.78	0.63	2.83
Between Piako & Waihou Rivers	< 13	1.78	0.70	2.53
Miranda	< 13	1.78	0.69	2.57
Kaiaua	< 13	1.78	0.40	4.47
Wilson Bay	27.5	0.81	0.16	5.07
Kawakawa Bay	33	0.68	0.07	9.71
Sully Reef, Ponui Is.	39	0.57	0.17	3.34
Musick Point, Half Moon Bay	57	0.39	0.03	13.01
Coromandel Wharf	41	0.55	0.04	14.87
Te Puru	< 13	1.78	0.33	5.36
Waimangu Pt.	22	1.02	0.16	6.53
Rangipukea Is.	34	0.66	0.11	6.16
Tararu	< 13	1.78	0.59	3.00

Table 5.27: Comparison of Maximum wave height predicted by Tsunami and Equations 5.1-5.3 for 2.1 m displacement along Segment B. The wave heights predicted by 'TSUNAMI' were generated from doubling of the vertical displacement, and extending the generation time step length from 0.5 s to 10 s.

Location	Distance from Source (km)	Max H. prediction from Equations (m)	Max H. prediction from 'TSUNAMI' (m)	Equation/ Tsunami prediction
Base of the Firth of Thames	19	0.74	0.25	2.91
Waihou River Mouth	18	0.78	0.21	3.65
Moanataiare	15	0.94	0.21	4.48
Between Piako and Waihou Rivers	18	0.78	0.23	3.46
Miranda	17	0.83	0.25	3.37
Kaiaua	11.5	1.23	0.42	2.93
Wilson Bay	17.5	0.81	0.20	4.03
Kawakawa Bay	23	0.61	0.04	14.19
Sully Reef, Ponui Is.	29	0.49	0.13	3.83
Water Front, Auckland City	~60	0.24	0.00	--
Musick Point, Half Moon Bay	49	0.29	0.00	145.00
Coromandel Wharf	31	0.46	0.02	21.91
Te Puru	11	1.28	0.37	3.48
Waimangu Pt.	12	1.18	0.16	7.41
Rangipukea Is.	24	0.59	0.07	8.08
Tararu	13	1.09	0.20	5.37

Table 5.28: Comparison of Maximum wave height predicted by Tsunami and Equations 5.1-5.3 for 2.1 m displacement along Segment C. The wave heights predicted by 'TSUNAMI' were generated from doubling of the vertical displacement, and extending the generation time step length from 0.5 s to 10 s.

Location	Distance from Source (km)	Max H. prediction from Equations (m)	Max H. prediction from 'TSUNAMI' (m)	Equation/ Tsunami prediction
Kaiaua	17	1.32	0.27	4.83
Waimangu Pt.	<13	1.78	0.70	2.54
Deadmans Pt.	<13	1.78	0.28	6.26
Wilson Bay	<13	1.78	0.60	2.97
Miranda	25	0.9	0.26	3.41
Base of Firth of Thames	28.5	0.79	0.27	2.95
Moanataiari	23	0.97	0.23	4.20
Te Puru	16	1.4	0.33	4.30
Ponui Is.	20	1.12	0.26	4.39
Pakihi Is.	19	1.19	0.10	12.27
Ruakura Pt.	15.5	1.44	0.15	9.84
Orere Pt.	<13	1.78	0.46	3.85
Wharekawa Pt.	13	1.78	0.40	4.40
Rangipukea Is.	15	1.44	0.16	9.24
Man O War Bay, Waiheke Is.	25.5	0.88	0.06	14.91
Tapu	<13	1.78	0.46	3.83
Whakakaiwhara Pt.	25	0.9	0.01	150.00
Ruthe Passage	21	1.07	0.11	9.73
Waikawau	<13	1.78	0.58	306.73

Table 5.29: Comparison of Maximum wave height predicted by Tsunami and Equations 5.1-5.3 for 2.1 m displacement along Segment D1. The wave heights predicted by 'TSUNAMI' were generated from doubling of the vertical displacement, and extending the generation time step length from 0.5 s to 10 s.

Location	Distance from Source (km)	Max H. prediction from Equations (m)	Max H. prediction from 'TSUNAMI' (m)	Equation/ Tsunami prediction
Te Kawau Pt.	25.5	1.11	0.23	4.92
Rakino Is.	36.1	0.78	0.05	16.60
Man O War Bay, Waiheke Is.	< 14	2	0.27	7.52
Motuoruhi Is.	< 14	2	0.81	2.46
Moturua Is.	14	2	0.34	5.94
Whanganui Is.	< 14	2	0.90	2.22
Coromandel Wharf	18	1.57	0.09	18.25
Rangipukea Is.	< 14	2	0.85	2.35
Deadmans Point	< 14	2	0.81	2.48
Rotorua Is.	< 14	2	0.81	2.48
Ruthe Passage	< 14	2	0.74	2.71
Browns Bay	53	0.53	0.04	15.14
Northern Waiheke Channel	< 14	2	0.50	3.98
Mania Harbour	~16	1.76	0.17	10.62
Ruakura Pt.	17	1.66	0.30	5.53
Orere Pt.	17	1.66	0.51	3.27
Waimangu Pt.	20	1.41	0.41	3.41
Base of Firth of Thames	47	0.6	0.29	2.04
Moanataiare	41	0.69	0.26	2.63

Table 5.30: Comparison of Maximum wave height predicted by Tsunami and Equations 5.1-5.3 for 7.35 m displacement along Segment D2. The wave heights predicted by 'TSUNAMI' were generated from doubling of the vertical displacement, and extending the generation time step length from 0.5 s to 10 s.

Location	Distance from Source (km)	Max H. prediction from Equations (m)	Max H. prediction from 'TSUNAMI' (m)	Equation/ Tsunami prediction
Kaiaua	30	1.87	0.61	3.04
Moanataiari	39	1.44	0.59	2.45
Coromandel Wharf	20	2.81	0.21	13.07
Howick/Half Moon Bay	34	1.65	0.01	126.92
Kawakawa Bay	< 20	2.82	0.39	7.26
Wilson Bay	< 20	2.82	1.38	2.04
Orere Pt.	< 20	2.82	1.24	2.27
Waiheke Channel	< 20	2.82	0.38	7.35
Sandspit passage	< 20	2.82	0.19	14.46
Miranda	38	1.48	0.63	2.36
Wind Pt.	35	1.61	0.59	2.71
Ponui Is. (Scully Reef)	< 20	2.82	2.41	1.17
Ponui Is. (NE tip)	< 20	2.82	3.5	0.81
Ruthe Passage	< 20	2.82	3.36	0.84
Base of Firth of Thames	45	1.25	0.63	1.99
Te Kouma	~20	2.82	0.26	10.88
Auckland City water front	50	1.12	0.00	560.00
Man O War Bay, Waiheke Is.	< 20	2.82	0.69	4.10
*Waiheke Is.	< 20	2.82	1.5	1.88
Rangipukea Is.	< 20	2.82	1.27	2.22
Deadmans Pt.	< 20	2.82	1.85	1.52
Waikawau	21	2.68	0.89	3.01
Tapu	26	2.16	0.62	3.49
Te Puru	32	1.76	0.62	2.85
Tararu	37	1.52	0.56	2.72
Ruakura Pt.	< 20	2.82	0.77	3.68
Waimangu Pt.	< 20	2.82	1.09	2.58
Wharekawa Pt.	25	2.25	0.62	3.61
Rotoroa Is.	< 20	2.82	3.5	0.81
Tarahiki	< 20	2.82	3.9	0.72
Pakatoa Is (NE face)	< 20	2.82	4	0.71
Pakatoa Is (SW face)	< 20	2.82	0.7	4.03

* Waikeke Island at the following location: 175° 11' 30" E 36° 46' 54" S (NZ Geodetic Datum 1949)

Comparison of maximum wave height predictions made by 'TSUNAMI' and Equations 5.1-5.3 (Tables 5.26-5.30) indicate the following:

1. For displacement along Segments A, B, and C, and D1 predictions made by 'TSUNAMI' are consistently smaller and are outside the factor of uncertainty (1.5) associated with Equations 5.1-5.3. The inconsistency observed between the above prediction methods is believed to occur because 'TSUNAMI' is under predicting

maximum wave height. 'TSUNAMI' is a linear model, designed to simulate tsunami generation in deep water. The modelled sea floor displacements occur in water depths less than ~40 m and it is suggested that the 'TSUNAMI' model is unable to cope with the highly non-linear wave processes that occur in shallow water.

2. For the scenario involving displacement along Segment D2, several locations close to the source, namely Pakatoa, Tarahiki, Rotoroa and Ponui Islands, the wave height predictions made by 'TSUNAMI' are within the factor of uncertainty (1.5) associated with Equations 5.1-5.3, and are, in some cases larger than wave height predictions made by the empirical formula.

   Given that (i) unlike the empirical formulae, 'TSUNAMI' is able to account for wave attenuation or reinforcement caused by wave propagation, and (ii) for locations within a distance R_0 from the source (Refer to Equation 5.2), wave height predictions made by the empirical formulae reach an upper limit, for some cases, 'TSUNAMI' may be the more appropriate prediction tool. Hence, should large displacement occur within a distance R_0 from adjacent land and over complex bathymetry, as is the situation for Segment D2, the 'TSUNAMI' model may have more accurate wave height predictions.

Given the above limitations associated with each prediction method, it is recommended that the largest wave height estimate predicted by either method, should be the height employed for hazard planning purposes. For all cases, excepting a few island locations close to the source in the Segment D2 scenario, the largest wave heights are predicted by Equations 5.1-5.3.

5.9 SUMMARY

The deep water generation and deep and shallow water propagation model 'TSUNAMI', was used to simulate tsunami generation and propagation in the Firth of Thames and Hauraki Gulf.

Five fault displacement events were simulated, these involved 2.1 m of vertical displacement along Segments A, B, C, and D1 and 7.35 m of displacement along Segment D2. The magnitude of displacement along Segment D2 was determined using conclusions drawn from core palynology discussed by Pocknall et al. (1989).

The first five simulations involved surface displacement width of approximately 1.25 km. 'TSUNAMI' simulations involving this surface rupture width predicted small maximum wave heights for all scenarios i.e maximum predicted *mainland* wave height is only 0.64 m. Simulated current velocities are depth-averaged results. The maximum simulated current velocity, 0.13 $m.s^{-1}$, is therefore deemed insignificant.

The wave heights predicted by 'TSUNAMI' appear too small for vertical displacements in order of 2.1 m and 7.35 m. An empirical formula developed by Abe (1995), which estimates the height of regional tsunami at a particular site as a function of propagation distance, suggests local sub-marine earthquakes of moment magnitudes 6.5-7.1 should produce wave heights considerably larger than those predicted by 'TSUNAMI'. In an attempt to further understand whether 'TSUNAMI' was predicting wave heights in the right order of magnitude, further simulations involving increased width of surface displacement were undertaken. The results indicated that there is a linear relationship between the displacement volume and the maximum predicted wave height at the shore. Hence, simulations involving increased fault width predicted larger wave heights. Despite this, the wave heights predicted by 'TSUNAMI' simulations were consistently smaller than those predicted by the method suggested by Abe (1995), 85% smaller on average (i.e. only 15 % of wave heights predicted by Equations 5.1-5.3).

This discrepancy between wave height predictions and the limitations associated with applying a linear, deep water generation model in shallow water, prompted a further simulation employing the finite difference hydrodynamic circulation model, '3DD' in 1 dimension. This was undertaken to provide further comparison with wave height results suggested by simulations undertaken using the 'TSUNAMI' model. Comparing results generated by '3DD' and 'TSUNAMI' indicate that for displacement along Segment A:

a) The wave form simulated by '3DD' and 'TSUNAMI' are significantly different.
b) The maximum wave height above the displacement zone predicted by the 'TSUNAMI' model is significantly less than the vertical displacement on the sea floor.
c) The 'TSUNAMI model predicts that wave height decays rapidly with distance from the source region.
d) 'TSUNAMI' predicts wave propagation velocities that are inconsistent with shallow water theory.

Varying the duration and number of time steps over which tsunami generation was to occur, identified the following solutions to points d) and b):

- Increasing the time step duration for the generation phase produced acceptable wave propagation velocities, and
- An error in the code caused the 'TSUNAMI' model to employ only half of the stipulated vertical displacement. Hence, wave heights predicted from all prior 'TSUNAMI' simulations actually resulted from 1.05 and 3.675 m of vertical displacement.

Consequently, the 'TSUNAMI' model was employed to re-simulate tsunami generation and propagation using an adjusted set of generation conditions. The results suggest that because 'TSUNAMI' does not account for the highly non-linear wave processes that occur in shallow water, this model is generally under predicting maximum wave height. However, this model is able to account for attenuation and reinforcement caused by wave propagation, and is not restricted by an upper wave height limit at locations close to the source. Consequently, where large displacement occurs within complex bathymetry and in close proximity to the source, as is the situation for Segment D2, the 'TSUNAMI' model may have more accurate wave height predictions.

Given the above limitations associated with each prediction method, it is recommended that the largest wave height estimate predicted by either method, should be the height employed for hazard planning purposes. For all cases, excepting a few island locations close to the source in the Segment D2 scenario, the largest wave heights are predicted by Equations 5.1-5.3.

5.10 REFERENCES

Abe, K., Estimate of Tsunami Run-up Heights from Earthquake Magnitudes, In *Tsunami: Progress in Prediction, Disaster Prevention and Warning*, Y. Tsuchiya and N. Shuto (Eds), Kluwer Academic Publishers, Netherlands, p. 21-35.

Adams, R.D., Muir, M.G., and Kean, R.J., 1972. Te Aroha Earthquake, 9 January 1972. *Bulletin of New Zealand Society for Earthquake Engineering*, Vol. 5, No.2, p. 54-58.

Black, K.P., Oldman, J.W., and Bell, R.G., 1996. *Numerical Hydrodynamic and Thermodynamic Modelling of Nearshore Offshore Exchange Processes*, NIWA Internal Report NOD602/1., 33 p.

de Lange, W.P., and Healy, T.R., 1997. Numerical modeling of tsunamis associated with marl diapirism off Poverty Bay, New Zealand. In Proceedings of the 13th Combined Australasian Coastal and Ocean Engineering Conference and 6th Australasian Port and Harbour Conference, Christchurch, 1997, p.1043-1047.

de Lange, P.J., and Lowe D.J., 1990. History of vertical displacement of Kerepehi Fault at Kopouatai bog, Hauraki Lowlands, New Zealand, since c. 10 700 years ago, *New Zealand Journal of Geology and Geophysics*, Vol. 33, p. 277-283.

de Lange, W.P., 1997. Tsunami Manual, Department of Earth Sciences, University of Waikato, New Zealand, 14 p.

de Lange, W.P. 1988. Scientist and Senior Lecturer at Waikato University, 25 November.

de Lange, W.P., and Hull, A.G., 1994. *Tsunami Hazard for the Auckland Region*, Earth Sciences Department, University of Waikato, and Institute of Geological and Nuclear Science Limited, p. 37.

Heaton, T.H., 1990. Evidence for and implications of self-healing pulses of slip in earthquake rupture, *Physics of the Earth and Planetary Interiors*, Vol. 64, p. 1-20.

Hochstein, M.P., Tearney, K., Rawson, S., Davey, F.J., Davidge, S., Henrys, S., and Backshall, D., 1986. Structure of the Hauraki Rift (New Zealand). In W.I. Reilly and B.E. Harford (ed), *Recent Crustal Movements of the Pacific Region*, Royal Society of New Zealand Bulletin 24. Wellington, The Royal Society of New Zealand. p.333-348.

Hull, A., 1999. Scientist at MORST, email to author, 3 January.

Kanamori, H., and Kikuchi, M., 1993. The 1992 Nicaragua earthquake: a slow tsunami earthquake associated with subducted sediments, *Nature*, Vol. 361, p. 714-716.

Okal, E.A., 1988. Predicting Large Tsunamis, *Natural Hazards,* Vol. 1, p. 67-96.

Pocknall, D.T., Gregory, M.R., and Greig, D.A., 1989. Palynology of core 80/20 and it's implications for understanding Holocene sea level changes in the Firth of Thames, New Zealand, *Journal of the Royal Society of New Zealand,* Vol. 19, No. 2, p.171-179.

Prasetya, G.S., 1998. *Modelling Volcanic Tsunamis.* M.Sc. Thesis, University of Waikato. 108 p.

Priestley, K.F., 1989. Source parameters of the 1987 Edgecumbe earthquake, New Zealand, *New Zealand Journal of Geology and Geophysics*, Vol. 32, p. 31-42.

Smith, E.G.C., and Oppenheimer, C.M.M., 1989. The Edgecumbe earthquake sequence: 1987 February 21 to March 18, *New Zealand Journal of Geology and Geophysics*, Vol. 32, p. 31-42.

Walters, R.A., and Henry, R.F., 1995. TRIGRID Users Manual GKS version, 121 p.

Webb, T., 1998. Scientist at IGNS, email to author, 3 September.

Zhdanov, M.A., 1991. An analytical model of tsunamis generated by earthquakes, In: *Tsunamis in the World, Fifteenth International Tsunami Symposium*, S. Tinti (ed), Kluwer Academic Publishers, Netherlands, p. 77-94.

Chapter 6

TELETSUNAMI SIMULATIONS

1.1 INTRODUCTION

This chapter aims to investigate how shoaling processes occurring during wave propagation affect tsunami wave height in the Firth of Thames, and in so doing, determine which localities adjacent to the Firth of Thames are likely to be subjected to attenuation or amplification of tsunami waves of varying period. Such an investigation allows an assessment of whether distantly or locally (through displacement along the Kerepehi Fault) generated tsunami represents a more significant hazard.

The above issues were investigated by undertaking simulations driven by 0.5 m amplitude teletsunami, for 10, 15, 20, 25 and 30 minute wave periods. The hydrodynamic circulation model, '3DD' (Refer to Appendix 10) was utilised for teletsunami propagation simulations.

6.2 MODEL SET-UP

6.2.1 Finite Difference Grid

The finite difference grid of the Hauraki Gulf employed for teletsunami simulations undertaken using '3DD' is comprised of 65 by 105 cells, each 1500 m square, which equates to an area of 97.5 km by 157.5 km. Cells are referred to their i and j cell numbers. Grid cell (i=1,j=1) is located at the bottom left corner of the model grid with the i co-ordinate increasing to the right (positive x direction) an the j co-ordinate increasing up the grid (positive y direction) (Figure 6.1). Cells are set in a grid aligned true north, the origin (i=1, j=1) of which is located at 2640000 E 6437500 N (NZMG) or 174° 27'E, 37°15'S (NZ Geodetic Datum 1949), (Black et al., 1996).

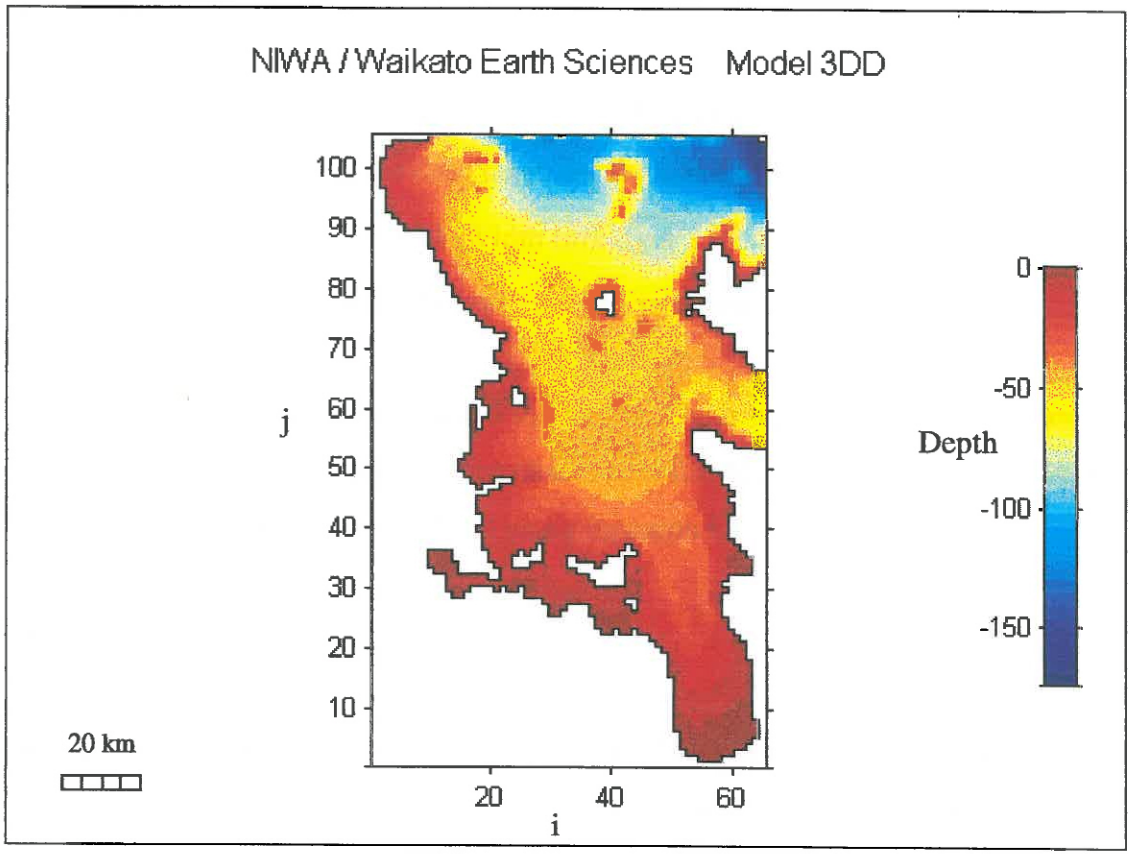

Figure 6.1: '3DD' model grid employed during teletsunami simulations.

6.2.2 Model Bathymetry

The model bathymetry is a gridded array with depth values assigned to the grid cell mid-point (Black, 1995). The model bathymetry is based on the original Proctor and Greig (1989) bathymetry as supplied by Malcom Greig, NIWA Wellington (Black et al, 1996). The bathymetric depths in the model grid are in relation to chart datum, which in the Hauraki Gulf lies 1.425 m below mean sea level.

6.2.3 Boundary Conditions

Simulation of teletsunami requires the input of a sinusoidal wave at open ocean boundaries, which for this grid are situated along the northern and eastern boundaries (Figure 6.1). The boundary files were set-up to simulate a 0.5 m amplitude wave approaching from the direction most likely for distantly generated tsunamis, the north-east. The phase lag of each cell was then calculated using Equation 6.1:

$$\phi_1 = \Delta t/T*360 \qquad \textbf{6.1}$$

where ϕ_1 is the phase difference between boundary $cell_{ij}$ and boundary $cell_{i-1\ j-1}$, T is the wave period, and Δt is the time taken for the wave to move across each boundary cell. Δt is equal to: Cell Width (m)/$\sqrt{g.h}$,

where g is the acceleration due to gravity, and h is the average water depth across $cell_{ij}$.

The phase lag for $cell_{ij}$ is then added to the total phase lag of the previous boundary cell ($cell_{i+1\ j+1}$). The initial phase, the phase for cell i=65, j=105 is equal to 90° as the model 3DD calculates the water level using Equation 6.2:

$$\zeta = h + A\cos\left(\frac{2\pi t}{T} - \phi\right) \qquad \textbf{6.2}$$

where ζ is the water level, h is the mean sea level (1.425 m above Chart datum), A is the amplitude of the wave (0.5 m), t is the model time (s), T is the wave period (s) and ϕ is the phase.

6.3 TELETSUNAMI SIMULATION FOR 5 WAVE PERIODS

Teletsunami simulations were undertaken for five scenarios, each involving five different wave periods typical of tsunamis: 10 minutes, 15 minutes, 20 minutes, 25 minutes, and 30 minutes. All scenarios applied a 0.5 m amplitude (1 m high) wave as a sea level forcing mechanism on the northern and eastern (open ocean) model grid boundaries. This amplitude was selected as it is of a similar magnitude[6] to oscillations observed in the Hauraki Gulf during the 1960 Chilean tsunami, the most extensive tsunami this century (de Lange, 1983).

For all scenarios, the model was run with a fifteen second time step, for a total number of time steps equivalent to 10 wave cycles. The results were stored at a frequency that ensured 20 data points per cycle. From the resulting data, time series data of water

[6] Fluctuations exceeding 0.6m were recorded in the Waitemata Hr. during the 1960 Chilean tsunami.

elevation were extracted from twenty four sites primarily located in the Firth of Thames (Figure 6.2, Table 6.2).

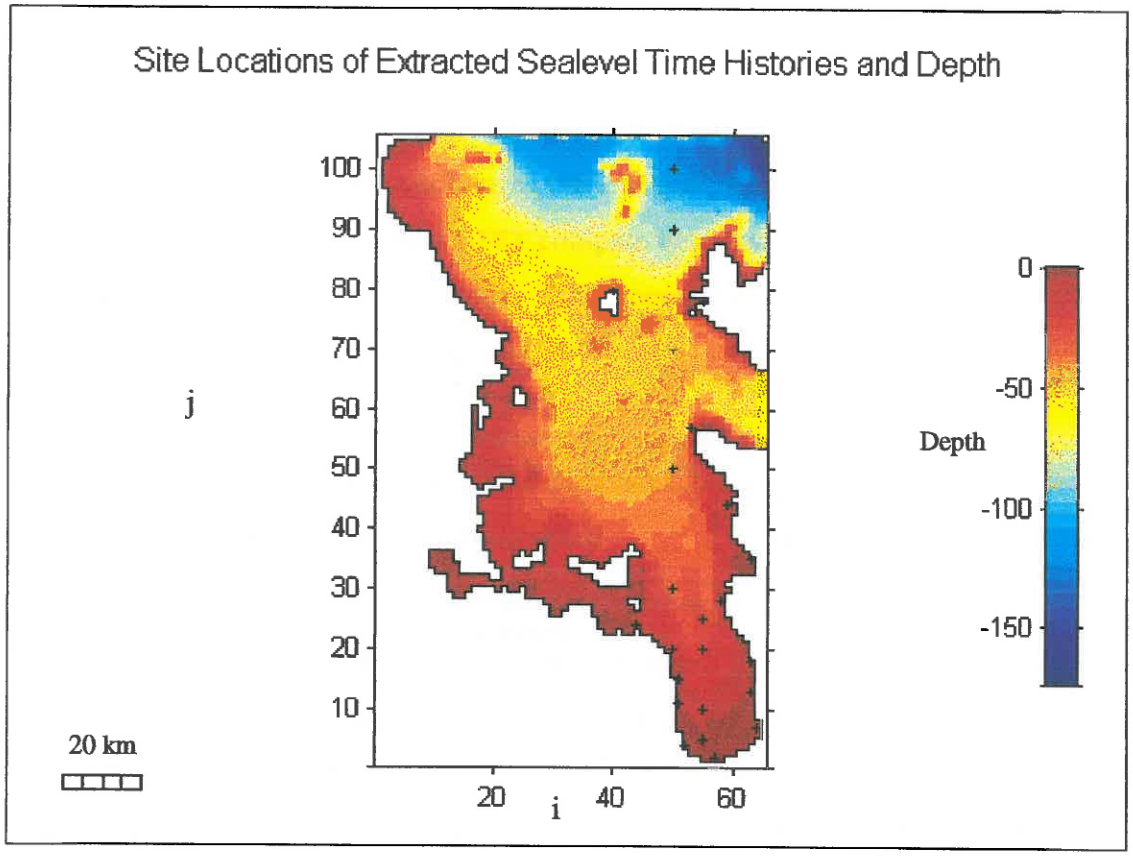

Figure 6.2: Figure illustrating the location of the sites for which sea level time histories were extracted, indicated by '+'. The sites focus primarily on the Firth of Thames. The background represents the depth of bathmetry employed for '3DD' simulations.

Amplitude attenuation/gain was determined for all extracted locations, for all periods, by measuring the maximum amplitude observed at any location (Refer to Table 6.3 and Appendix 11). Amplitude attenuation/gain was calculated by comparison with the wave amplitude at the model boundary (Equation 6.3).

$$A_a = A_x/A_B \qquad 6.3$$

where A_a is the amplitude attenuation/gain, A_x is the amplitude at location x, some location in the Hauraki Gulf, and A_B is the average amplitude at the model boundary. As amplitude attenuation was determined by comparison with wave amplitude at the model boundary, amplitude attenuation/gain reflects changes occurring in response to (i) shoaling across the continental shelf, and (ii) any other anomalous effects specific to location e.g. wave focusing.

6.4 RESULTS AND DISCUSSION

Firstly, the results of the above teletsunami simulations were compared against historical observations recorded during the 1960 Chilean tsunami. This enabled an assessment of the accuracy of wave height predictions made by model '3DD'.

Within the region covered by the model grid, there are 3 historical observations recorded (Refer to Table 6.1; de Lange, 1983; Fraser, 1998). Table 6.1 illustrates the wave heights predicted by model '3DD' compare very favourably with observed wave heights[7]. This suggests that the model '3DD' accurately simulated propagation of the 1960 Chilean tsunami into the Hauraki Gulf.

Table 6.1: Comparison of wave heights observed during the 1960 Chilean tsunami and those predicted by the model '3DD' (* Fraser, 1998; ✦ de Lange, 1983).

Location	Cell No.	Observation	Observed Wave Height (m)	Predicted Wave Height (m)
Great Barrier Is.	55, 85, 1	*1.5 m high waves recorded at Great Barrier Island.	1.5	1.70
Leigh	22, 71, 1	✦1.2 m surge washed away bridge supports.	2.4	2.44
Waitemata Hr.	20, 31, 1	✦Fluctuations exceeding 0.6 m recorded in the Waitemata Hr.	> 0.6	0.76

Following this, sea level elevation time series for 24 locations, were extracted from the results produced during the above five teletsunami simulations (Refer to Figure 6.2). This allowed the maximum predicted sea level elevation (relative to mean sea level) and amplitude attenuation/gain to be determined for each site (Tables 6.1 and 6.2).

6.4.1 Maximum Predicted Sea level Elevations

The results presented in Table 6.2 indicate the following:

1. For all locations except at Colville Bay, Little Barrier Island and Port Fitzroy, Great Barrier Island, the maximum rise above mean sea level occurs for 30 minute period waves.
2. For locations in the Firth of Thames the largest predicted rise above mean sea level is in the order of 0.5 m.

[7] Note the exact locations of the historical observations were not recorded which prevented comparison of wave heights at the exact same locations.

3. Within the Firth of Thames, Tapu shows the largest predicted rise above mean sea level. For 25 and 30 minute waves, the wave heights predicted at Tapu are higher than all other Firth of Thames sites.
4. At 30 minute periods, the maximum rise above mean sea level for sites in the Firth of Thames are of similar magnitude to sites much closer to the northern and eastern grid boundaries where sea level forcing occurs.
5. During 10 minute period waves, the maximum predicted sea level elevation is consistently below mean sea level.
6. For all wave periods, Port Fitzroy on Great Barrier Island, the maximum predicted sea level elevation is consistently below mean sea level.
7. For all wave periods investigated here, the maximum rise above mean sea level in the Firth of Thames, is less than that generated by displacement along the Kerepehi Fault (Refer to Chapter 5).

Table 6.2: Summary of maximum predicted water elevation (relative to mean sea level) for all locations with extracted sea level time history data.

Location		WAVE PERIOD (minutes)				
		10	15	20	25	30
	Cell No. (x, y, z)	Maximum Water Elevation above Mean Sea Level (m)				
Miranda	52, 4, 1	-0.053	0.053	0.322	0.122	0.467
Thames	64, 7, 1	-0.055	0.072	0.281	0.139	0.422
Base of Firth of Thames	57, 2, 1	-0.054	0.097	0.272	0.138	0.456
Tapu	63, 18, 1	-0.001	0.052	0.231	0.164	0.488
Te Puru	63, 13, 1	-0.014	0.083	0.232	0.107	0.389
Deadmans Pt.	58, 28, 1	0.021	0.050	0.141	0.093	0.264
Whakatiwai	51, 11, 1	-0.031	0.054	0.306	0.085	0.469
Waihihi Bay	51, 15, 1	-0.017	0.063	0.216	0.078	0.399
Waimangu Pt.	50, 20, 1	0.003	0.048	0.149	0.096	0.363
Ruakura Pt.	44, 24, 1	-0.004	0.119	0.173	0.086	0.228
Coromandel Hr.	63, 35, 1	0.033	0.067	0.137	0.264	0.414
Colville Bay	59, 44, 1	0.044	0.184	0.324	0.228	0.254
N. tip of Coromandel Peninsula	53, 57, 1	0.104	0.280	0.293	0.360	0.450
Port Fiztroy, Great Barrier Is.	55, 78, 1	-0.054	0.014	-0.040	-0.023	-0.195
Little Barrier Is.	40, 80, 1	0.398	0.731	0.358	1.042	0.541
cell 55, 5, 1	55, 5, 1	-0.054	0.070	0.266	0.105	0.363
cell 55, 10, 1	55, 10, 1	-0.032	0.047	0.227	0.085	0.323
cell 55, 20, 1	55, 20, 1	0.001	0.054	0.148	0.077	0.238
cell 55, 25, 1	55, 25, 1	0.014	0.058	0.157	0.080	0.223
cell 50, 30, 1	50, 30, 1	0.022	0.105	0.137	0.079	0.220
cell 50, 50, 1	50, 50, 1	0.046	0.157	0.173	0.176	0.215
cell 50, 70, 1	50, 70, 1	0.150	0.147	0.281	0.243	0.522
cell 50, 90, 1	50, 90, 1	0.146	0.231	0.286	0.439	0.440
cell 50, 100, 1	50, 100, 1	0.301	0.278	0.315	0.439	0.451

6.4.2 Amplitude Attenuation Graphs

Table 6.3 and amplitude attenuation graphs produced from extracted sea level time history data indicate two general patterns: (i) wave amplitude becomes more attenuated (smaller values in Table 6.3) with decreasing period, and (ii) amplitude becomes more attenuated with increasing distance from sea level forcing boundaries. However, some locations have amplitudes that deviate from the above trends.

Sites located on the western margin and at the base of the Firth of Thames (e.g. Whakatiwi, Waihihi Bay, Miranda, Thames) illustrate comparatively large amplitudes at 20 minute wave periods. The enhancement of wave amplitude observed for 20 minute period waves may be due to an amplified seiche. This can occur if the tsunami wave is periodic and in phase with the natural free oscillating frequency of the embayment (de Lange, 1988). This possibility was investigated using Merians formula (Equation 6.4) which defines the fundamental frequency of a basin.

$$f_0 = \frac{(gh)^{\frac{1}{2}}}{4B} \qquad \textbf{6.4}$$

where f_0 = fundamental frequency of a basin, g = acceleration due to gravity, h = water depth, and B = length of basin.

Applying the dimensions of the Firth of Thames to the above formula gives a f_0 of $6.92 \times 10_{-5}$ Hz or a period of 14 448 seconds (4 hours). Consequently, the tsunami wave period and the natural free oscillating frequency of the Firth of Thames can not be synchronous, hence the comparatively high sea level elevations observed in the Firth of Thames for 20 minute wave periods is not due an amplified seiche.

Also some locations outside of the Firth of Thames illustrate enhanced amplitudes at 15 minute period and reduced amplitudes at 30 minute periods (e.g. Ruakura Point, Little Barrier Island, cell 50, 50, 1.). There appear to be no apparent trend to these observations.

The above anomalies may be an artifact of the model resulting from the coarse grid size (Refer to end of Section 6.4.2).

Wave amplitude attenuation/ gain does not decrease with increasing distance from source for the following situations:

1. Closer investigation of wave amplitude/gain values from cell 50, 100, 1 (near open ocean boundary) to cell 55,5,1 (at base of Firth of Thames) reveals that for higher wave periods (20, 25, and 30 minute periods), wave amplitude attenuation/gain decreases with increasing distance from the source, until the Firth of Thames is reached, at which point amplitude attenuation/gain begins to increase with increasing distance. The trend of increasing wave amplitude with distance up the Firth of Thames could be attributed to waves shoaling as they approach shallower water. However, along the sides of the Firth of Thames the wave height also increases even though there is no associated shallowing of the water depth. Another possibility is that the confined area of the Firth of Thames is causing focusing of wave energy due to lateral reflections, which resulted in an increase in wave amplitude. This trend is most pronounced at longer wave periods and is also evident in the Coromandel Harbour.

   Pronounced amplitude reinforcement has been observed in the Firth of Thames during propagation of other long period waves, such as storm surge (~3 hour wave period) and M_2 tides (12.42 hour wave period). Tide gauge measurements indicate the water level difference across the Hauraki Gulf is 0.6 m for high tide and 0.4 m for low tide, with the largest tidal amplitudes being observed in the Firth of Thames (Black et al., 1995).

2. Although approximately the same distance from the sea level forcing boundaries, Little Barrier Island and Port Fitzroy have amplitude attenuation/gain values at extreme ends of the values presented in Table 6.3. Irrespective of wave period, Port Fitzroy acts to attenuate wave amplitude as all predicted amplitudes are less than 1% of the 0.5 m amplitude employed at the northern and eastern boundaries. In contrast to this, Little Barrier Island show limited attenuation and for some periods (15 and 25 minutes) significant amplitude gain.

Despite the agreement between observed and predicted wave heights, the above results should be regarded with caution, particularly for short period waves where the wavelength in shallow water is equitable to the model grid spacing (1500 m). Usually it is recommended that at least four grid points per wavelength are required to accurately model wave propagation. This recommendation is not satisfied for water depths less than: 1.1 m for 30 minute wave periods, 1.6 m for 25 minute wave periods, 2.5 m for 20 minute wave periods, 4.5 m for 15 minute wave periods, and 10.2 m for 10 minute period waves. This may partially explain the variability and lack of trend observed in wave height predictions for short period waves.

Table 6.3: Summary of amplitude attenuation/gain (as a proportion of wave amplitude at the model boundary) for all locations with extracted sea level time history data. Amplitude attenuation/gain was calculated by dividing the maximum wave amplitude at each location by the wave amplitude at the model open ocean boundary (i.e. by 0.5 m).

Location		WAVE PERIOD				
		600 s	900 s	1200 s	1500 s	1800 s
	Cell No. (x, y, z)	Amplitude Attenuation for Maximum Observed Peak				
Miranda	52, 4, 1	0.01	0.11	0.31	0.27	0.49
Thames	64, 7, 1	0.015	0.12	0.35	0.33	0.51
Base of Firth of Thames	57, 2, 1	0.012	0.16	0.42	0.38	0.68
Tapu	63, 18, 1	0.065	0.09	0.14	0.29	0.68
Te Puru	63, 13, 1	0.05	0.09	0.11	0.22	0.45
Deadmans Pt.	58, 28, 1	0.08	0.08	0.11	0.18	0.36
Whakatiwai	51, 11, 1	0.03	0.05	0.18	0.17	0.56
Waihihi Bay	51, 15, 1	0.02	0.08	0.17	0.12	0.41
Waimangu Pt.	50, 20, 1	0.02	0.06	0.13	0.28	0.47
Ruakura Pt.	44, 24, 1	0.02	0.21	0.11	0.23	0.17
Coromandel Harbour	63, 35, 1	0.05	0.13	0.19	0.45	0.6
Colville Bay	59, 44, 1	0.06	0.31	0.42	0.51	0.34
N. tip of Coromandel Peninsula	53, 57, 1	0.16	0.49	0.55	0.69	0.77
Port Fiztroy, Great Barrier Is.	55, 78, 1	0.001	0.004	0.007	0.003	0.003
Little Barrier Is.	40, 80, 1	0.77	1.44	0.62	1.98	0.94
cell 55, 5, 1	55, 5, 1	0.009	0.13	0.38	0.21	0.51
cell 55, 10, 1	55, 10, 1	0.03	0.09	0.1	0.14	0.29
cell 55, 20, 1	55, 20, 1	0.018	0.07	0.06	0.12	0.27
cell 55, 25, 1	55, 25, 1	0.02	0.08	0.11	0.12	0.23
cell 50, 30, 1	50, 30, 1	0.02	0.16	0.12	0.18	0.25
cell 50, 50, 1	50, 50, 1	0.04	0.33	0.25	0.37	0.34
cell 50, 70, 1	50, 70, 1	0.27	0.23	0.49	0.49	0.88
cell 50, 90, 1	50, 90, 1	0.31	0.47	0.55	0.87	0.9
cell 50, 100, 1	50, 100, 1	0.58	0.56	0.62	0.87	0.91

6.5 SUMMARY

The maximum sea level elevation and amplitude attenuation/gain calculated from sea level time histories extracted from 24 locations indicate:

1. Generally, the maximum rise in sea level elevation and amplitude attenuation/gain decrease with: (i) increasing distance from open ocean boundaries, and (ii) decreasing wave period. Some locations have predicted wave amplitudes that deviate from this trend, for example Little Barrier Island and Port Fitzroy.
2. For locations situated on the western margin and at the base of the Firth of Thames, 20 minute period waves produce larger amplitudes than waves of 25 minute period, causing a deviation from the above trend.
3. The confined nature of the Firth of Thames embayment acts to focus wave energy resulting in increased wave amplitudes. This is consistent with historical data, which indicate amplitude reinforcement has been observed in the Firth of Thames for other long period waves e.g. M2 tides. The maximum predicted amplitude increase as a result of wave focussing by the Firth of Thames is in the order of 0.25 m (30 min wave period, comparing Tapu and Ruakura Pt). This represents 50% of the amplitude at the open ocean boundary and is therefore considered significant. For the longest simulated wave period (30 min.), townships adjacent to the Firth of Thames all have maximum predicted rise above mean sea level between 0.36 and 0.49 m. The largest of these, 0.49 m, is observed at Tapu.
4. Within the Firth of Thames and for all wave periods investigated here (10-30 minute period), the maximum rise above mean sea level caused by a teletsunami of similar magnitude to 1960 Chilean tsunami, the most extensive tsunami this century, is less than that generated by displacement along the Kerepehi Fault (Refer to Chapter 5). Hence it is suggested that a teletsunami of this magnitude, represents a less significant hazard than tsunamis locally generated along the Kerepehi Fault.

Despite the agreement between observed and predicted wave heights, the above results should be regarded with caution: in shallow water the wavelength associated with short period waves is small and hence there are less than the recommended number of grid cells per wavelength. Consequently, wave propagation in very shallow water may not be well represented by this grid cell size (1500 m).

6.6 REFERENCES

Black, K.P., 1995. *The numerical model 3DD and support software*, Occasional Report No.19, Department of Earth Science, University of Waikato, New Zealand.

Black, K.P., Oldman, J.W., and Bell, R.G., 1996. *Numerical Hydrodynami and Thermodynamic Modelling of Nearshore Offshore Exchange Processes*, NIWA Internal Report NOD602/1, pp. 18-20.

Camfield, F.E., 1980. *Tsunami engineering*, U.S. Army Coastal Engineering Research Center Special Report No. 6., 222 p.

de Lange, W.P., 1983. *Tsunami Hazard.* M.Sc. Thesis, University of Waikato, 250 p.

de Lange, W.P., 1988. *Wave Climate and Sediment Transport within Tauranga Harbour, in the Vicinity of Pilot Bay.* Ph.D. Thesis, University of Waikato, p. 6.1-6.7.

Fraser, R.J., 1998. *Historical Tsunami Database for New Zealand.* M.Sc. Thesis, University of Waikato, p. 58.

Proctor, R. and Greig, M.J.N., 1989. A numerical model investigation of the residual circulation in the Hauraki Gulf, New Zealand. *New Zealand Journal of Marine and Freshwater Research*, Vol., 23, pp. 421-442.

Chapter 7

NUMERICAL MODELLING OF TSUNAMI INUNDATION

7.1 INTRODUCTION

The township of Thames is the home of around 6 800 people. Approximately 2500 of these people live in Moanataiare (Statistics New Zealand, 1997), a low-lying region adjacent to the Firth of Thames coastline, which is frequently inundated by storm surges (e.g. 14 July 1995, 31 December 1996) and has the potential to be inundated by tsunamis. Historic inundation events have resulted in millions of dollars of damage to the community. For example the 14 July 1995 storm surge reached 2.5 m above mean sea level and caused $3-4 million worth of damage (de Lange, 1996). Tsunami inundation is associated with high current velocities as well as elevated water levels and consequently has the potential to cause significantly more damage than that generated during storm surge inundation. Inundation maps can help to mitigate the risk associated with tsunami inundation by aiding regional planners.

The results of tsunami generation and propagation simulations undertaken using 'TSUNAMI' indicate wave height maximums at Thames are small, being of the order of 0.6 m (corrected vertical displacement, increased time step and 5.8 km surface rupture width). However, comparison with predictions made by Equation 5.1-5.3 and the hydrodynamic circulation model '3DD' suggest the 'TSUNAMI' model is under predicting maximum wave height for simulations involving tsunami generation in very shallow water, (displacement along Segments A, B, and C, Refer to Chapters 4 and 5). Accounting for this and the potential that: (i) future displacement magnitudes could be larger than those predicted here; and (ii) the effect of displacement in soft sediments and non-linear effects not modelled by 'TSUNAMI', may generate significantly larger wave heights, Thames is considered the region with the greatest potential for damage to property, and loss of life.

In this chapter potential tsunami inundation is modelled using the 'TUNAMI N2' finite difference model (Refer to Appendix 12), with the aim of generating an inundation

map for the Thames region (Figure 7.1). The results are presented in the form of inundation maps and inundation time history figures, for user selected regions. These results and the limitations of the 'TUNAMI N2' model are then discussed and conclusions regarding tsunami inundation risk are made.

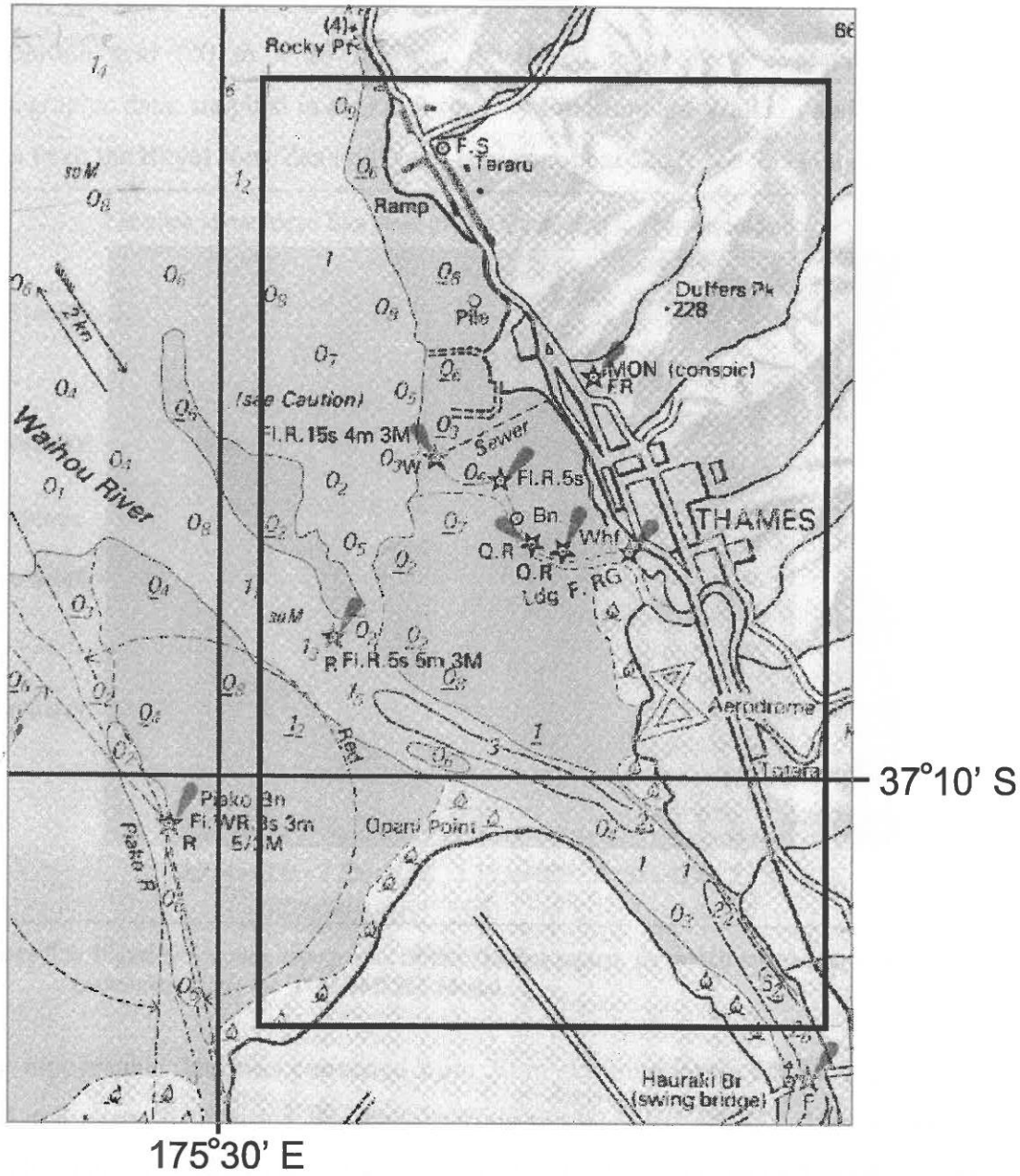

Figure 7.1: Extract from the Royal New Zealand Navy Hydrographic Chart NZ533 illustrating the region inundation modelling was undertaken for (Black Box).

7.2 MODEL SET-UP

7.2.1 Finite Difference Grid

The finite difference grid used for inundation simulations undertaken with the 'TUNAMI N2' model, encompasses the coastline adjacent to Thames, extending from 175°30'18.8"E, 37°06'28.2"S to 175°33'51.8"E, 37°11'15.4"S (NZ Geodetic Datum 1949), (2733000E 6452000N to 2738000E 6443000N (NZ Map Grid Series, T12)). This high resolution grid (20 m x 20 m) was developed using New Zealand Map Grid topographic data, supplied in digital format by Environment Waikato and bathymetric data from the Royal New Zealand Navy Hydrographic Chart NZ 533 (Figure 7.2).

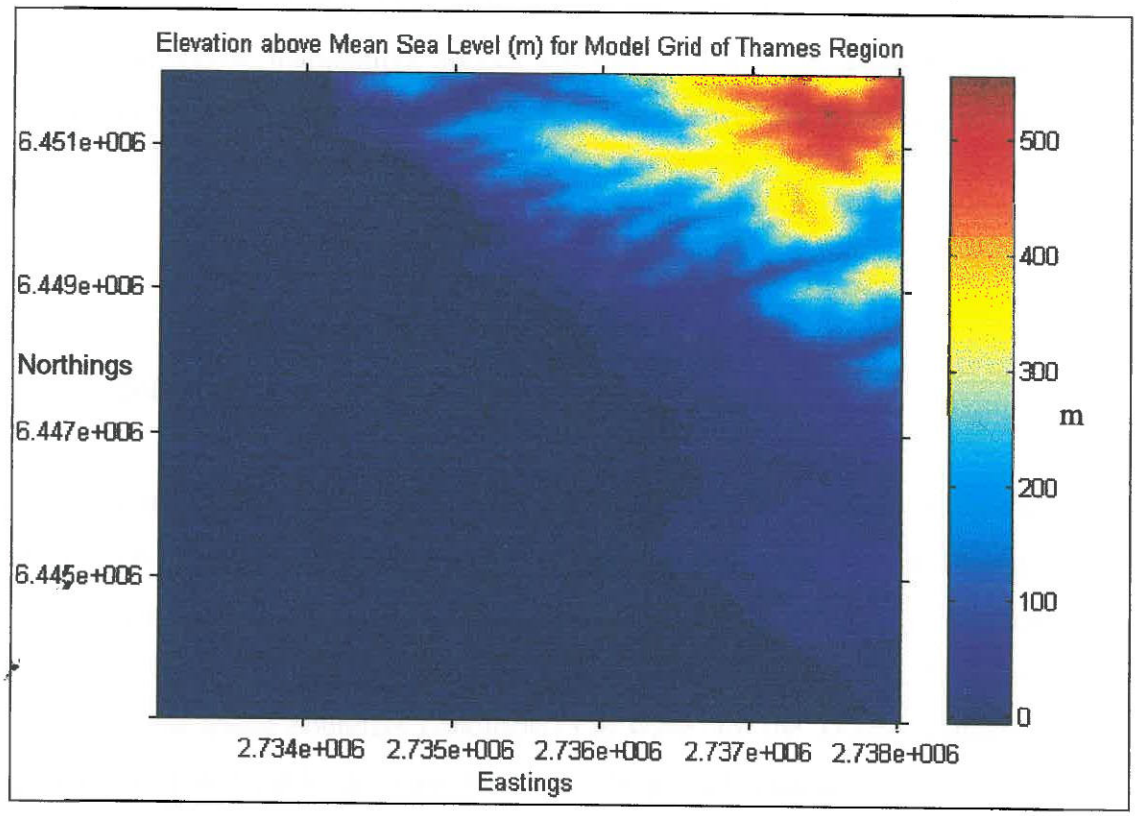

Figure 7.2: Figure illustrating topography of the Thames region, for which inundation modelling was undertaken using the 'TUNAMI N2' Model.

The topographic data was converted from 20 m contours into a 251*451 grid with 1 grid cell every 20 m using the digital terrain model 'ARC INFO'. The bathymetric data for a given 20 m by 20 m grid cell was obtained by digitising bathymetric heights from the Hydrographic Chart NZ 533, converting the digitised data to make it relative to mean sea level, and linearly interpolating between the digitised data using the krigging function on the 'SURFER' program.

7.2.2 Boundary Conditions

Initially it was intended that the results of the tsunami generation and propagation modelling, undertaken using 'TSUNAMI', be used as the boundary condition for the inundation modelling. However, the wave heights simulating during the tsunami generation and propagation modelling are clearly not large enough to cause inundation in the Thames region (Refer to Chapter 5). However, given the uncertainties associated with employing the deep water generation model, 'TSUNAMI' in shallow water (the Firth of Thames), tsunami inundation modelling was implemented using a significantly larger wave (3 m amplitude) as the initial boundary condition. The 3 m amplitude (ten minute period) wave is an arbitrary choice that is large enough to cause inundation whilst maintaining model stability[8]. The 3 m amplitude wave was employed as a sea level forcing mechanism on the western boundary of the model grid.

7.3 INUNDATION SCENARIOS

Tsunami inundation was simulated for two scenarios: (i) Scenario 1 simulated the inundation caused by the above boundary condition (3 m wave) for the Thames region *without* the presence of any protection structures. Sea level forcing continued until 1800 s or for approximately 3 wave cycles; (ii) Scenario 2 simulated the inundation caused by the above boundary condition (3 m wave) for the Thames region with the protection of stop banks at some locations. Stop bank protection was simulated by including an additional boundary file stipulating locations where a 3.5 m vertical seawall should be emplaced. Seawalls were emplaced along the shoreline south of the Kauaeranga River mouth as consistent with stop bank locations presented on Map NZMS 260 T12. Sea level forcing continued for 3 wave cycles (1800 s).

[8] Modelling attempts for larger waves (5 m amplitude) were made but these generated steep shoreline gradients, creating instabilities in the 'TUNAMI N2' model, causing an overflow error to occur.

7.4 RESULTS

The 'TUNAMI N2' model outputs inundation modelling results in two forms: (i) maximum water elevation (above mean sea level), predicted at any time during the simulation, for all model grid cells, and (ii) inundation height time histories at user specified locations.

7.4.1 Scenario 1 – Without Seawall Protection

Inundation Map

The following inundation map (Figure 7.3 and Figure 7.4) represents the maximum inundation height predicted to occur at anytime during the 12 000 s simulation, for all model grid cells. The results indicate that south of Tararu to northern Moanataiare/ Kuranui Bay is the region impacted by the most severe inundation heights. This occurs in response to wave focussing caused by wave refraction around the northern extent of the Waihou River Ebb Tide Delta (Figure 7.1).

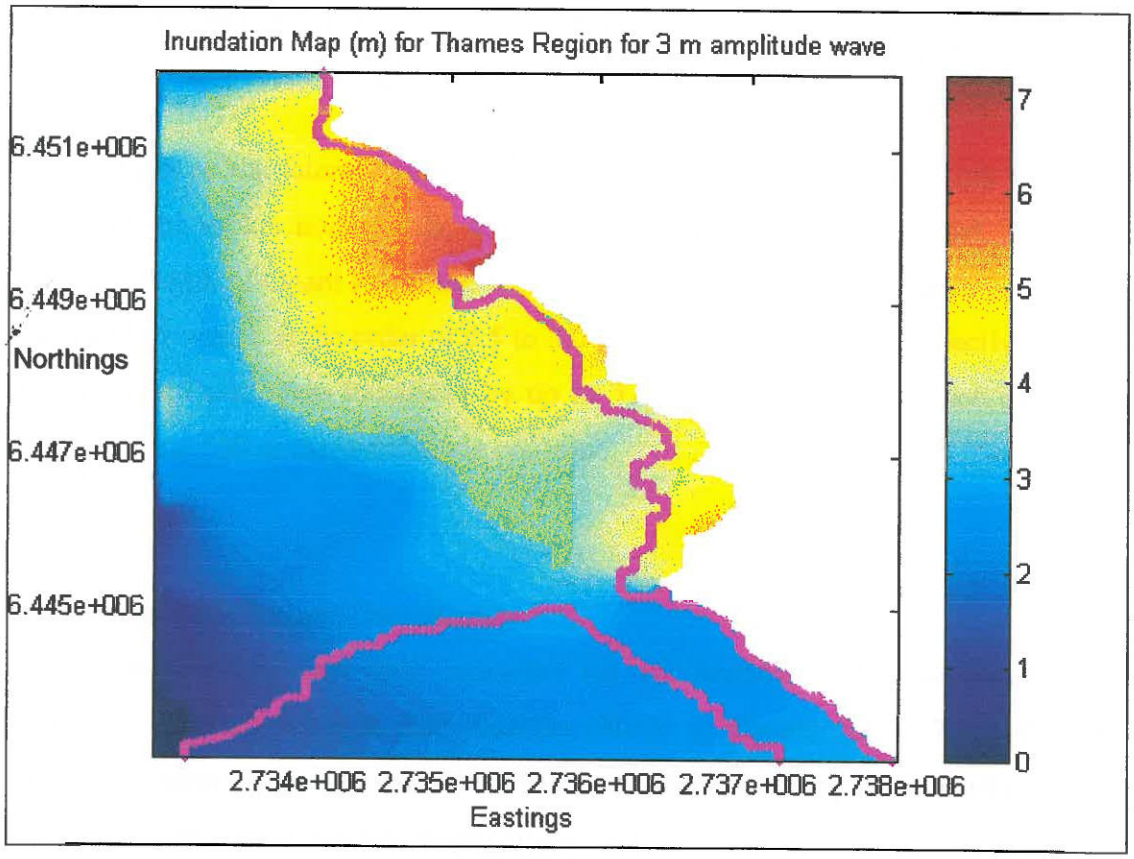

Figure 7.3: Inundation Map for the Thames region. Maximum water elevation is expressed in m above mean sea level and represents inundation levels resulting from the input of a 3 m amplitude wave at the western grid boundary. Pink stars represent the coastline.

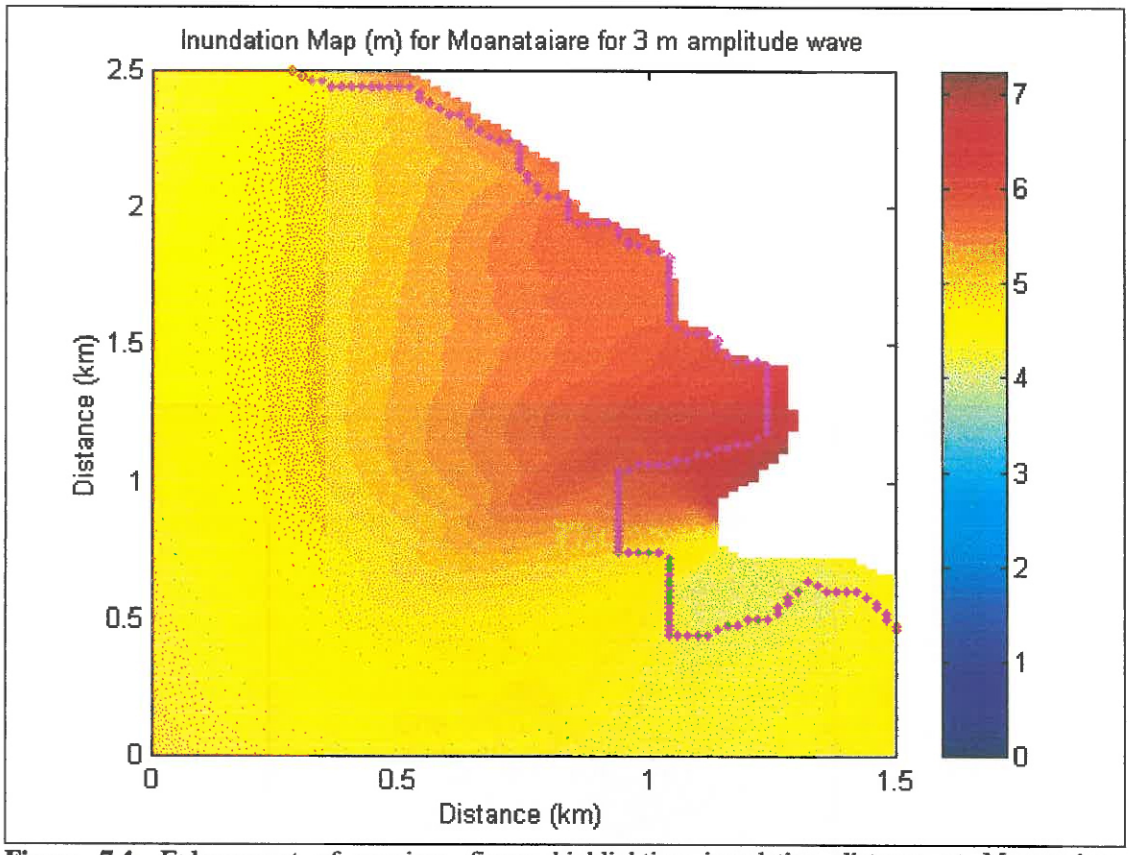

Figure 7.4: Enlargement of previous figure highlighting inundation distance at Moanataiare. Maximum water elevation is expressed in m above mean sea level and represents inundation levels resulting from the input of a 3 m amplitude wave at the western grid boundary. Pink stars represent the coastline. This enlargement is positioned at 2734000E 6451000N to 2735500E 6448500N (NZ Map Series).

With regards to the lateral extent of inundation, the low lying land south of Opani Point and the region north of the aerodrome are most severely impacted. The low lying land south of Opani Point and homes adjacent to Orango Road were completely inundated by waves in the order of 0.5 to 3.0 m. The Aerodrome and directly north of this (Rhodes Park) were inundated by up to 5 m of water for a distance extending approximately 550 m eastward of the coastline.

Inundation Wave Height Time History

Inundation time histories were extracted for 10 locations (Refer to Figure 7.5). Figures of inundation height time histories (Refer to Figures 7.6 to 7.15) illustrate inundation occurring in 3 peaks. This reflects the three, 3 m amplitude waves used for sea level forcing at the western model grid boundary.

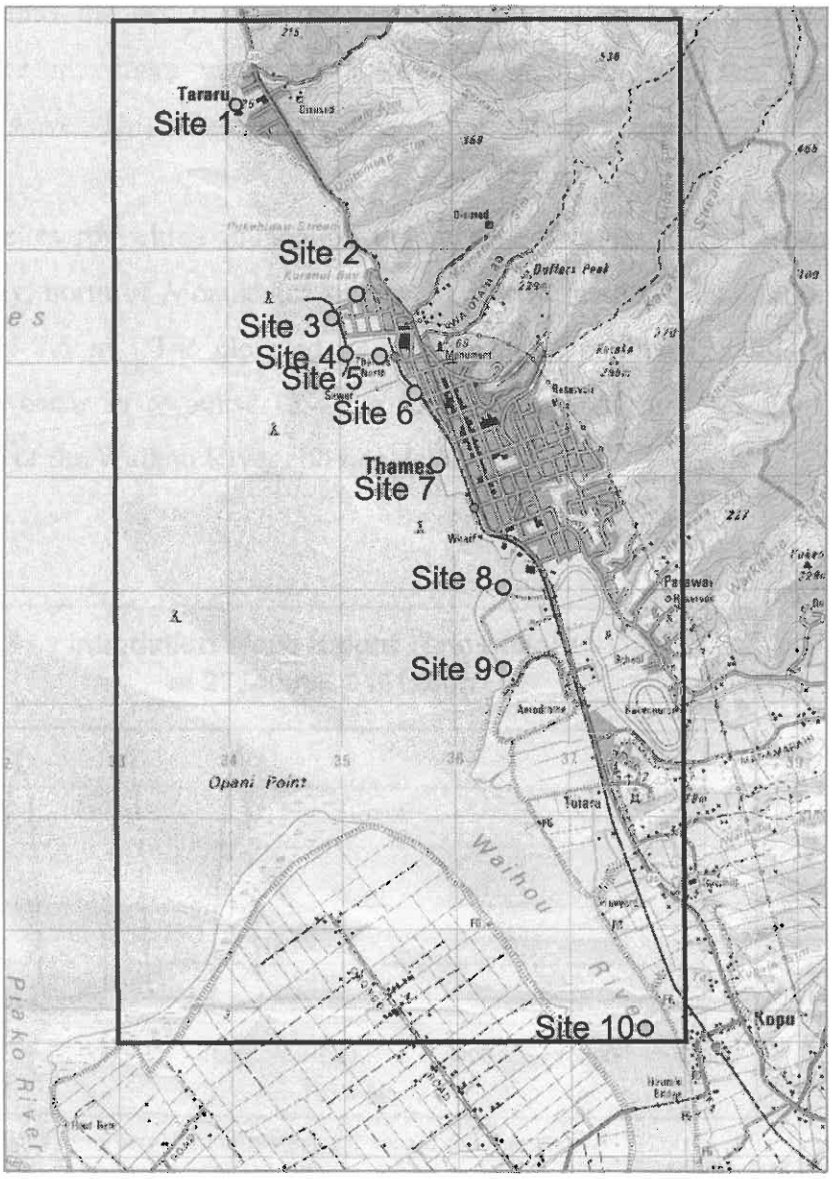

Figure 7.5: Figure illustrating locations for which Inunation wave time histories were extracted. The map background is an enlargement of Map NZMS 260 T12. The black box represents the region inundation modelling was undertaken for.

With Site 10 being the exception, all 3 peaks for a given location are of similar magnitude (within ± 8% of the maximum wave peak height). Site 10 is the located near the center of the Waihou River and represents the most southern site, being only 120 m from the southern model boundary. This site shows evidence of 3 additional peaks, lagging behind the 3 comparatively large peaks (Refer to Figure 7.15). These are believed to be an artifact of the model, generated by reflection of the previous wave peak from the southern model boundary. In addition, the narrow morphology of the river limits the decay of water level elevation occurring between subsequent peaks, hence maximum water level elevation increases with the onset of each subsequent wave. This behaviour has been reported in tidal inlets.

Of the 10 sites for which inundation height time histories were extracted, Site 2, Kuranui Bay, north of Moanataire shows the largest predicted inundation height, in the order of 7.5 m. The elevated inundation levels predicted at this location are believed to occur in response to wave focussing caused by refraction around the northern tip of the Waihou River ebb tide delta.

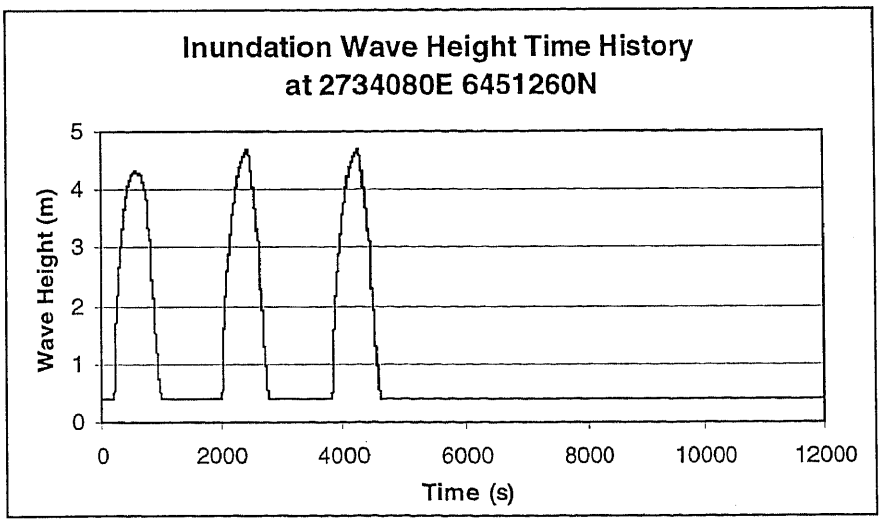

Figure 7.6: Inundation height time history for location 2734080 E 6451260 N (Site 1) resulting from three 3 metre amplitude, 10 minute period waves used for sea level forcing at the western model grid boundary.

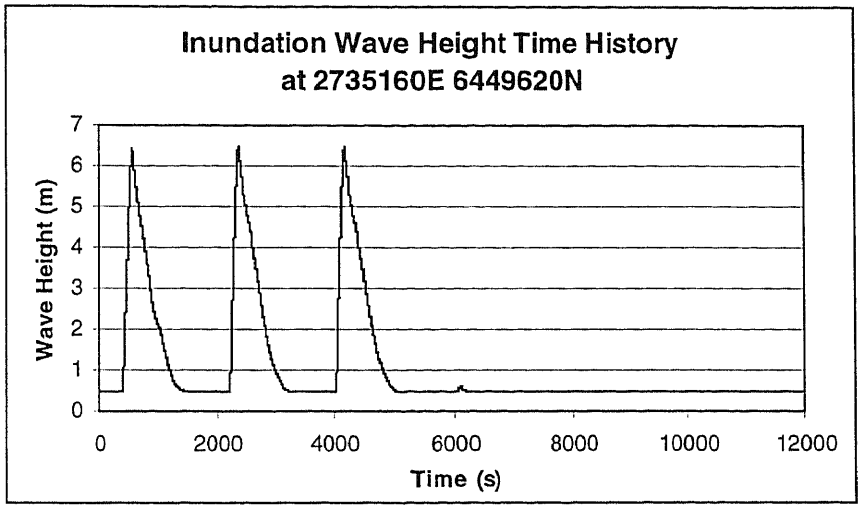

Figure 7.7: Inundation height time history for location 2735160 E 6449620 N (Site 2) resulting from three 3 metre amplitude, 10 minute period waves used for sea level forcing at the western model grid boundary.

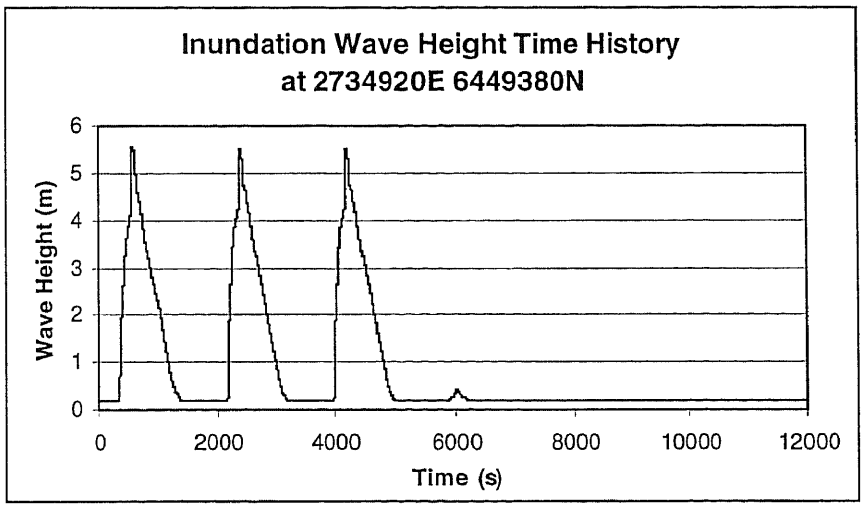

Figure 7.8: Inundation height time history for location 2734920 E 6449380 N (Site 3) resulting from three 3 metre amplitude, 10 minute period waves used for sea level forcing at the western model grid boundary.

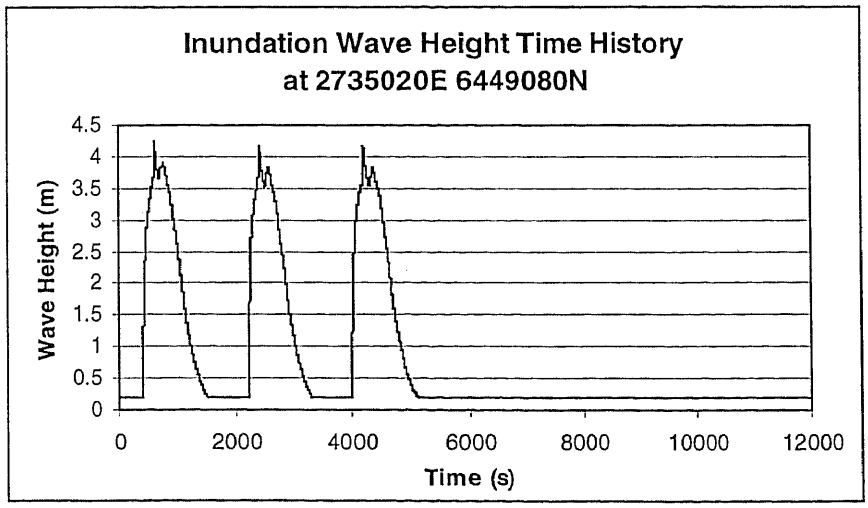

Figure 7.9: Inundation height time history for location 2735020 E 6449080 N (Site 4) resulting from three 3 metre amplitude, 10 minute period waves used for sea level forcing at the western model grid boundary.

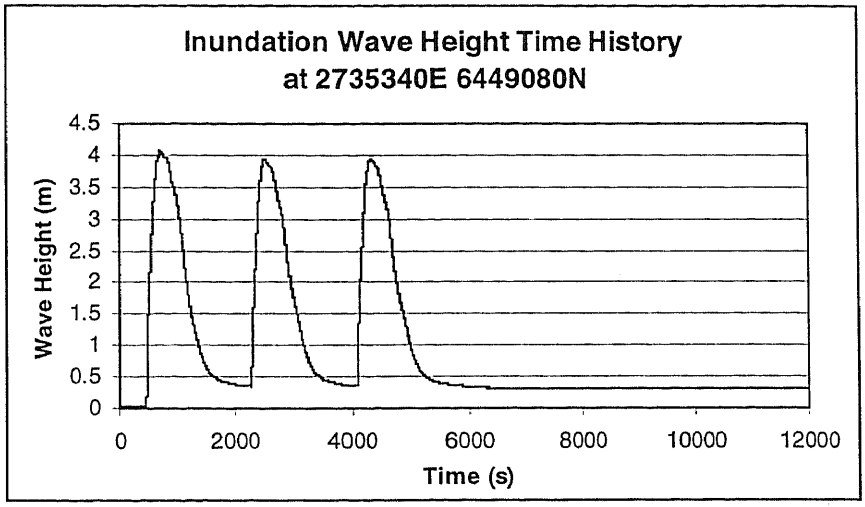

Figure 7.10: Inundation height time history for location 2735340 E 6449080 N (Site 5) resulting from three 3 metre amplitude, 10 minute period waves used for sea level forcing at the western model grid boundary.

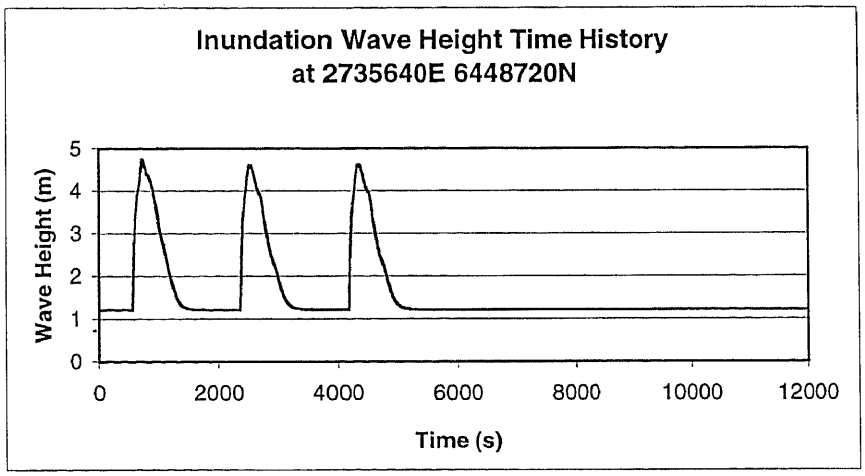

Figure 7.11: Inundation height time history for location 2735640 E 6448720 N (Site 6) resulting from three 3 metre amplitude, 10 minute period waves used for sea level forcing at the western model grid boundary.

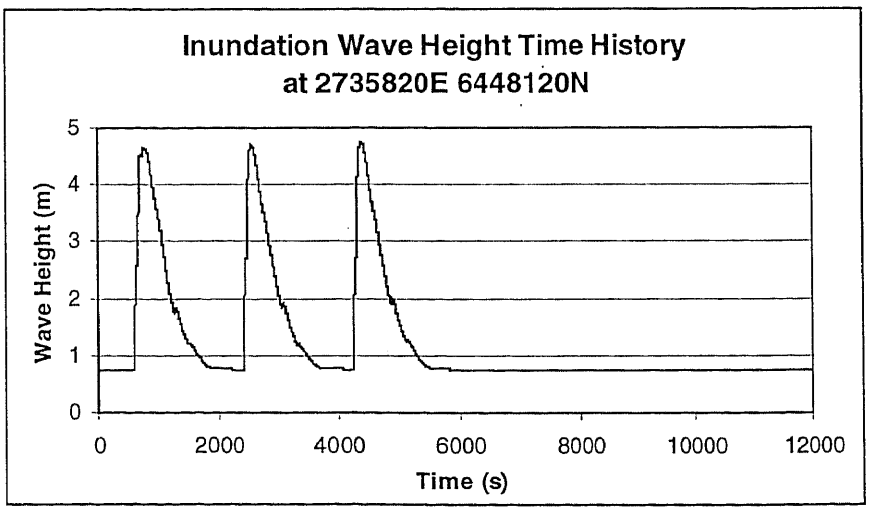

Figure 7.12: Inundation height time history for location 2735820 E 6448120 N (Site 7) resulting from three 3 metre amplitude, 10 minute period waves used for sea level forcing at the western model grid boundary.

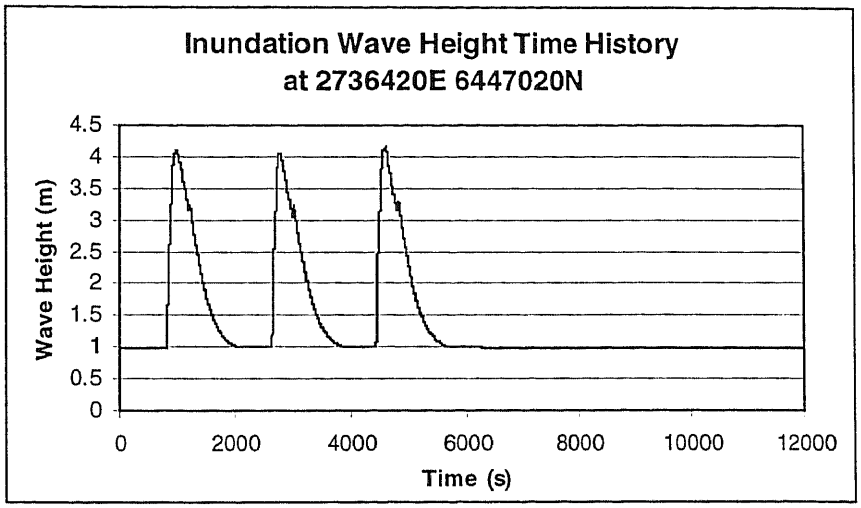

Figure 7.13: Inundation height time history for location 2736420 E 6447020 N (Site 8) resulting from three 3 metre amplitude, 10 minute period waves used for sea level forcing at the western model grid boundary.

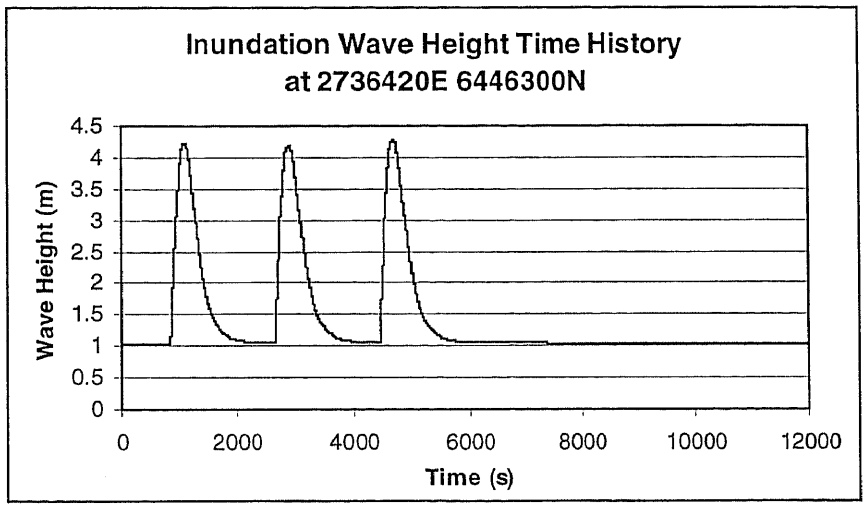

Figure 7.14: Inundation height time history for location 2736420 E 6446300 N (Site 9) resulting from three 3 metre amplitude, 10 minute period waves used for sea level forcing at the western model grid boundary.

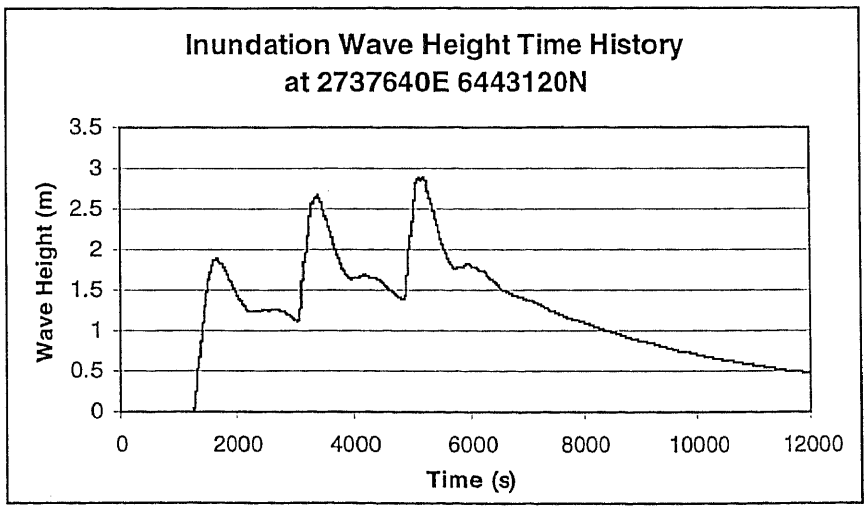

Figure 7.15: Inundation height time history for location 2737640 E 6443120 N (Site 10) resulting from three 3 metre amplitude, 10 minute period waves used for sea level forcing at the western model grid boundary.

Table 7.1: Summary of the time of maximum inundation height for the 10 locations for which inundation time histories were extracted.

Site No.	Eastings	Northings	Maximum Height (m)	Time of Max. H. (hrs, min, sec)
1	2734080	6451260	4.68	0, 40, 54
2	2735160	6449620	6.46	0, 39, 28
3	2734920	6449380	5.56	0, 9, 55
4	2735020	6449080	4.24	0, 10, 22
5	2735340	6449080	4.09	0, 12, 1
6	2735640	6448720	4.74	0, 12, 14
7	2735820	6448120	4.76	1, 12, 32
8	2736420	6447020	4.16	1, 16, 37
9	2736420	6446300	4.28	1, 18, 28
10	2737640	6443120	2.9	1, 26, 22

7.4.2 Scenario 2 – With Seawall Protection

Inundation Map

The following inundation map (Refer to Figure 7.16) represents the maximum inundation height predicted to occur at anytime during the 12 000 s simulation with protection structures, for all model grid cells. Inclusion of the seawall during Scenario 2 simulations has had no significant impact on inundation north of the Kauaeranga River mouth. The most severe inundation heights, in the order of 7 m are still experienced between Tararu and Moanataiare.

South of the Kauaeranga River mouth, in the region where 3.5 m seawalls were emplaced along the coastline, inundation heights and the distance of horizontal run-up is significantly reduced. Inundation of the low-lying land south of Opani Pt and homes in this vicinity, is limited. Maximum inundation height in this region has reduced to approximately 1 m and extends no further than 1 km in land from the seawall. Further north, in the vicinity of the Aerodrome, maximum inundation height has reduced from 5 to 4 m and extends a maximum distance of approximately 450 m eastward of the coastline.

Seawall inclusion, whilst protecting inland locations, channels water into the Waihou River, causing an approximate 1 m increase in maximum water elevation and an anticipated increase in current speed.

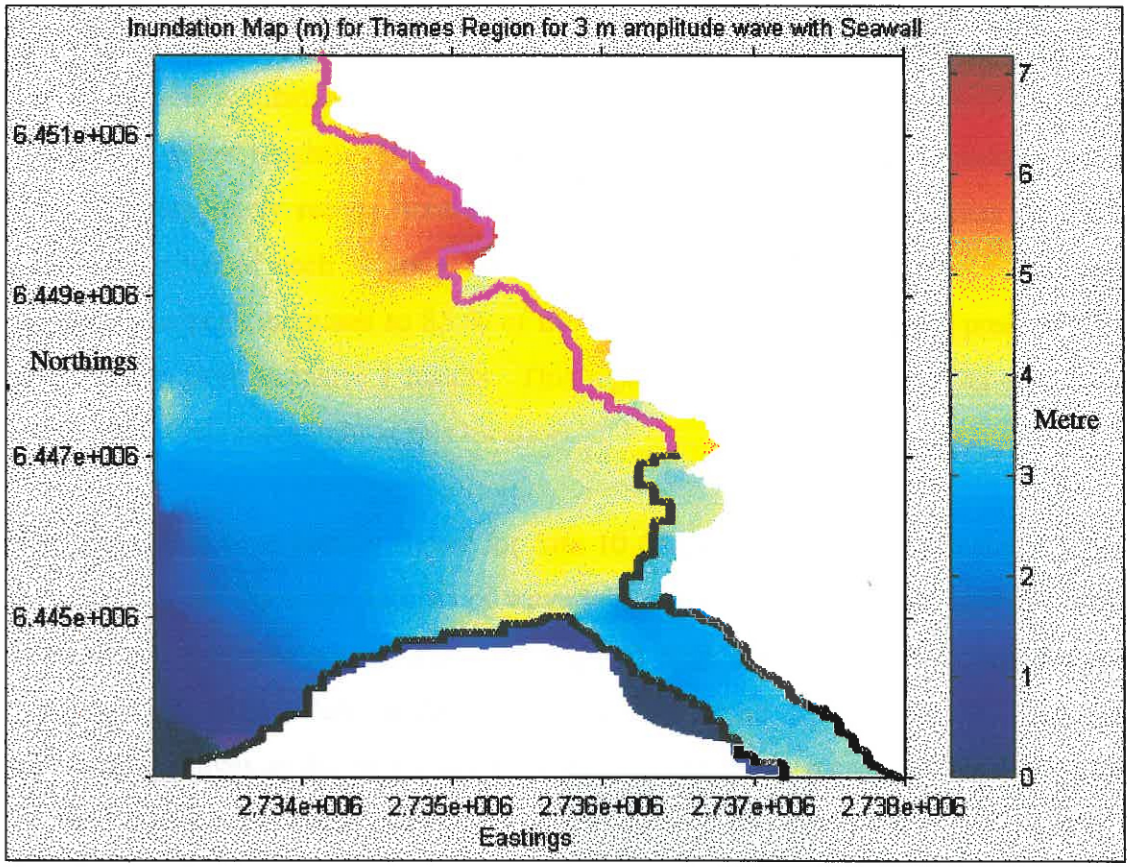

Figure 7.16: Inundation Map for the Thames region. Maximum water elevation is expressed in m above mean sea level and represents inundation levels resulting from the input of a 3 m amplitude wave at the western grid boundary. Pink stars represent the coastline. The black line represents the location of a 3.5 m stopbank.

Inundation Wave Height Time History

Inundation wave height time histories were extracted for the same 10 locations discussed in Scenario 1 results (Refer to Figure 7.5). Inclusion of the seawall during the 2nd simulation (Scenario 2) caused no significant change to predicted inundation north of the Kauaeranga River mouth, as is reflected in graphs of extracted time histories for sites 1-7 (Refer to Figures 7.17-7.23). Figures of extracted inundation time histories for locations south of the Kauaeranga River mouth (adjacent to the seawall - Figures 7.24 – 7.26) illustrate (i) wave form shapes and, (ii) maximum inundation wave heights (Refer to Table 7.2) in contrast to those predicted for the same locations, during the simulation without protection structures.

Site 8, located on the southern bank of the Kauaeranga River, illustrates a spike in the 3rd wave peak (Figure 7.24) that causes a 0.71 m increase in the maximum predicted inundation height.

Scenario 2 results for Site 9 (adjacent to the aerodrome) show the water elevation of the initial peak is substantially less than that observed during Scenario 1 (only 68 % of Scenario 1 wave height). However, in the Scenario 2 simulation, inundated water does not completely recede between peaks. Hence, wave peak elevation increases with the arrival of each ensuing wave peak, so that the elevation of the third and largest wave peak increases to 85 % of the maximum inundation height predicted for this location from Scenario 1 results. This represents a 0.6 m reduction in maximum predicted inundation height at this location.

The inundation time history figure for Site 10 (Figure 7.26), situated in the Waihou River, illustrates the same number of wave peaks as predicted from Scenario 1 results but exhibits a spikier wave form. Such spikes have been recorded during tsunami inundation of tidal inlets in Japan. These may result from interaction between consecutive waves as the first wave is unable to completely recede before inundation of the 2nd wave. A 0.66 m increase in maximum inundation height is predicted at this location.

Table 7.2 summarises the information presented in Figure 7.17 to Figure 7.26.

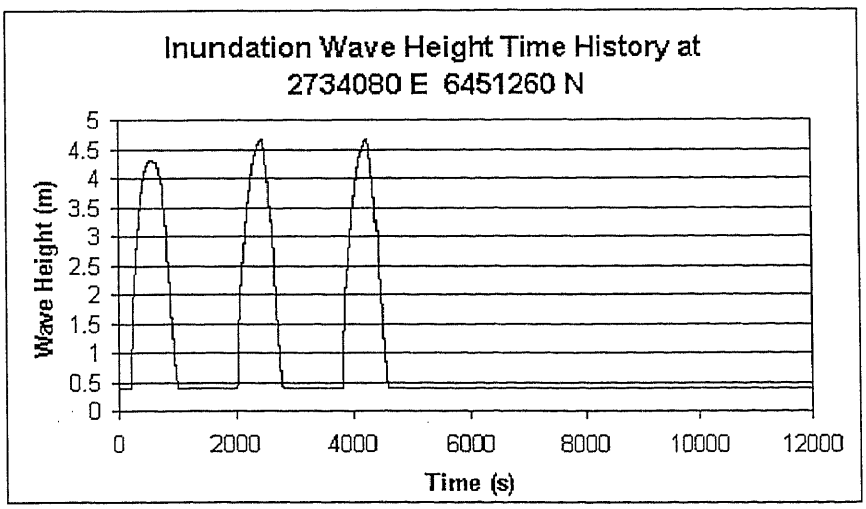

Figure 7.17: Inundation height time history for location 2734080 E 6451260 N (Site 1) resulting from three 3 metre amplitude, 10 minute period waves used for sea level forcing at the western model grid boundary for the simulation undertaken with the 3.5 m seawall.

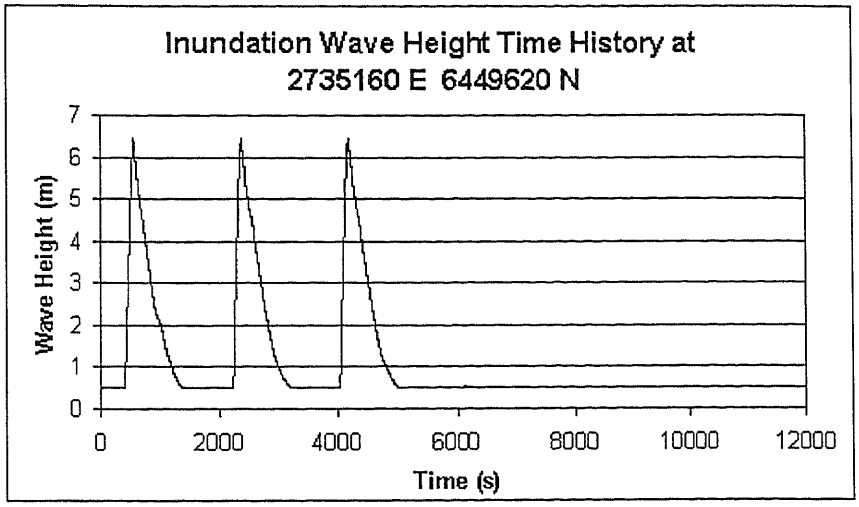

Figure 7.18: Inundation height time history for location 2735160 E 6449620 N (Site 2) resulting from three 3 metre amplitude, 10 minute period waves used for sea level forcing at the western model grid boundary for the simulation undertaken with the 3.5 m seawall.

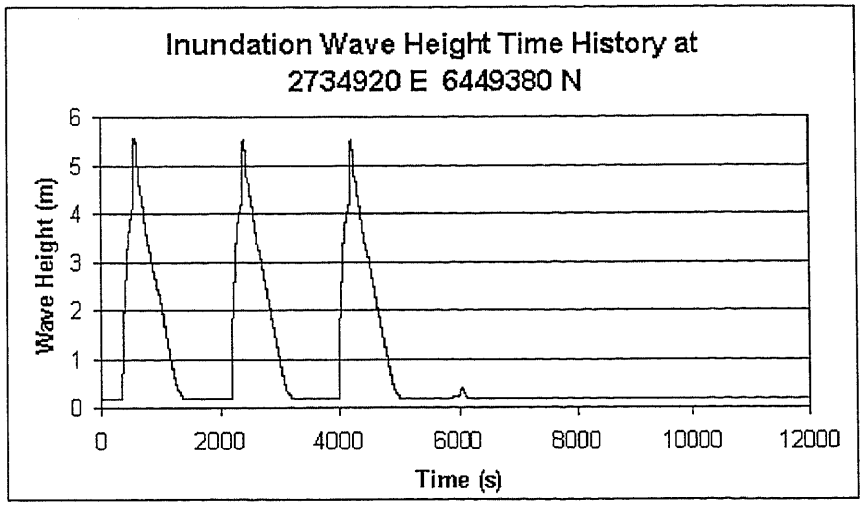

Figure 7.19: Inundation height time history for location 2734920 E 6449380 N (Site 3) resulting from three 3 metre amplitude, 10 minute period waves used for sea level forcing at the western model grid boundary for the simulation undertaken with the 3.5 m seawall.

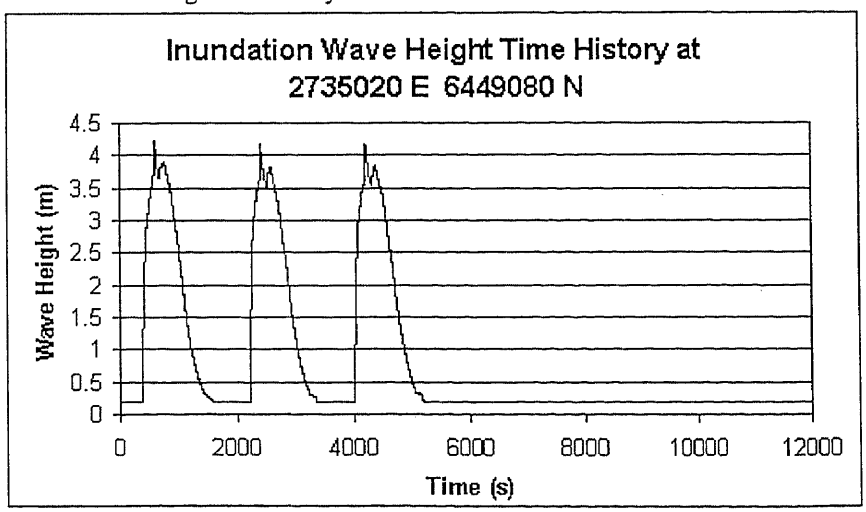

Figure 7.20: Inundation height time history for location 2735020 E 6449080 N (Site 4) resulting from three 3 metre amplitude, 10 minute period waves used for sea level forcing at the western model grid boundary for the simulation undertaken with the 3.5 m seawall.

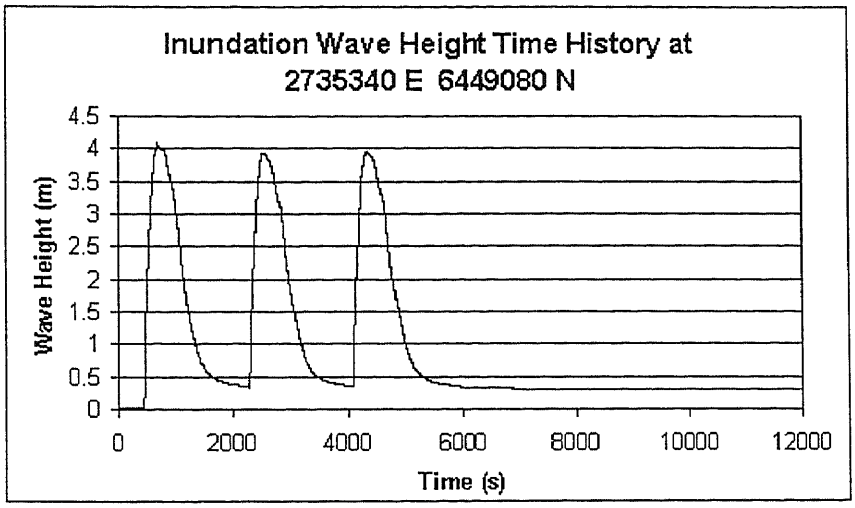

Figure 7.21: Inundation height time history for location 2735340 E 6449080 N (Site 5) resulting from three 3 metre amplitude, 10 minute period waves used for sea level forcing at the western model grid boundary for the simulation undertaken with the 3.5 m seawall.

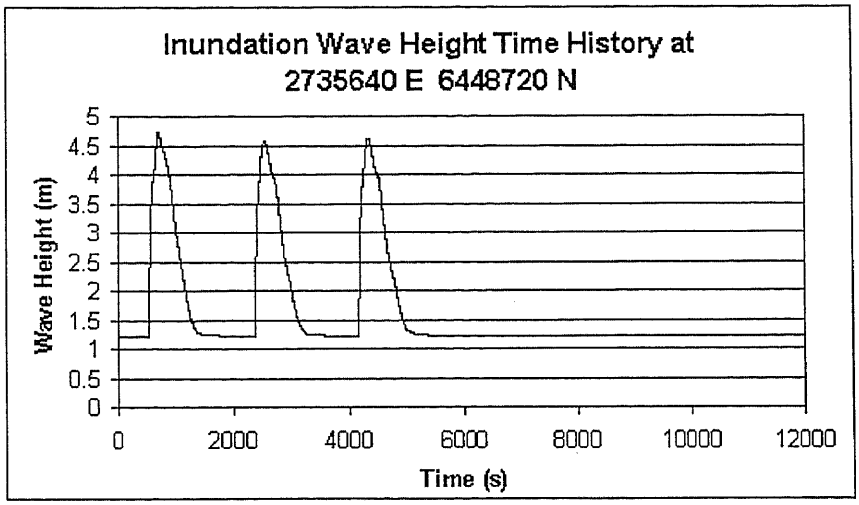

Figure 7.22: Inundation height time history for location 2735640 E 6448720 N (Site 6) resulting from three 3 metre amplitude, 10 minute period waves used for sea level forcing at the western model grid boundary for the simulation undertaken with the 3.5 m seawall.

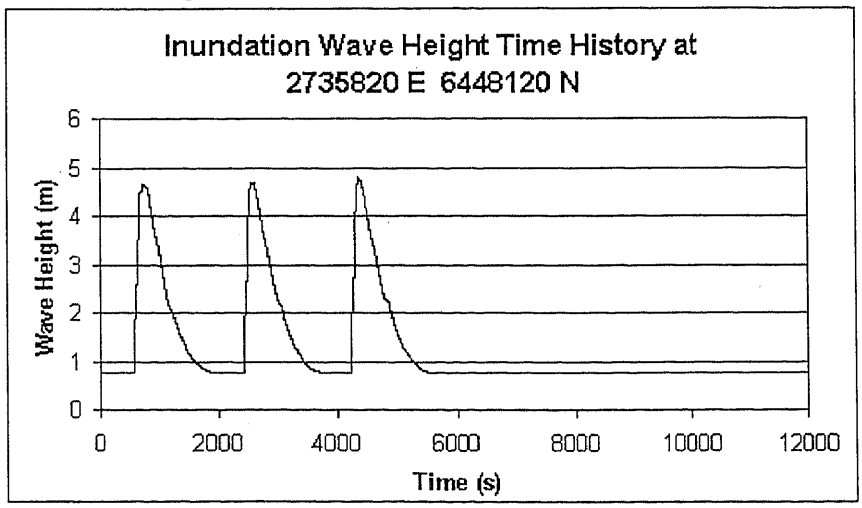

Figure 7.23: Inundation height time history for location 2735820 E 6448120 N (Site 7) resulting from three 3 metre amplitude, 10 minute period waves used for sea level forcing at the western model grid boundary for the simulation undertaken with the 3.5 m seawall.

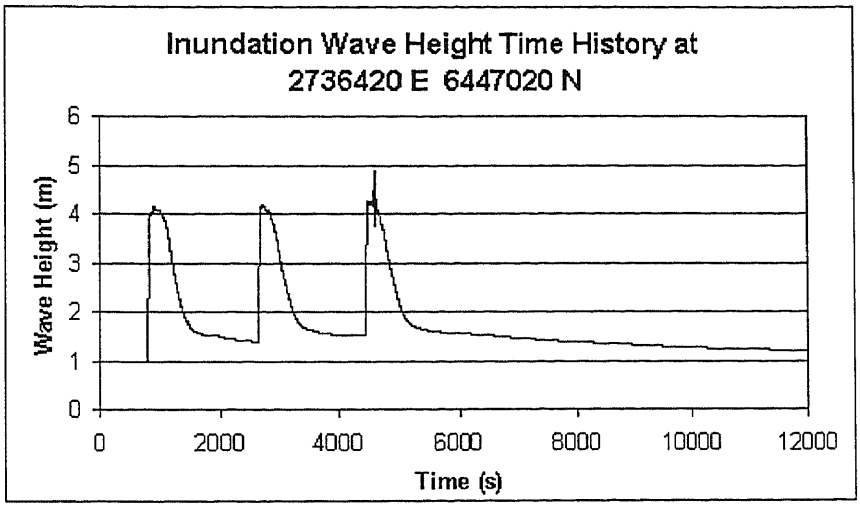

Figure 7.24: Inundation height time history for location 2736420 E 6447020 N (Site 8) resulting from three 3 metre amplitude, 10 minute period waves used for sea level forcing at the western model grid boundary for the simulation undertaken with the 3.5 m seawall.

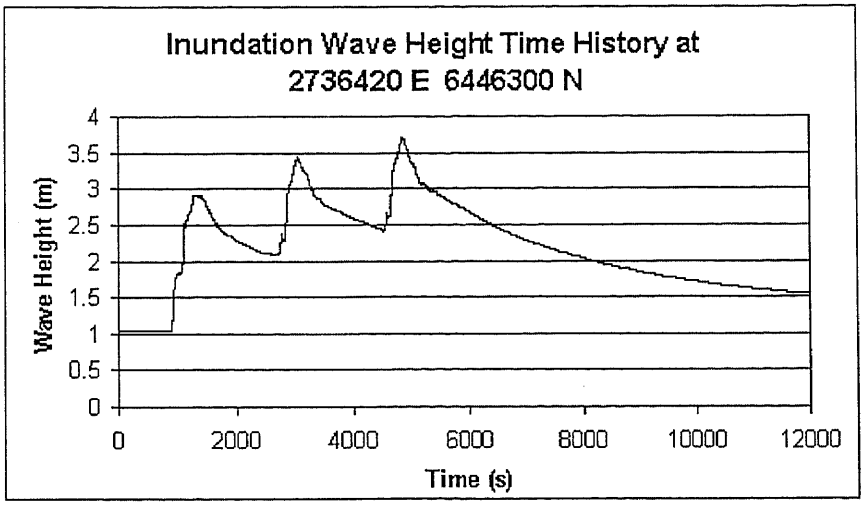

Figure 7.25: Inundation height time history for location 2736420 E 6446300 N (Site 9) resulting from three 3 metre amplitude, 10 minute period waves used for sea level forcing at the western model grid boundary for the simulation undertaken with the 3.5 m seawall.

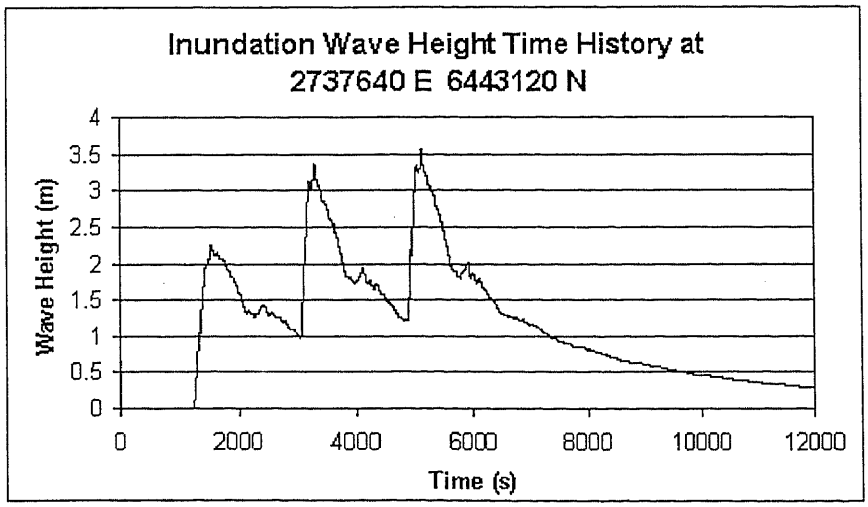

Figure 7.26: Inundation height time history for location 2737640 E 6443120 N (Site 10) resulting from three 3 metre amplitude, 10 minute period waves used for sea level forcing at the western model grid boundary for the simulation undertaken with the 3.5 m seawall.

Table 7.2: Summary of the time of maximum inundation height with seawall protection for the 10 locations for which inundation time histories were extracted.

Site No.	Eastings	Northings	Maximum Height (m)	Time of Max. H. (hrs, min, sec)
1	2734080	6451260	4.68	0, 40, 45
2	2735160	6449620	6.45	1, 9, 29
3	2734920	6449380	5.56	0, 9, 46
4	2735020	6449080	4.24	0, 10, 14
5	2735340	6449080	4.09	0, 11, 55
6	2735640	6448720	4.74	0, 12, 9
7	2735820	6448120	4.79	1, 12, 26
8	2736420	6447020	4.87	1, 16, 26
9	2736420	6446300	3.7	1, 20, 37
10	2737640	6443120	3.56	1, 25, 6

7.5 DISCUSSION

The accuracy of tsunami inundation height maximums and time histories presented in this chapter are limited by three main sources of error: (i) the limitations associated with the mathematical techniques used to generate the numerical model, (ii) bathymetric data resolution, and (iii) assumptions regarding the representation of physical processes.

7.5.1 Limitations of Numerical Technique

Like all hydrodynamic finite difference models, the 'TUNAMI N2' model requires the equations of motion and the continuity of mass equation to be approximated by discrete difference equations (Refer to Appendix 12). Discretization introduces numerical round off errors. The 'TUNAMI N2' model employs a leap frog scheme, which is a central difference scheme with a 2^{nd} order truncation error (Goto and Ogawa, 1995).

7.5.2 Limitations of Bathymetric Data

The excitation and propagation of tsunamis is strongly affected by the coastal topography which can cause focusing and defocusing of tsunami energy (Kanamori and Kikuchi, 1993; Titov and Synolakis, 1997). Consequently, the accuracy of all inundation models is limited by the resolution of bathymetric and topographic data input into the model. To realistically simulate the inundation of a tsunami wave, the model requires that resolution be fine enough to accurately represent the smallest topographic feature that may significantly enhance wave heights, for example small gullys. Therefore the model grid is usually required to be 50 m x 50 m or less. Hence it is recommended that before undertaking any future numerical modelling investigations of tsunami inundation in the Thames region, hydrographic surveys should be undertaken in order to obtain higher resolution bathymetric data for this region.

7.5.3 Physical Process Assumptions

The 'TUNAMI N2' model is further limited by assumptions regarding the representation of physical processes. 'TUNAMI N2' does not account for the effect obstructions such as buildings and trees will have on the direction, speed and extent of tsunami inundation.

7.6 SUMMARY

The numerical model 'TUNAMI N2' was used to simulate tsunami inundation in the Thames region. A 3 m amplitude, 10 minute period wave was used as a sea level forcing mechanism on the western boundary of the model grid. Tsunami inundation was simulated for two scenarios: (i) without protection of seawalls, and (ii) with protection of 3.5 m seawalls at shoreline locations south of the Kauaeranga River mouth.

The results of the above simulations indicate the following:

1. For both scenarios, the region south of Tararu to northern Moanataiare/Kuranui Bay is impacted by the most severe inundation heights (in the order of 7 m).
2. Horizontal inundation is most severe: (i) on low lying land south of Opani Point for Scenario 1 (completely inundated), and (ii) north of the aerodrome for Scenarios 1 and 2 (horizontal inundation of up to 450-550 m).
3. The presence of the seawall: (i) reduces the extent of tsunami inundation, particularly in the region south of Opani Point, and (ii) focuses wave energy into the Waihou River causing an increase in water level and an increase in current velocity.

7.7 REFERENCES

de Lange, W.P., 1996. Storm Surges, *Tephra*, Vol. 15, No. 1, p. 24-31.

Goto, C., and Ogawa, Y., 1995. *Numerical Method of Tsunami Simulation with the Leap-Frog Scheme, Part 1: Shallow water theory and its difference scheme*, IUGG/IOC TIME project Manuals, 66 p.

Kanamori, H., and Kikuchi, M., 1993. The 1992 Nicaragua earthquake: a slow tsunami earthquake associated with subducted sediments, *Nature*, Vol. 361, p. 714-716.

Statistics New Zealand, 1997. *1996 Census of Population and Dwellings: Population and Dwellings*, Wellington, New Zealand, 177 p.

Titov, V.V., and Synolakis, C.E., 1997. Extreme inundation Flows During the Hokkaido-Nansei-Oki Tsunami, *Geophysical Research Letters*, Vol. 24, No. 11, p. 1315-1318.

Chapter 8

CONCLUSIONS

8.1 INTRODUCTION

A review of 'active' faults in the Auckland region identified the Kerepehi Fault as a potential tsunami source. The Kerepehi Fault transects NNW through the central region of the inner Hauraki Gulf (Hochestein et al., 1986). A tsunamigenic event along the Kerepehi Fault has not occurred during historical times, consequently the most suitable way to assess the tsunami hazard represented by this fault is by way of numerical simulation. This required that the offshore segments of the Kerepehi Fault be characterised using 135 km of shallow seismic sub-bottom profiles. The data were used to locate the submarine extension of the Kerepehi Fault and determine the potential vertical displacement.

8.2 MAJOR FINDINGS

The findings on tsunami generation and propagation in the Firth of Thames and Hauraki Gulf are as follows:

- The offshore Kerepehi Fault trends NNW up the central Firth of Thames and is divided into four segments by three WSW-ENE trending transverse faults. The full extent and the exact location of the most northern segment, Segment D could not be determined from the available data, so two alternative locations are proposed (Figure 8.1). 2.1 m of displacement is most likely for any given event along Segments A, B, C, and D1. 7.35 m of displacement is most likely to occur along Segment D2.

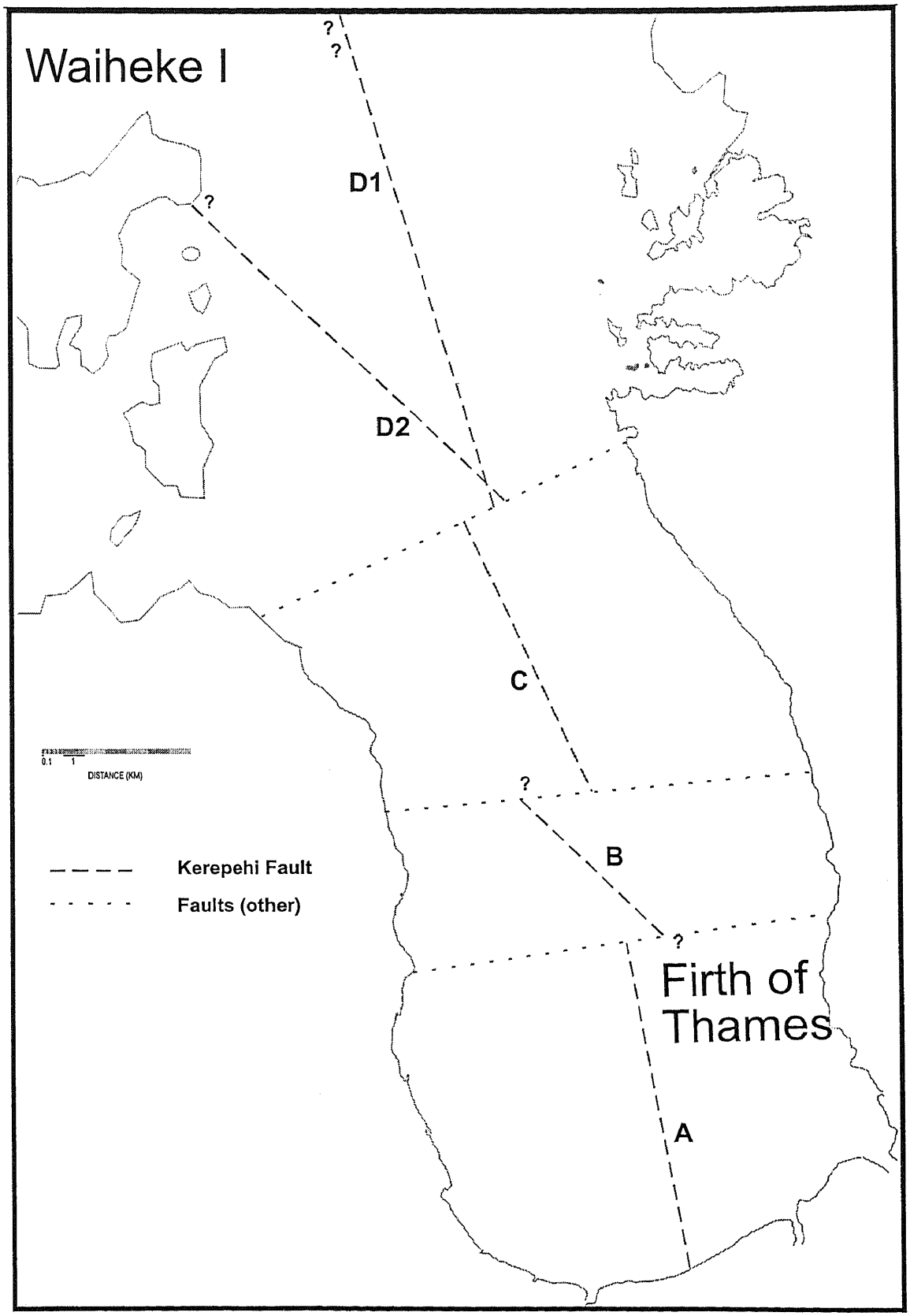

Figure 8.1: Figure illustrating the proposed location for four offshore segments of the Kerepehi Fault based on analysis and interpretation of seismic sub-bottom profiles undertaken in this study.

- Most Credible Earthquake (M.C.E.) predictions are summarised in Table 8.1.

Table 8.1: Summary of the location, likely vertical displacement for a given displacement event and Most Credible Earthquake Magnitude presented as M_W values.

Segment	Southern End Point		Northern End Point		Likely Vertical Displacement/Event	M.C.E. (M_w)
	Long. (E)	Lat. (S)	Long. (E)	Lat. (S)		
A	175°27'53"	37°12'32"	175°25'15"	37°04'41"	2.1	6.7
B	175°25'51"	37°04'31"	175°21'30"	37°01'19"	2.1	6.5
C	175°23'47"	37°01'09"	175°19'55"	36°54'32"	2.1	6.7
D1	175°20'35"	36°54'12"	175°15'38"	36°42'50"	2.1	6.8
D2	175°20'59"	36°54'03"	175°11'36"	36°46'48"	7.35	7.1

- The potential impact of the above vertical displacements (Table 8.1) with regards to tsunami hazard, was investigated for each of the above segments for fault widths of (a) 1.25 km, and (b) 5.8 km, using a linear deep water generation and shallow water propagation model, 'TSUNAMI'. The following conclusions are drawn from the results:

  (i) The 'TSUNAMI' model predicts a linear relationship between the volume of material displaced and the maximum wave height at the shore.

  (ii) Maximum predicted wave heights are small for simulations involving both surface rupture widths (Refer to Table 8.2).

Table 8.2: Summary of Maximum wave heights predicted by 'TSUNAMI' for 1.25 km and 5.8 km surface rupture widths.

Segment	1.25 km Surface Rupture Width		5.8 km Surface Rupture Width	
	Max. Wave Height	Location	Max. Wave Height	Location
A	0.64	Base of Firth of Thames	0.78	Base of Firth of Thames (displacement node)
B	0.05	Wharekawa	0.20	Kaiaua
C	0.075	Waimangu Pt.	0.33	Waimangu Pt.
D1	0.09	Whanganui Is.	0.41	Whanganui Is.
D2	2.18	Pakatoa Is.	3.19	Pakatoa Is. (displacement node)

The small magnitude of the maximum predicted wave heights (Segment D2 being the exception) prompted comparison with estimates generated from formula presented in Abe (1995), in an attempt to determine if 'TSUNAMI' had predicted wave heights of the correct order of magnitude. The empirical formulas (Equation 5.1-5.3, Refer to

Chapter 5) estimate the height of regional tsunami at a particular site as a function of propagation distance. Comparison of the two predictive methods illustrated that the 'TSUNAMI' numerical model predicts wave heights that are on average, approximately 1/7 of the magnitude of run-up heights predicted by equations presented in Abe (1995). The difference between maximum wave heights predicted by the two methods is greater than the 1.5 factor of uncertainty associated with the formula (Abe, 1995). This suggests that 'TSUNAMI' is under predicting maximum shoreline wave heights. To further test this hypothesis, a further simulation was undertaken using the hydrodynamic circulation model, '3DD'. Detailed comparison between the outputs of the '3DD' and 'TSUNAMI' model revealed that for all previous 'TSUNAMI' simulations:

(i) An error in the code caused the 'TSUNAMI' model to employ only half of the stipulated vertical displacement. Hence wave heights predicted from all prior 'TSUNAMI' simulations actually resulted from 1.05 and 3.68 m of vertical displacement.

(ii) The short duration of the generation phase time step (0.5 s) had resulted in unrealistic wave propagation velocities. Increasing the time step from 0.5 s to 10 s generated wave propagation velocities consistent with shallow water theory.

Consequently an adjusted set of generation conditions for the 'TSUNAMI' model was used to re-simulate tsunami generation and propagation. The results suggest that because 'TSUNAMI' does not account for the highly non-linear wave processes that occur in shallow water, this model is generally under predicting maximum wave height. However, this model is able to account for attenuation and reinforcement caused by wave propagation, and is not restricted by an upper wave height limit at locations close to the source. Consequently, where large displacement occurs within complex bathymetry and in close proximity to the source, as is the situation for Segment D2, the 'TSUNAMI' model may have more accurate wave height predictions.

Given the above limitations associated with each prediction method, it is recommended that the largest wave height estimate predicted by either method, should be the height employed for hazard planning purposes. For all cases, excepting a few island locations close to the source in the Segment D2 scenario, the largest wave heights are predicted by Equations 5.1-5.3.

- Simulations of teletsunami propagation into the Hauraki Gulf were undertaken using the model '3DD'. Simulations involved a range of wave periods and employed a wave height of similar magnitude to the 1960 Chilean tsunami (0.5 m amplitude at the model boundary). The results suggest the following:
  (i) for wave periods between 10 and 30 minutes, generally, maximum predicted rise above mean sea level increases with increasing wave period,
  (ii) the confined nature of the Firth of Thames acts to focus wave energy resulting in elevated wave heights in this location, and
  (iii) of the townships adjacent to the Firth of Thames, the maximum predicted rise above mean sea level (0.49 m) is observed at Tapu.

Wave heights observed during the 1960 Chilean tsunami and those predicted by model '3DD' are in strong agreement. However, the coarse grid employed by '3DD' (1500 m) limits the number of grid cells per wavelength. Consequently wave propagation in shallow water may not be fully represented, particularly for short period waves. Hence, the above results should be regarded with caution.

- The probable extent of tsunami inundation occurring in the Thames region was investigated using the non-linear finite difference model, 'TUNAMI N2'. The results indicate that should a tsunami of at least moderate amplitude (3 m) be generated in the Firth of Thames:
  (i) the most severe run-up heights occur in the region extending from south of Tararu to northern Moanataiare/Kuranui Bay;
  (ii) without protection structures the most severe horizontal inundation is predicted to occur on low lying land south of Opani Point where run-up heights in the order of 0.5-3.0 metres flood farmland and homes adjacent to Orongo Road;
  (iii) with protective structures, the most severe horizontal inundation is predicted to occur in the vacinity of the Aerodrome and Rhodes Park, where maximum run-up heights are approximately 4 m and extend a maximum distance of approximately 450 m eastward of the coastline; and
  (iv) the presence of the seawall (i) reduces the extent of tsunami inundation, particularly in the region south of Opani Point, and (ii) focuses wave

energy into the Waihou River causing an increase in water level and an anticipated increase in current velocity.

8.3 IMPLICATIONS FOR CIVIL DEFENCE

Numerical modelling of tsunami generation, propagation and inundation undertaken in this study has the following implications for Civil Defence:

- The greatest risk to Thames is associated with displacement along an adjacent fault segment, which produces wave heights in the order of 1.8 m.
- The largest wave heights (~ 4 m) were generated by displacement in deep water and had the most severe impact upon Pakatoa, Ponui, and Rotorua Islands. The maximum *mainland* wave height resulting from displacement along the Kerepehi Fault impacts at Deadmans Point and is in the order of 2.8 m.
- The overall tsunami hazard associated with displacement along the Kerepehi Fault is low.
- The maximum amplitude reinforcement occurring in the Firth of Thames in response to teletsunami is equivalent to 50 % of the amplitude at the open ocean boundary and is considered significant. Amplitude reinforcement in the Firth of Thames is consistent with observations made for other long period waves (Black, 1996).
- For townships adjacent to the Firth of Thames, the maximum predicted rise above mean sea level caused by teletsunami of similar magnitude to the 1960 Chilean tsunami was between 0.36 and 0.49 m. The largest of these, 0.49 m, is observed at Tapu.
- A teletsunami of this magnitude, represents a less significant hazard than tsunamis locally generated along the Kerepehi Fault for townships adjacent to the Firth of Thames.
- Should a tsunami of at least moderate amplitude (3 m) enter or be generated in the Firth of Thames, at least 7 metres of vertical run-up is likely to occur between Tararu and Moanataiari, and land adjacent to the Thames aerodrome will be horizontally inundated by up to 450 m.

8.4 FUTURE RESEARCH

The findings of this study suggest several aspects that should be addressed by future research:

- It is recommended future investigations into the tsunamigenic potential of the Kerepehi Fault should undertake sediment coring adjacent to this fault in order to determine its actual movement history.
- There is a need to develop a non-linear, shallow water tsunami generation and propagation model capable of accurately predicting maximum wave heights and current velocities in the Firth of Thames.
- It is recommended that before undertaking any future numerical modelling investigations of tsunami inundation in the Thames region, hydrographic surveys should be undertaken in order to obtain higher resolution bathymetric data for this region.

8.5 REFERENCES

Abe, K., 1995. Estimate of Tsunami Run-up Heights from Earthquake Magnitudes, In *Tsunami: Progress in Prediction, Disaster Prevention and Warning*, Y. Tsuchiya and N. Shuto (Eds), Kluwer Academic Publishers, Netherlands, p. 21-35.

Black, K.P., Oldman, J.W., and Bell, R.G., 1996. *Numerical Hydrodynamic and Thermodynamic Modelling of Nearshore Offshore Exchange Processes*, NIWA Internal Report NOD602/1, pp. 18-20.

Hochstein, M.P., Tearney, K., Rawson, S., Davey, F.J., Davidge, S., Henrys, S., and Backshall, D. 1986. Structure of the Hauraki Rift (New Zealand), In W.I. Reilly and B.E. Harford (eds). *Recent Crustal Movements of the Pacific Region*, Royal Society of New Zealand Bulletin 24. Wellington, The Royal Society of New Zealand, p. 334-348.

Appendix One

SEISMIC REFLECTION METHOD

A1.1 INTRODUCTION

For the purpose of understanding the seismic reflection method, we can consider the Earth's crust to be made up of a number of layers of rock with different physical properties. Seismic reflection involves bouncing acoustic energy off the interface between rock layers of contrasting acoustic impedance. Acoustic impedance is a function of rock density and compressional wave velocity; the harder the rock the greater the acoustic impedance (Kearey & Brooks, 1991). In marine environments, the seismic reflection method measures the time taken for a seismic wave to travel through the crust and return to the hydrophone (towed behind the vessel) after reflection from layers of contrasting acoustic impedance. The time taken is known as the Two-way Travel Time (TWT). By repeating this process as the boat moves forward, a seismic sub-bottom record can be produced which displays the TWT against horizontal distance, resulting in profiles that represent sub-bottom geology. If the velocity profile of the water column and the various layers of sediment or rock is known, the TWT time can be converted to depth to different reflectors.

A1.2 THE SEISMIC WAVE

Parcels of elastic strain energy (otherwise known as seismic energy) propagate out from the seismic source in the form of a seismic wave. There are two groups of seismic waves: body waves and surface waves. Of these there are two types of body waves capable of propagating through the body of an elastic solid (e.g. the earth); compressional waves (P-waves) and shear waves (S-waves). These are therefore the two wave types of interest in the seismic reflection method (Kearey & Brooks, 1991).

A1.3 AMPLITUDE OF THE REFLECTED WAVE

Upon reaching an interface with an acoustic impedance contrast, seismic energy is reflected and refracted. The relative proportion of energy reflected or refracted is dependent upon the acoustic impedance contrast, (normally incident ray) and the angle of incidence (oblique incident ray). For a normally incident ray, the reflection coefficient, R is given by:

$$R = \frac{Z_2 - Z_1}{Z_2 + Z_1} \qquad \text{A1.1}$$

where:

R = the reflection coefficient and is the ratio of the amplitude of the reflected ray to the amplitude of the incident ray.

Z_1 = the acoustic impedance of layer 1

Z_2 = the acoustic impedance of layer 2 (Kearey & Brooks, 1991).

For an obliquely incident ray, the relative amplitude of reflected and refracted waves is dependent upon the angle of incidence (Figure A1.1).. When an incident P wave strikes the interface at an oblique angle, reflected and refracted S waves are generated (Kearey & Brooks, 1991; McQuillin et al., 1984). The calculation for the relative amplitudes of these four phases (P reflected, P refracted, S reflected, S refracted) is complex and need not be discussed here, but can be found, for example in Ewing et al. (1957). However, seismic wave reflections will typically be generated from interfaces with reflection coefficients in the order of 0.1 (McQuillen et al., 1984).

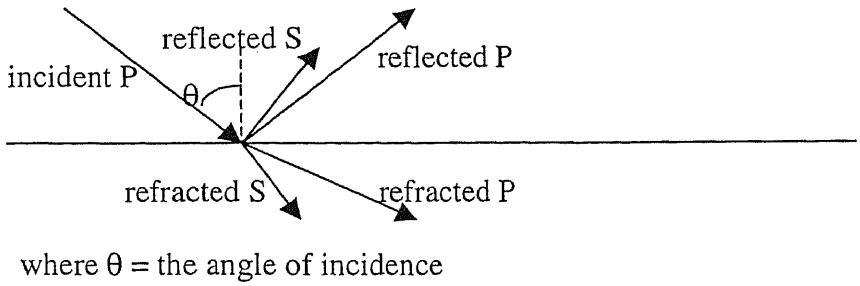

Figure A1.1: Reflected and refracted P- and S-rays generated by a P-ray obliquely incident on an interface of acoustic impedance contrast (From Kearey & Brooks, 1991).

A1.4 ANGLE OF WAVE REFLECTION & REFRACTION

As S-rays are of only minor importance in seismic surveying (Kearey & Brooks, 1991), only the reflection and refraction angles of P-rays will be discussed.

Snells Law (Equation A1.2) can be used to predict the angle of reflection or refraction of a seismic wave.

$$\frac{\sin\theta_1}{\sin\theta_2} = \frac{v_1}{v_2} \qquad \text{A1.2}$$

where:

θ_1 = angle of incidence

θ_2 = angle of refraction

v_1 = wave velocity in layer 1

v_2 = wave velocity in layer 2

Hence, for normally incident rays, the reflected ray travels back at the same angle as the incident ray and the transmitted ray continues into layer 2 at the same angle of travel as in layer 1. For obliquely incident rays, the refracted P-ray travels through the lower layer with a changed direction of propagation. The reflected ray has a reflection angle equal to the angle of incidence (Figure A1.2).

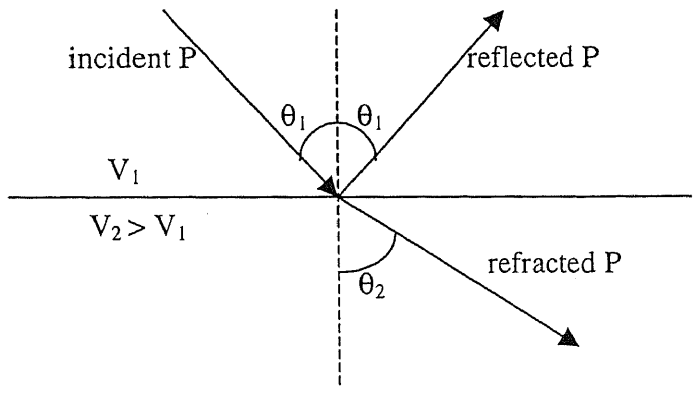

Figure A1.2: Reflected and refracted P-rays associated with a P-ray obliquely incident on an interface of acoustic impedance contrast (From Kearey & Brooks, 1991).

A1.5 REFERENCES

Kearey, P., and Brooks. M., 1991. *An Introduction to Geophysical Exploration*, 2nd edition. London, Blackwell Scientific Publications, 254 p.

McQuillin, R., Bacon, B., and Barclay, W., 1984. *An Introduction to Seismic Interpretation: Refection Seismics in Petroleum Exploration,* London, Graham & Trotman Limited. 287 p.

Appendix Two

SEISMIC EQUIPMENT SPECIFICATIONS

Geopulse model 5420A Power Supply

SIZE: (H) 25.25 in x (W) 23.5 in x (D) 16 in
(38.74 cm) (59.7 cm) (40.6 cm)

WEIGHT: 175 Pounds / 79.4 kg

CHASSIS: Aluminum with two handels per end for carrying and lashing down. Bottom skids for protection.

POWER: 115 VAC/230VAC +/-10%; 50/60 Hz +/-2Hz; 25 Amp peak surges. 30 Amp breaker recommended.

OUTPUT: 3750VDC nominal, energy selectable:

Energy (J)	Max Rate (pps)
105	8.5
175	5
280	3
350	2.5
455	2
525	1.7

Note: These energy levels are for the 5420A Power Supply only. When operating with the 5813A GeoPulse Acoustic Source refer to its manual for maximum energy levels.

KEY INPUT: Isolated input BNC. Positive or negative level trigger, TTL, CMOS compatible, 3.5V to 35V and fiber optic input connector. (Spectral response; λ = 800nm, input > 10μW minimum.

ENVIRONMENTAL: -5 to 50 degrees centigrade (operational).
-15 to 85 degrees centigrade (storage).

FEATURES: Ferroresonant capacitor charging transformer for minimal line interference; energy meter; line filters for output transient suppression; top cover and capacitor cover H.V. interlocks; forced air ventilation (no oil).

Geopulse model 5813A Acoustic Source

SIZE: 15 " square x 3.5" overall height.

(38 cm) (8.9 cm)

WEIGHT: In air 27 lbs., in water 16l lbs
(12.2 kg) (7.3 kg)

MOUNTING
HOLES: 11.5: square pattern for 0.5" hardware.
(29.2 cm) (12.5 mm)

SOURCE
LEVEL: 220 dB re 1 µPa @ 1m @ 350 Joules.
(typical) 218 dB re 1 µPa @ 1m @ 280 Joules.
213 dB re 1 µPa @ 1m @ 105 Joules.

MAXIMUM POWER INPUT: 360 Joules @ 2 pps (720W).

MAXIMUM VOLTAGE INPUT: 4kV

MAXIMUM OPERATING DEPTH: 32 ft. (10 m).

CONNECTORS: (2) # 1/0 AWG pins – mating connector BA5000-10225
(2 required per unit)

Geopulse model 5812A Catamaran Tow Vehicle

SIZE: (H) 11 in x (W) 38 in x (D) 52 in
(132 cm) (96.5 cm) (28 cm)

WEIGHT: 103 lbs / 79.4 kg

MATERIALS: Foam filled PVC floats with stainless steel frame and hardware.

OPERATING SPEED: To 5 knots

TOWING
CONFIGURATION: Surface tow with 2 towing/steering lines.

FEATURES: One man deployable; virtually unsinkable; frame provides protection for acoustic source.

Geopulse model 5210A Receiver

AMPLIFIER: (input & intermediate)

INPUT: Differential, CMRR 100dB @ 60 Hz. 1 Meg Ohm differential input. O, -20dB gain, switch selectable. Overload indicator on its output.

SENSITIVITY: 30µVrms in produces 1Vrms out.

100dB total ga in with TVG.

SIGNAL TO NOISE RATIO: 20 dB (full gain, 1kHz BW at 1kHz CF).

COARSE GAIN: 0, 20, 40dB and water column TVG (WC TVG – equal to water attenuation, -10 to 30dB from 2 to 200ms).

FINE GAIN: 0 to 30dB in 3dB steps. Overload indicator on its output.

FILTER:

LOW PASS & HIGH PASS: Active type, maximally flat, 24dB/octave min. roll off. 0.02kHz to 15kHz * adjustable in steps of approximately 0.5 octave increments. Gain = 0dB

* Control knobs interlock to prevent overlap.

TVG AND DELAY:

TVG DYNAMIC RANGE: 30 dB

RATE: Flat (approximately) to 30 dB in 14 msec.

DELAY, MANUAL: Fine adjust 1ms to 14ms, multiplier x1, x10, and x100. Internal switch selectable to x1000 (Delay starts at key out pulse; TVG starts at end of delay).

DELAY, AUTO: Bottom track function, TVG gain at minimum until first bottom return received.

AGC:

ATTACK: Attack time constant adjustable from 300 μs to 300 ms.

DECAY: Decay time constant adjustable from 330 μs to 300 ms.

RANGE: AGC control voltage gain, 20dB.

KEY PROGRAMMER:

Divide by	1-9
Multiply by	1-9
Max. rate in	20 pulses/sec
Min rate in	1 pulse/2 sec (multiply mode only)

CONNECTORS:

KEY IN: 2-15V (+ or -) leading edge triggered. Pulse length < 50 ms, max. rate 20pps.

KEY OUT: Pulse width 1 ms, TTL compatible.

KEY OUT ISOLATED: Pulse width 1 ms, transformer coupled, 50 Ohm min. load.

KEY OUT OPTIC: Infra red emitting Diode, λ = 940nm for complete isolation to a high voltage acoustic source power supply.

EVENT MARK IN: Optically islolated to accept a p ositive input p ulse of 5-15V. 5V CMOS Triggerable. Min. width 100µs.

TAPE IN: ±10Vpp max signal in from tape recorder.

TAPE OUT: Signal out to tape recorder green and amber LED's on = 1Vpp out.

POWER: 115/230VAC ± 10%, 47-63Hz, 45 watts max.

ENVIRONMENTAL: -5 to 50° C operational
-15 to 85° C storage

MECHANICAL: 19" L x 17" W x 7-0.5" H
(48 cm L x 43 cm W x 19 cm H)

30 lbs (13.6kg)

Appendix Three

THEORY OF DATA PROCESSING

A3.1 INTRODUCTION

The seismic signal that is returned to the receiver contains a range of components, not all of which are desirable e.g. convoluted signals and noise generated from the boat, surface swell and diffraction. Data processing is necessary to remove noise and enhance the signal to a degree that enables the seismic section to be analysed and interpreted. The principles behind a variety of data processing techniques are briefly outlined below.

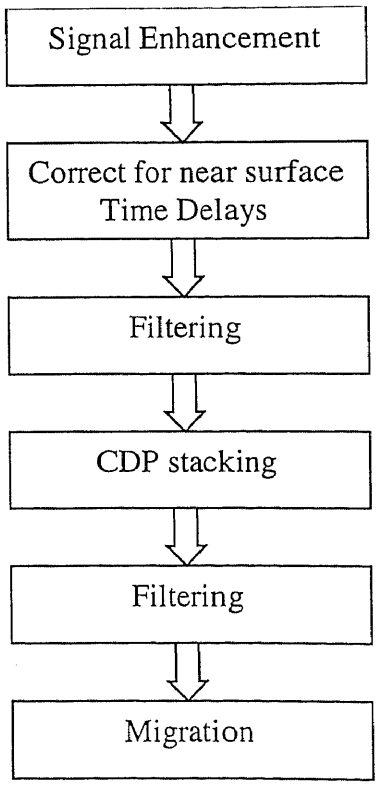

Figure A3.1: Flow diagram illustrating the standard data processing techniques in the usual process order.

A3.2 SIGNAL ENHANCEMENT

The processing techniques described within this section are those that can be undertaken immediately, when the reflected signal is received and before the initial print from the Graphic Recorder.

Gain:

To 'gain' a trace is to enhance sub-bottom details by modifying the amplitude values of the seismic trace in order to correct for the natural energy decrease of the seismic wave (Cape, 1989). This is most commonly undertaken by applying a spherical divergence correction, or using an automatic gain control (AGC) (Cape, 1989). The Model 5210A Geopulse Receiver employed by the University and the D.S.E is capable of applying either of these corrections as the signal is received. For the spherical divergence correction, the gain can be delayed by a specific time increment, delayed manually, or operated automatically, being triggered by the first reflector (Allan, 1990). "Spherical divergence correction uses a user-input velocity function to calculate the decrease in wave strength (or amplitude) as a function of distance. The inverse of this function is then applied to correct for the geometric spreading" (Cape, 1989, pg. 25). The Automatic gain control either manually or automatically maintains signal output at a constant level (Allan, 1990). This "is accomplished by multiplying each sample by a value determined using the average amplitude over a user-specified window centred about the sample. This is done for each sample of the seismic trace and has the effect of equalising the amplitudes with time" (Cape, 1989, pg. 25).

During data collection in the Firth of Thames, the Model 5210A Geopulse Receiver was set-up with the 'Time Varying Gain" function on. This partially compensates for natural wave attenuation and consequently generates a more even image density across the display (G. Crook, pers. comm.).

Frequency Bandpass Filtering:

Band-pass filtering requires examination of the data in order to determine the frequency at which the noise and signal occur. The frequency range over which the signal is dominant can be specified and frequencies outside this range are attenuated (Cape, 1989). The Model 5210A Geopulse Receiver has bandpass filters that enable

high and low pass filtering of the signal (Allan, 1990). Within the Firth of Thames, the majority of reflected energy is around 3 kHz. For data collected by the D.S.E the frequency bandpass filter was set to 'open' between 1kHz & 10kHz enabling more reflected energy to be recorded (G. Crook, pers. comm.).

Swell Compensator:

The Model 5210A Geopulse Receiver also compensates for swell effects by calculating the average distance from the hydrophone array to the first reflector, during a given time interval and adjusting the returned signal in order to compensate for any anomalies (Allan, 1990).

A3.3 CORRECTING FOR NEAR-SURFACE TIME DELAYS

Static Correction:

The Static correction is applied to compensate for near surface time delays that can be generated from two distinct causes. Near surface time delays are generated if (i) the transducer and receiver are not on the same horizontal datum plane. In the marine environment this is easily compensated because the hydrophone is typically towed at constant depth so the same correction can be applied to all the data; (ii) There are rapid changes in water depth along a line, which may create strong velocity variations in the near surface. This can cause artificial lows in all succeeding reflectors. This delay is corrected by replacing the anomalous time intervals with those recalculated using the seabed/bedrock velocities. If not corrected, static shifts corrupt the seismic section and have the potential to introduce entirely synthetic structures into a section (McQuillian, et al., 1984). A static correction was not applied to the data analysed in this study because (i) the shot and receiver were in the same plane, and (ii) for the most part the bathymetry of the study region was a gentle slope.

A3.4 FILTERING

Filtering is the modification of the original waveform by altering the relative amplitudes and/or phase relations of the constituent sine components of the sound wave (Kearey & Brooks, 1991), and is inherent in any transmission system. Filtering of a seismic pulse will occur gradually as the source pulse travels through the earth (ground filtering effects) and in response to recording system effects (Keary & Brooks, 1991; McQuillin et al., 1984). Hence, the recorded seismic trace departs from an ideal seismic trace that would illustrate a series of spikes at TWTs corresponding to reflectors in the earth (McQuillin et al., 1984) (Figure A3.2). Instead, the actual returned trace has an altered complex waveform. The change in the waveform shape resulting from passage through a filter, can be defined mathematically and is known as convolution (Kearey & Brooks, 1991). As the signal passes through a recording system or propagates through the earth, convolution occurs as a result of absorption of higher frequencies, and scattering and generation of multiple wavetrains (Cape, 1989; Kearey & Brooks, 1991) (Refer to appendix 4). Convolution of the seismic trace is corrected for by employing a technique called deconvolution.

Inverse Filters (Deconvolution):

Deconvolution is the analytical process of removing the effect of some previous filtering operation (convolution) (Keary & Brooks, 1991). Unlike simple frequency filters, inverse filters are able to discriminate against noise occurring at the same frequency as the reflected signal by boosting the amplitude spectrum at higher frequencies, thus improving signal character. The resulting signal more closely approaches the ideal seismic spectrum (series of spikes) (McQuillian et al., 1984), thus improving the vertical resolution.

There are several deconvolution operations that can be employed in the marine environment e.g. *deverberation* removes ringing associated with multiple reflections in a water layer and *whitening* equalises the amplitude of all frequency components within the recorded frequency band so that the output approaches that of a spike function (Kearey and Brooks, 1991). Deconvolution can be undertaken either before stacking (Deconvolution Before Stacking: DBS) or after stacking (Deconvolution After Stacking: DAS) and is commonly employed at both stages of data processing

(Kearey & Brooks, 1991). However, the data analysed in this study was not processed beyond the initial signal enhancement processes (i.e. gain, bandpass filtering and swell compensating) hence, deconvolution was not undertaken at any stage. Consequently, it was hard to identify individual closely spaced reflectors and interpret lateral changes in waveforms. This problem is common in non-deconvoluted seismic data. (McQuillian, 1984).

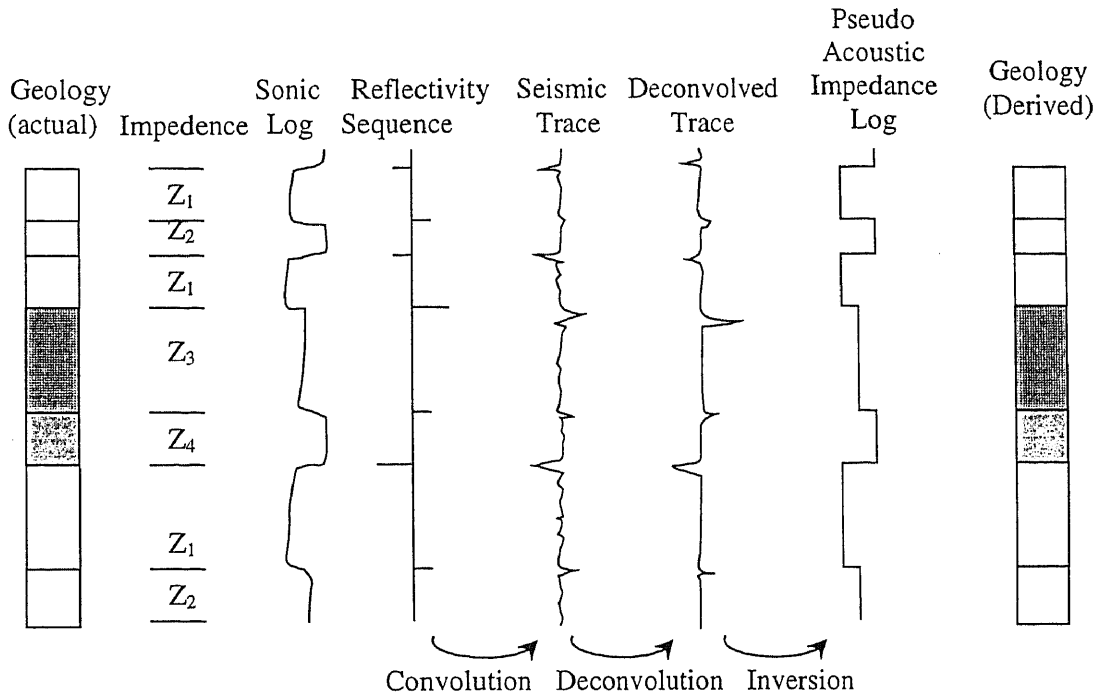

Figure A3.2: The Convolutional Model (From Easton Wren, 1984).

Frequency Filtering:

Frequency filtering can be undertaken as the signal is received. This is discussed above in section *A3.2 Signal Enhancement.*

Velocity Filtering (f-K Filtering):

The aim of velocity filtering is to remove coherent noise events from seismic records (Kearey & Brooks, 1991). This is undertaken by transforming a seismic pulse from t-x space into the F-K or frequency-wavenumber domain using 2-dimensional Fourier transforms and then plotting the apparent wave number against frequency. The resulting straight line gradient is equivalent to the apparent velocity (or event dip),

thus reflection events are separated as a function of dip (or apparent velocity) (Cape, 1989). Coherent noise events can be then be removed by their anomalous dip (Figure A3.3) (Kearey & Brooks, 1991).

The data analysed in this study has not undergone velocity filtering and as a consequence much of the signal is masked by diffraction patterns.

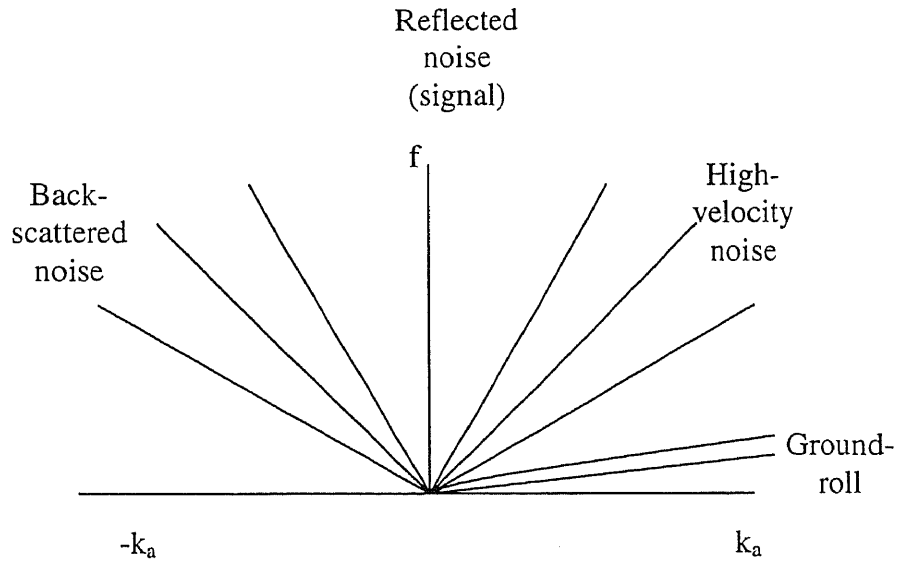

Figure A3.3: An f-k plot for a typical shot gather containing reflection events and different types of noise (From Kearey & Brooks, 1991).

A3.5 C.D.P. STACKING

The aim of a Common Depth Point (CDP) Stack is to improve the Signal to Noise Ratio (SNR). A CDP stack is undertaken by collecting a number of records, each with an increasing distance x, between the source and receiver. These reflections are then adjusted for the normal moveout (NMO) and added together to create a CDP stack, which approximates a zero offset section (McQuillin et al., 1984). The normal moveout is the difference between t_0, the TWT at 0 offset and t_x, the TWT at a finite offset. i.e. NMO = $t_0 - tx$ where x represents offsets 1, 2, ...n. (Figure A3.4).

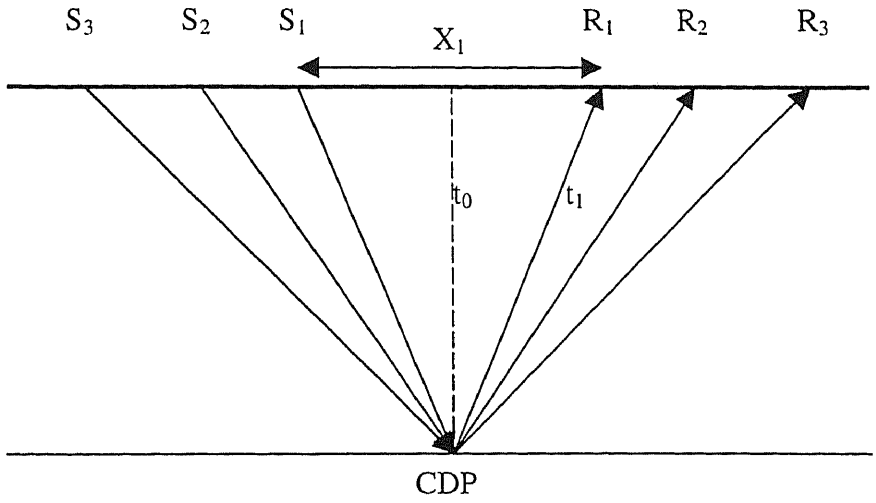

Figure A3.4: Geometry of the CDP gather (adapted from McQuillian, 1984). The source-receiver distance x is called the offset, S_1 and R_1 represent the source position and receiver position respectively for the first reflection.

As the data analysed in this study was not available in digital form, it has not undergone CDP stacking.

A3.6 MIGRATION

Migration is the process which attempts to reposition reflector segments to give the TWT section the geometry of a depth display (McQuillin et al., 1984). This requires the reflector to be placed under (or 'migrated' to) the correct surface location at a corrected vertical reflection time (Kearey & Brooks, 1991). Migrating a seismic section collapses diffractions, collapses buried focus effects into synclines, steepens anticlines and moves dipping events updip making them steeper (Cape, 1989). For example, in an unmigrated section with dipping reflectors, the true reflectors A & B (figure A3.5) are positioned directly below the position where the reflector is received (X & Y respectively, where XC=XA and YD=YB). Thus generating an apparent reflector with lesser dip, positioned further downdip than is actually the case. Only if the reflector is horizontal should the reflector point be placed directly below the receiver position.

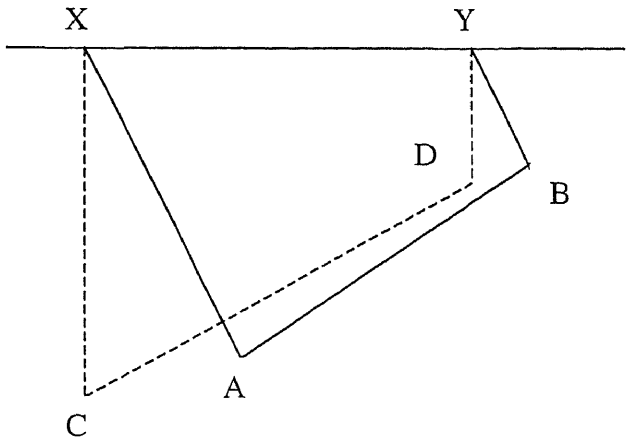

Figure A3.5: Actual event AB produces apparent event CD.

However, we cannot just assume that the reflection originates in the vertical plane through the seismic line. In the presence of cross-dip or local reflecting bodies (like a salt dome) the reflection point originates out of the plane of the section (Anstey, 1982; Kearey & Brooks, 1991). Therefore, the equal time surface for any reflection should be considered a sphere as opposed to a circle. Hence the concept of three-dimensional migration is introduced. However, three-dimensional migration requires three-dimensional survey data to provide information of cross dip. Therefore, two-dimensional survey data such as that analysed within this study are constrained to lie in the plane of the section. Note, however, that the seismic data available for this study have not undergone any form of migration.

A3.7 REFERENCES

Allan, T.M.H., 1990. *A High Resolution Seismic Study of the offshore extension of the Waihemo Fault System*, M.Sc. Thesis, University of Otago, Otago, New Zealand.

Anstey, A.N., 1982. *Simple Seismics*. Boston, U.S.A., International Human Resources Development Corporation. p. 6-11

Cape, C.D., 1989. Seismic Reflection Data Acquisition, Processing and Interpretation: A Set of Teaching Exercises, *Geophysics Division Technical Report No. 107*, Department of Scientific and Industrial Research, Wellington, New Zealand, 64 p.

Crook, G., 1998. Defence Operational Technical Support Est. (D.S.E.), email to author, 26 August.

Easton Wren, A., 1984. *Geophysics for Geologists*, Third Edition, Petrel Consultants Ltd, Calgary, Canada.

Kearey, P., and Brooks. M., 1991. *An Introduction to Geophysical Exploration*, 2nd edition. London, Blackwell Scientific Publications, 254 p.

McQuillin, R., Bacon, B., and Barclay, W., 1984. *An Introduction to Seismic Interpretation: Refection Seismics in Petroleum Exploration,* London, Graham& Trotman Limited, 287 p.

Appendix Four

MATHEMATICAL DEFINITION OF CONVOLUTION

Convolution:

"Convolution is a mathematical operation which combines two functions together to produce a third. In seismology it can be thought of as replacing each reflection coefficient spike with a scaled wavelet. For discrete functions sampled at a constant time increment (sample rate), the formal definition of convolution is as follows" (Cape, 1989):

Given two functions

$w_i = i = 0, 1, \ldots, L_w$ (wavelet)

$r_j = j = 0, 1, \ldots, L_r$ (reflectivity series)

the convolution of w_i and r_j ($w_i * r_j$) equals:

$$s_k = \sum_{j=0}^{L_w} w_j r_{k-j} \qquad \text{(seismogram)}$$

$$k = 0, 1, \ldots, L_s = L_w + L_r - 1.$$

As defined In: Cape, C.D., 1989. Seismic Reflection Data Acquisition, Processing and Interpretation: A Set of Teaching Exercises, *Geophysics Division Technical Report N. 107*, Department of Scientific and Industrial Research, 64 p.

Appendix Five

SEISMIC STRATIGRAPHY DEFINITIONS

Baselap: The lapout at the lower boundary of a depositional sequence. Two important types are recognized: *Onlap*: Is baselap in which an initially horizontal stratum laps out against an initially inclines surface, or in which an initially inclined stratum laps out up dip against a surface of greater initial inclination. *Downlap*: Is baselap in which an initially inclined stratum terminates down dip against an initially horizontal or inclined surface.

Depositional Sequence: A stratigraphic unit composed of a relatively conformable succession of genetically related strata and bounded at it's top and base by unconformities or their correlative conformities.

Downlap: *See Baselap*

Conformity: A surface that separates younger strata from older rocks, but along which there is o physical evidence or erosion or non-deposition and no significant hiatus is indicate

Hiatus: Total interval of geologic time that is not represented by strata at a specific position along a stratigraphic surface. If the hiatus encompasses a significant interval of geologic time, the stratigraphic surface is an unconformity.

Onlap: *See Baselap*

Toplap: The lapout at the upper boundary of a depositional sequence. In low resolution seismic sections toplap may appear as truncation.

Truncation: *Erosional truncation*: The lateral termination of a stratum by erosion. Strata tend to remain parallel and terminate abruptly rather than tapering to the upper boundary of the depositional sequence. *Structural truncation*: lateral

termination of stratum by structural disruption e.g. faulting, gravity sliding, salt flowage or igneous intrusion.

Unconformity: A surface of erosion or non-deposition that separates younger strata from older rocks and represents a significant hiatus.

As defined In: Mitchum, R.M., Vail, P.R., and Thompson, S., 1977. Seismic Stratigraphy & Global changes in sea level, Part 2: The Depositional Sequence as a Basic Unit for Stratigraphic Analysis. In C.E. Payton. *Seismic Stratigraphy – applications to hydrocarbon exploration,* Tulsa, Oklahoma, U.S.A., American Association of Petroleum Geologists Memoir 26, p. 53-62.

Appendix Six

IDENTIFYING FAULT MARGINS BELONGING TO THE KEREPEHI FAULT SYSTEM

A6.1 METHOD

- Kerepehi Fault – segment A

  Placed Kerepehi Fault (K.F.) through diffracted zone of track 2 because:

  i) Diffraction is commonly associated faulting. Diffraction is noise generated by structures, usually with abrupt boundaries from things like fault margins and lithology changes.

  ii) Fits in well with confirmed onland segment of K.F (de Lange & Lowe, 1990).

- Transecting fault 1

  This fault was required because K.F. north of this region doesn't match with Kerepehi Fault south of this region.

  i) Track 2: The transverse fault was chosen to pass through a fault zone of limited vertical displacement located at shot 72 (track 2).

- Kerepehi Fault – segment B

  i) Track 5: Segment B passes through a diffracted zone near thinnest point of recent sedimentation. This is expected if the geology outlined in Hochstein et al, (1986) is correct.

  ii) Track 4: Passes through the western margin of zone of intense diffraction and uplift and just to the west of the point of thinnest sedimentation, like in track 5.

  iii) Track 3: Segment B passes through western margin of intensely disturbed signal

- Transecting fault 2

  This fault was required because K.F. north of this region doesn't match with Kerepehi Fault south of this region.

  i) Track 3: This transecting fault passes through a mottled, disturbed segment of track 3.

  ii) The presence of this fault explains the truncation of the i) disturbed section in the NIWA data line and ii) sequences in track W20-W21.

- Kerepehi Fault – segment C

  This segment of the Kerepehi Fault is clearly out-lined by the New Zealand Defence Force (D.S.E.) data. The Kerepehi Fault lies to the west of the uplifted block, which is consistent with the geology outlined by Hochstein (1986).

- Transecting fault 3

  The location of this fault is fairly ambiguous although the current position corresponds with: i) two very disturbed patches of data (NIWA data) and ii) a fault margin on SE end of track 2130-2225.

- Kerepehi Fault – segment D

  Location of segment D is also fairly ambiguous. The estimated location of this segment is based on the termination of uplifted highs observed in NIWA data and uplifted highs within D.S.E. data.

A6.2 REFERENCES

de Lange, P.J. & Lowe, D.J. 1990, History of vertical displacement of Kerepehi Fault at Kopouatai bog, Hauraki Lowlands, New Zealand, since 10700 years ago, *New Zealand journal of Geology and Geophysics*, Vol. 33, p. 277-283.

Hochstein, M. P., Tearney, K., Rawson, S., Davey, F. J., Davidge, S., Henrys, S., Backshall, D. 1986, Structure of the Hauraki Rift (New Zealand*); Royal Society of New Zealand Bulletin 24.*

Appendix Seven

LOWER CONFIDENCE LIMIT FOR RETURN PERIOD

A7.1 LOWER CONFIDENCE LIMIT

Given that *the displacement times are random points on a time line* the return period (in years) is related to the average number of exceedances per year through the simple relation (Bardsley, 1981):

$$\alpha_D = \frac{1}{\lambda_D} \qquad \textbf{A.7.1}$$

where α_D = return period
λ_D = average number of exceedances per year.

Given the number of past exceedances in the record a conservative lower 95% confidence bound to the true return period using the following equation:

$$\frac{2R}{\chi^2_{.95}(2J_D + 2)} \qquad \textbf{A.7.2}$$

where R = record length in years
$\chi^2_{.95}$ = chi-squared value for 95% confidence
J_D = number of displacement events in R years

de Lange and Lowe (1990) fitted step functions to the age versus offset data for an onland segment of the Kerepehi Fault near the Kopouatai peat bog. The results suggested four offset events had occurred over the last 11 000 years. Applying equation A.6.2 to this information (R = 11 000, J_D = 4, $\chi^2_{.95}$ = 1.8307)

$$\text{Conservative lower 95\% confidence bound} = \frac{2R}{\chi^2_{.95}(2J_D + 2)}$$

$$= \frac{2 \bullet 11000}{18.307}$$

$$= 1201.73 \text{ years}$$

Hence we can be at least 95% certain that the true return period is at least 1202 years.

A7.2 REFERENCES

Bardsley, W.E., 1981. Note on the time to flood exceedance. *Journal of Hydrology*, Vol. 49, p.395-399.

de Lange, P.J. & Lowe, D.J. 1990, History of vertical displacement of Kerepehi Fault at Kopouatai bog, Hauraki Lowlands, New Zealand, since 10700 years ago, *New Zealand journal of Geology and Geophysics*, Vol. 33, p. 277-283.

Appendix Eight

CALCULATING MOMENT MAGNITUDE, M_W

A8.1 INTRODUCTION

The magnitude of a tsunami wave is directly dependent upon the amount of energy being supplied by a seismic source. M_w is a moment magnitude scale. It is based directly on an estimate of the radiated energy. Consequently it provides a more suitable estimate of energy available for tsunami generation than other magnitude scales such as M_L (local magnitude), M_s (surface wave magnitude), or M_b (body wave magnitude), which are characterise earthquake source strength with narrow-band time domain amplitude measurements and are inclined to become saturated at large magnitudes (Hanks & Kanamori, 1979).

Following the method outlined by Hanks & Kanamori (1979), the Moment Magnitude, M_w is directly depend upon the Seismic Moment, M_0. Therefore M_0 must be calculated in order to obtain M_w, which requires knowledge of the following fault parameters: surface rupture length, fault slip, focal depth and fault dip.

A8.2 CALCULATING M_0

M_0 is calculated from the product of the fault area, fault slip and rigidity (A. Hull, pers. comm., 1998) (Refer to Equation A8.1).

$$M_0 = A.\bar{s}.R \qquad \textbf{A8.1}$$

Fault area is determined from the fault dip, focal depth and surface rupture length using simple mathematics. De Lange and Hull (1994) provided estimates of the fault dip and focal depth for the Kerepehi Fault of 60° and 10 km respectively. Surface

rupture length was determined from analysis of seismic sub-bottom profiles. The fault area is the displaced fault plane area and can be calculated using the following equation (Equation A8.2):

$$A = \frac{F}{\sin D} L \qquad \textbf{A8.2}$$

where:

F = focal depth (m)

D = fault dip (degrees)

L = surface rupture length (m)

Fault slip was calculated from the expected average vertical displacement and fault dip angle using the following equation (Equation A8.3):

$$\bar{s} = \frac{\bar{d}}{\sin D} \qquad \textbf{A8.3}$$

where:

s = average fault slip

d = average vertical displacement

D = fault dip (degrees).

Rigidity for crust rocks is in the order of 3×10^{10} Nm^2.

A8.3 CALCULATING M_W

Once an estimate of M_0 has been obtained M_w is calculated using Equation A8.4. This equation is the S.I. equivalent of an equation presented in Hanks and Kanamori (1979) (A. Hull, pers. comm., 1998).

$$M_w = \frac{2}{3}(\log_{10} M_0 - 9.05) \qquad \textbf{A8.4}$$

A8.4 REFERENCES

de Lange, W.P., and Hull, A.G., 1994. *Tsunami Hazard for the Auckland Region*, Earth Sciences Department, University of Waikato, and Institute of Geological and Nuclear Science Limited, p. 37.

Hanks, T.C., and Kanamori, H., 1979. A Moment Magnitude Scale, *Journal of Geophysical Research*, Vol. 84, No. B5, p 2348-2350.

Hull, A., 1998. email to author, 27 November.

Appendix Nine

GRAPHICAL SIMULATION RESULTS

This appendix presents a series of figures that graphically summarise the wave height and current velocities resulting from simulations undertaken using the wave generation and propagation model, 'TSUNAMI' (initial version). These results were generated by simulating 2.1 m of vertical displacement along Segments A, B, C and D1, and 7.35 m of displacement for Segment D2 with a surface rupture with of 1.25 km.

SCENARIO 1: DISPLACEMENT ALONG SEGMENT A:

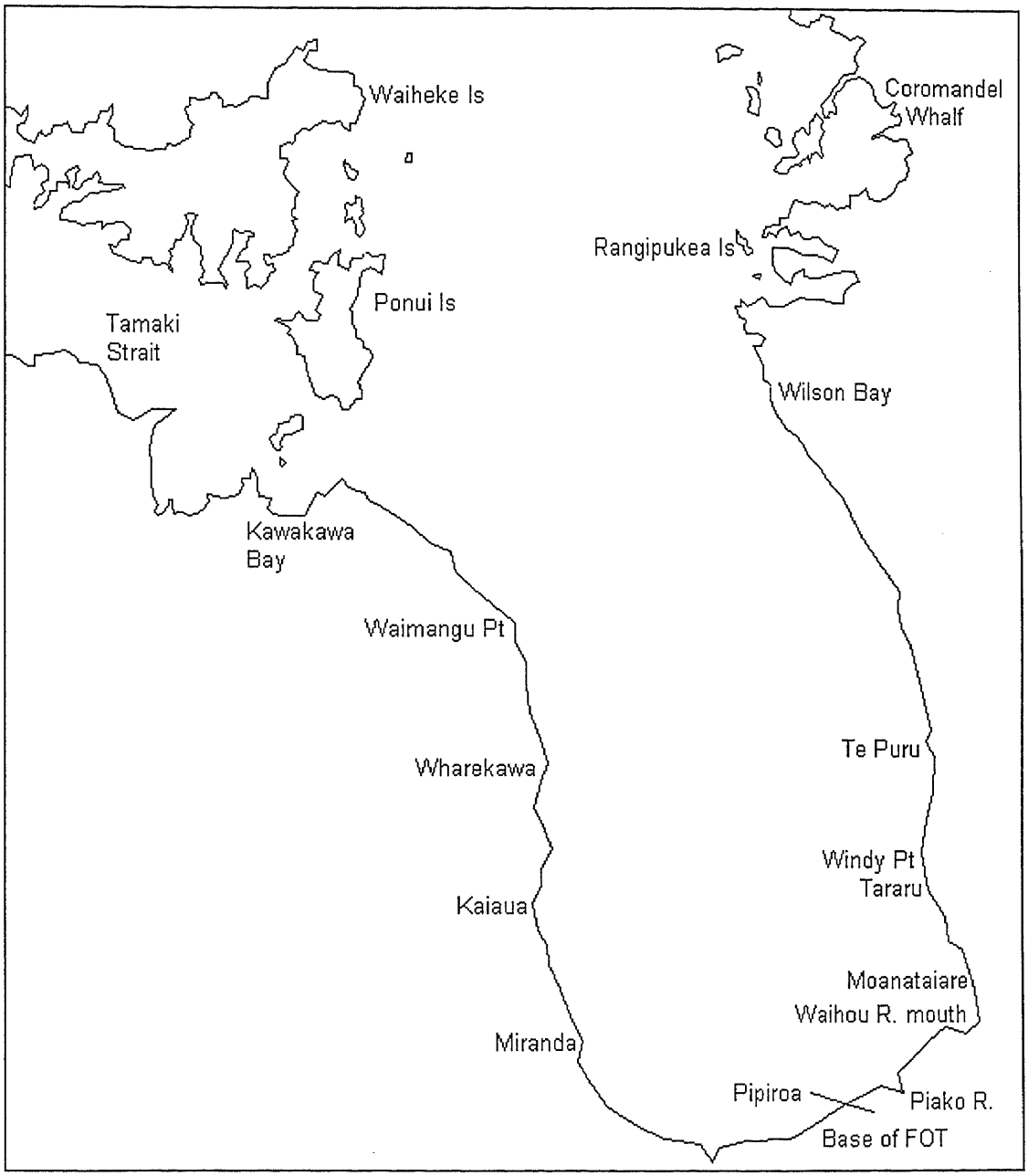

Figure A9.1: Map illustrating locations mentioned during discussion of wave heights and current velocities resulting from displacement along segment A & B.

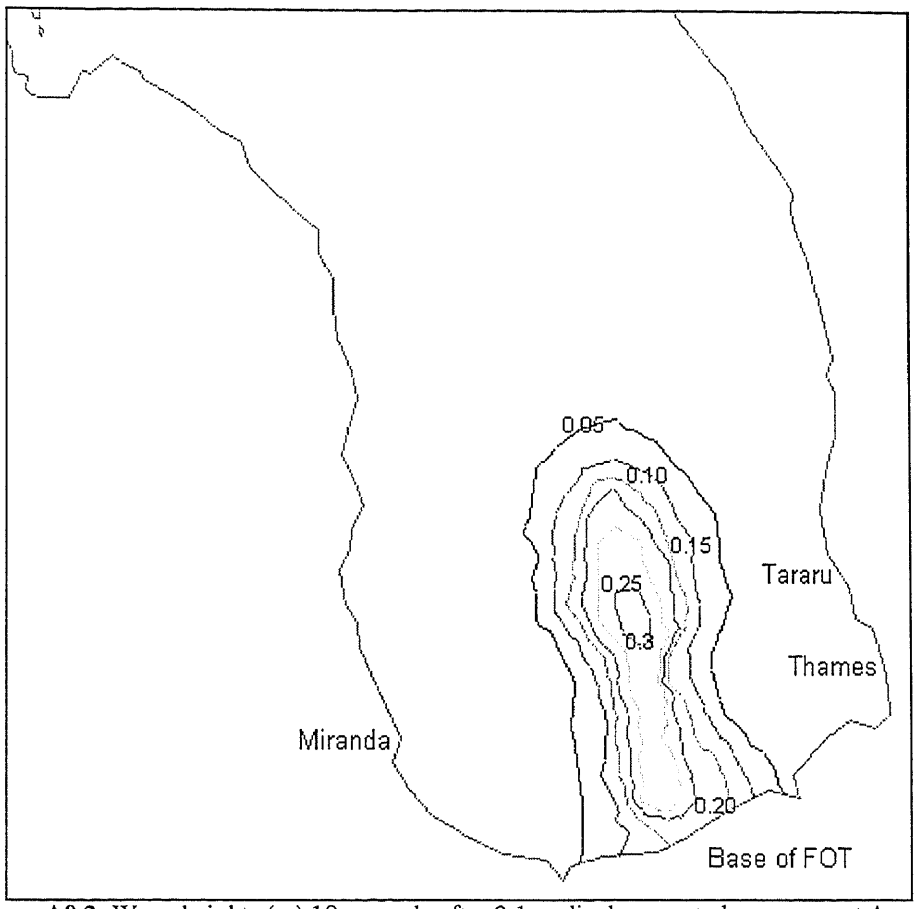

Figure A9.2: Wave heights (m) 10 seconds after 2.1 m displacement along segment A.

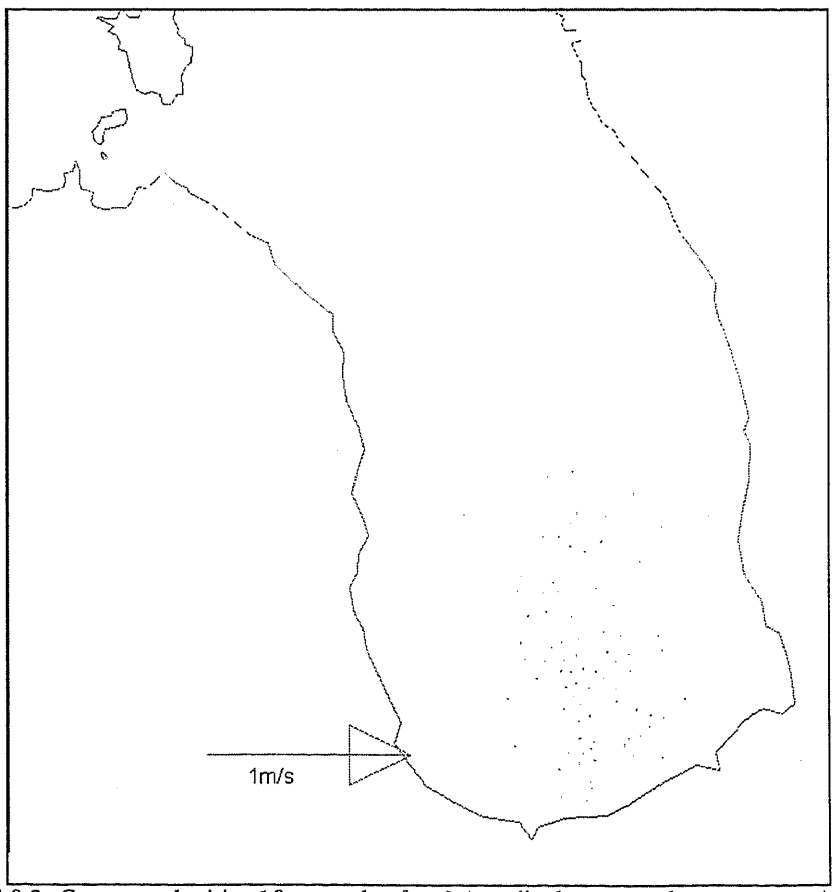

Figure A9.3: Current velocities 10 seconds after 2.1 m displacement along segment A.

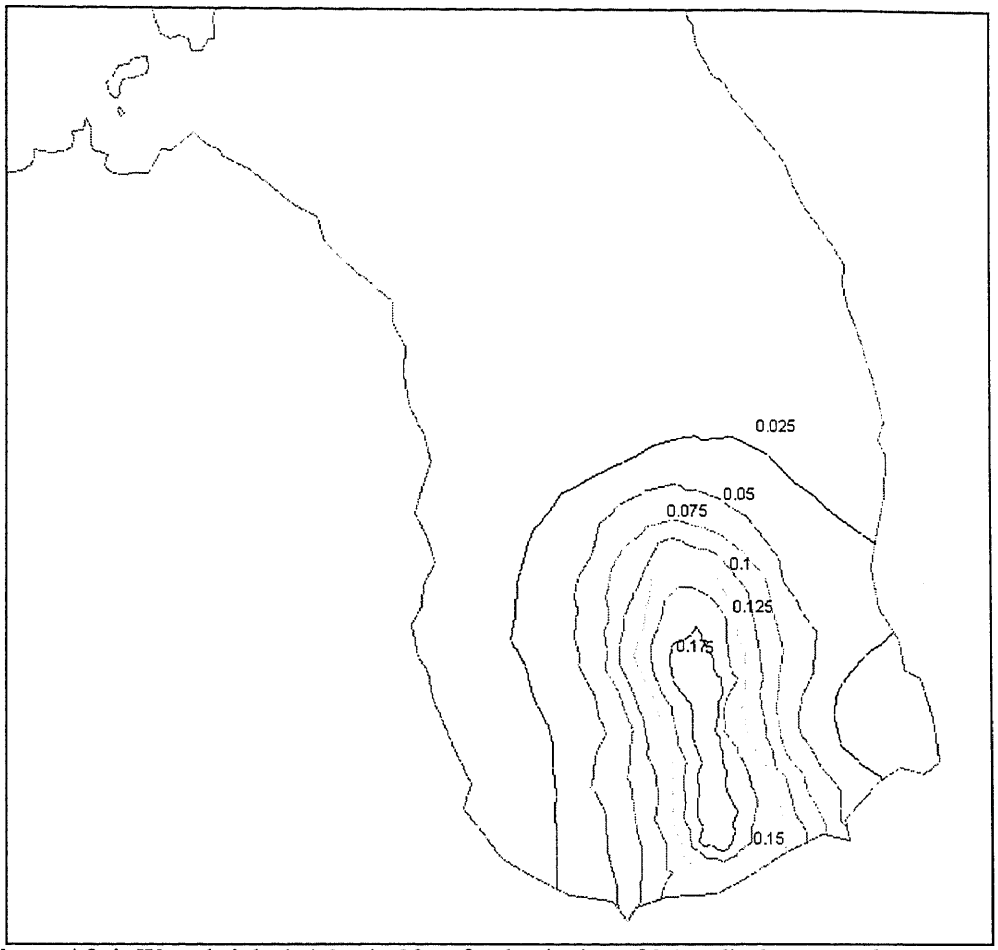

Figure A9.4: Wave height (m) 3 min 30 s after beginning of 2.1 m displacement along segment A

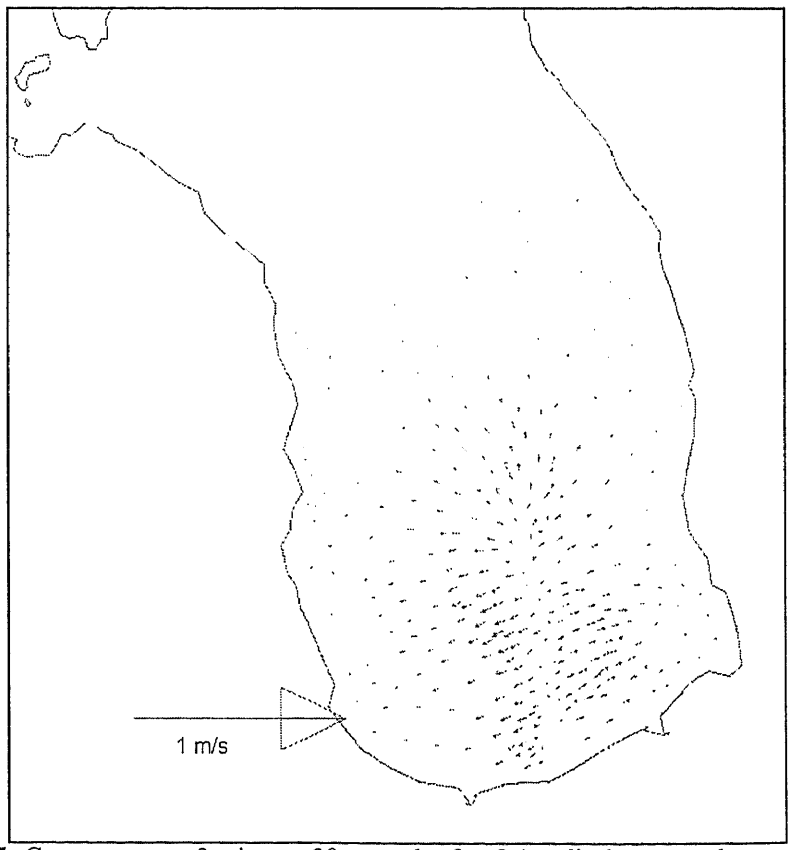

Figure A9.5: Current pattern 3 minutes 30 seconds after 2.1 m displacement along segment A.

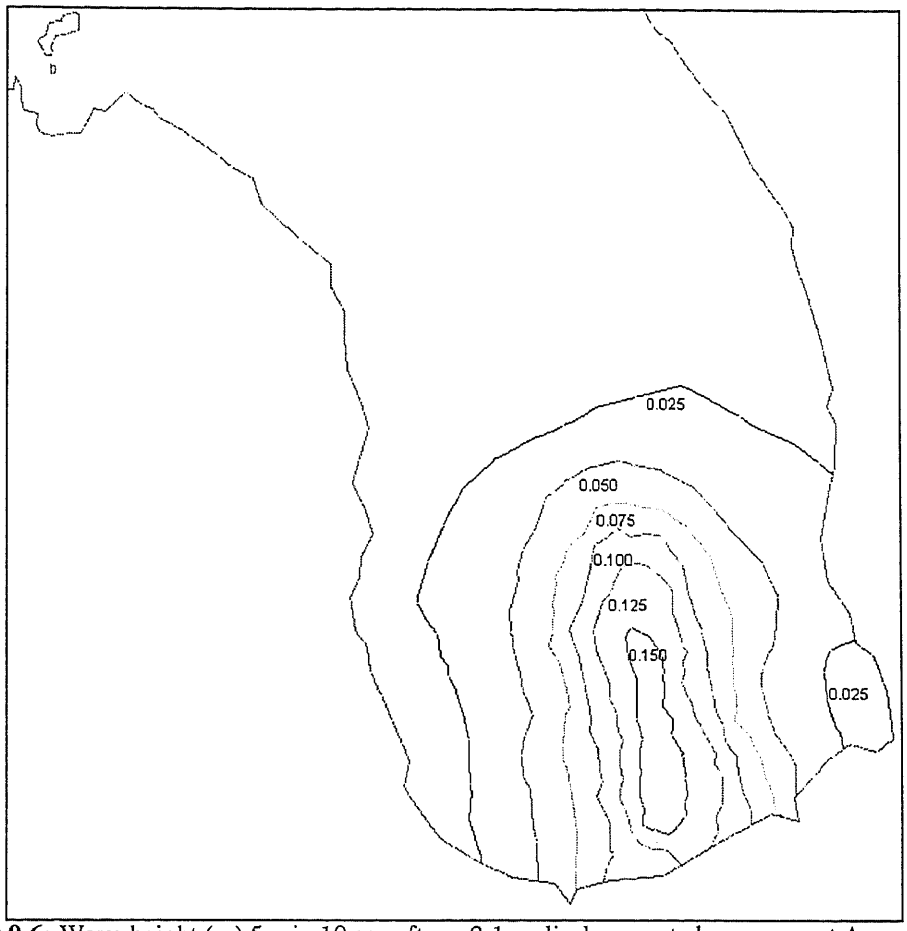

Figure A9.6: Wave height (m) 5 min 10 sec after a 2.1 m displacement along segment A.

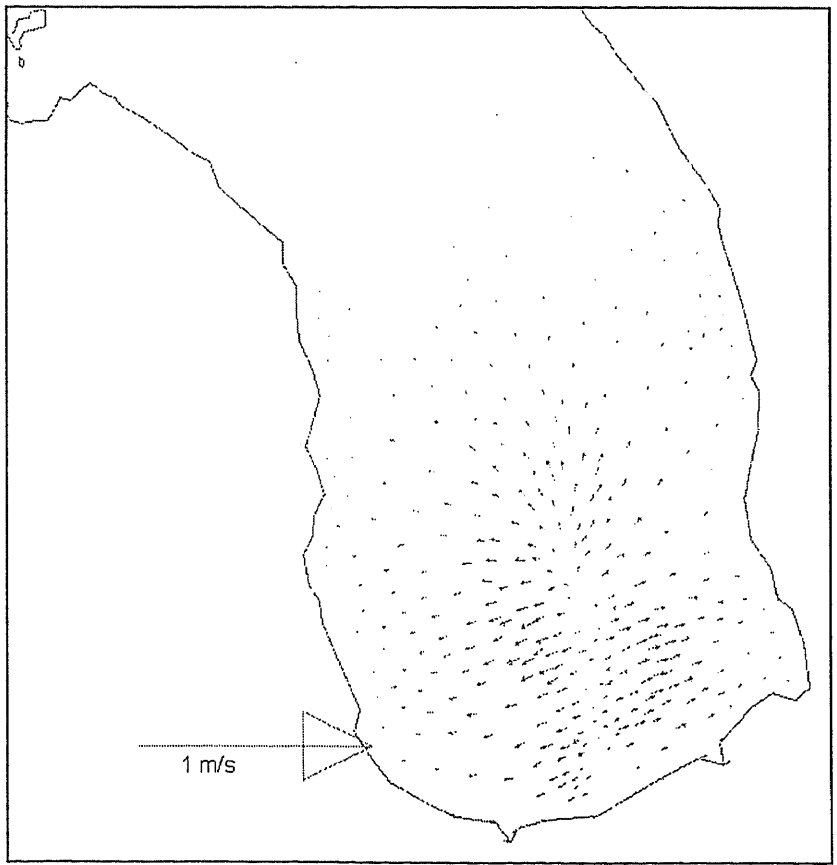

Figure A9.7: Current pattern 5 min. 10 sec after 2.1 m displacement along segment A.

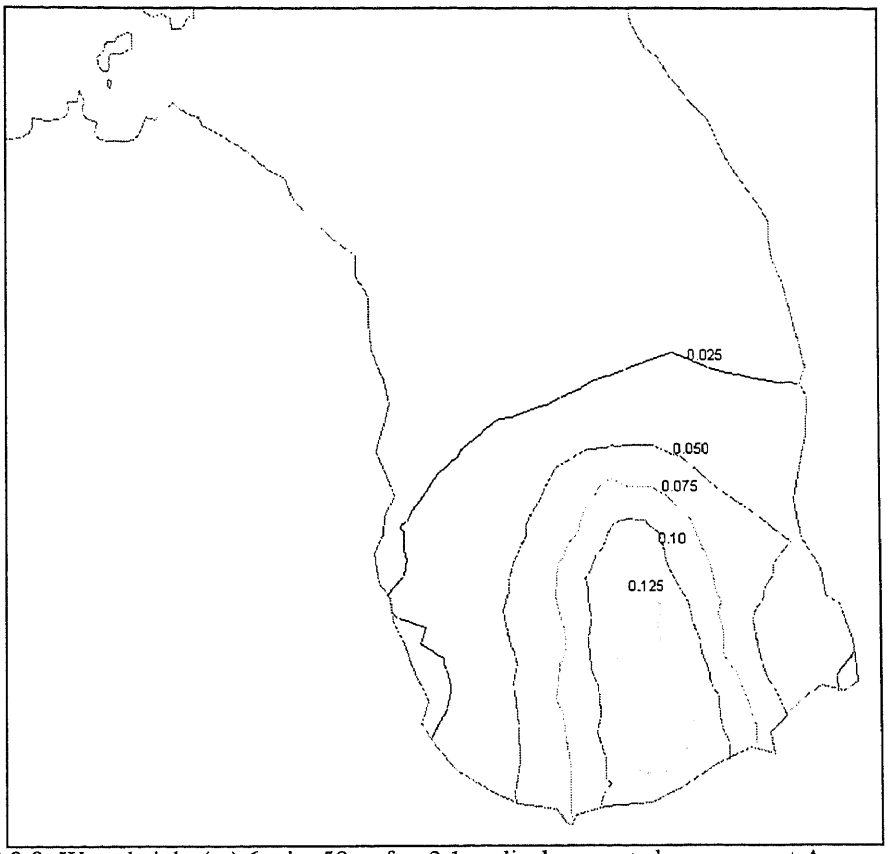

Figure A9.8: Wave height (m) 6 min. 50 s after 2.1 m displacement along segment A.

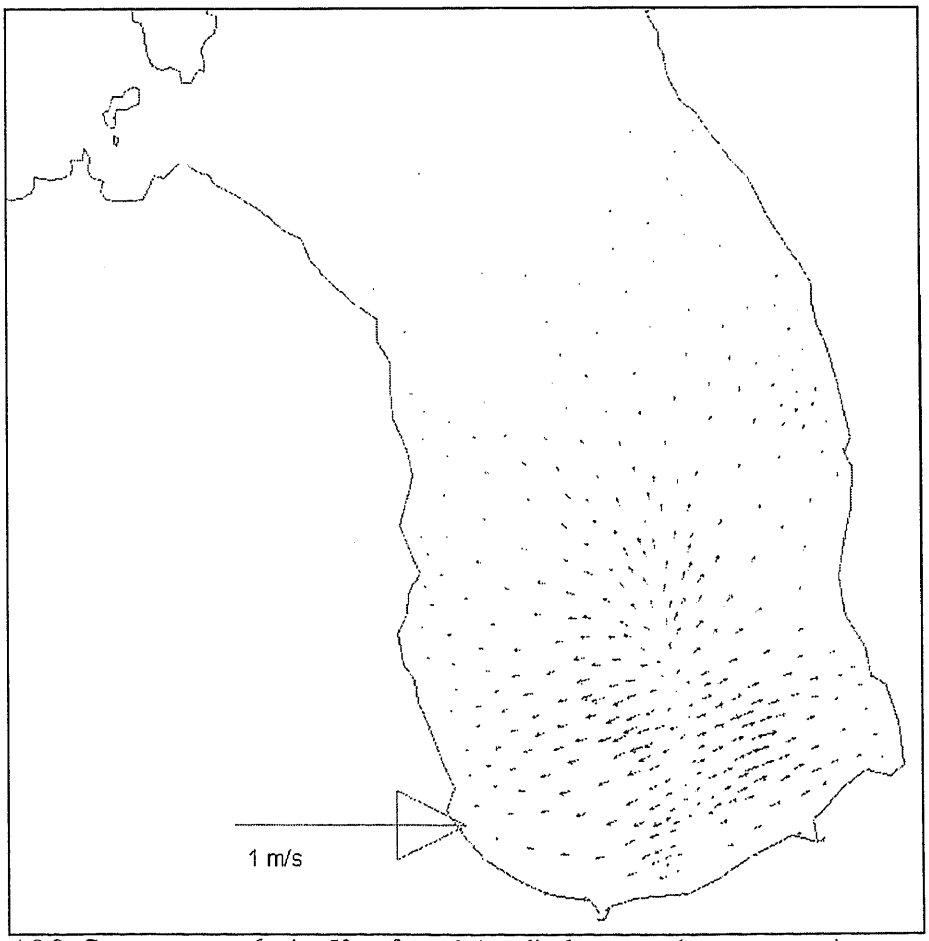

Figure A9.9: Current pattern 6 min. 50 s after a 2.1 m displacement along segment A.

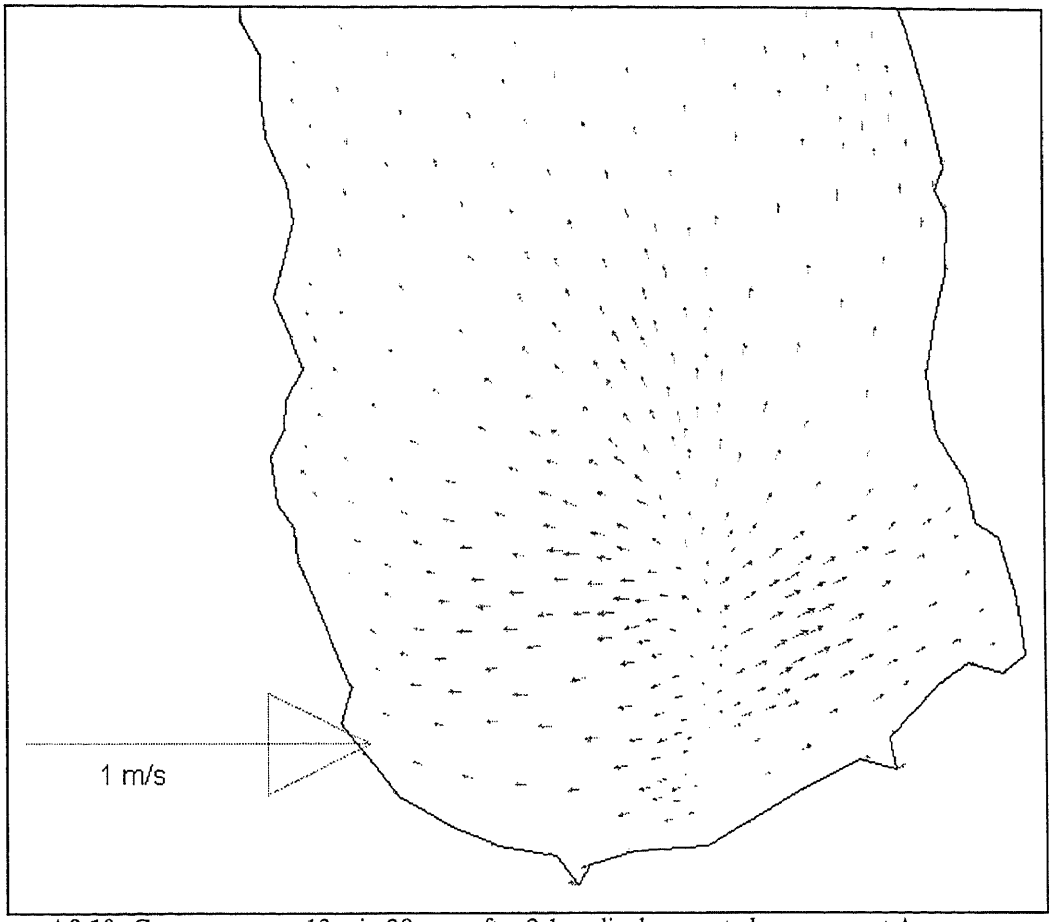

Figure A9.10: Current pattern 13 min 30 sec. after 2.1 m displacement along segment A

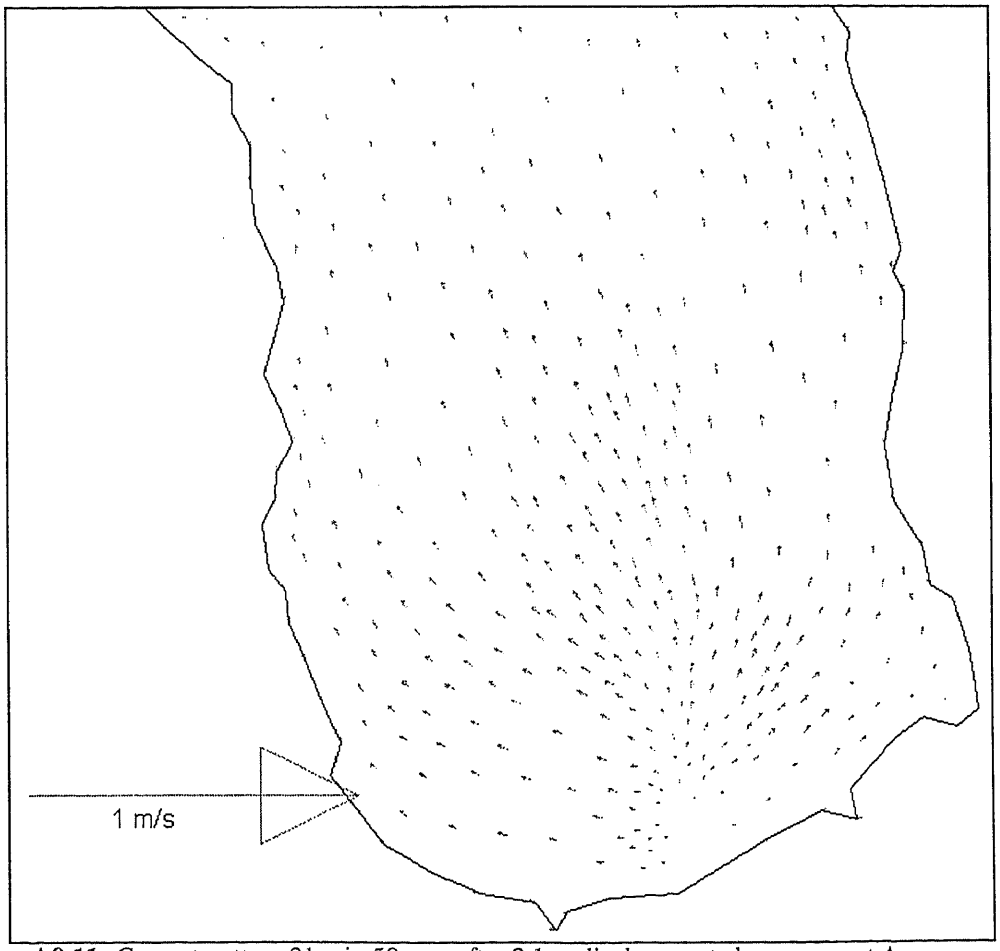

Figure A9.11: Current pattern 21 min 50 sec. after 2.1 m displacement along segment A.

SCENARIO 2: DISPLACEMENT ALONG SEGMENT B

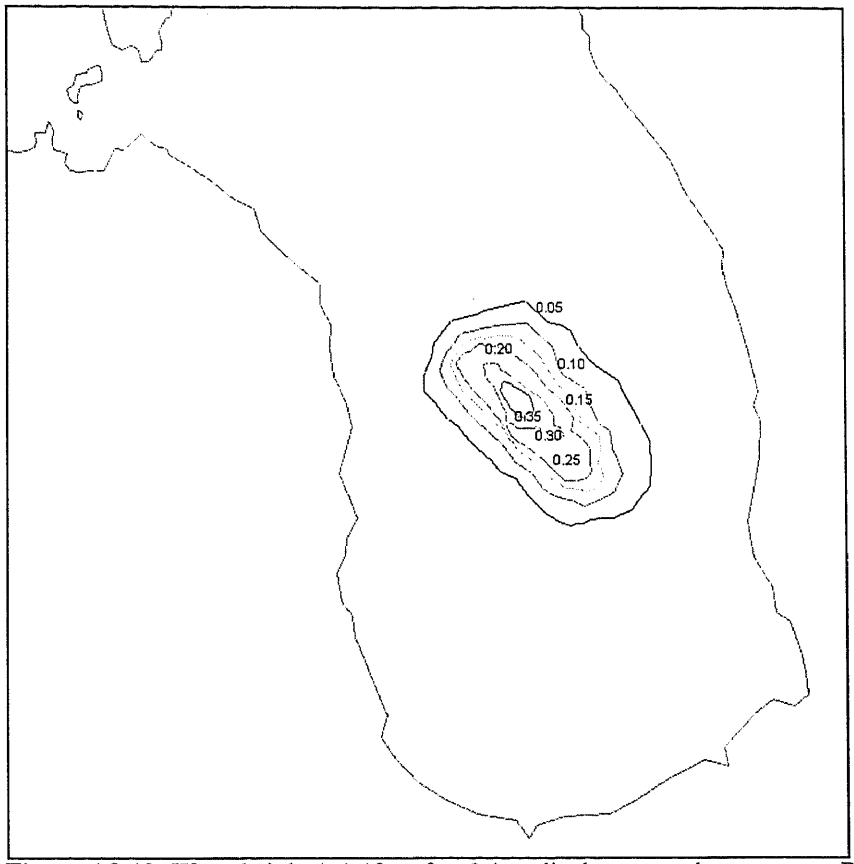

Figure A9.12: Wave height (m) 10 s after 2.1 m displacement along segment B.

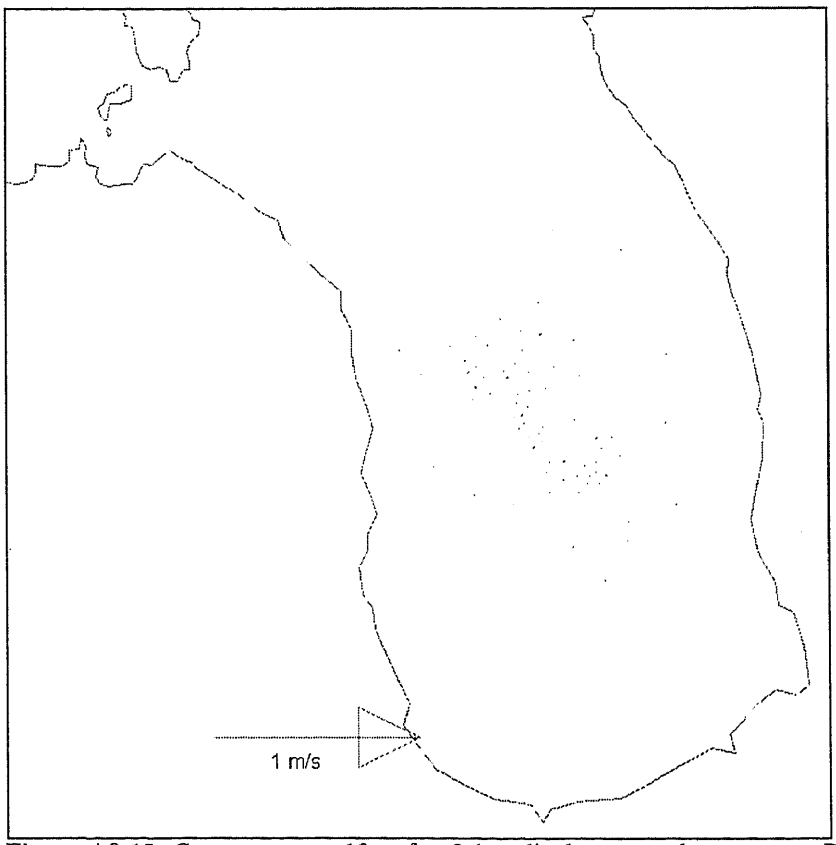

Figure A9.13: Current pattern 10 s after 2.1 m displacement along segment B.

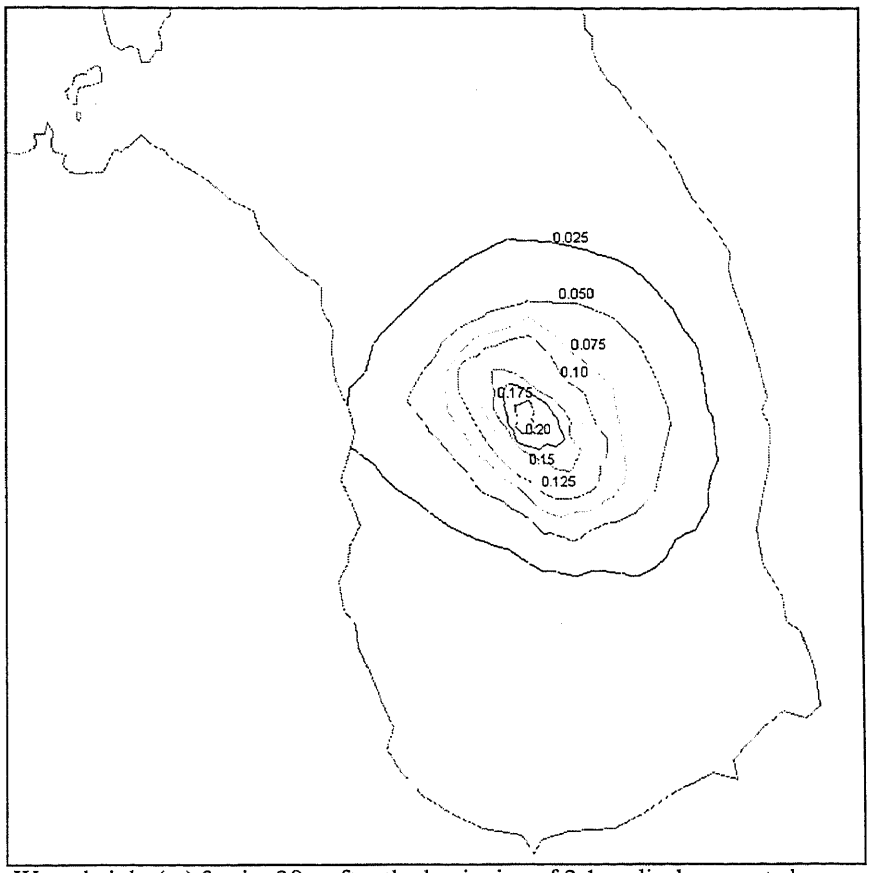

Figure A9.14: Wave height (m) 3 min. 30 s after the beginning of 2.1 m displacement along segment B.

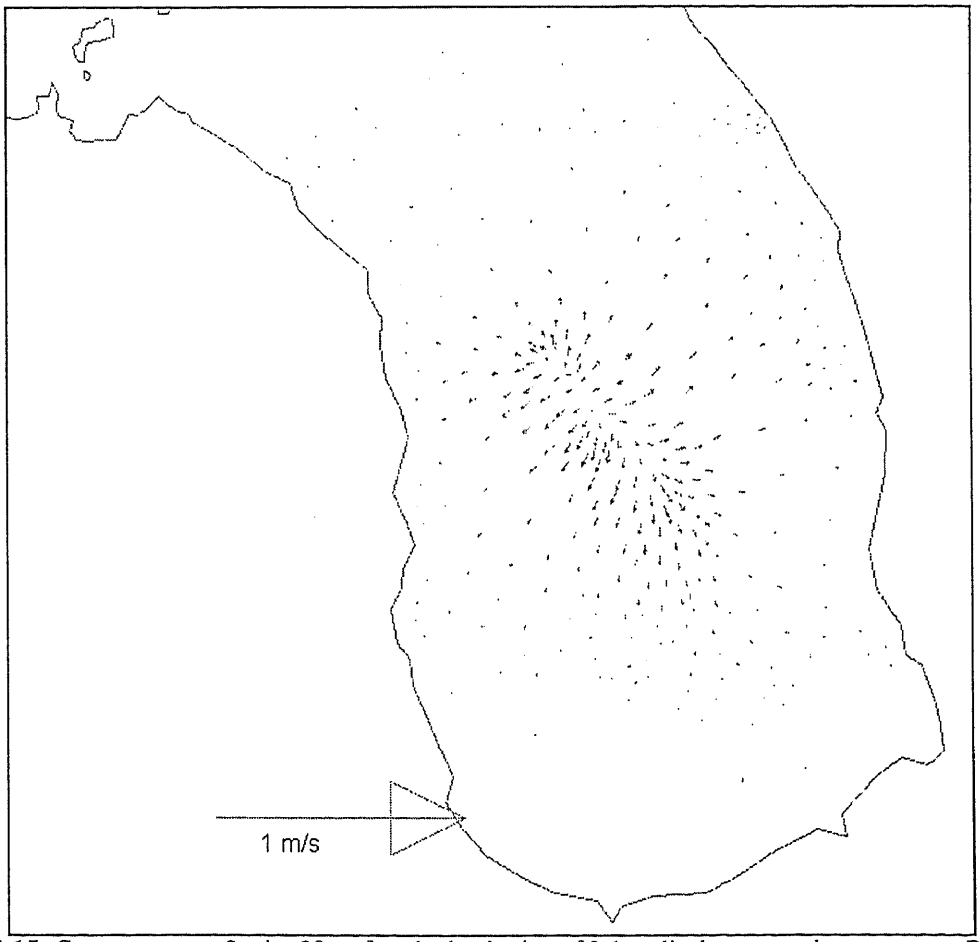

Figure A9.15: Current pattern 3 min. 30 s after the beginning of 2.1 m displacement along segment B.

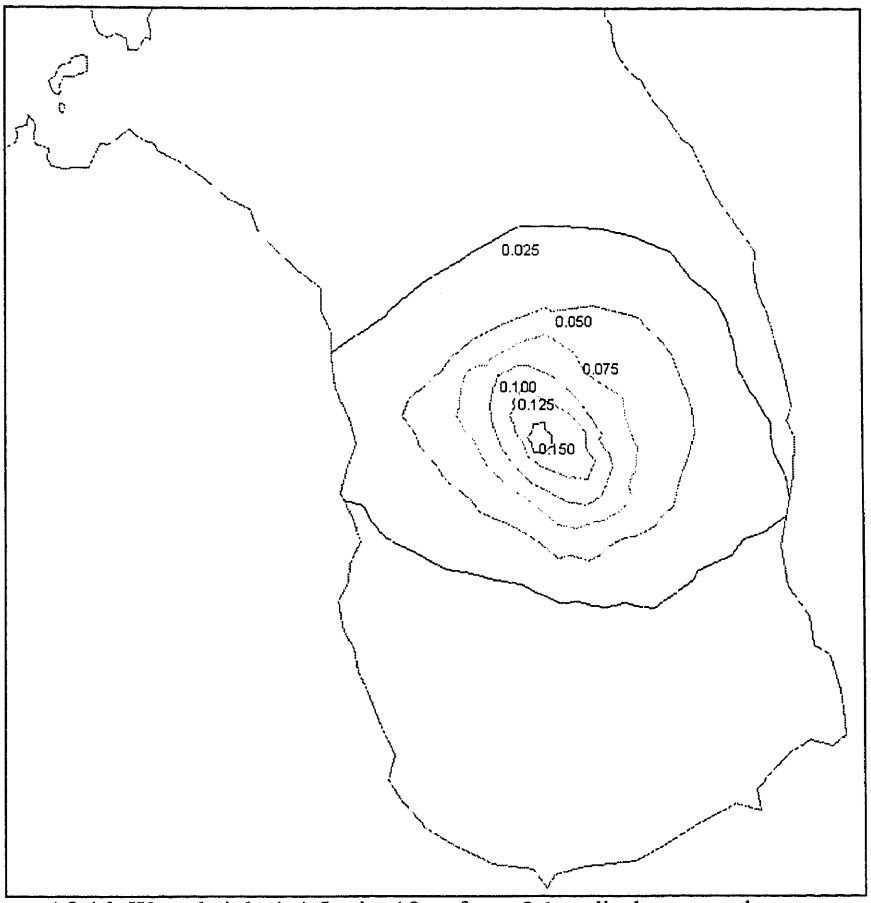

Figure A9.16: Wave height (m) 5 min. 10 s after a 2.1 m displacement along segment B.

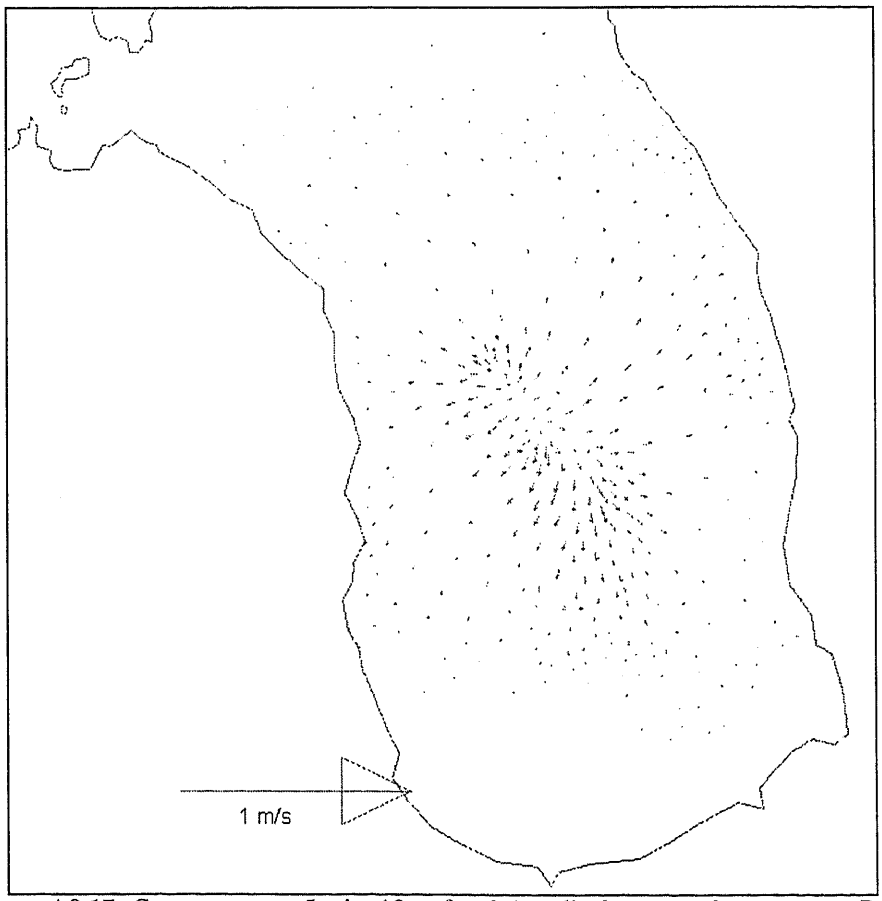

Figure A9.17: Current pattern 5 min. 10 s after 2.1 m displacement along segment B.

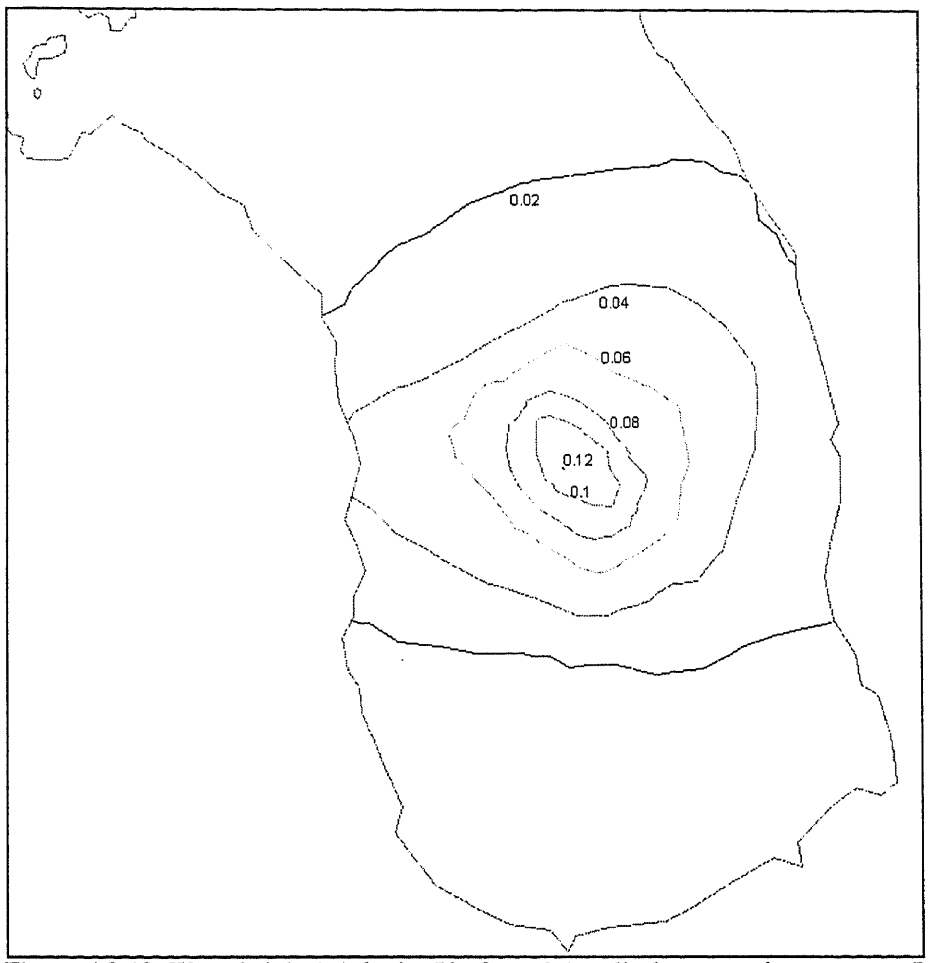

Figure A9.18: Wave height (m) 6 min. 50 after a 2.1 m displacement along segment B.

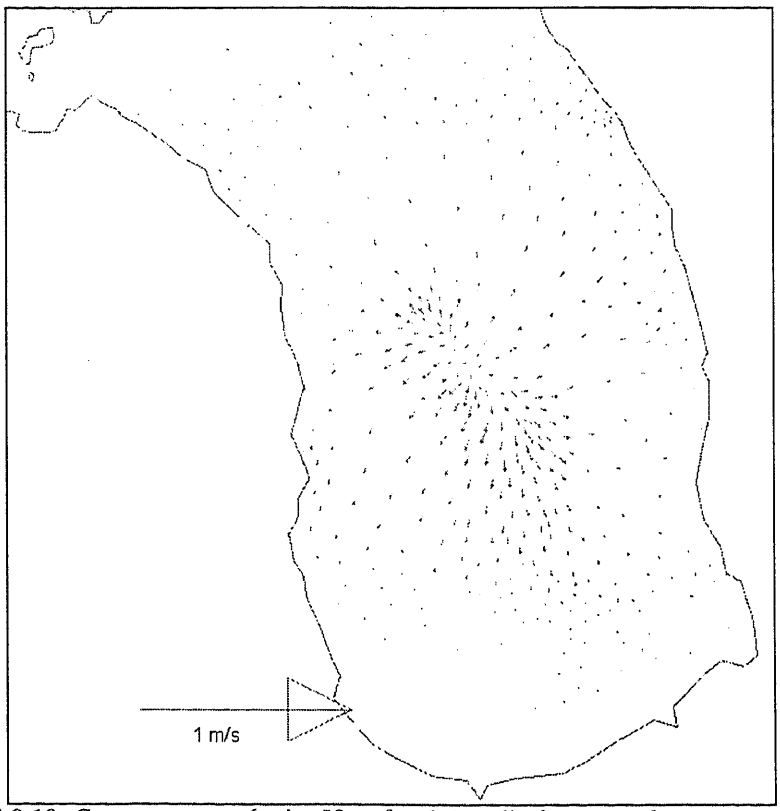

Figure A9.19: Current pattern 6 min. 50 s after 2.1 m displacement along segment B.

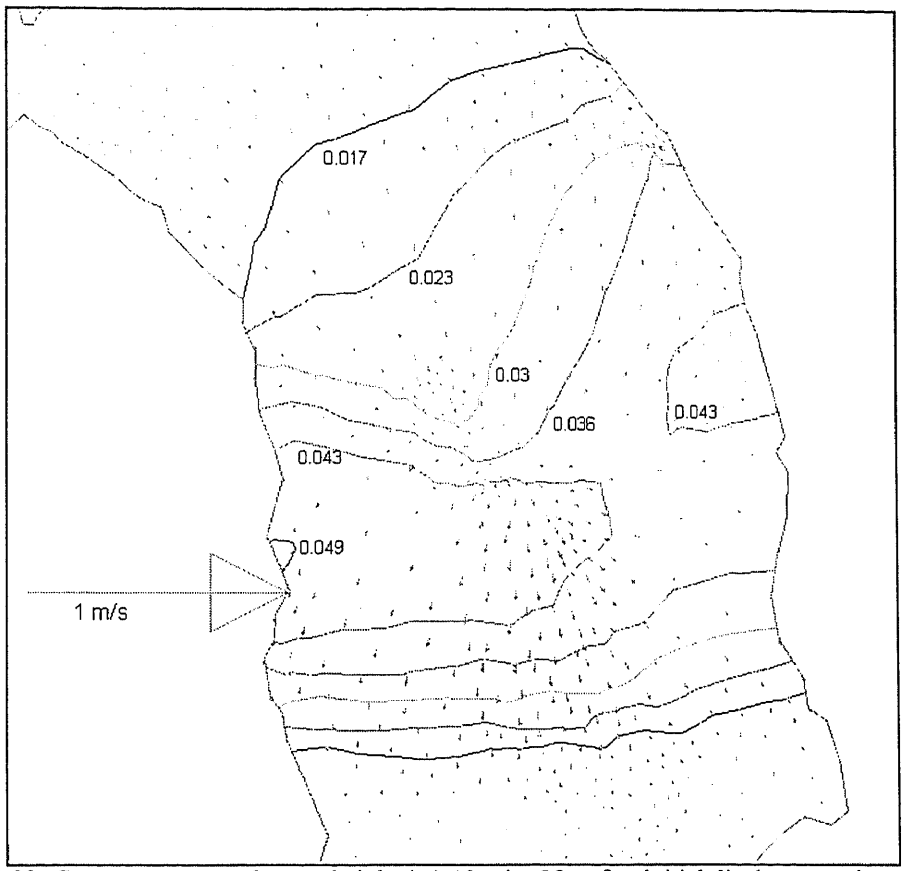

Figure A9.20: Current pattern and wave height (m) 13 min, 30 s after initial displacement began.

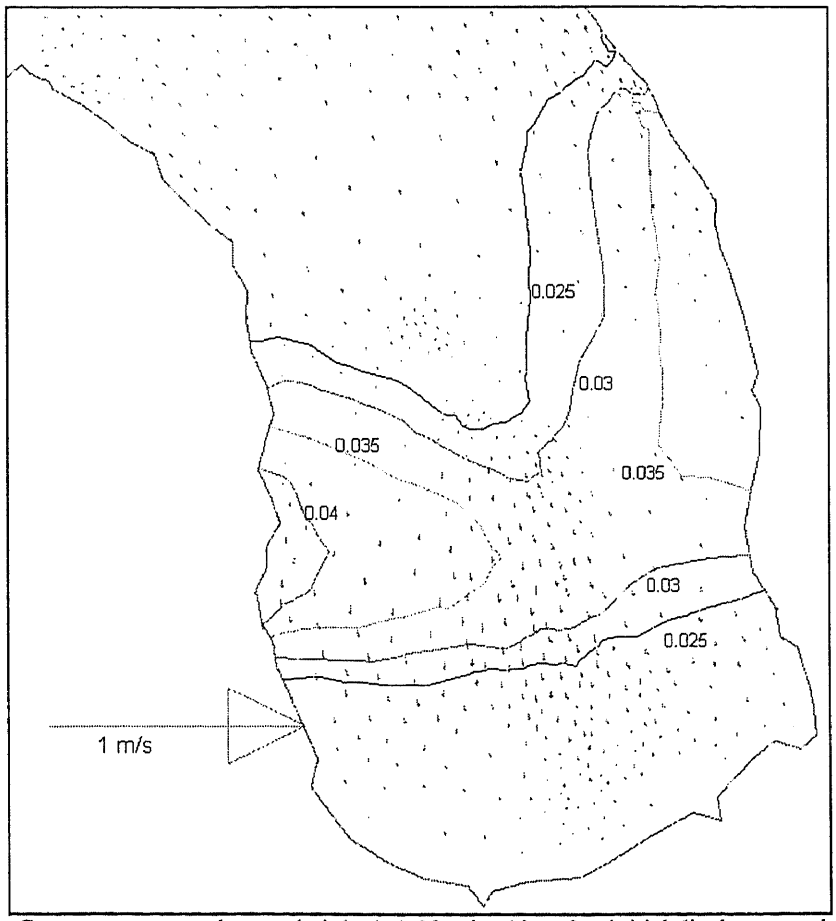

Figure A9.21: Current pattern and wave height (m) 20 min, 10 s after initial displacement began.

SCENARIO 3: DISPLACEMENT ALONG SEGMENT C

Figure A9.22: Map illustrating locations mentioned during discussion of wave heights and current velocities resulting from displacement along segment C.

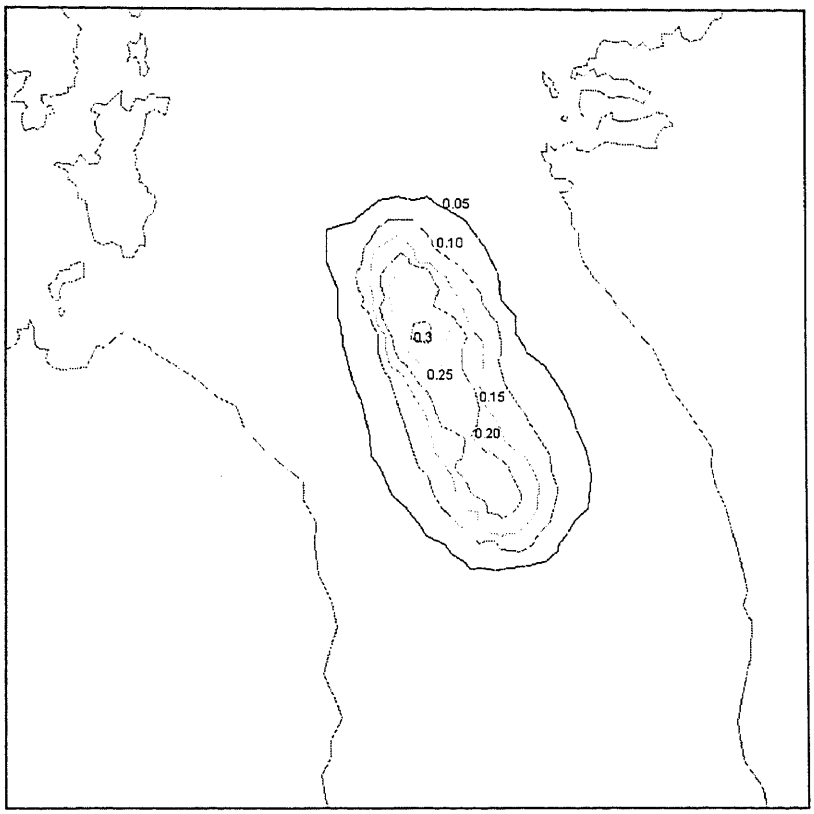

Figure A9.23: Wave height (m) 10 s after beginning of 2.1 m displacement along segment C.

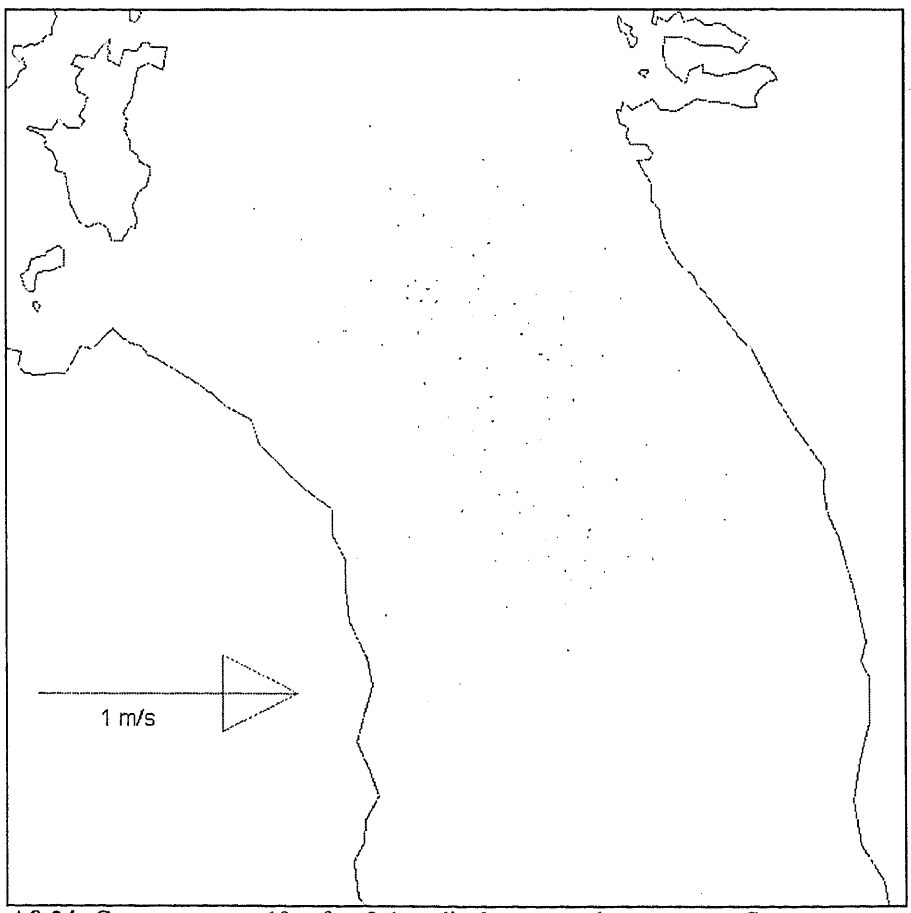

Figure A9.24: Current pattern 10s after 2.1 m displacement along segment C.

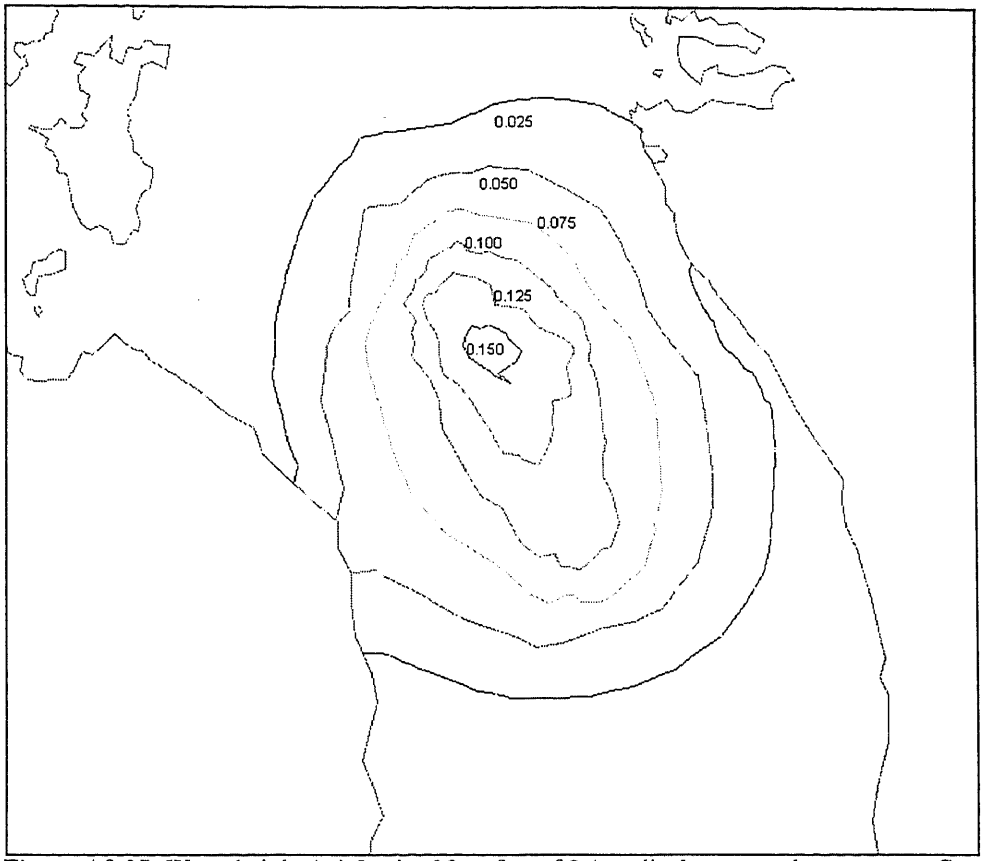

Figure A9.25: Wave height (m) 3 min. 30 s after of 2.1 m displacement along segment C.

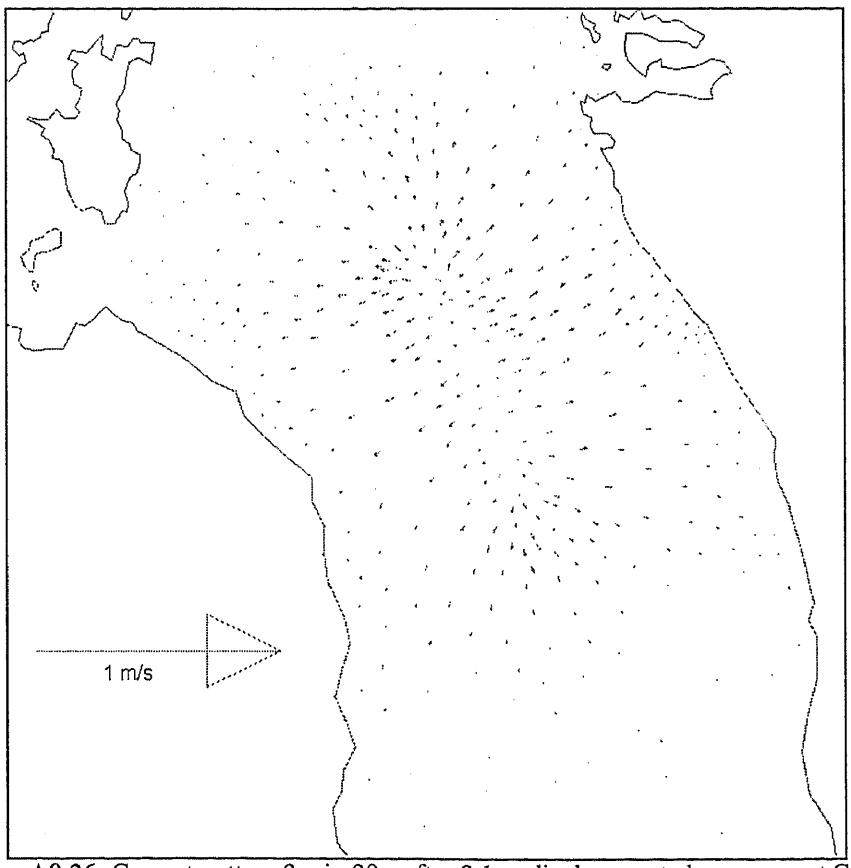

Figure A9.26: Current pattern 3 min 30 s after 2.1 m displacement along segment C.

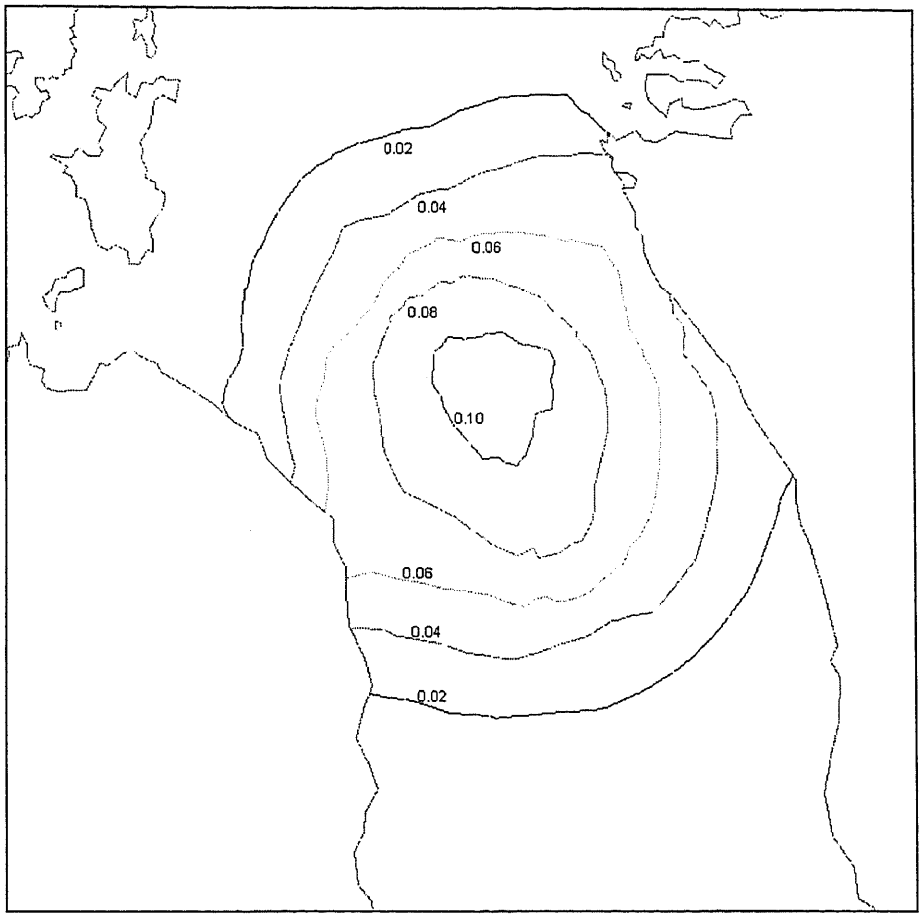

Figure A9.27: Wave height (m) 5mins 10 s after of 2.1 m displacement along segment C.

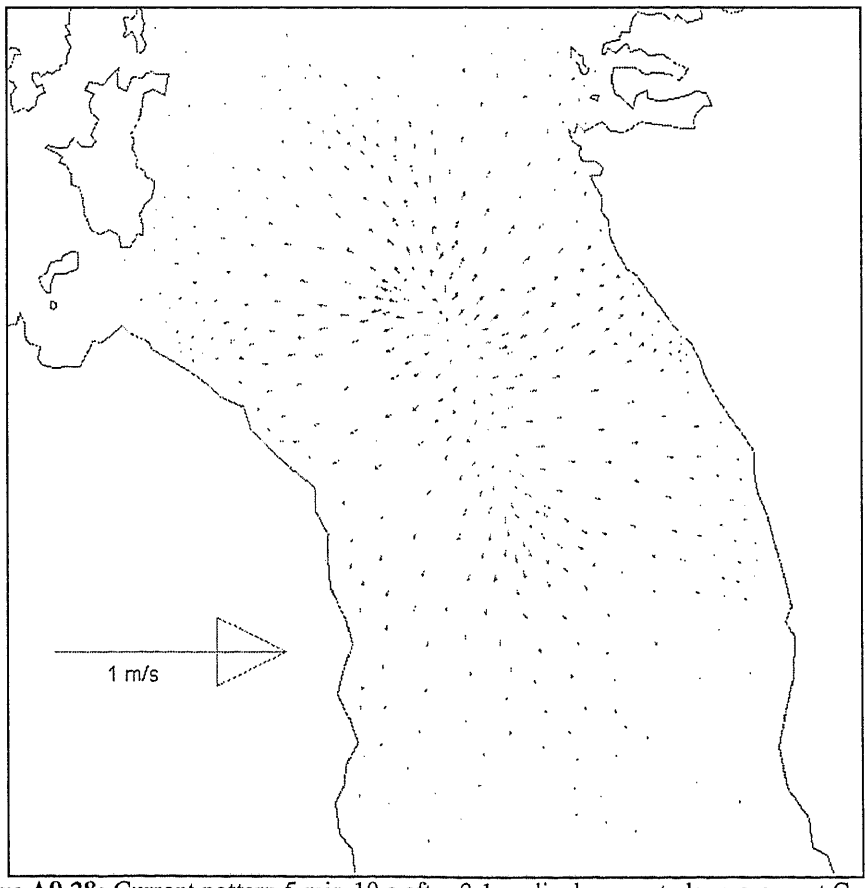

Figure A9.28: Current pattern 5 min 10 s after 2.1 m displacement along segment C.

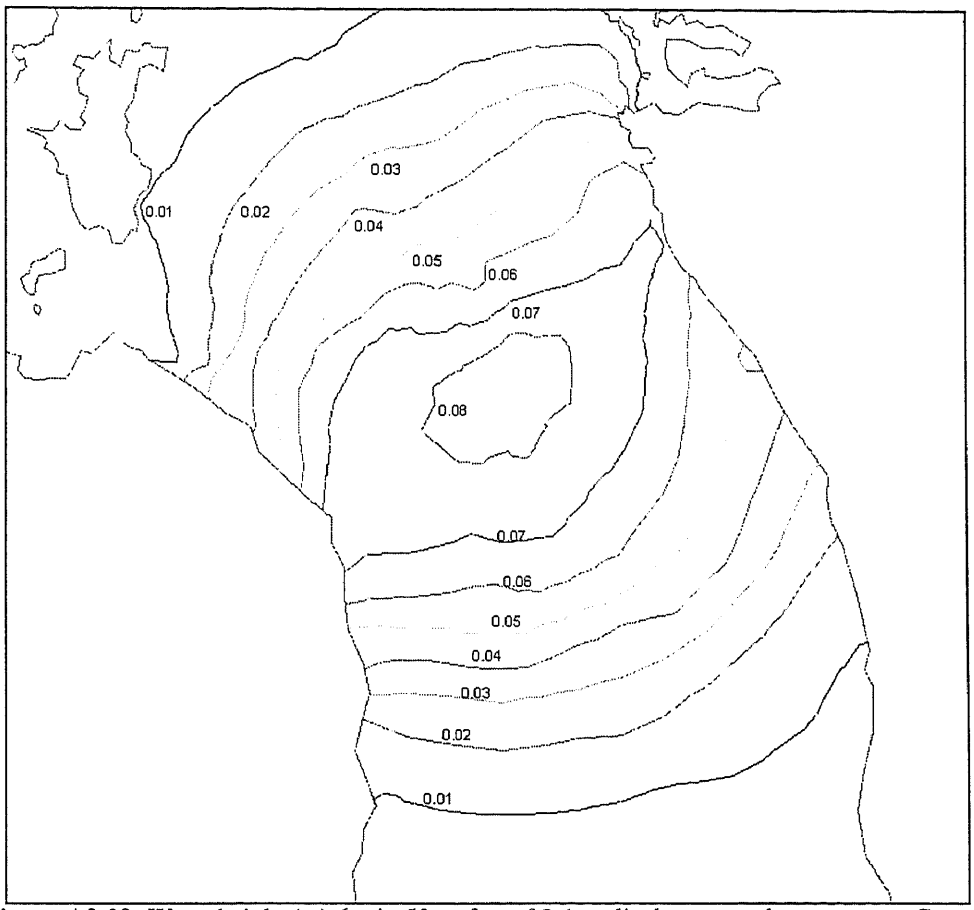

Figure A9.29: Wave height (m) 6 min 50 s after of 2.1 m displacement along segment C.

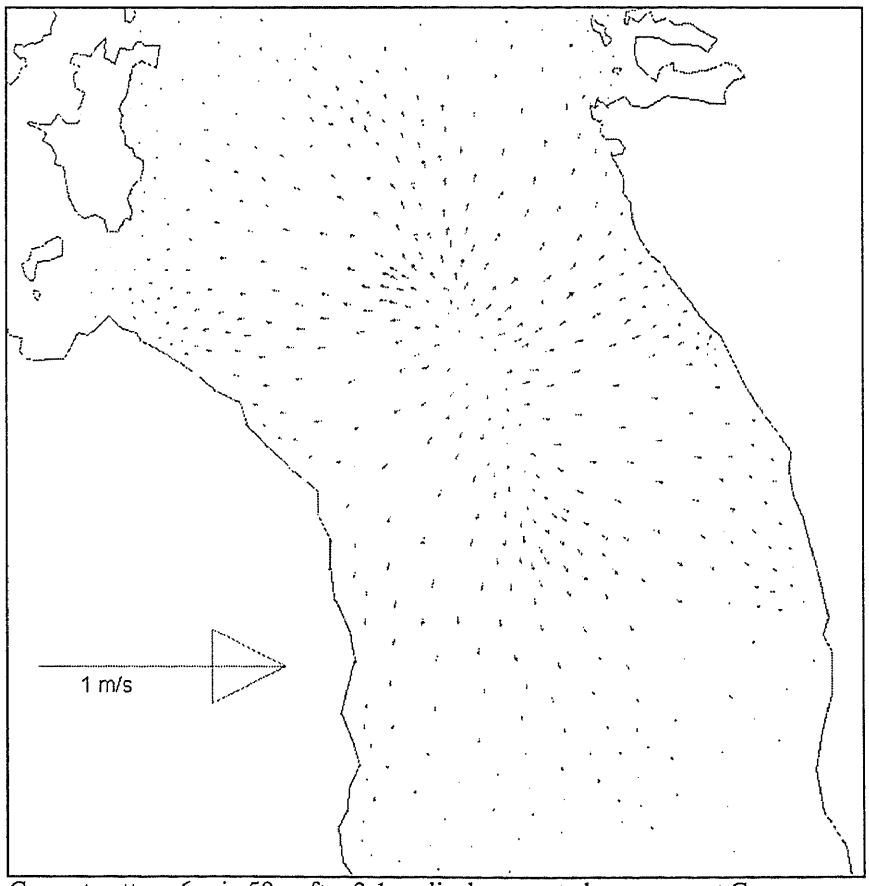

A9.30: Current pattern 6 min 50 s after 2.1 m displacement along segment C.

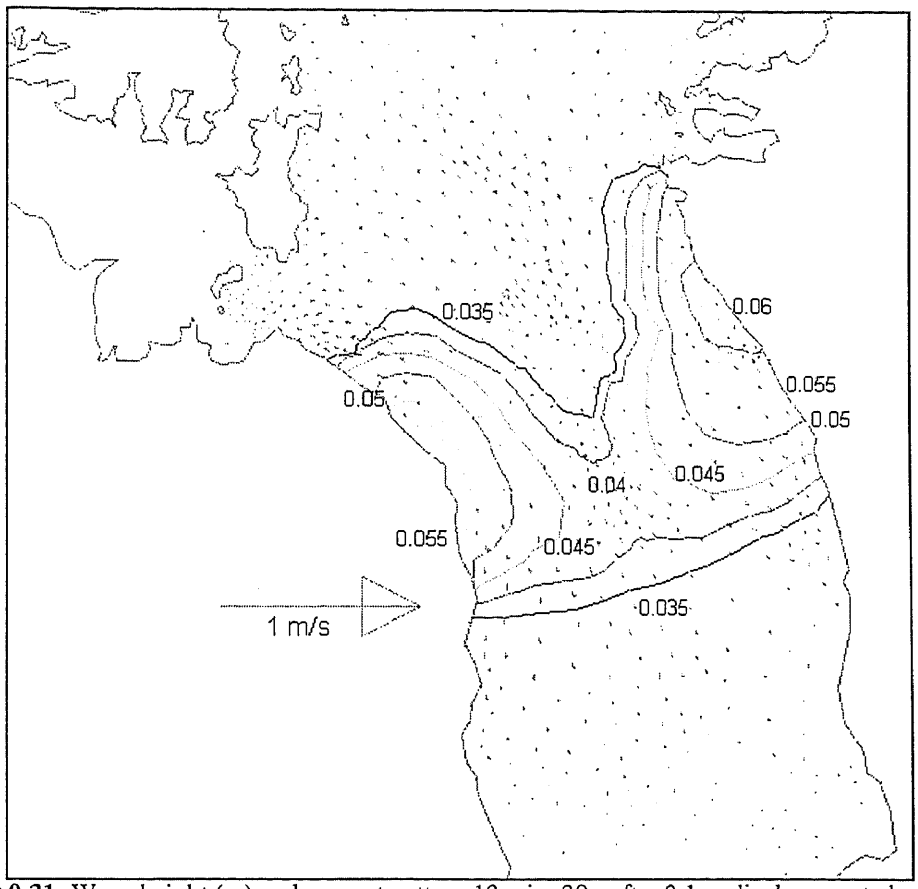

Figure A9.31: Wave height (m) and current pattern 13 min. 30 s after 2.1 m displacement along segment C.

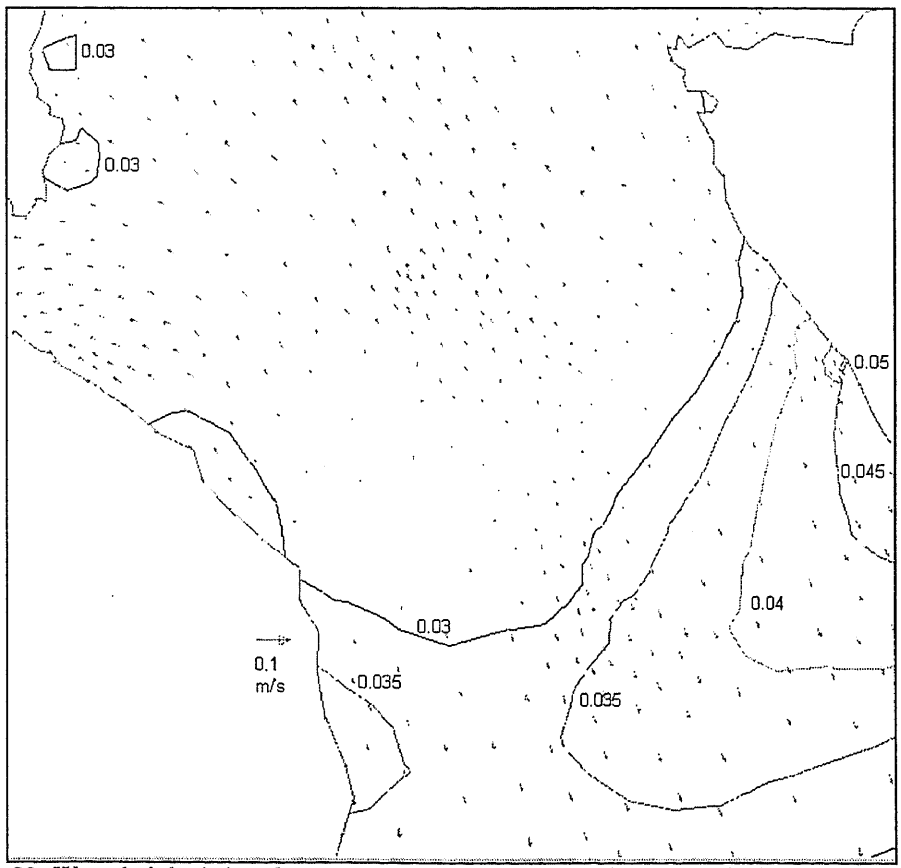

Figure A9.32: Wave height (m) and current pattern 20 min. 10 s after 2.1 m displacement along segment C.

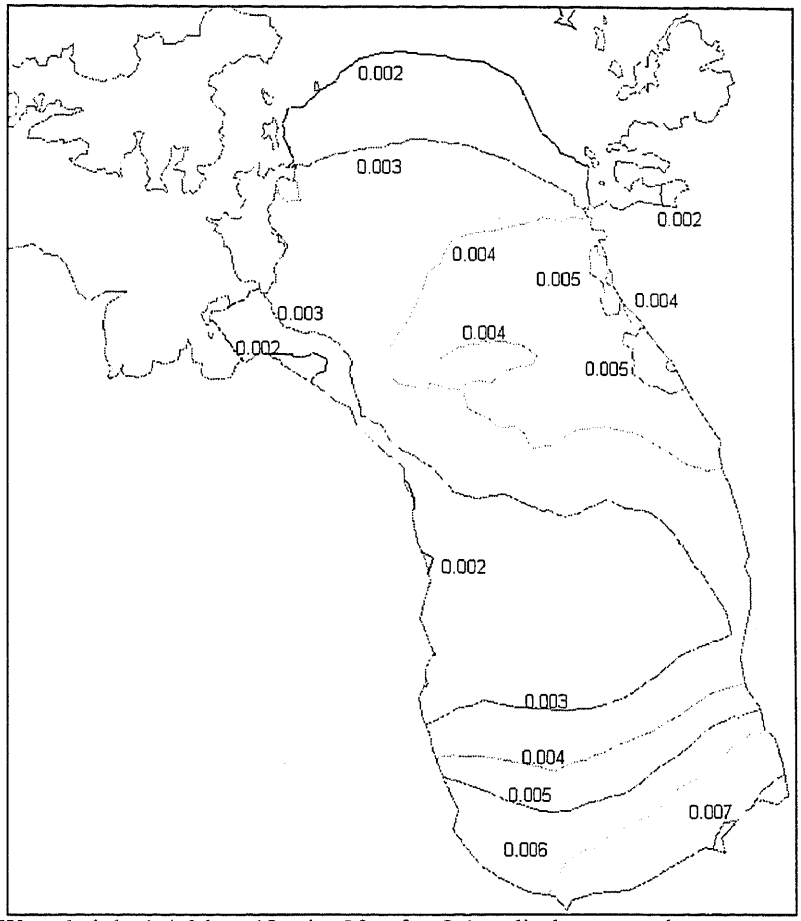

Figure A9.33: Wave height (m) 2 hrs, 18 min, 30s after 2.1 m displacement along segment C.

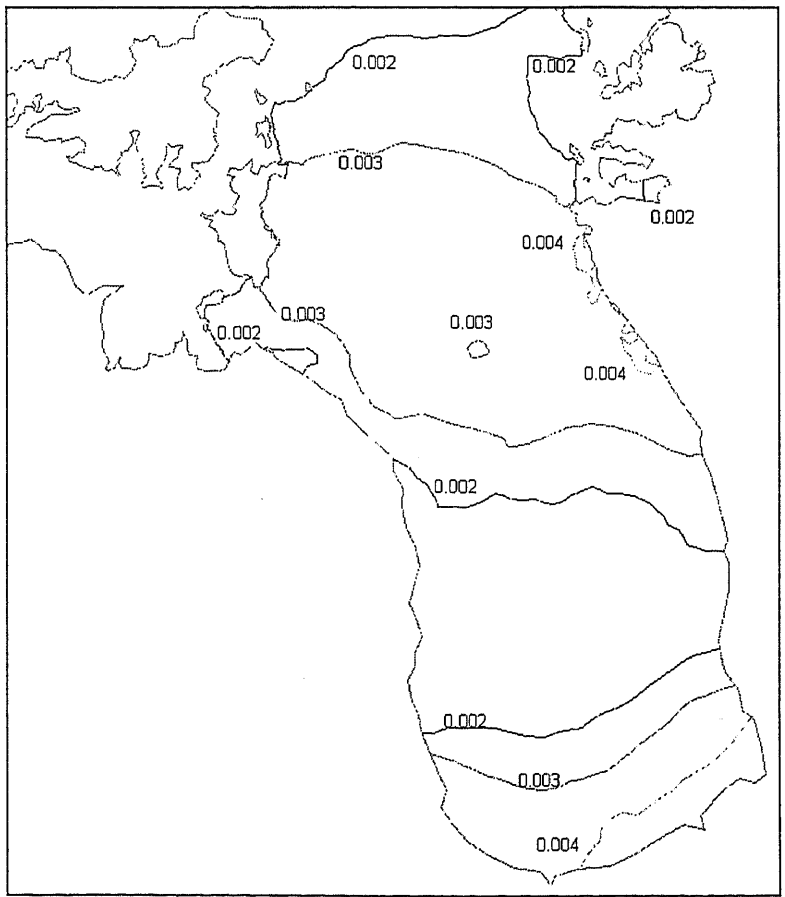

Figure A9.34: Wave height (m) 2 hrs, 26 min, 50s after 2.1 m displacement along segment C.

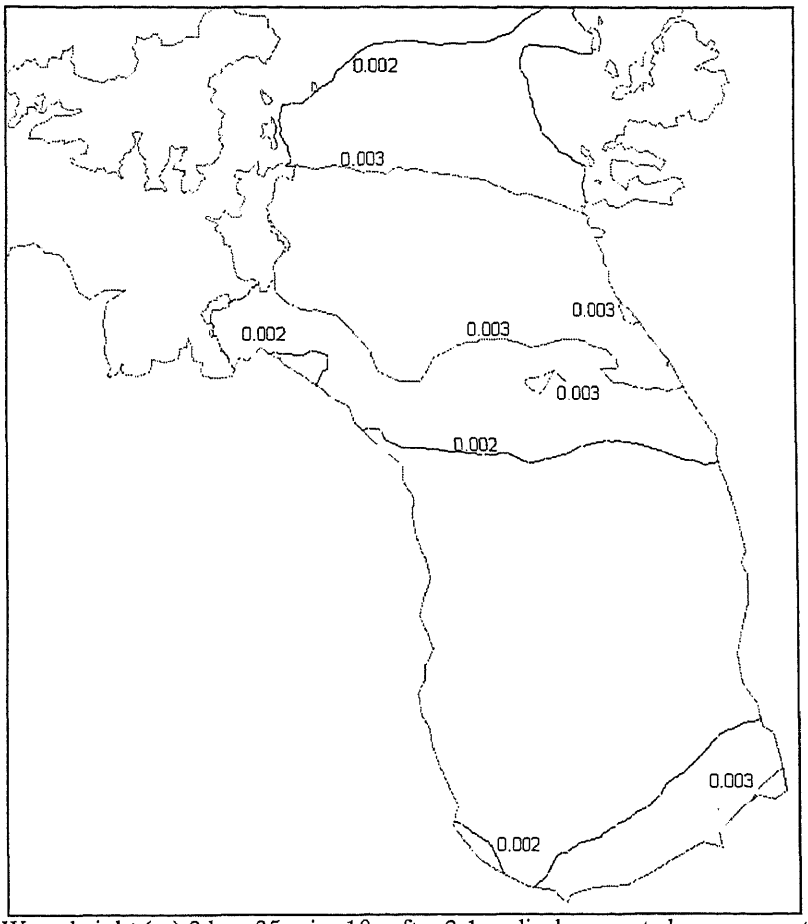

Figure A9.35: Wave height (m) 2 hrs, 35 min, 10s after 2.1 m displacement along segment C.

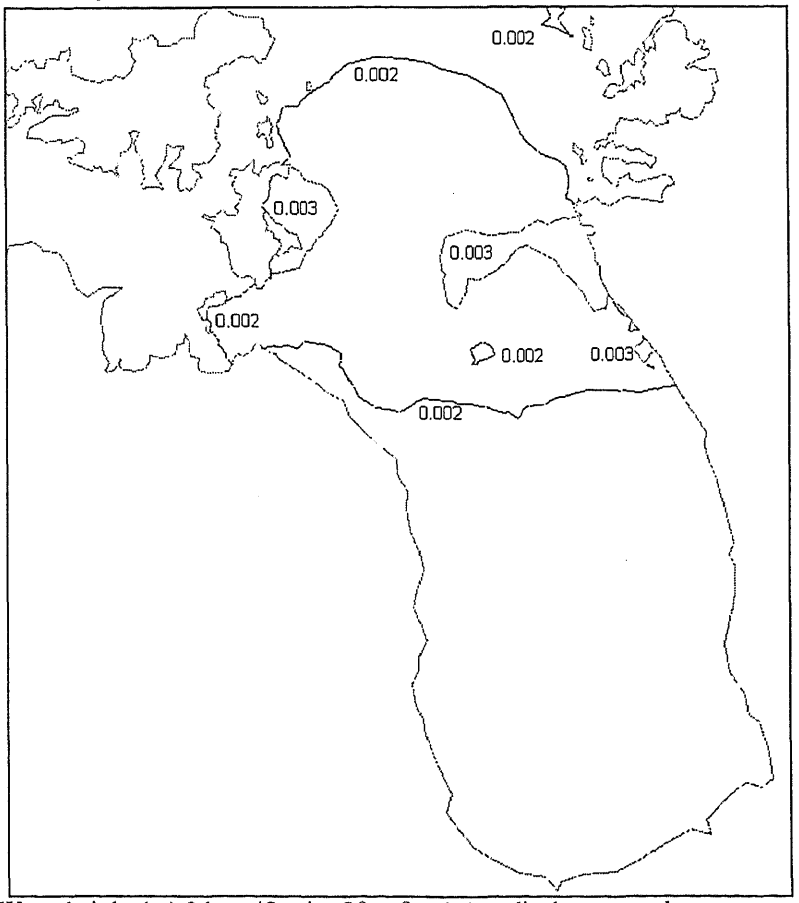

Figure A9.36: Wave height (m) 2 hrs, 43 min, 30s after 2.1 m displacement along segment C.

SCENARIO 4: DISPLACEMENT ALONG SEGMENT D1

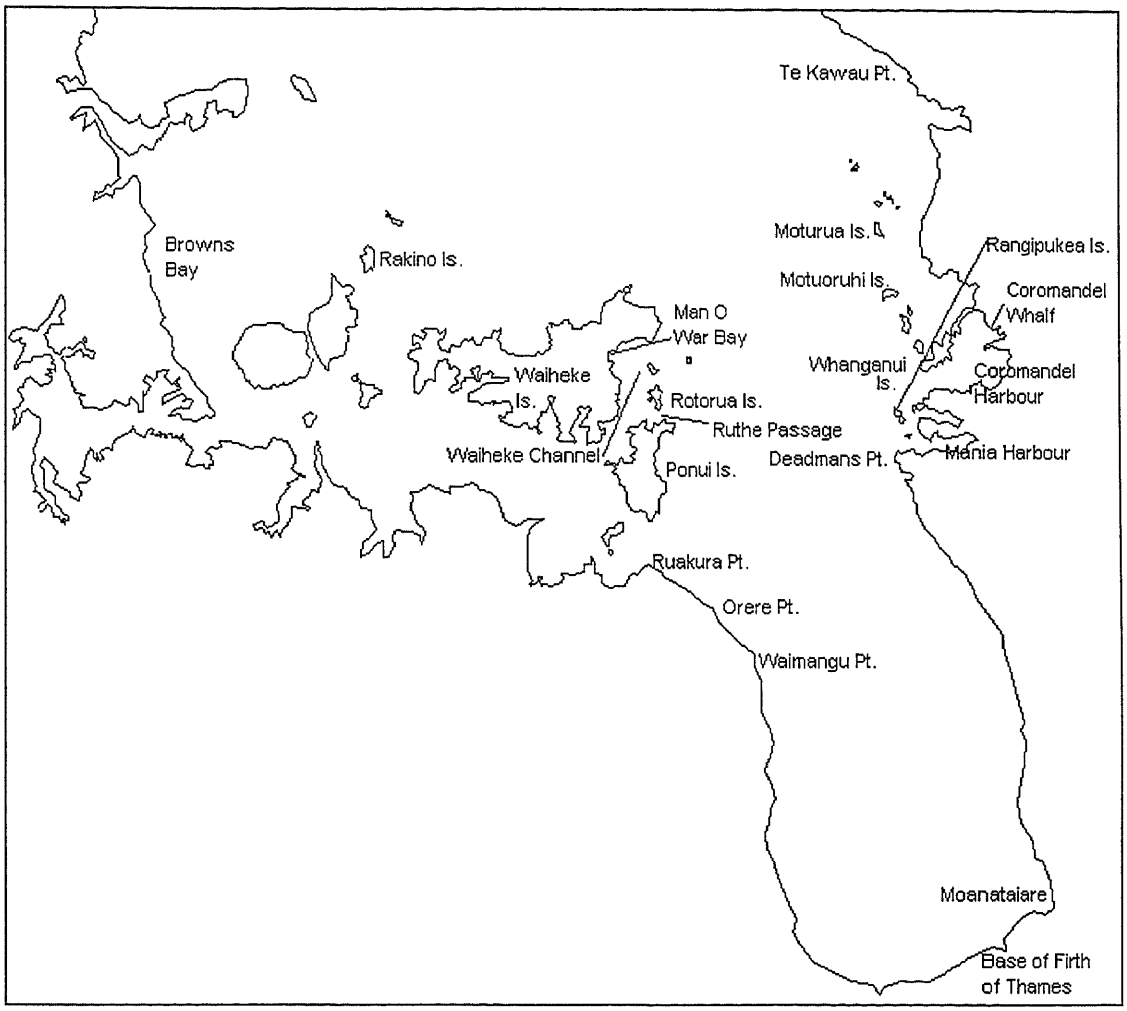

Figure A9.37: Map illustrating locations mentioned during discussion of wave heights and current velocities resulting from displacement along segment D1.

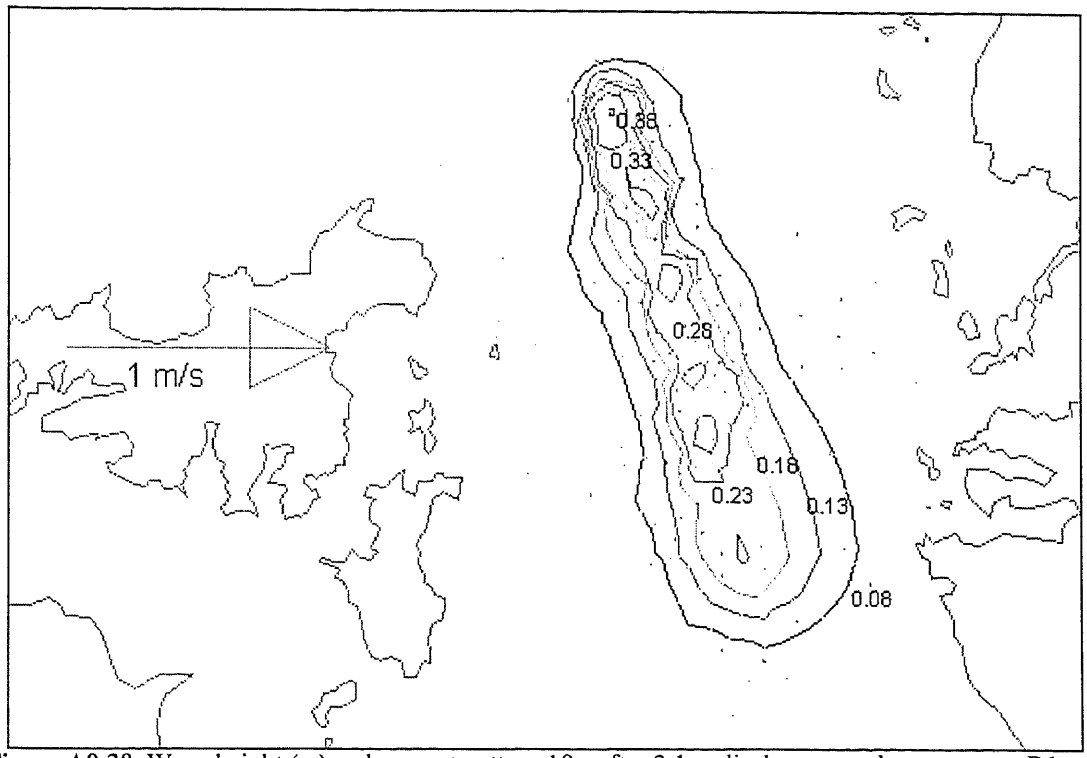

Figure A9.38: Wave height (m) and current pattern 10 s after 2.1 m displacement along segment D1.

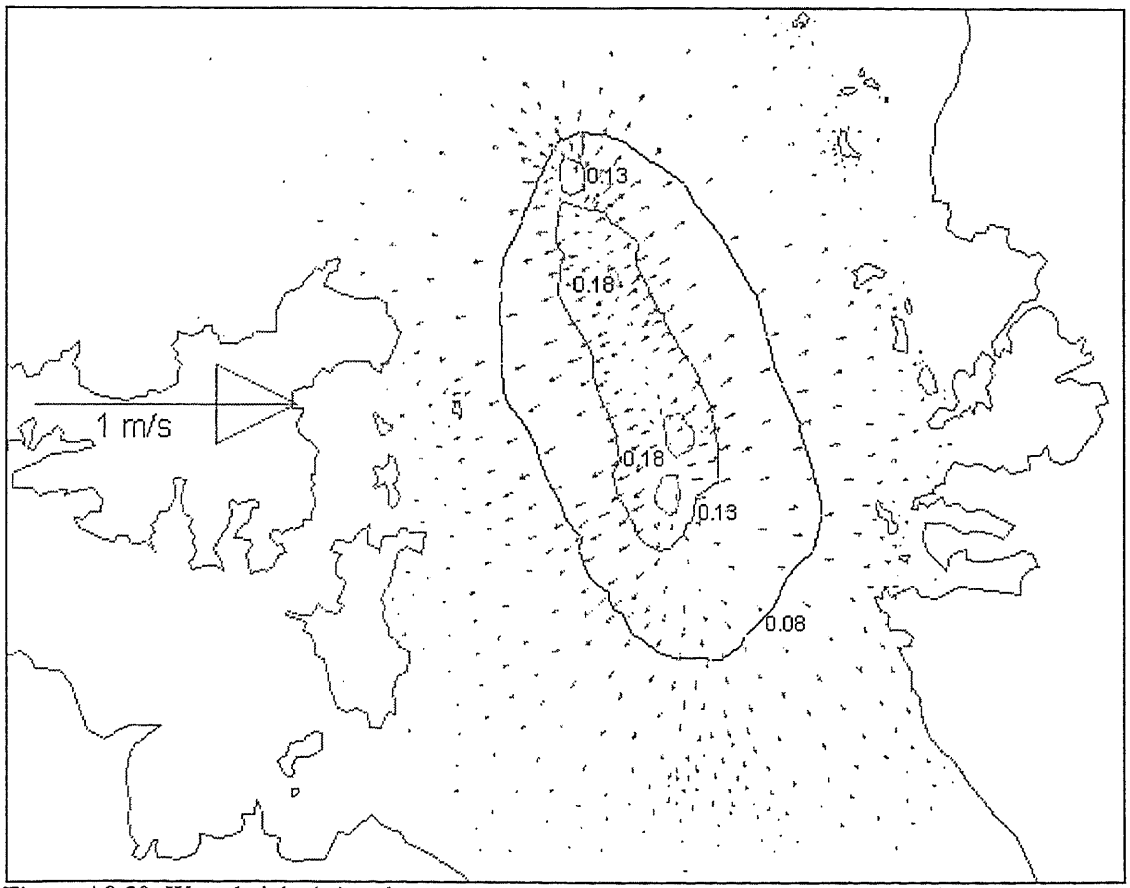

Figure A9.39: Wave height (m) and current pattern 3.5 min after 2.1 m displacement along segment D1.

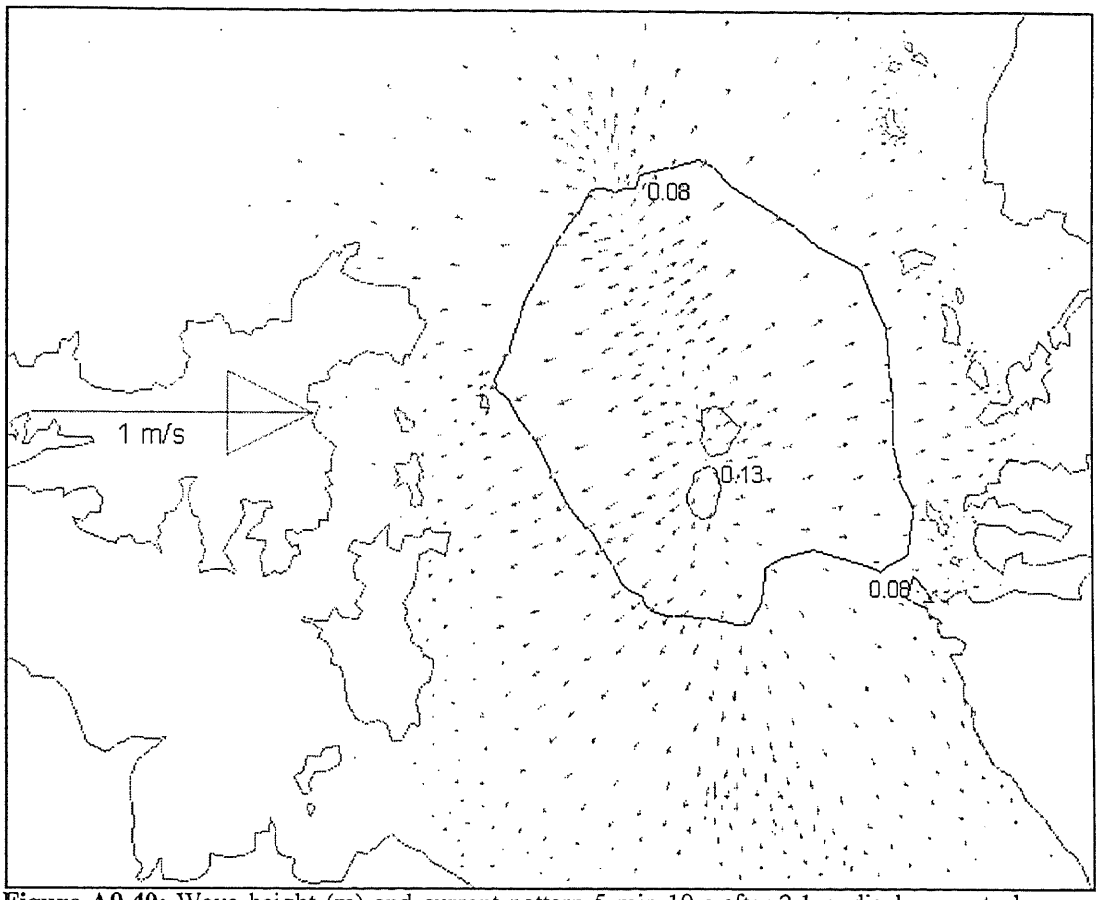

Figure A9.40: Wave height (m) and current pattern 5 min 10 s after 2.1 m displacement along segment D1.

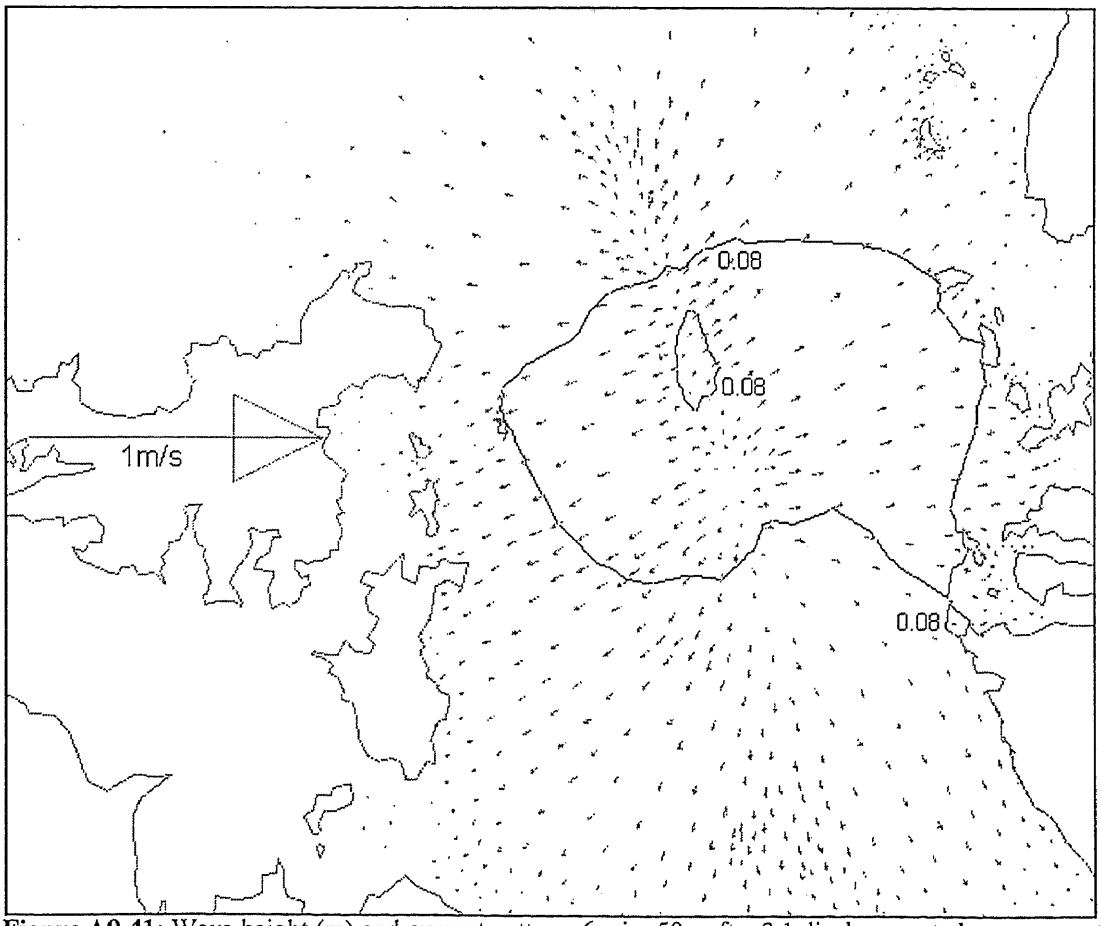

Figure A9.41: Wave height (m) and current pattern, 6 min, 50 s after 2.1 displacement along segment D1.

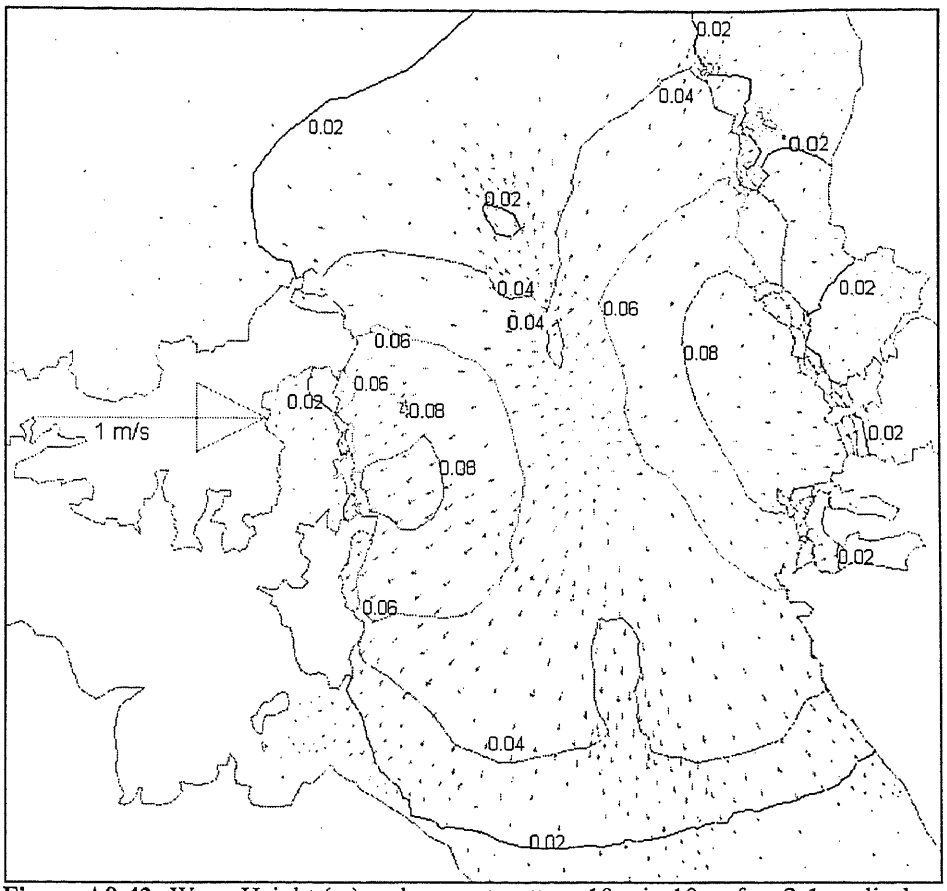

Figure A9.42: Wave Height (m) and current pattern 10 min 10 s after 2.1 m displacement along segment D1.

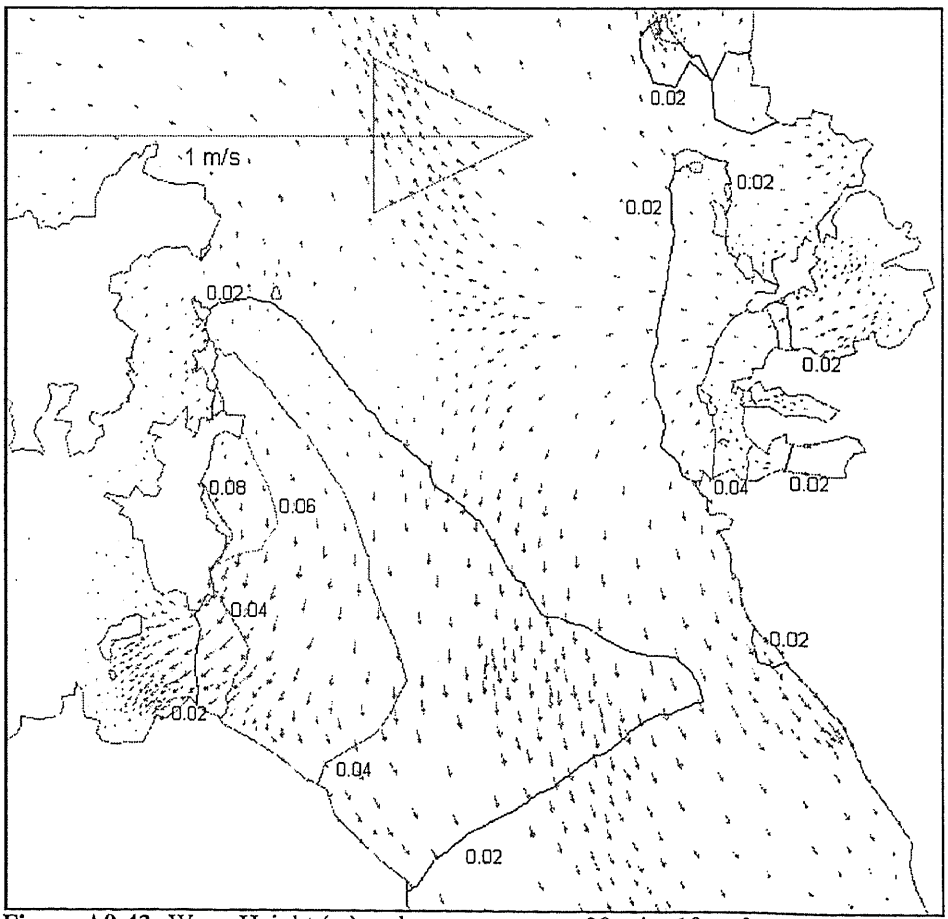

Figure A9.43: Wave Height (m) and current pattern 20 min, 10 s after 2.1 m displacement along segment D1.

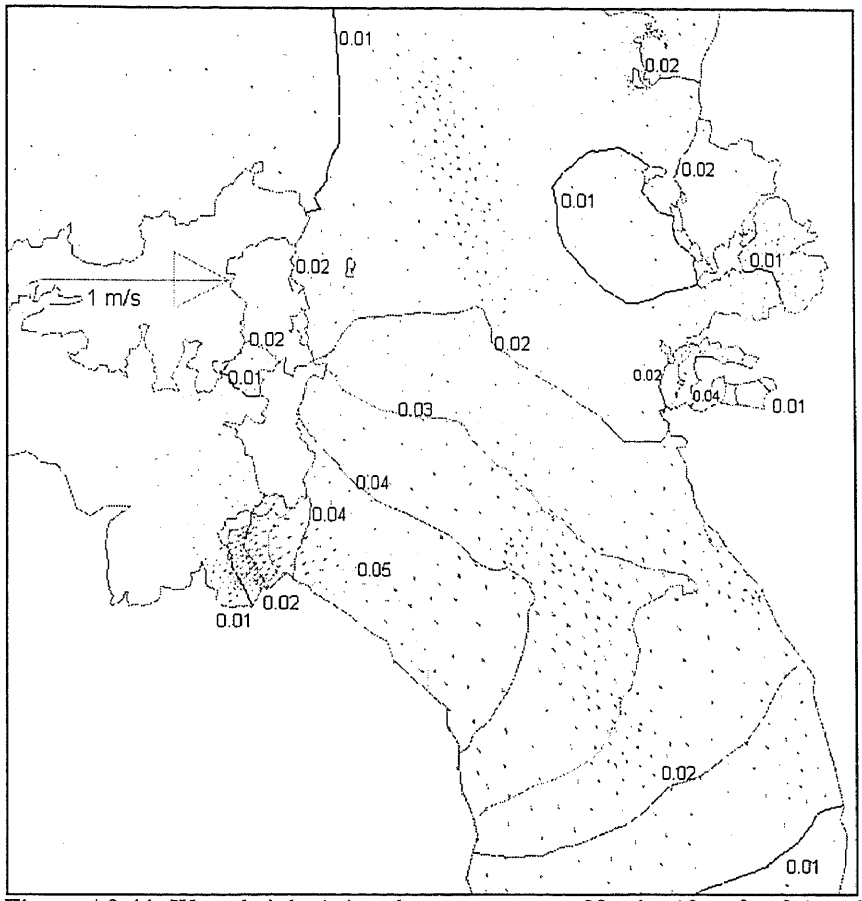

Figure A9.44: Wave height (m) and current pattern 30 min. 10 s after 2.1 m displacement along segment D1.

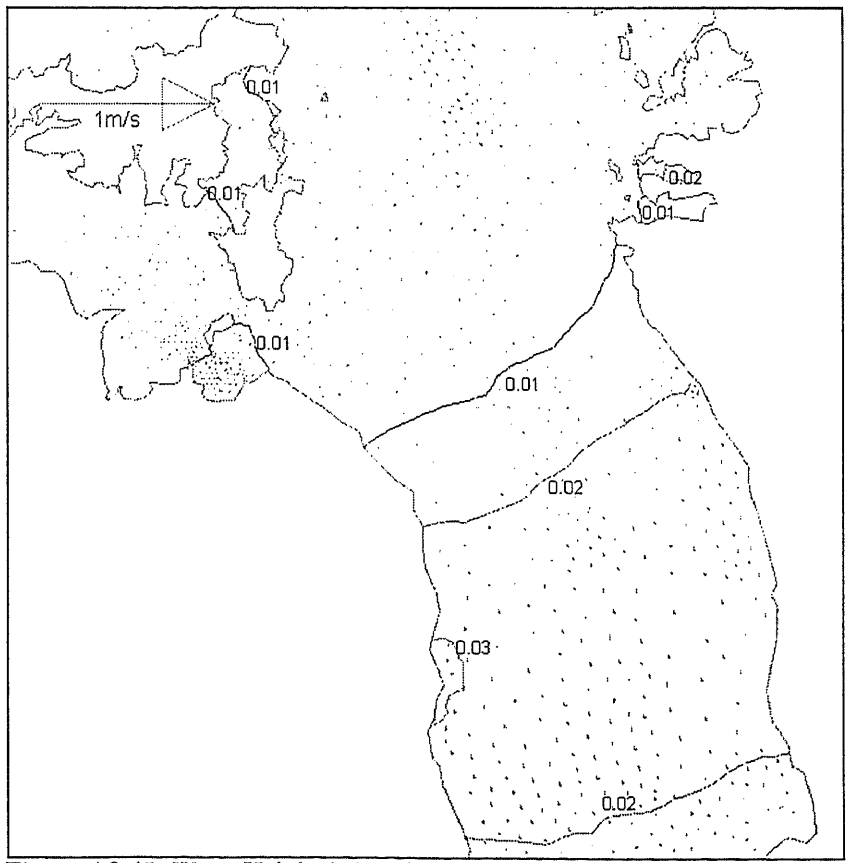

Figure A9.45: Wave Height (m) and current pattern 1 hr 3 min. and 30 s after 2.1 m displacement along segment D1.

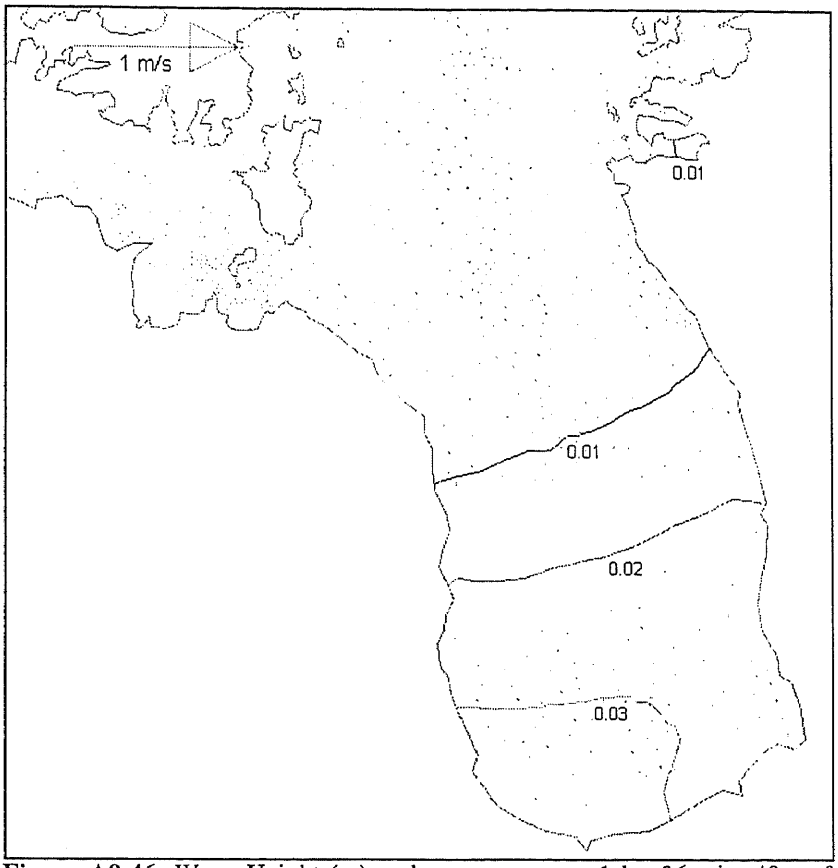

Figure A9.46: Wave Height (m) and current pattern 1 hr, 36 min, 40 s after 2.1 m displacement along segment D1.

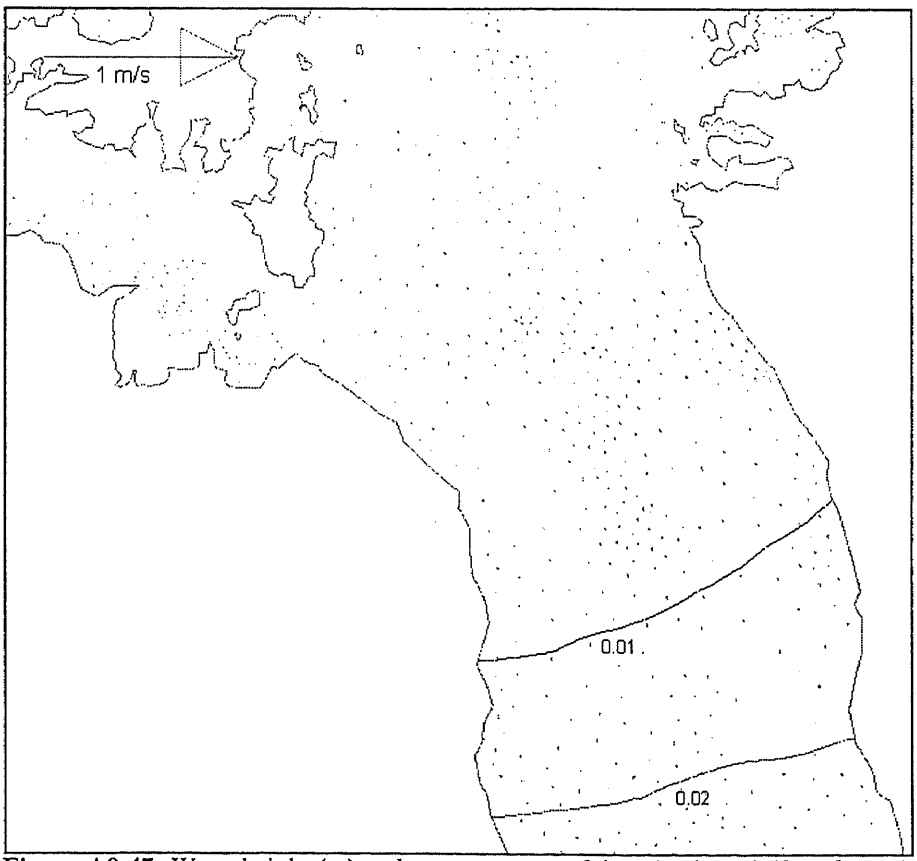

Figure A9.47: Wave height (m) and current pattern 2 hrs, 1 min and 50 s after 2.1 m displacement along segment D1.

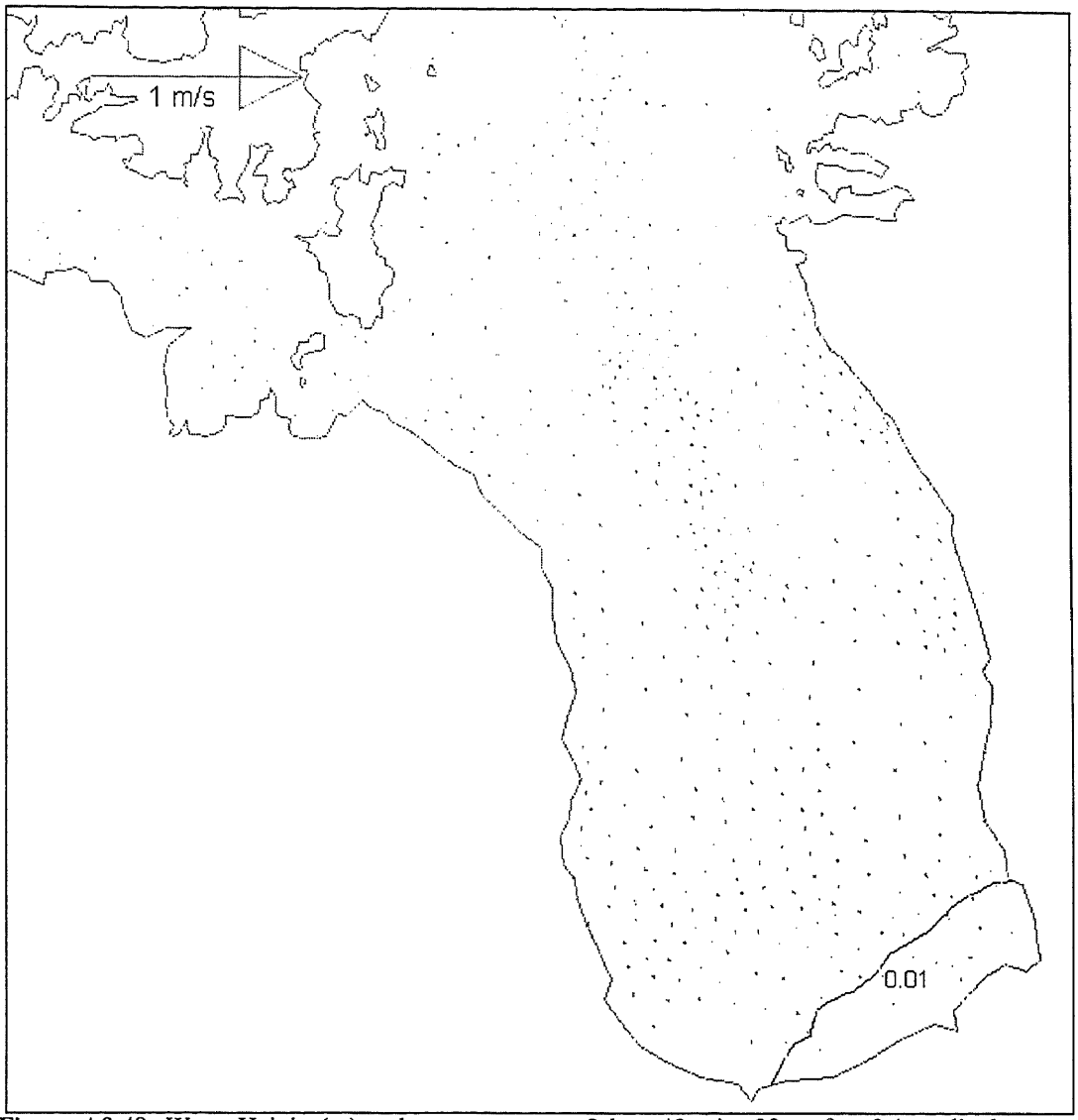

Figure A9.48: Wave Height (m) and current pattern 2 hrs, 43 min. 30 s after 2.1 m displacement along segment D1.

SCENARIO 5: DISPLACEMENT ALONG SEGMENT D2

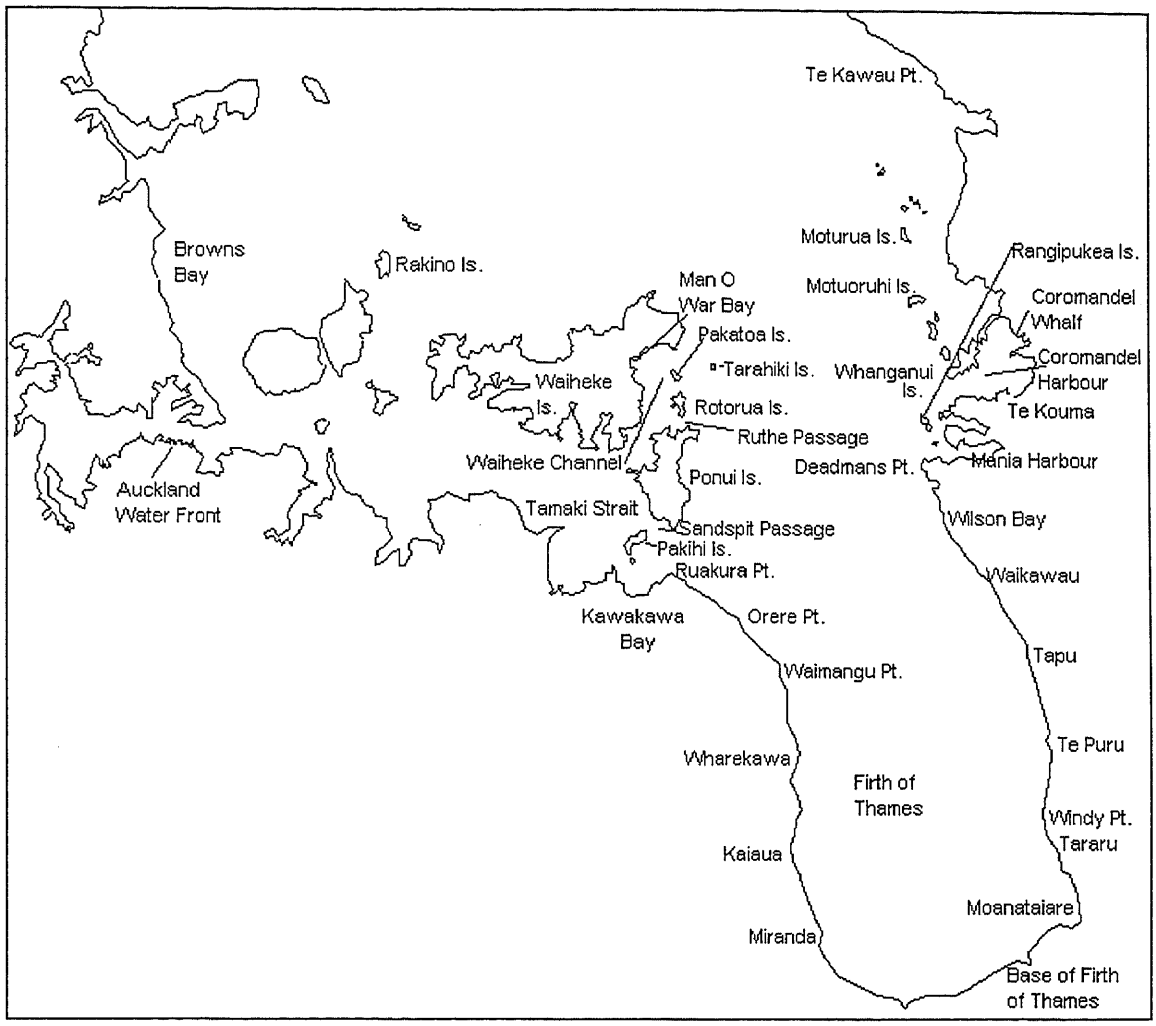

Figure A9.49: Map illustrating locations mentioned during discussion of wave heights and current velocities resulting from displacement along segment D2.

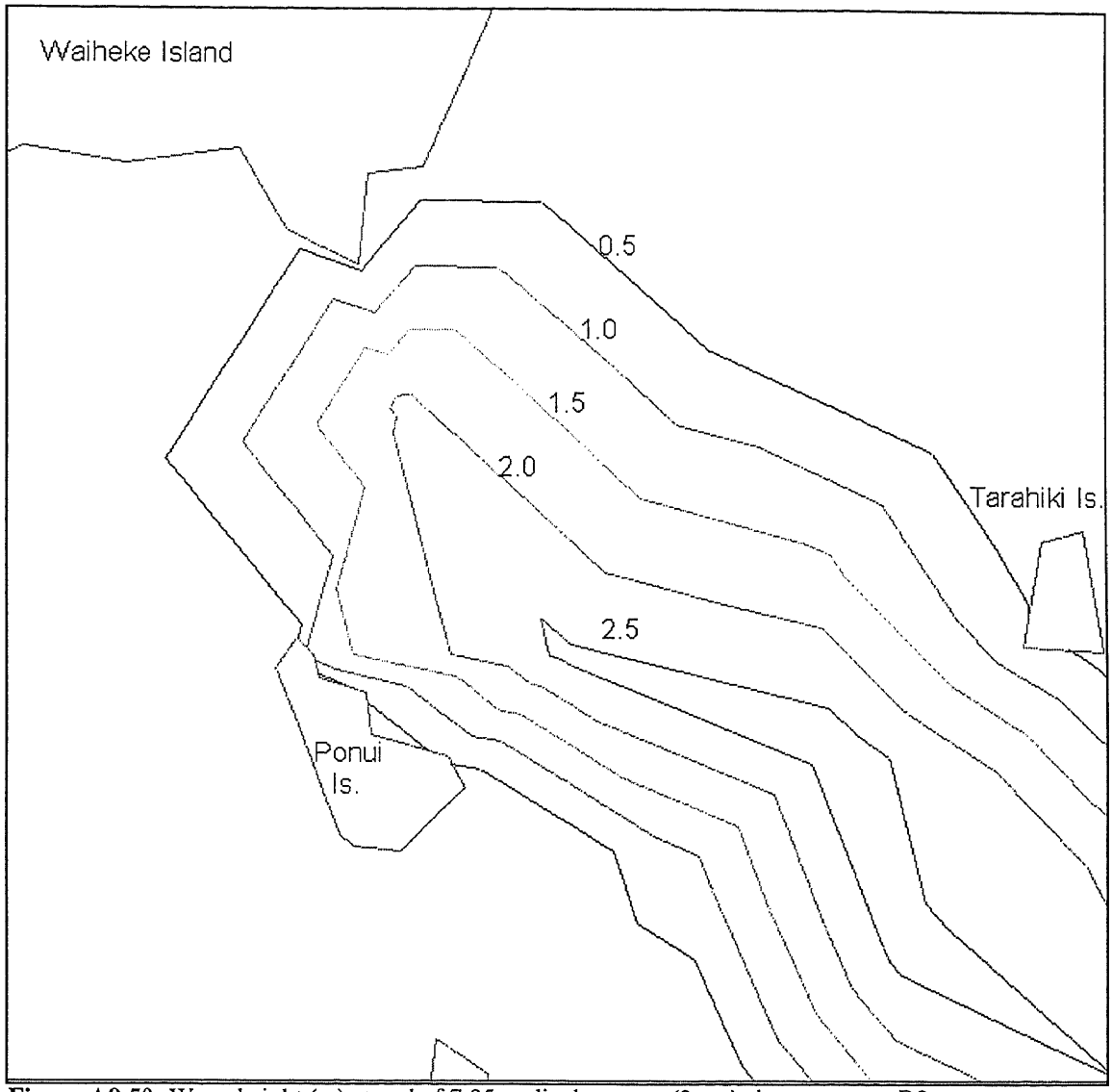

Figure A9.50: Wave height (m) at end of 7.35 m displacement (2 sec) along segment D2.

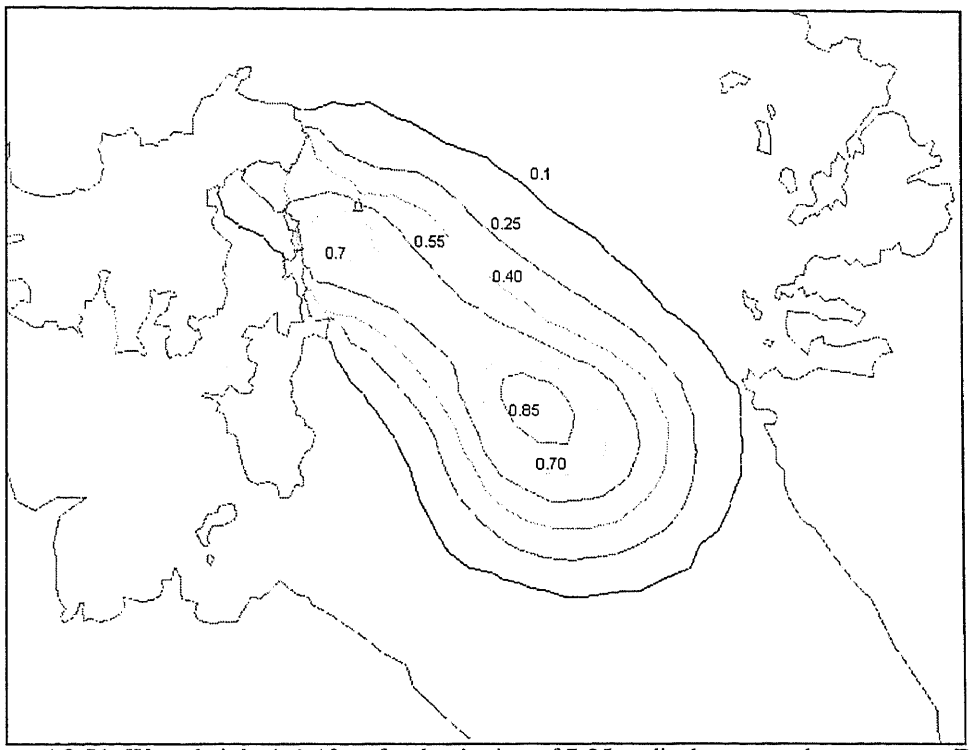

Figure A9.51: Wave height (m) 10 s after beginning of 7.35 m displacement along segment D2.

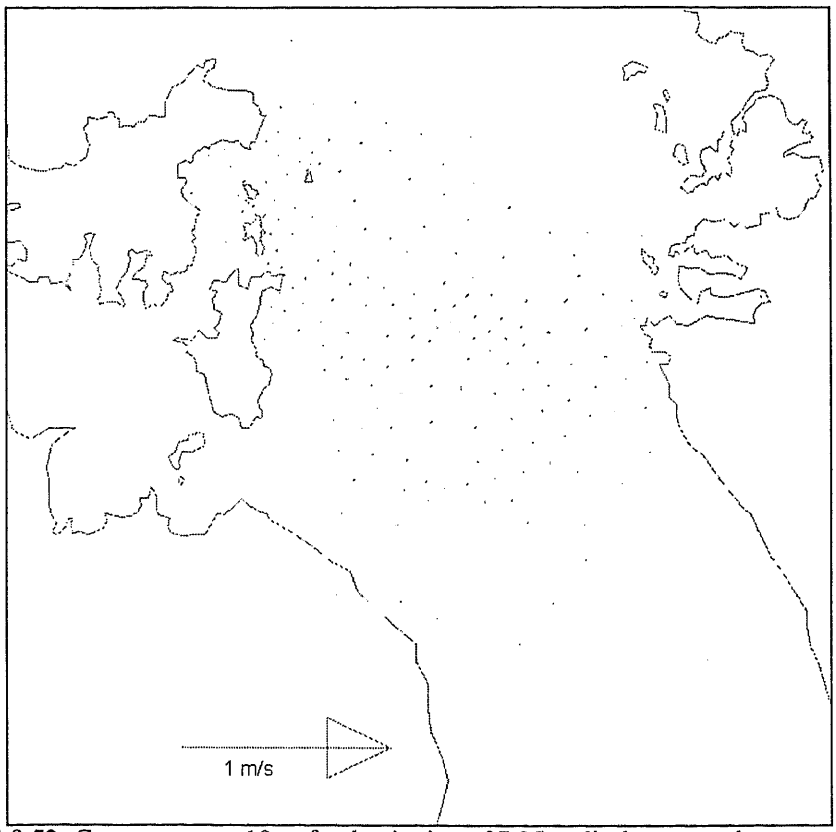

Figure A9.52: Current pattern 10 s after beginning of 7.35 m displacement along segment D2.

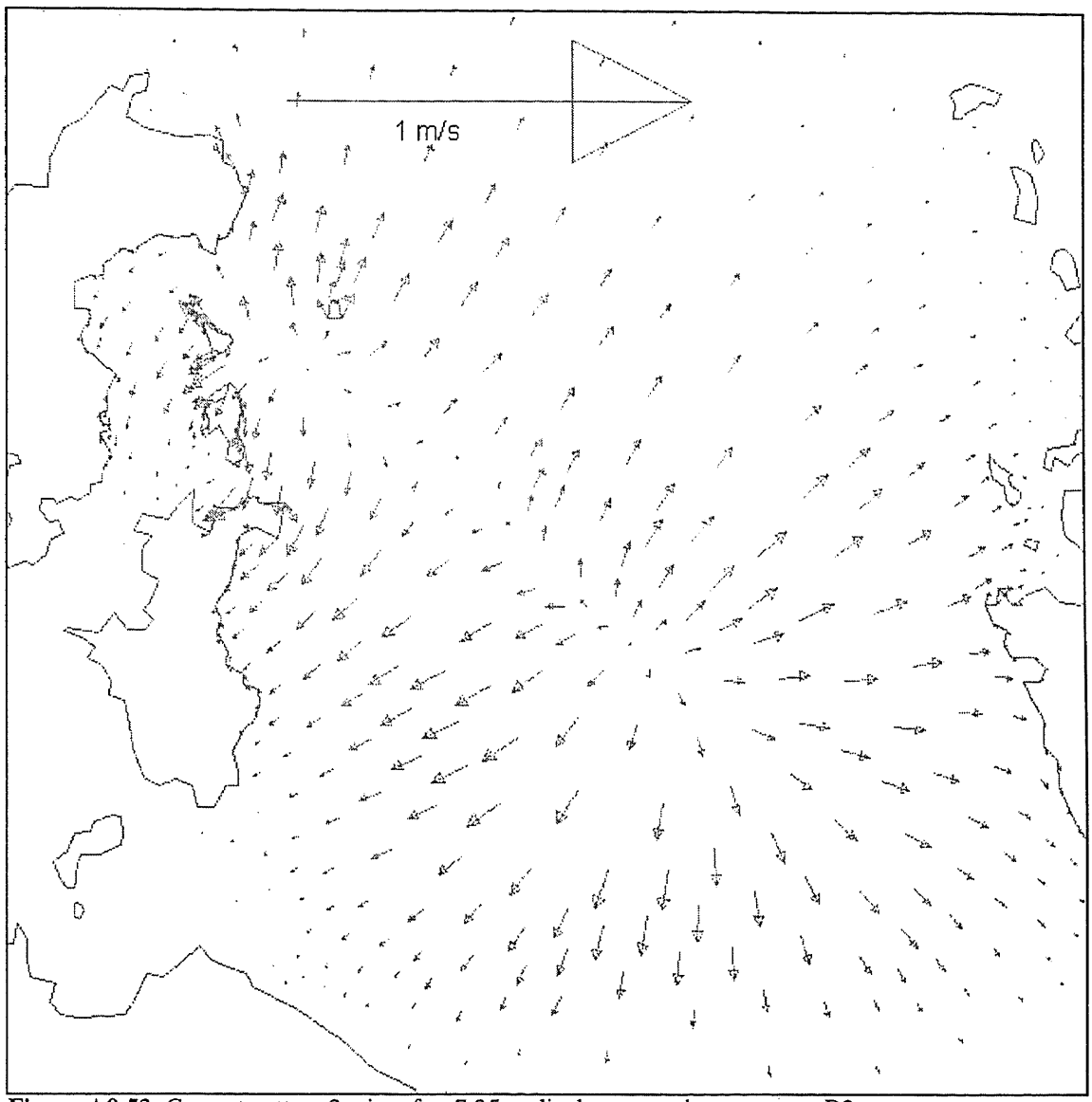

Figure A9.53: Current pattern 2 min. after 7.35 m displacement along segment D2.

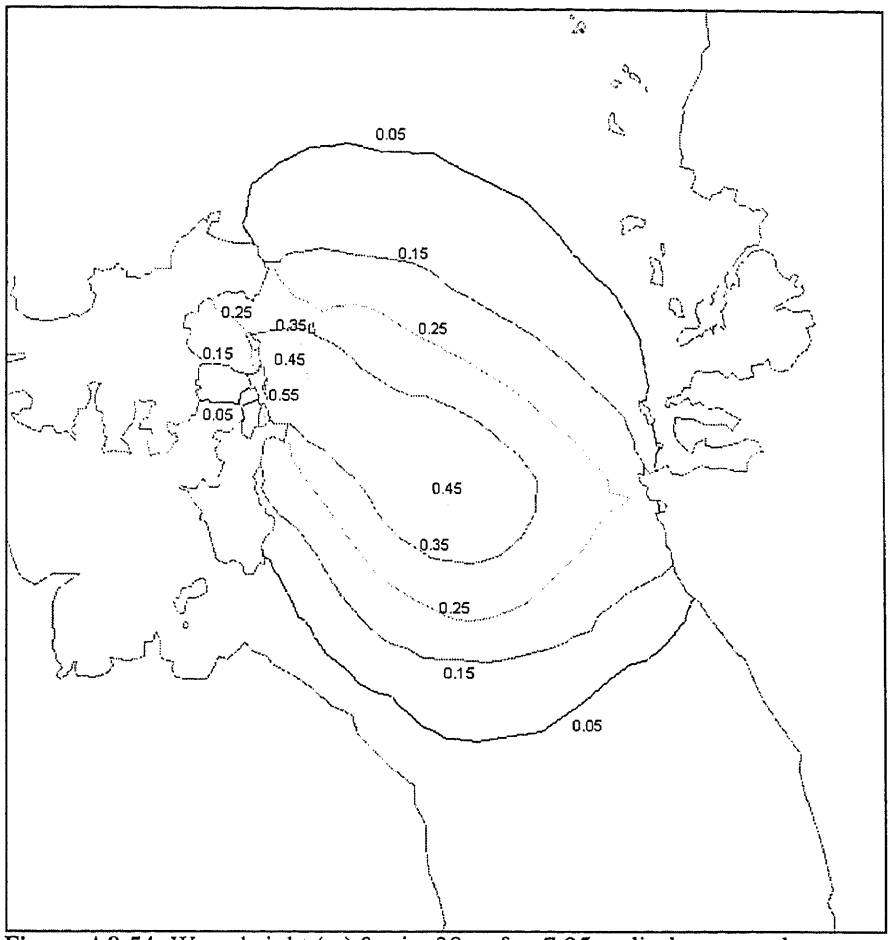

Figure A9.54: Wave height (m) 3 min. 30 s after 7.35 m displacement along segment D2

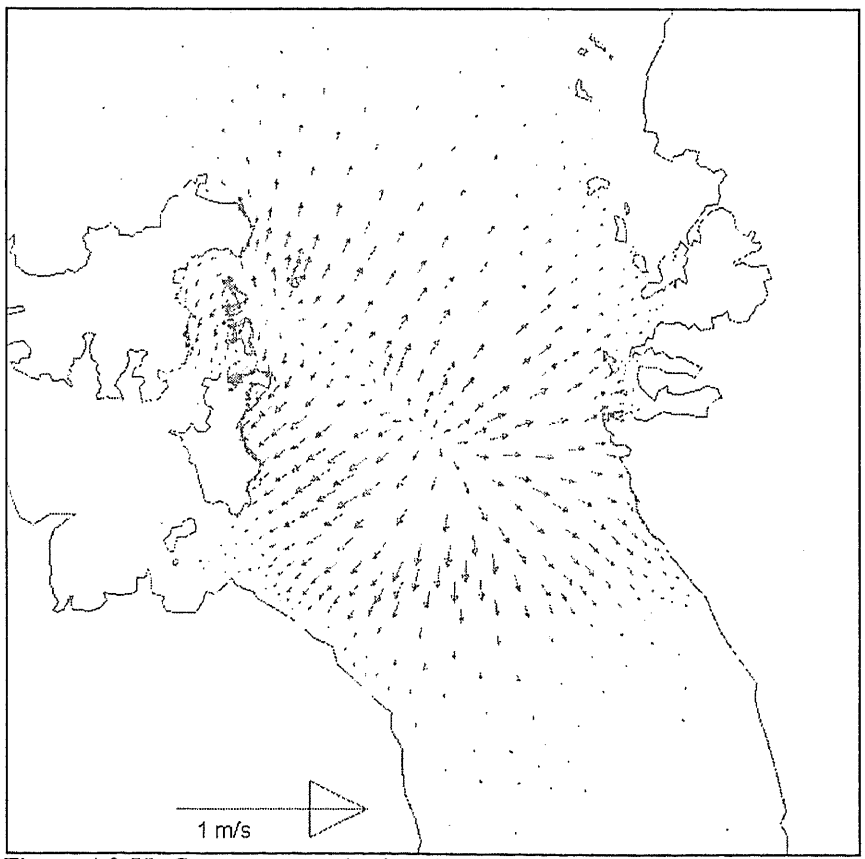

Figure A9.55: Current pattern 3 min. 30 s after 7.35 m displacement along segment D2

Figure A9.56: Wave height (m) 5 min. 10 s after a 7.35 m displacement along segment D2.

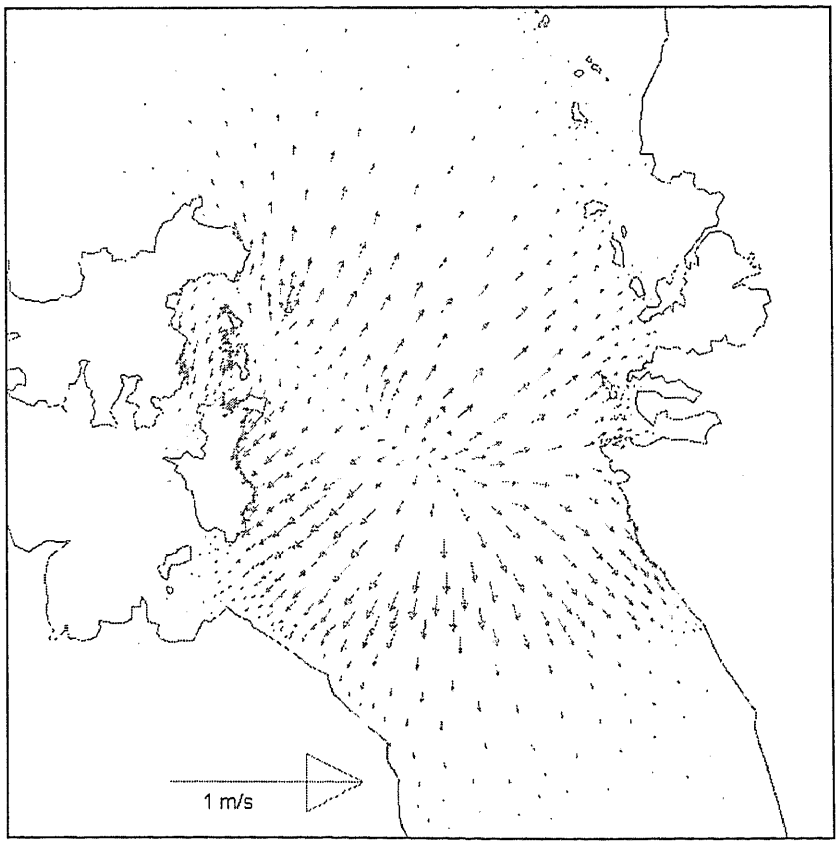

Figure A9.57: Current pattern 5 min. 10 s after 7.35 m displacement along segment D2.

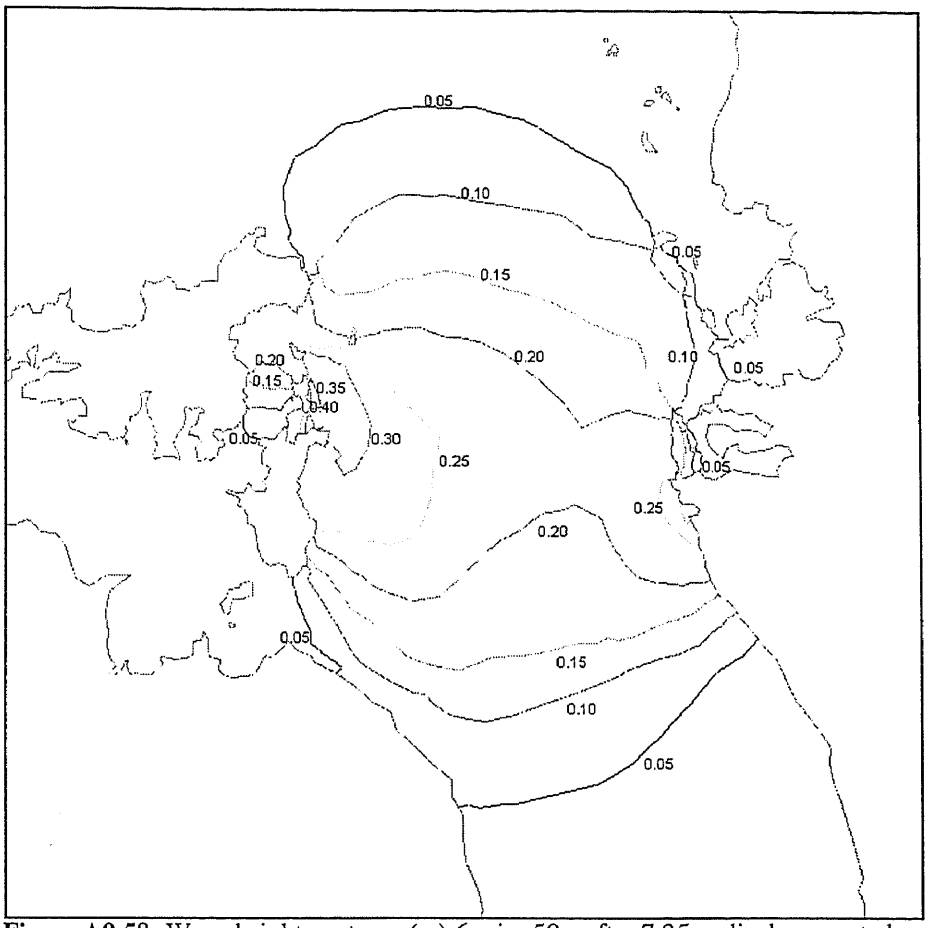

Figure A9.58: Wave height contours (m) 6 min. 50 s after 7.35 m displacement along segment D2.

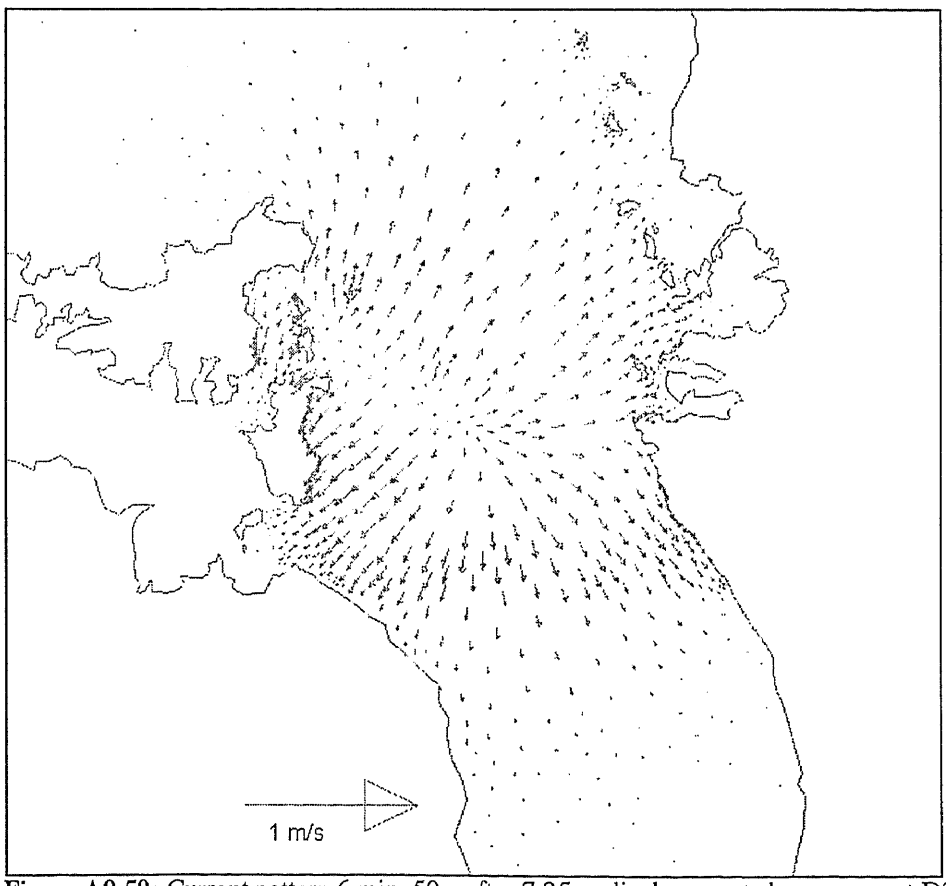

Figure A9.59: Current pattern 6 min. 50 s after 7.35 m displacement along segment D2.

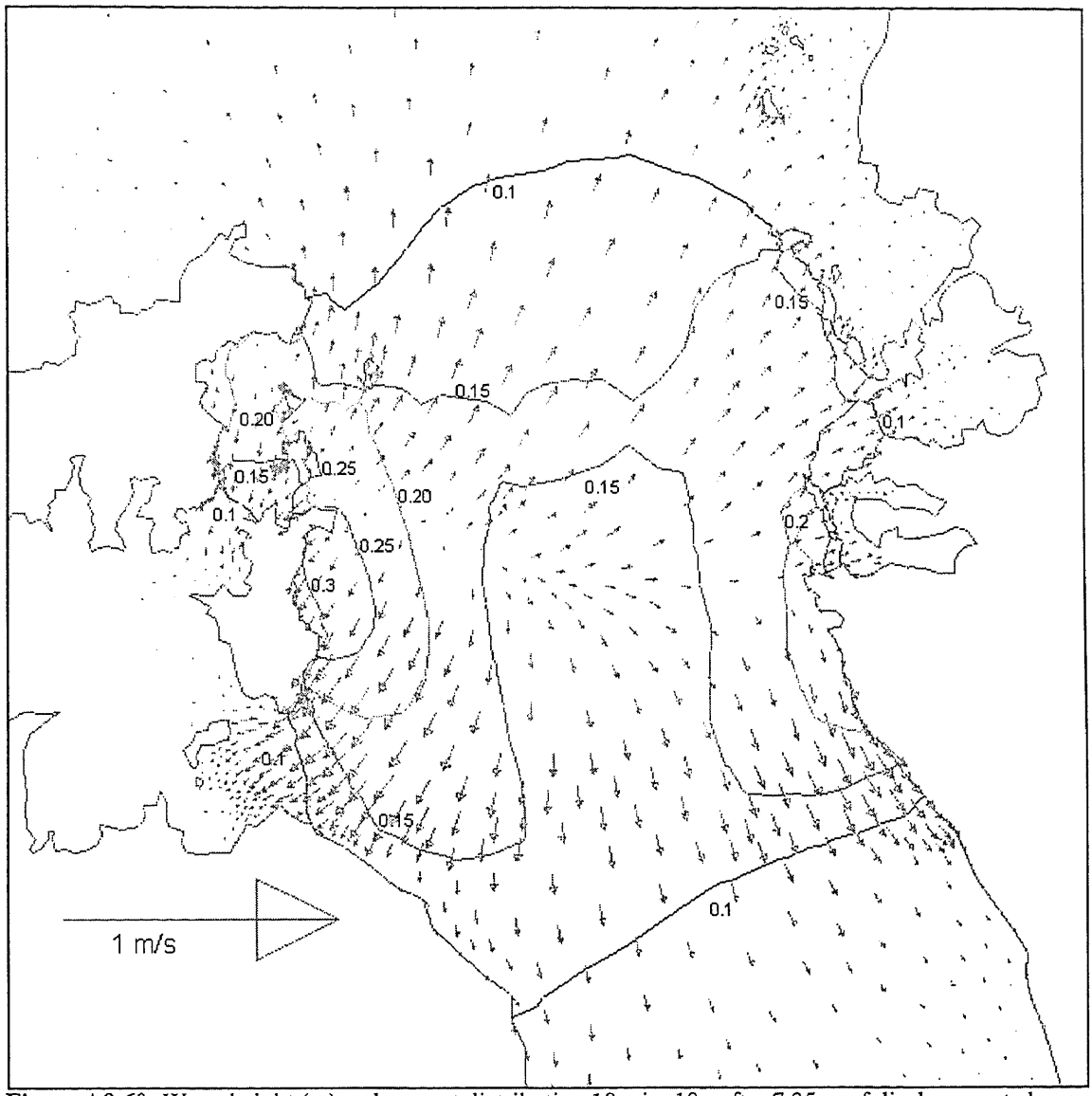

Figure A9.60: Wave height (m) and current distribution 10 min, 10 s after 7.35 m of displacement along segment D2.

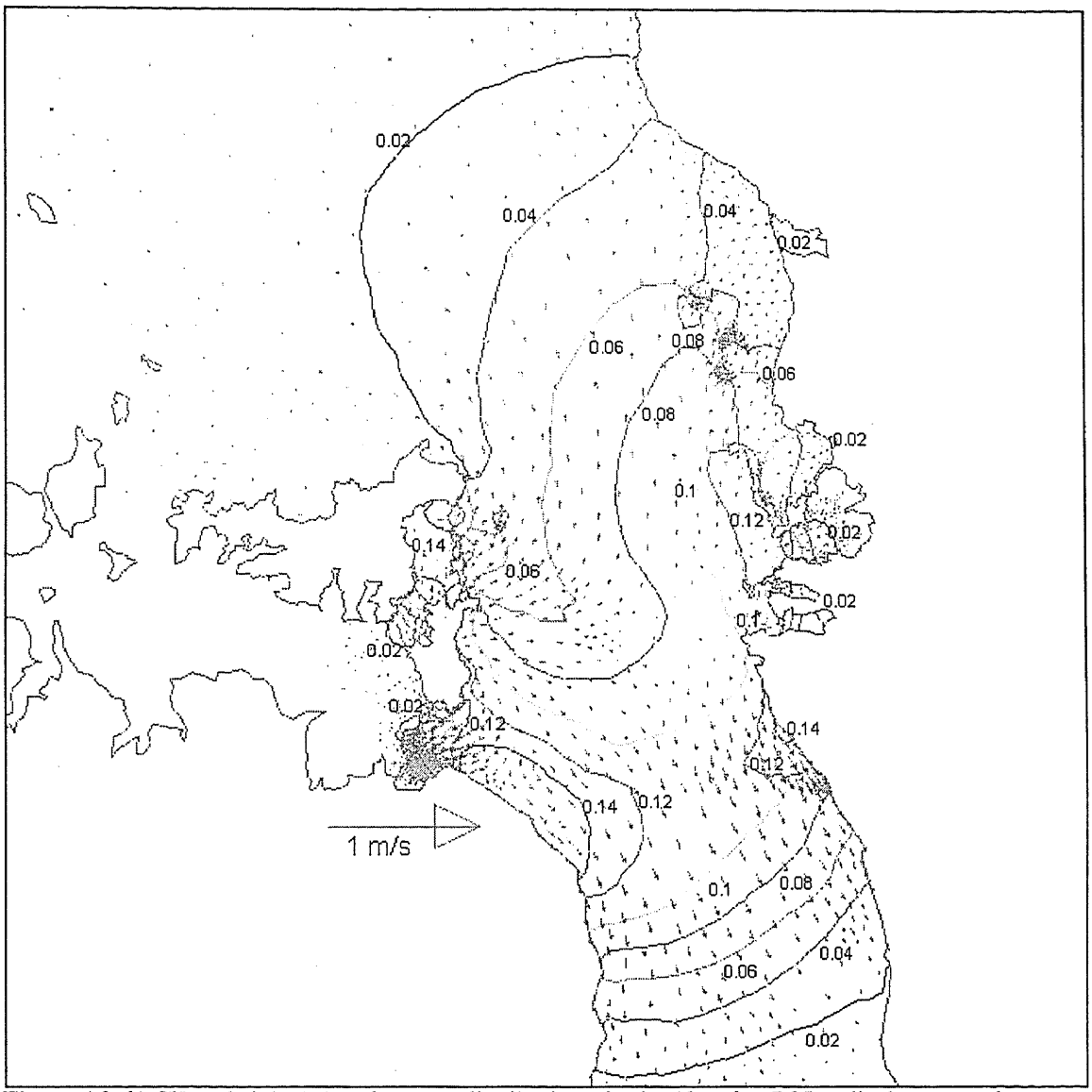

Figure A9.61: Wave height (m) and current distribution 20 min. 10 s after 7.35 m displacement along segment D2.

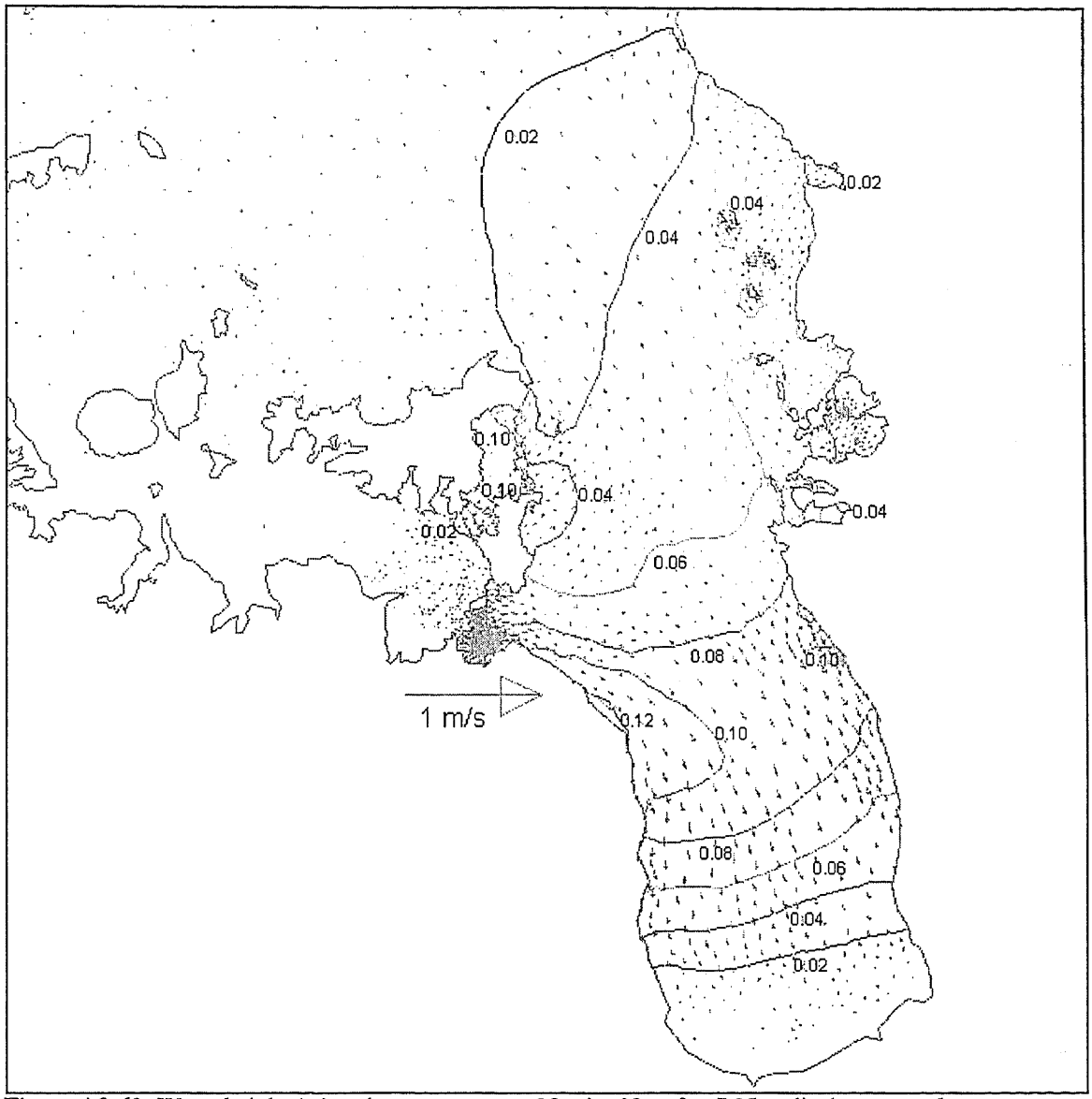

Figure A9.62: Wave height (m) and current pattern 30 min, 30 s after 7.35 m displacement along segment D2.

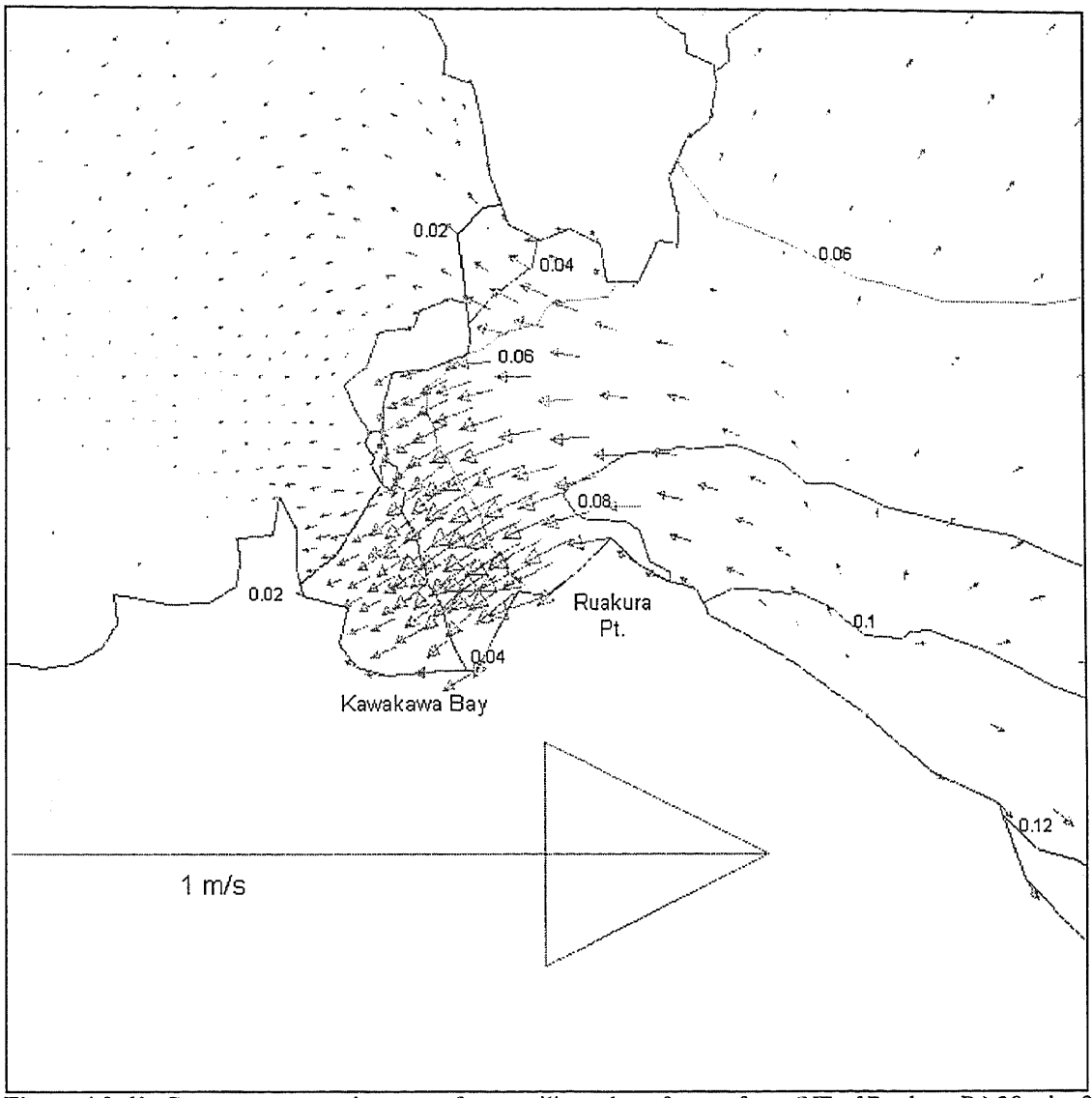

Figure A9.63: Currents propagating away from trailing edge of wave front (NE of Ruakura Pt) 30 min, 30 sec after 7.35 m displacement along segment D2.

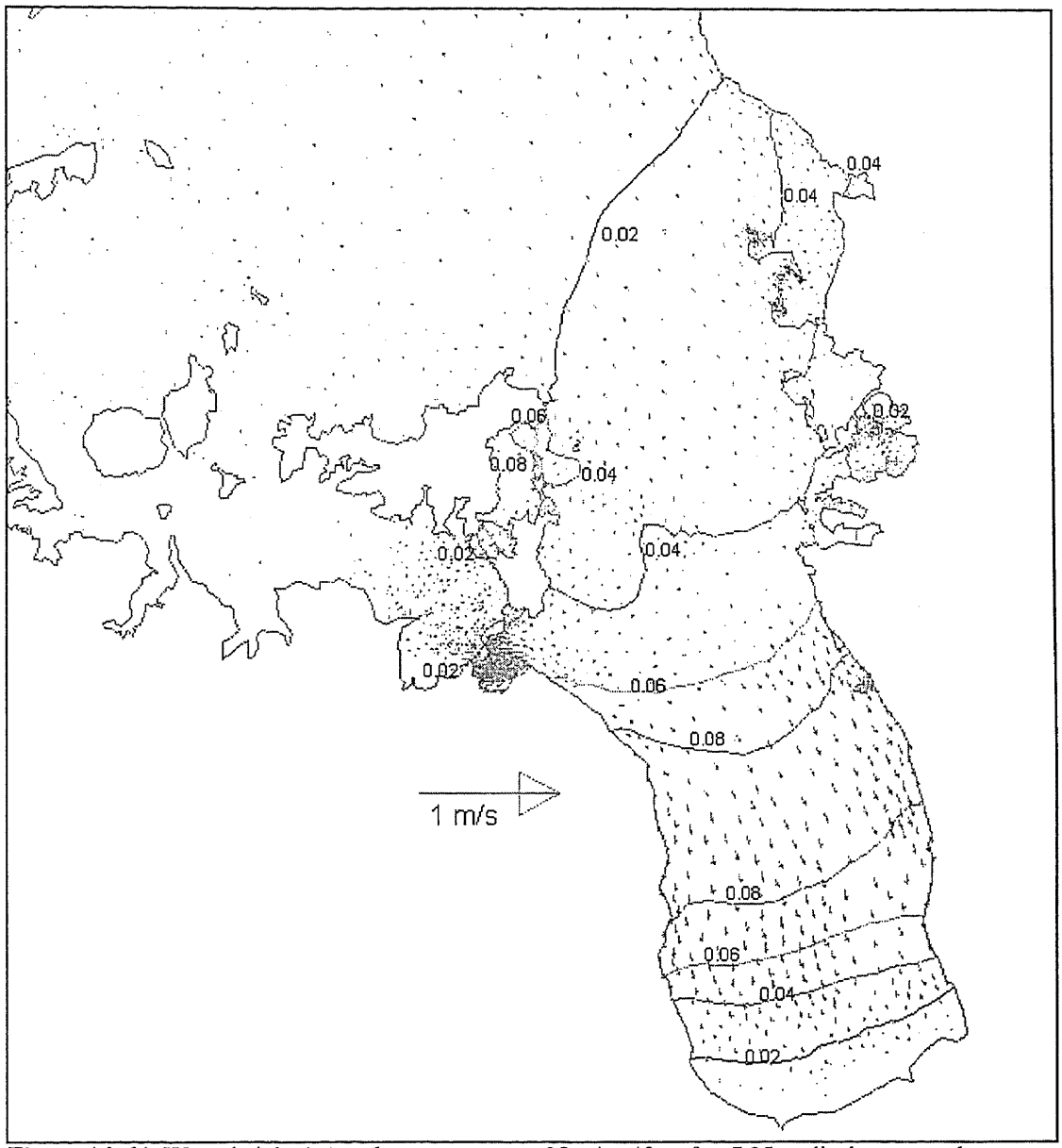

Figure A9.64: Wave height (m) and current pattern 38 min. 40 s after 7.35 m displacement along segment D2.

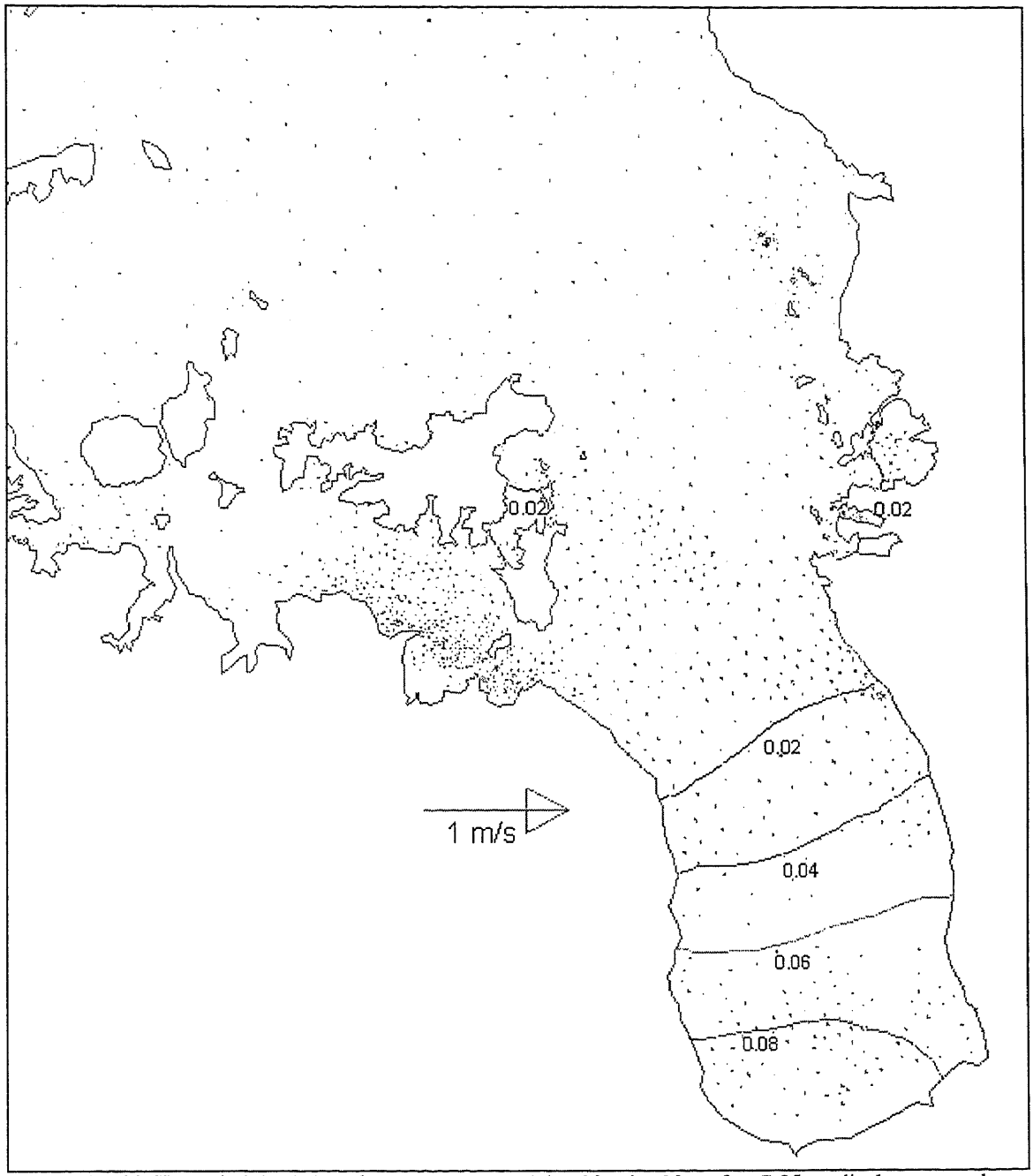

Figure A9.65: Wave height (m) and current pattern 1 hr, 20 min, 20 s after 7.35 m displacement along segment D2.

Appendix Ten

THE HYDRODYNAMIC CIRCULATION MODEL, 3DD

A10.1 INTRODUCTION

3DD is a 3-dimensional circulation and transport model written with general code and can therefore be applied to a wide range of environments. It has been used in vertically stratified or homogeneous conditions within oceanic, shallow water and continental shelf environments to produce current speed and direction, sea levels and temperature, salinity and density structure (Black, 1996).

The basis of 3DD, the momentum and continuity equations, are briefly summarised below. The long period of tsunami waves deems the vertical velocity component insignificant in comparison to the horizontal (Mei, 1983). Consequently, the pressure distribution through the water column is not influenced by vertical water movement and is essentially hydrostatic. For such conditions the vertical acceleration is less than that generated by the force of gravity and can therefore be ignored. Hence the conservation of mass and momentum equations need only be solved for two dimensions.

The model solves the in 2-dimensional momentum and continuity equations for the circulation explicitly on a Eulerian grid (Black, 1996).

A10.2 THE MOMENTUM AND CONSERVATION OF MASS EQUATIONS

The hydrodynamic model 3DD is based upon the momentum and mass equations. The momentum equation (Equation A10.3 and A10.4) describes the water body acceleration or retardation that occurs when a force or friction is applied (Tian, 1997).

The momentum equation is derived from Newtons 2nd Law of motion (equation A10.1):

$$\sum F_x = ma_x \qquad \textbf{A10.1}$$

where F_x is the force in the x direction, m is the mass of the fluid and a_x is the particle acceleration in the x direction, which by definition is equal to, $a_x = \partial u/\partial t$ where u is the velocity in the x direction (Dean & Dalrymple, 1991). i.e. the rate of change of motion of a body is directly proportional to the resultant force acting on it and is in the direction of that force (Tian, 1997).

The mass conservation equation (Equation A10.4) ensures that the incompressible fluid mass within the model grid is conserved i.e. it is not be created or destroyed, and is used to calculate the total mass entering or leaving each model cell (Dean & Dalrymple, 1991; Tian, 1997).

Momentum equation

$$\frac{\partial u}{\partial t}+\frac{u\partial u}{\partial x}+\frac{v\partial}{\partial y}-fv=-\frac{g\partial\zeta}{\partial x}-\frac{1\partial P_{atm}}{\rho\partial x}+\frac{\rho_a\gamma W_x|W|}{\rho(d+\zeta)}-\frac{gu\left(u^2+v\right)^{1/2}}{C^2h}+A_H\left(\frac{\partial^2 u}{\partial x^2}+\frac{\partial^2 u}{\partial y^2}\right) \qquad \textbf{A10.2}$$

$$\frac{\partial v}{\partial t}+\frac{u\partial v}{\partial x}+\frac{u\partial}{\partial y}-fu=-\frac{g\partial\zeta}{\partial y}-\frac{1\partial P_{atm}}{\rho\partial y}+\frac{\rho_a\gamma W_y|W|}{\rho(d+\zeta)}-\frac{gv\left(u^2+v\right)^{1/2}}{C^2h}+A_H\left(\frac{\partial^2 v}{\partial x^2}+\frac{\partial^2 v}{\partial y^2}\right) \qquad \textbf{A10.3}$$

Mass equation

$$\frac{\partial\zeta}{\partial t}+\frac{\bar{o}}{\partial x}(d+\zeta)u+\frac{\bar{o}}{\partial y}(d+\zeta)v=0 \qquad \textbf{A10.4}$$

where t is the time, u and v are the vertically-averaged velocities in the x, y directions respectively, h is the total water depth, d is the water depth below the sea level datum,

ζ is the sea level above the sea level horizontal datum, g the gravitational acceleration, f the Coriolis parameter, P_{atm} the atmospheric pressure, A_H the horizontal eddy viscosity coefficient, ρ is the water density, ρ_a is the air density. C is 'Chezy's C' value and is defined as $C = 18\log_{10}(0.37d/z_o)$ where d is the water depth. f is the coriolis parameter, defined as $f = 2\Omega\sin\theta$ where $\Omega = 7.292*10^{-5}$ s^{-1}. W is the wind speed 10 m above sea level and W_x and W_y are the wind speeds in the x and y directions. γ is the wind drag coefficient and can be calculated using the following empirical formula: $\gamma = (0.8 + 0.065|W|)x10^{-3}$.

A10.3 REFERENCES

Black, K. P., 1996. *The Hydrodynamic model 3DD and Support Software*, Occasional Report No. 19, Department of Earth Sciences, University of Waikato, Private Bag 3105, Hamilton.

Dean, R. G. & Dalrymple, R. A., 1991. *Water wave mechanics for engineers and scientists*, Vol. 2: Advanced series on Ocean Engineering, Liu, P.L.-F. (ed.), Singapore: World Scientific.

Mei, C.C. 1989. *The Applied Dynamics of Ocean Surface Waves*, World Scientific Publishing Co. Pte. Ltd., Singapore, 740 p.

Tian, F., 1997. *Environmental aspects of Storm Runoff Discharge from a Timber Port, Tauranga, New Zealand*, D.Phil. Thesis, Department of Earth Sciences, The University of Waikato.

Appendix Eleven

AMPLITUDE ATTENUATION/GAIN GRAPHS

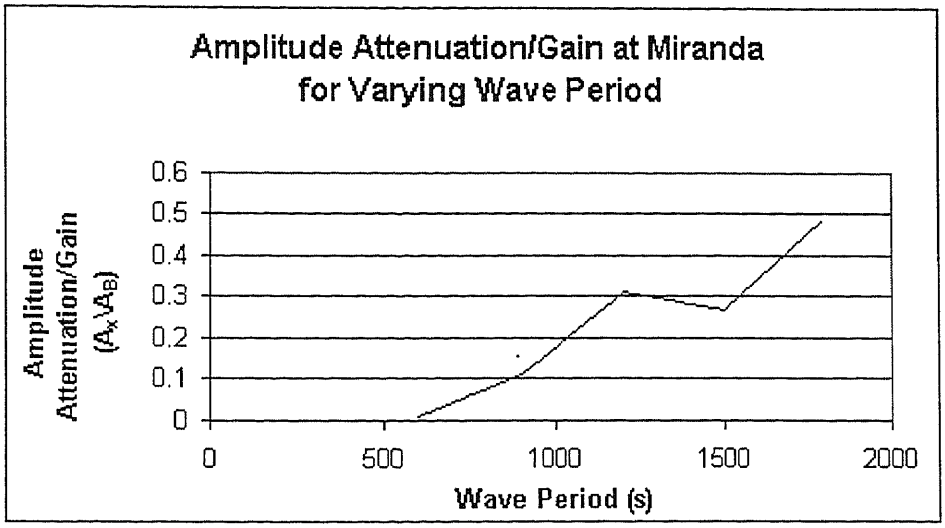

Figure A11.1: Figure illustrating the relationship between wave period and amplitude attenuation/gain at Miranda. Amplitude attenuation/gain is presented as a proportion of the amplitude at the open ocean boundary.

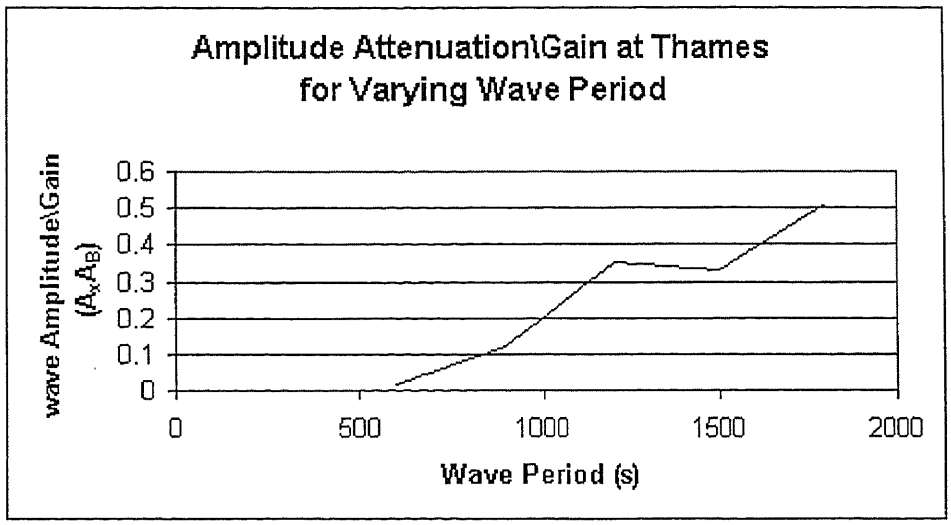

Figure A11.2: Figure illustrating the relationship between wave period and amplitude attenuation/gain at Thames. Amplitude attenuation/gain is presented as a proportion of the amplitude at the open ocean boundary.

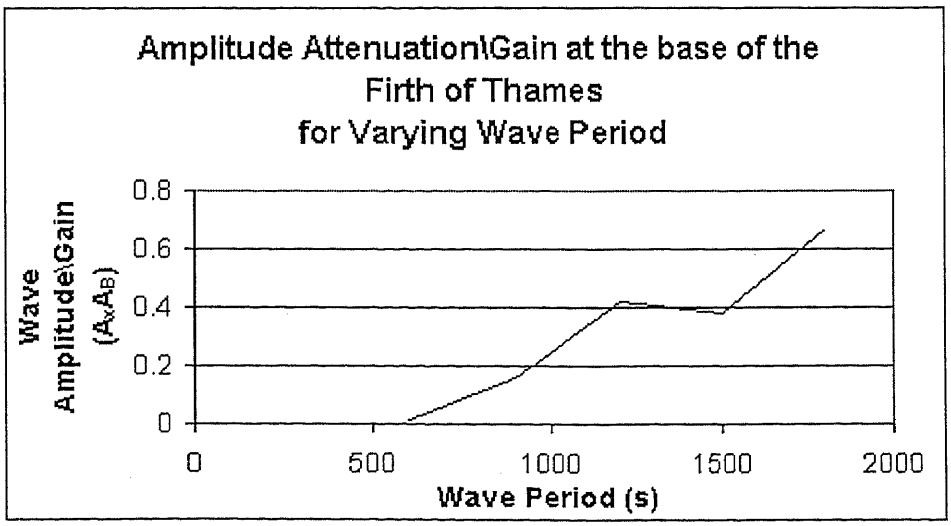

Figure A11.3: Figure illustrating the relationship between wave period and amplitude attenuation/gain at the base of the Firth of Thames. Amplitude attenuation/gain is presented as a proportion of the amplitude at the open ocean boundary.

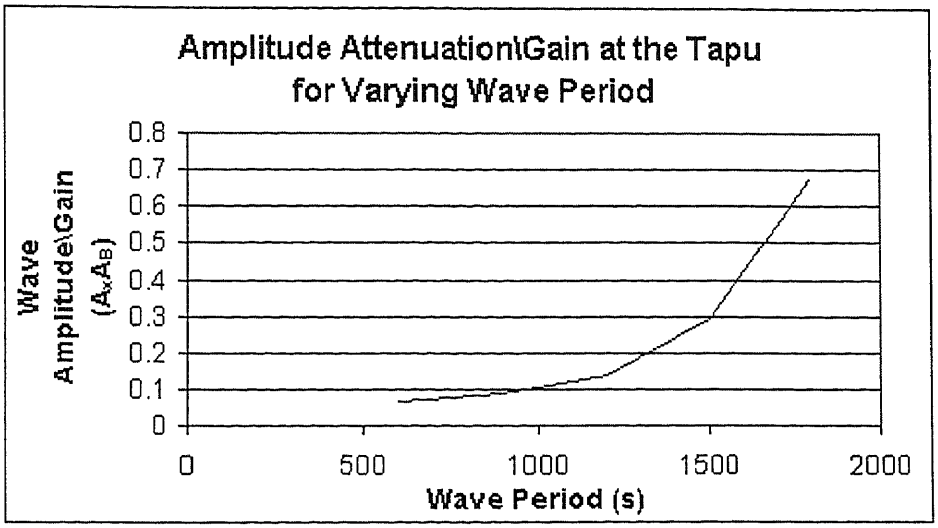

Figure A11.4: Figure illustrating the relationship between wave period and amplitude attenuation/gain at Tapu. Amplitude attenuation/gain is presented as a proportion of the amplitude at the open ocean boundary.

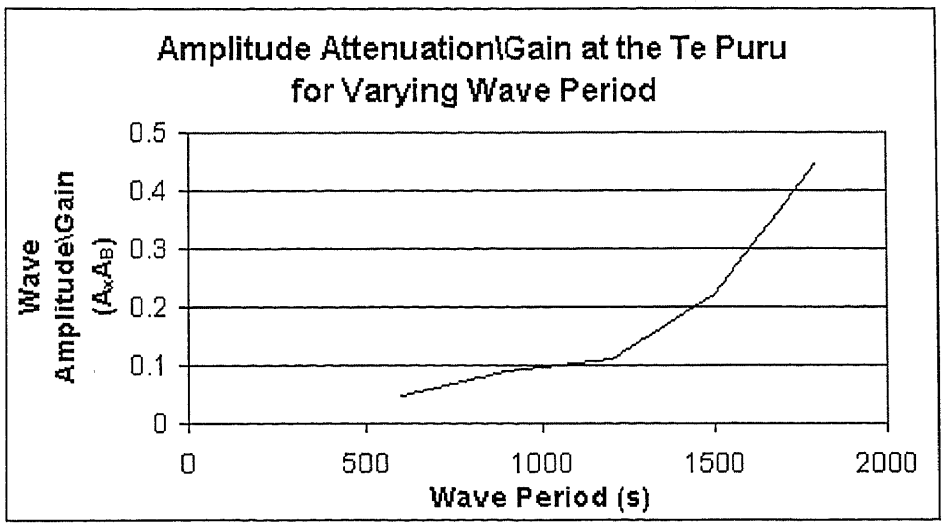

Figure A11.5: Figure illustrating the relationship between wave period and amplitude attenuation/gain at Te Puru. Amplitude attenuation/gain is presented as a proportion of the amplitude at the open ocean boundary.

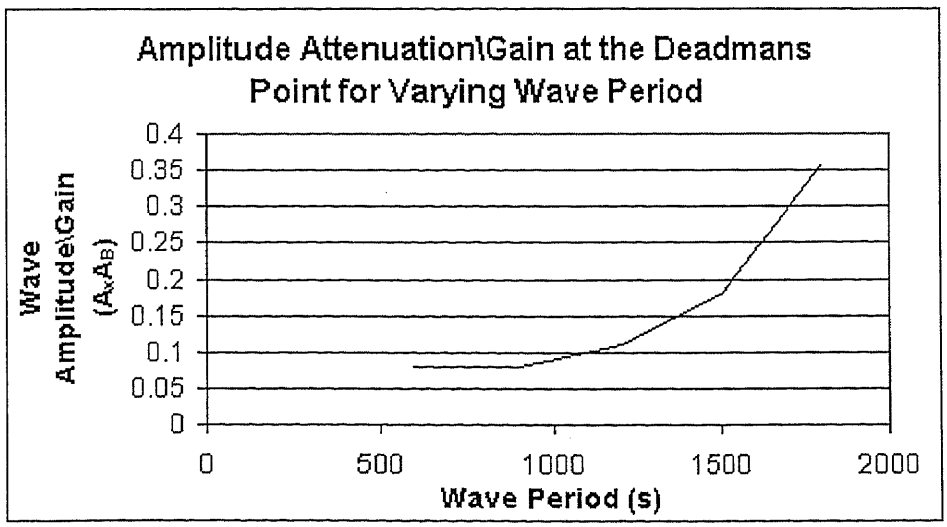

Figure A11.6: Figure illustrating the relationship between wave period and amplitude attenuation/gain at Deadmans Point. Amplitude attenuation/gain is presented as a proportion of the amplitude at the open ocean boundary.

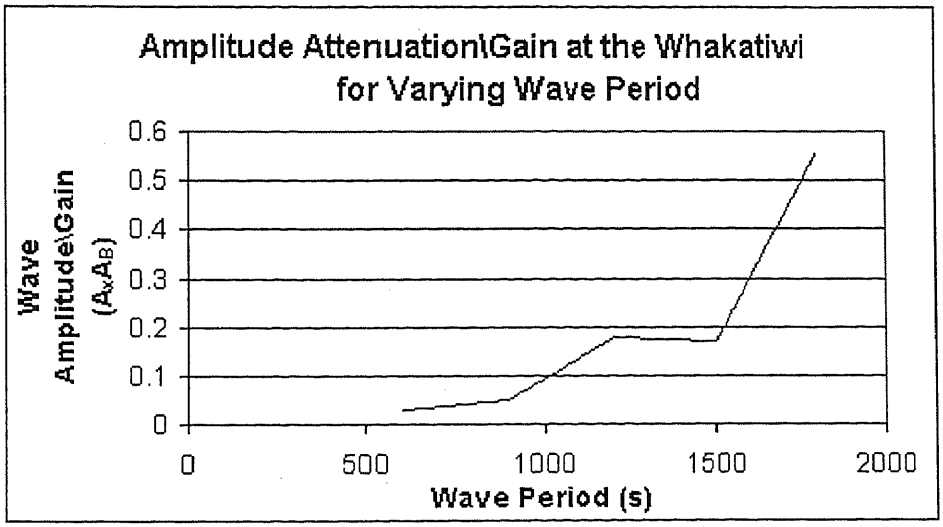

Figure A11.7: Figure illustrating the relationship between wave period and amplitude attenuation/gain at Whakatiwi. Amplitude attenuation/gain is presented as a proportion of the amplitude at the open ocean boundary.

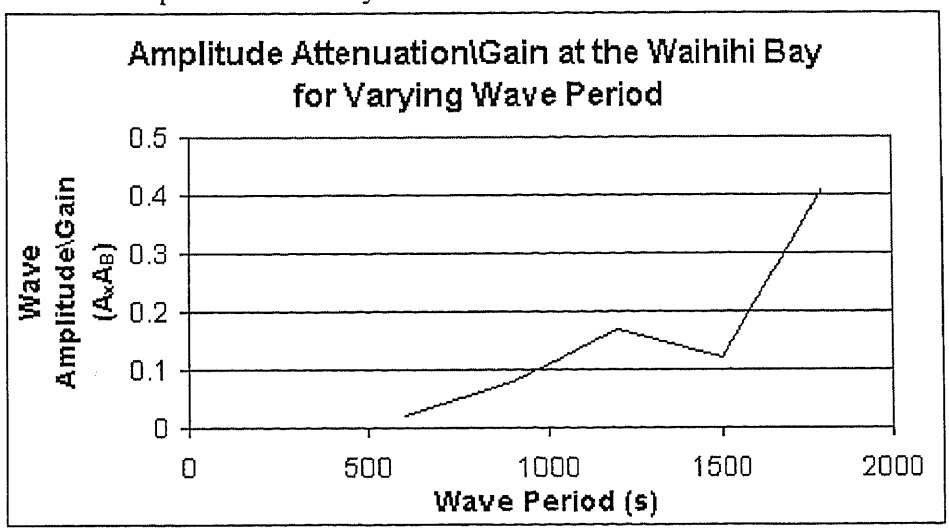

Figure A11.8: Figure illustrating the relationship between wave period and amplitude attenuation/gain at Waihihi. Amplitude attenuation/gain is presented as a proportion of the amplitude at the open ocean boundary.

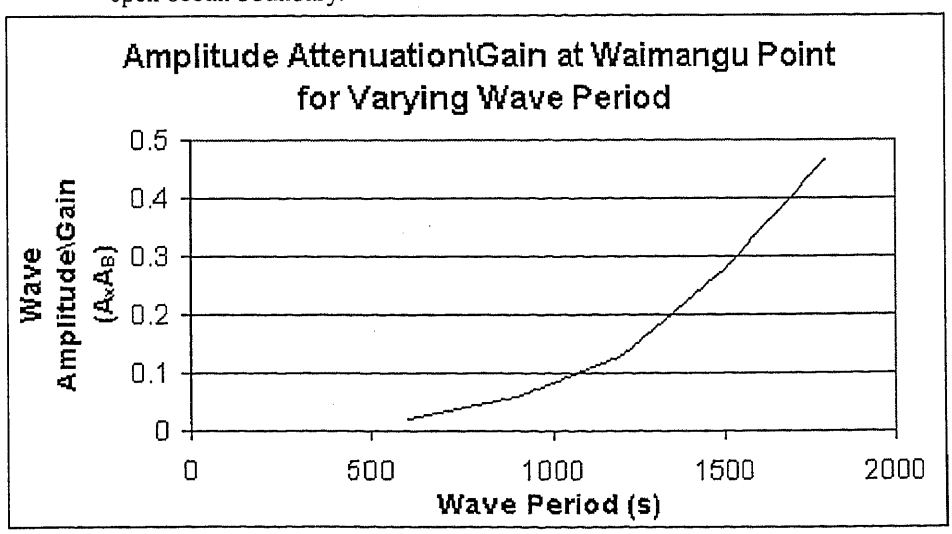

Figure A11.9: Figure illustrating the relationship between wave period and amplitude attenuation/gain at Waimangu Point. Amplitude attenuation/gain is presented as a proportion of the amplitude at the open ocean boundary.

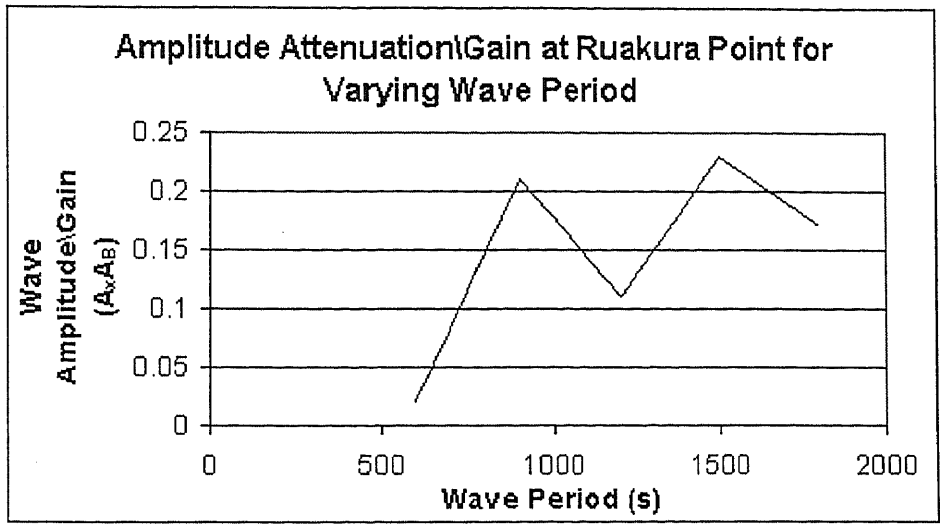

Figure A11.10: Figure illustrating the relationship between wave period and amplitude attenuation/gain at Ruakura Point. Amplitude attenuation/gain is presented as a proportion of the amplitude at the open ocean boundary.

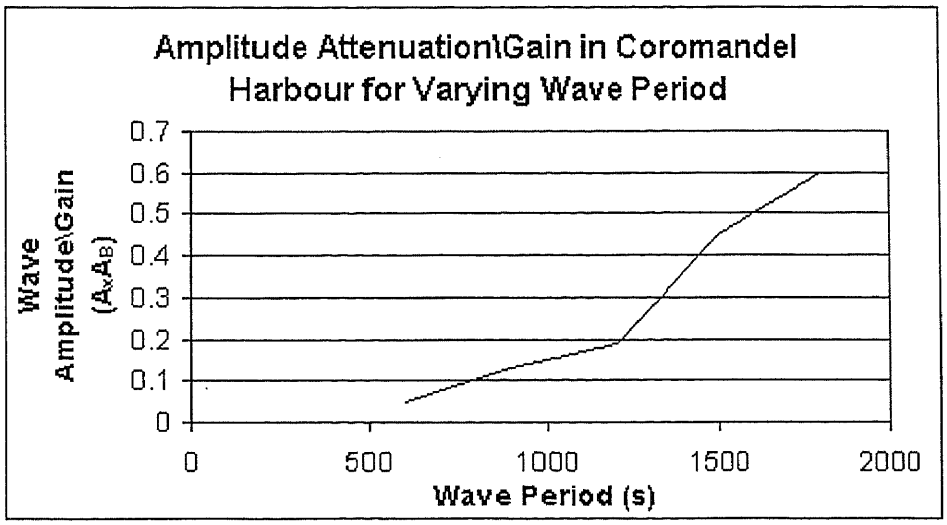

Figure A11.11: Figure illustrating the relationship between wave period and amplitude attenuation/gain at Coromandel Harbour. Amplitude attenuation/gain is presented as a proportion of the amplitude at the open ocean boundary.

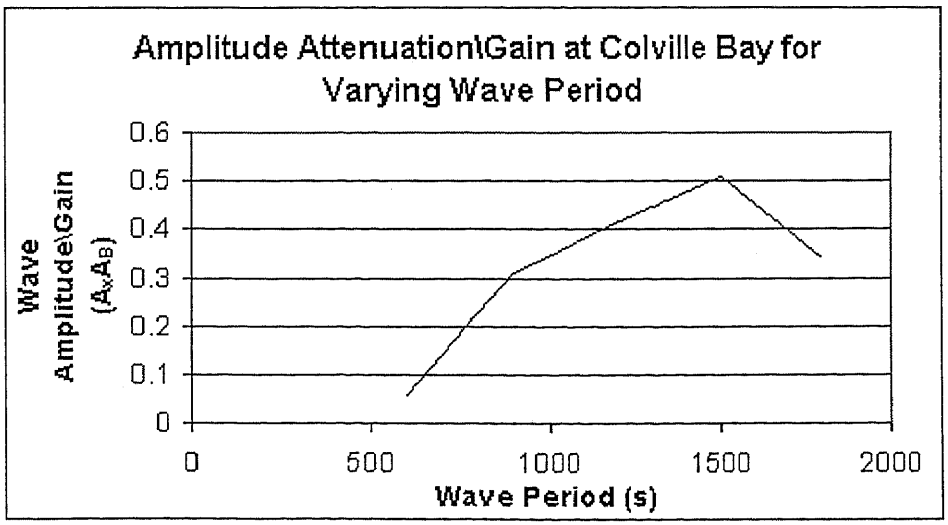

Figure A11.12: Figure illustrating the relationship between wave period and amplitude attenuation/gain at Colville Bay. Amplitude attenuation/gain is presented as a proportion of the amplitude at the open ocean boundary.

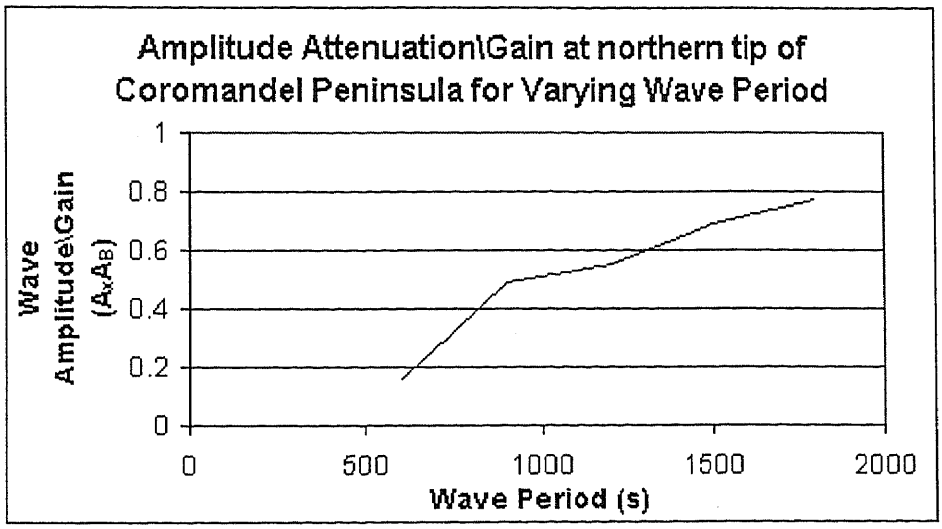

Figure A11.13: Figure illustrating the relationship between wave period and amplitude attenuation/gain at northern tip of the Coromandel Peninsula. Amplitude attenuation/gain is presented as a proportion of the amplitude at the open ocean boundary.

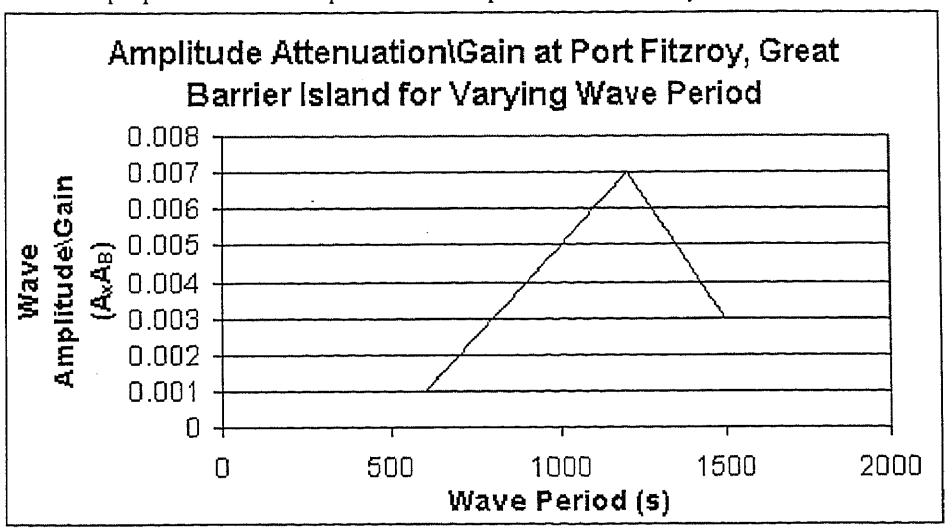

Figure A11.14: Figure illustrating the relationship between wave period and amplitude attenuation/gain at Port Fitzroy, Great Barrier Island. Amplitude attenuation/gain is presented as a proportion of the amplitude at the open ocean boundary.

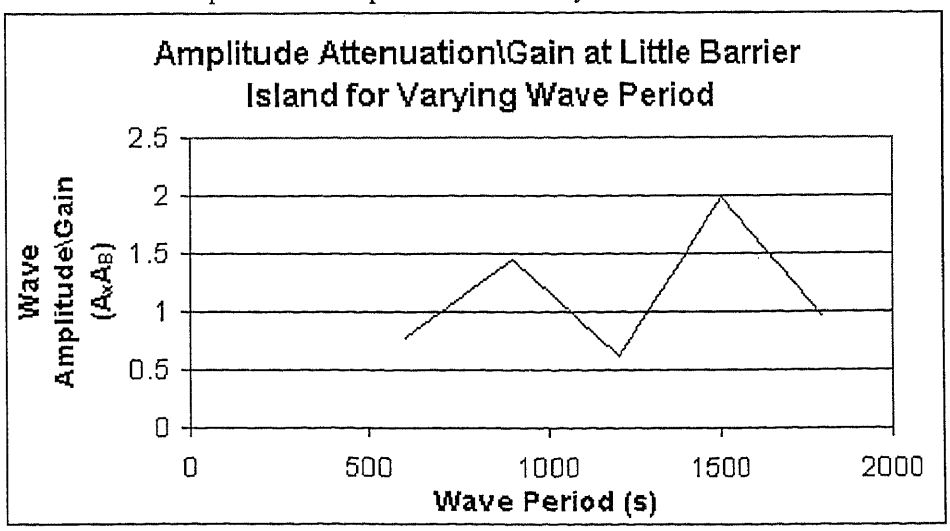

Figure A11.15: Figure illustrating the relationship between wave period and amplitude attenuation/gain at Little Barrier Island. Amplitude attenuation/gain is presented as a proportion of the amplitude at the open ocean boundary.

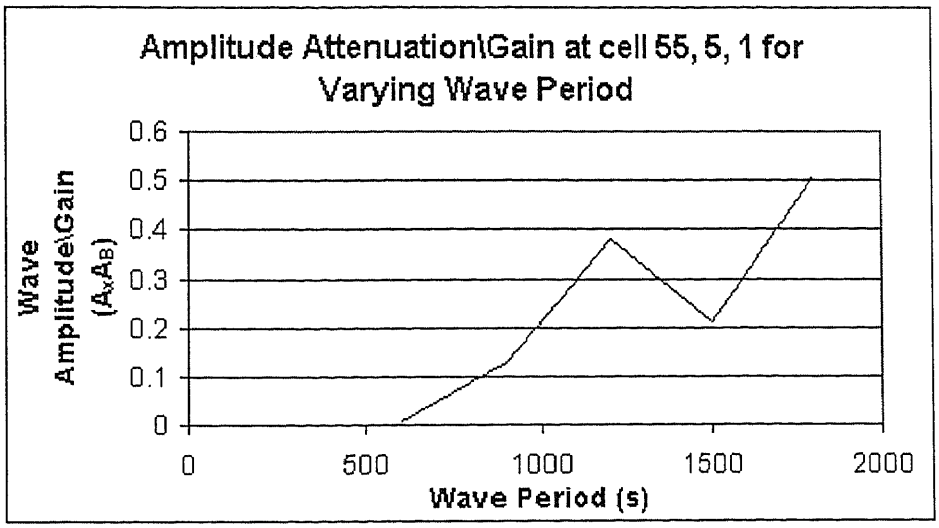

Figure A11.16: Figure illustrating the relationship between wave period and amplitude attenuation/gain at cell 55,5,1. Amplitude attenuation/gain is presented as a proportion of the amplitude at the open ocean boundary.

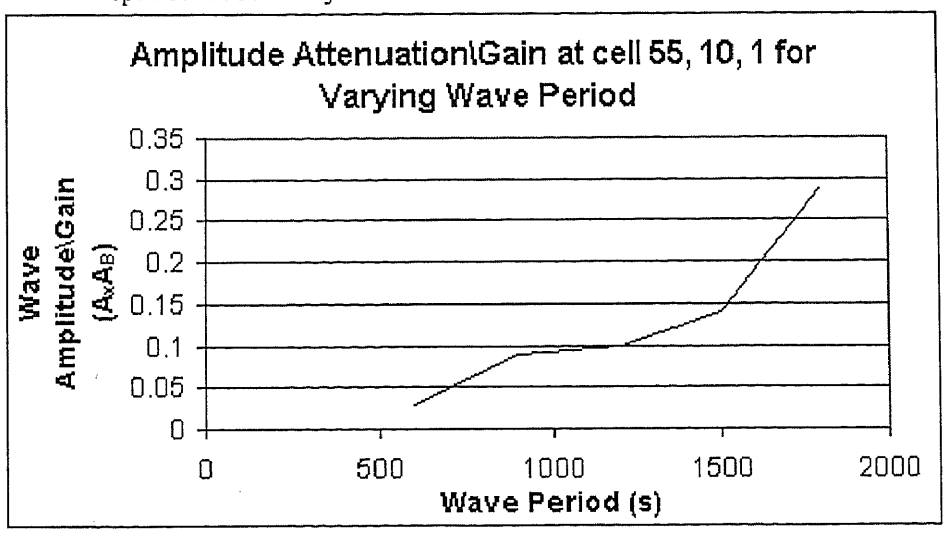

Figure A11.17: Figure illustrating the relationship between wave period and amplitude attenuation/gain at cell 55, 10, 1. Amplitude attenuation/gain is presented as a proportion of the amplitude at the open ocean boundary.

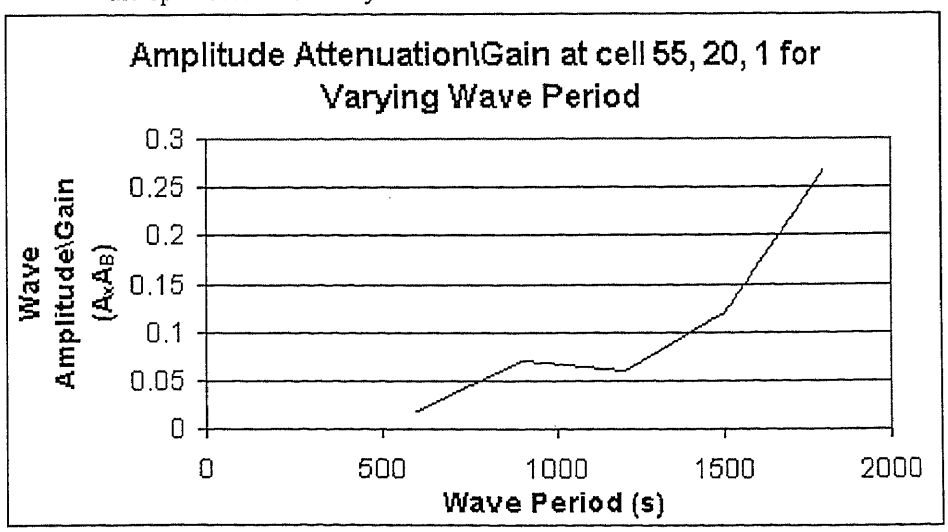

Figure A11.18: Figure illustrating the relationship between wave period and amplitude attenuation/gain at cell 55, 20,1. Amplitude attenuation/gain is presented as a proportion of the amplitude at the open ocean boundary.

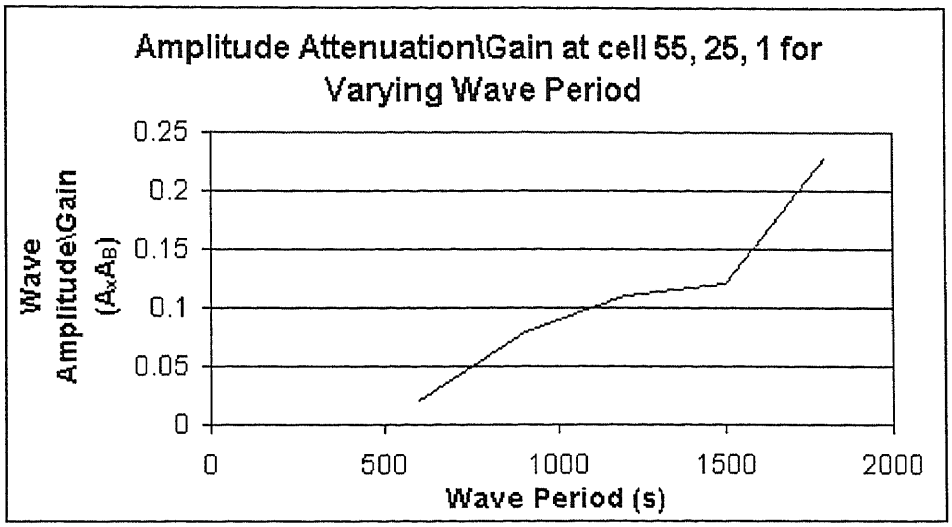

Figure A11.19: Figure illustrating the relationship between wave period and amplitude attenuation/gain at cell 55, 25, 1. Amplitude attenuation/gain is presented as a proportion of the amplitude at the open ocean boundary.

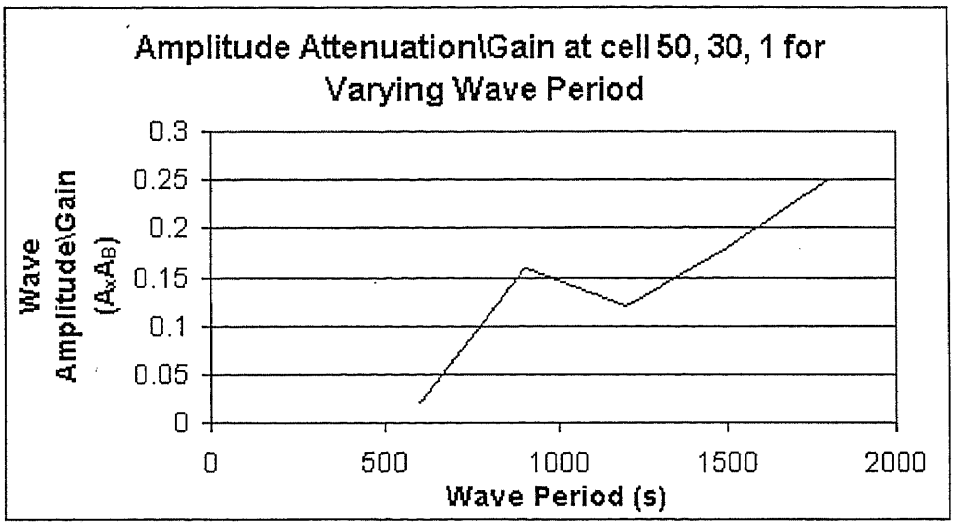

Figure A11.20: Figure illustrating the relationship between wave period and amplitude attenuation/gain at cell 50, 30, 1. Amplitude attenuation/gain is presented as a proportion of the amplitude at the open ocean boundary.

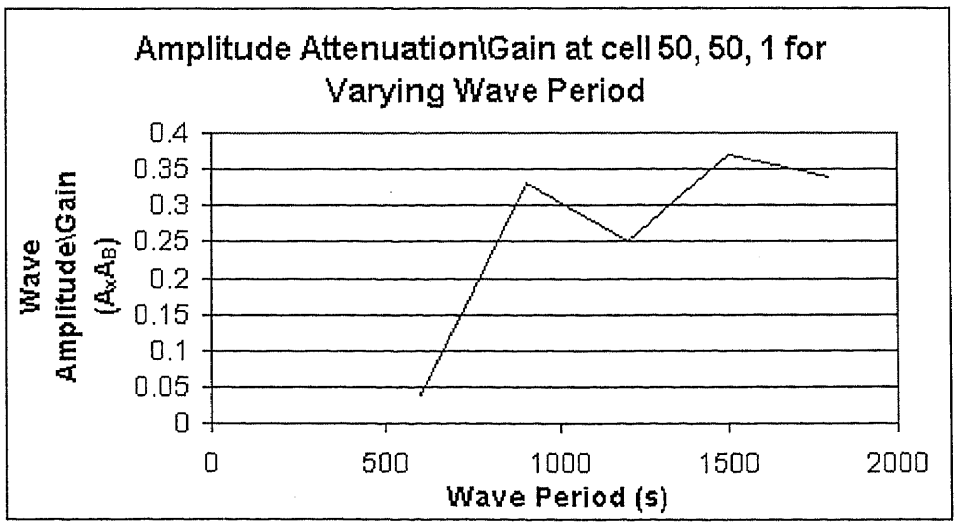

Figure A11.21: Figure illustrating the relationship between wave period and amplitude attenuation/gain at cell 50, 50, 1. Amplitude attenuation/gain is presented as a proportion of the amplitude at the open ocean boundary.

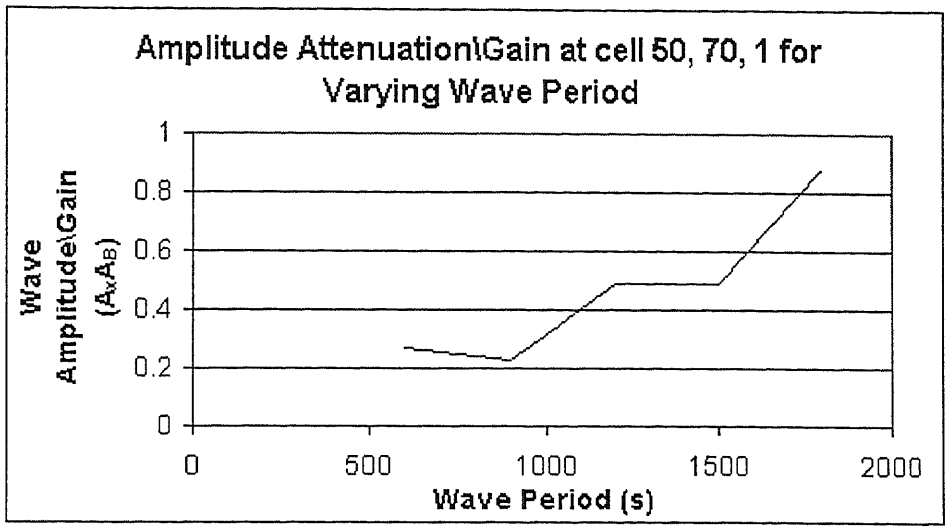

Figure A11.22: Figure illustrating the relationship between wave period and amplitude attenuation/gain at cell 50, 70, 1. Amplitude attenuation/gain is presented as a proportion of the amplitude at the open ocean boundary.

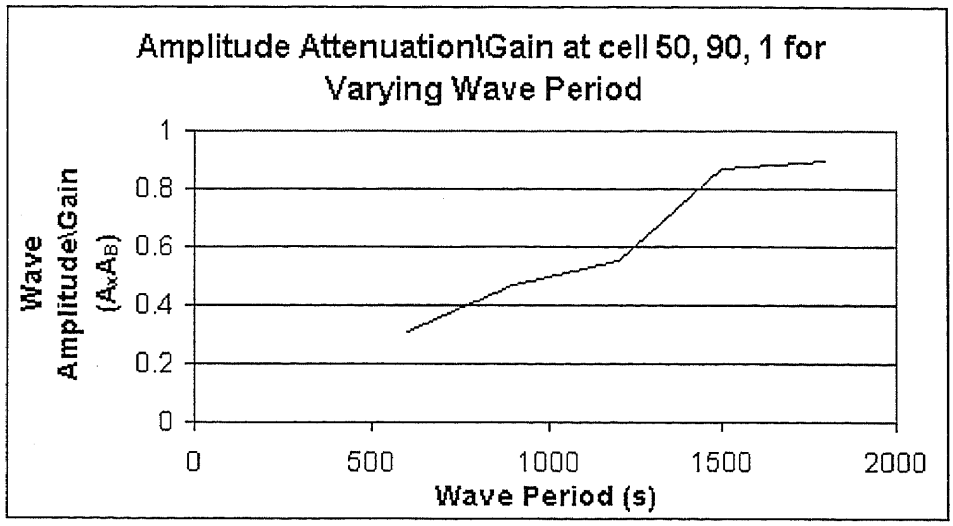

Figure A11.23: Figure illustrating the relationship between wave period and amplitude attenuation/gain at cell 50, 90, 1. Amplitude attenuation/gain is presented as a proportion of the amplitude at the open ocean boundary.

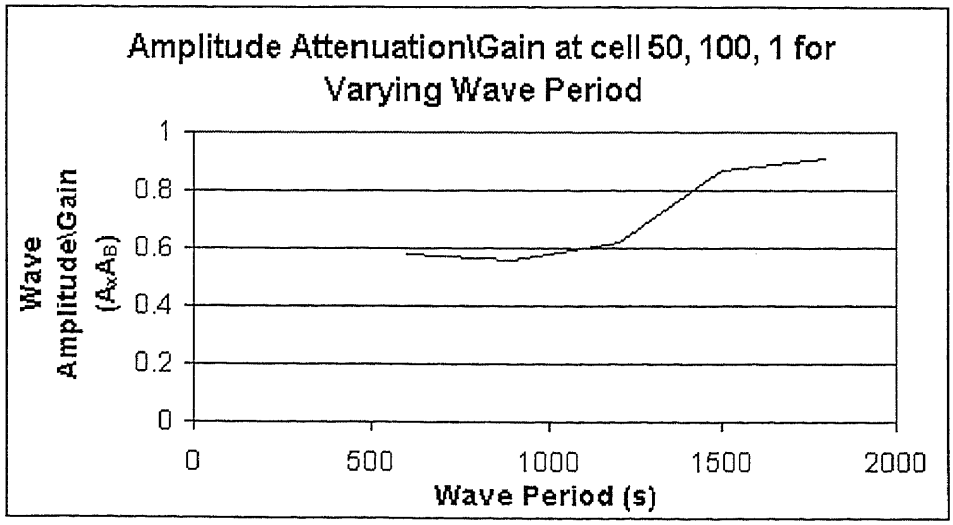

Figure A11.24: Figure illustrating the relationship between wave period and amplitude attenuation/gain at cell 50, 100, 1. Amplitude attenuation/gain is presented as a proportion of the amplitude at the open ocean boundary.

Appendix Twelve

'TUNAMI N2': FINITE DIFFERENCE INUNDATION MODEL

A12.1 INTRODUCTION

Numerical modelling of tsunami inundation was undertaken for the Thames region using a 2-dimensional non-linear, finite difference model, 'TUNAMI N2'. Finite difference modelling employs a regularly spaced grid in which the differential conservation laws governing hydrodynamic circulation are approximated by difference schemes at each element within the computational domain. Finite difference models are comparatively economic (quick computational time), robust and involve simpler programming.

A12.2 PRINCIPLES BEHIND THE FINITE DIFFERENCE METHOD

The real world system is simplified by dividing the computational domain into a series of regular four sided polygons, called elements. Hydrodynamic circulation within the model domain is then approximated by applying difference schemes to each element. These difference schemes discretize and therefore approximate the continuum *mass conservation* and the *momentum equations*. Following this, boundary and initial conditions are specified and the model is run for 'x' number of time steps (Figure A.1).

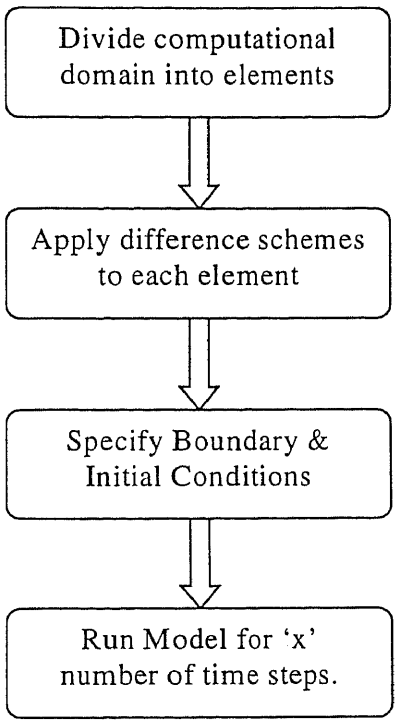

Figure A12.1: Flow chart summarising major concepts behind the development of a finite difference model.

A12.2.1 Shallow Water Wave Theory

Tsunami waves are classified as long waves. We can assume shallow water linear theory, i.e. $C = \sqrt{gh}$ (de Lange, 1983), applies to tsunamis if the ratio between water depth and deep water wave length is less than 0.05 (Komar, 1976). Given the worlds oceans are deepest at approximately 11 km, the this ratio will be less than 0.05 if tsunami deepwater wavelength is greater than 220 km. Applying shallow water wave theory, the following equation shows that this wavelength equates to a period of approximately 11 minutes.

$$L = T\sqrt{gh}$$

where T = wave period

g = gravitational acceleration 9.81 $m.s^{-2}$

h = still water depth

Tsunami wave periods typically exceed 11 minutes, hence tsunamis can be characterised as shallow water waves regardless of water depth (de Lange, 1983; Dean & Dalrymple, 1984).

Application of shallow water wave theory deduces that the horizontal velocity of water particles under long waves is uniform with depth (Dean & Dalrymple, 1991). Also, it is approximated that the pressure under long waves is hydrostatic as i) the ratio of water depth to wavelength is relatively small, ii) the curvature of trajectories is relatively small, and iii) the vertical acceleration of particles is negligible compared to the gravitational acceleration.

A12.2.2 Hydrodynamic Equations in 2-Dimensions

Given the above assumptions, the motion of long waves is well expressed by the following 2-dimensional hydrodynamic equations (Goto & Ogawa, 1995).

The Mass Conservation Equation:

$$\frac{\partial \eta}{\partial t}+\frac{\partial[u(h+\eta)]}{\partial x}+\frac{\partial[v(h+\eta)]}{\partial y}=0 \qquad \textbf{A12.2}$$

The Momentum Equations:

$$\frac{\partial u}{\partial t}+u\frac{\partial u}{\partial x}+v\frac{\partial u}{\partial y}+g\frac{\partial \eta}{\partial x}+\frac{\tau_x}{\rho}=0 \qquad \textbf{A12.3}$$

$$\frac{\partial v}{\partial t}+u\frac{\partial v}{\partial x}+v\frac{\partial v}{\partial y}+g\frac{\partial \eta}{\partial y}+\frac{\tau_y}{\rho}=0$$

where

x, y = horizontal coordinates

t = time

h = still water depth

η = vertical displacement of water surface above still water level

u = water particle velocity in the x-direction

v = water particle velocity in the y-direction

g = the gravitational acceleration

τ_x/ρ = bottom friction in the x-direction

τ_y/ρ = bottom friction in the y-direction

where:
$$\frac{\tau_x}{\rho} = \frac{gn^2}{D^{4/3}} u\sqrt{u^2+v^2} \qquad \textbf{A12.4}$$

$$\frac{\tau_y}{\rho} = \frac{gn^2}{D^{4/3}} v\sqrt{u^2+v^2}$$

and D is the total water depth given by h + η and n is Manning's roughness coefficient (Goto & Ogawa, 1995).

The above coordinates (x, y) relate to a Cartesian coordinate system where the origin and the (x, y) plane lie on the undisturbed water surface. The x and y axis are directed east and north respectively (Ramming & Zowalik, 1980; Figure A.2).

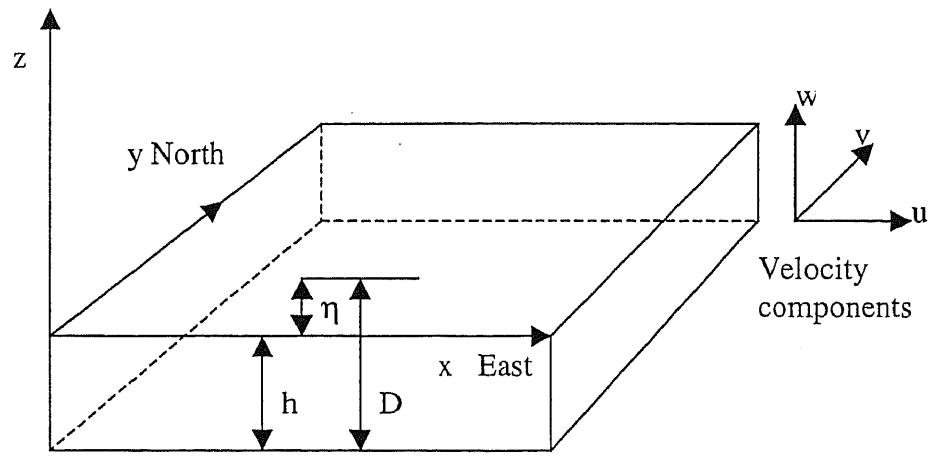

Figure A12.2: The Cartesian coordinate system (After Prasetya, 1998; Ramming & Zowalik, 1980; Dean & Dalrymple, 1984).

In a real fluid mass cannot be created or destroyed (Dean & Dalrymple, 1991). The conservation equation ensures that mass is conserved within each element (Figure A.3). The momentum equation is derived from Newton's 2nd law of motion which states that the rate of change of motion (acceleration) of a body is directly proportional to the resultant force acting upon it and is in the direction of that force. i.e. it describes the acceleration/retardation of the water body when forces are applied to it.

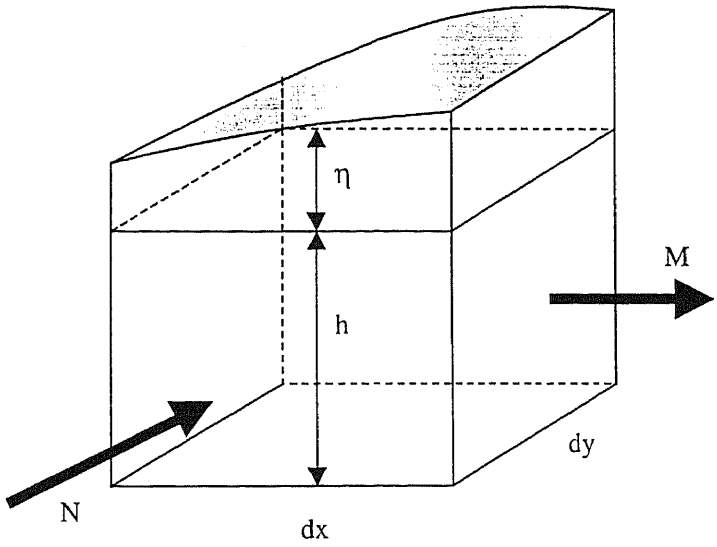

Figure A12.3: The continuity equation states that the sum of all net fluid inflows into a column of water (area dx.dy and height (η+h)) is balanced by an increase of fluid in the column, which is manifested by a change in height of the column (After Dean & Dalrymple, 1991).

A12.3 'TUNAMI N2' APPROACH

A12.3.1 Governing Equations

The finite difference model 'TUNAMI N2' applies an integrated form of the above equations A12.2 & A12.3. Integrating equations A12.2 & A12.3 from sea bottom to water surface generates the following set of equations:

The Mass Conservation Equation:

$$\frac{\partial \eta}{\partial t}+\frac{\partial M}{\partial x}+\frac{\partial N}{\partial y}=0 \qquad \textbf{A12.5}$$

The Momentum Equations:

$$\frac{\partial M}{\partial t}+\frac{\partial}{\partial x}\left(\frac{M^2}{D}\right)+\frac{\partial}{\partial y}\left(\frac{MN}{D}\right)+gD\frac{\partial \eta}{\partial x}+\frac{gn^2}{D^{7/3}}M\sqrt{M^2+N^2}=0 \qquad \textbf{A12.6}$$

$$\frac{\partial N}{\partial t}+\frac{\partial}{\partial x}\left(\frac{MN}{D}\right)+\frac{\partial}{\partial y}\left(\frac{N^2}{D}\right)+gD\frac{\partial \eta}{\partial y}+\frac{gn^2}{D^{7/3}}M\sqrt{M^2+N^2}=0$$

where

n = Manning's roughness coefficient

$$= \sqrt{\frac{fD^{1/3}}{2g}}$$

M = discharge flux in the x-direction

$= u(h + \eta)$

$= uD$

N = discharge flux in the y-direction

$= v(h + \eta)$

$= vD$

In the TUNAMI N2 model this set of equations has been used in preference to those presented as equations A12.2 and A12.3 because, when discretized, Equations A12.2 & A12.3 do not satisfy the conservation of mass (Goto & Ogawa, 1995).

Equations A12.5 & A12.6 are then approximated by difference equations that are solved for each element at every time step.

A12.3.2 Difference Scheme

The 'TUNAMI N2' model discretizes equations A12.5 & A12.6 using a central difference leap frog scheme generating a second order truncation error (Goto & Ogawa, 1995).

The truncation error refers to truncation of the Taylor series expansion. Application of the Taylor series (Equation A12.7) enables relationships between fluid properties at two closely spaced locations to be developed. If a continuous mathematical function F(x, y) of two independent variables is known at one location e.g. x_0, it can be approximated at another location, $x_0 + \Delta x$ (Dean & Dalrymple, 1991). If Δx is very small, truncation of the comparatively small values associated with terms involving $(\Delta x)^n$ where $n>1$ generates a very small error.

$$F(x_0+\Delta x,y)=F(x_0+y)+\Delta x\frac{\partial F(x_0,y)}{\partial x}+\frac{(\Delta x)^2}{2!}\frac{\partial^2 F(x_0,y)}{\partial x^2}+\ldots+\ldots+\frac{(\Delta x)^n}{n!}\frac{\partial^n F(x_0,y)}{\partial x^n}+\ldots \qquad \textbf{A12.7}$$

Taking the difference between the two Taylor series expansions for values of a continuous function F(x) at discrete points F_{i+1}, F_{i-1} yields a central difference of the first-order derivative (Equation A12.8; (Goto & Ogawa, 1995).).

$$\frac{\partial F}{\partial x}|i=\frac{1}{2\Delta x}[F_{i+1}-F_{i-1}]+O(\Delta x^2) \qquad \textbf{A12.8}$$

The above difference scheme is then applied to equations A12.5 & A12.6 in order to generate discrete difference equations which will approximate the continuous Mass Conservation and Momentum Equations (Goto & Ogawa, 1995).

In order to make it easy to set the boundary conditions, the leap-frog scheme assumes a computation location for η that is different from the computation locations of M & N (Figure A.4).

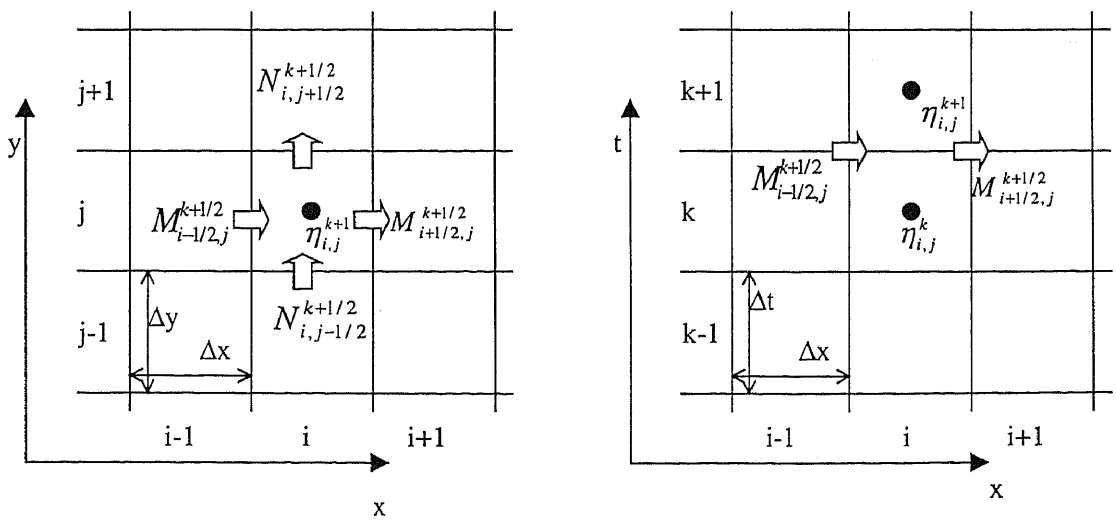

Figure A12.4: Arrangement of points for computation in the leap-frog method.

A12.4 DIFFERENCE EQUATION APPROXIMATIONS

The following information is derived directly from the 'TUNAMI' manual, 'Numerical Method of Tsunami Simulation with the leap-Frog Scheme', (Goto & Ogawa, 1995). Finite Difference modeling requires the continuous *Mass Conservation* and *Momentum Equations* to be discretely approximated by difference equations. The 'TUNAMI N2' model applies a central difference scheme of the first-order derivative (Equation A12.9).

$$\frac{\partial F}{\partial x}|i = \frac{1}{2\Delta x}[F_{i+1} - F_{i-1}] + O(\Delta x^2) \qquad \textbf{A12.9}$$

A12.4.1 Approximations of Mass Conservation Equation

Approximating the *Mass Conservation Equation* by the above central difference scheme yields the three following terms:

$$\frac{\partial \eta}{\partial t} = \frac{1}{\Delta t}\left[\eta_{i,j}^{k+1} - \eta_{i,j}^{k}\right]$$

$$\frac{\partial M}{\partial x} = \frac{1}{\Delta x}\left[M_{i+1/2,j}^{k+1/2} - M_{i-1/2,j}^{k+1/2}\right]$$

$$\frac{\partial N}{\partial y} = \frac{1}{\Delta y}\left[N_{i,j+1/2}^{k+1/2} - N_{i,j+1/2}^{k+1/2}\right]$$

Assuming values at k and k+1/2 time steps are known the only unknown $\eta_{i,j}^{k+1}$ is solved by:

$$\eta_{i,j}^{K+1} = \eta_{i,j}^{k} - \frac{\Delta t}{\Delta x}\left[M_{i+1/2,j}^{k+1/2} - M_{i-1/2,j}^{k+1/2}\right] - \frac{\Delta t}{\Delta y}\left[N_{i,j+1/2}^{k+1/2} - N_{i,j-1/2}^{k+1/2}\right] \qquad \textbf{A12.10}$$

A12.4.2 Approximation of Momentum Equation

The *Momentum Equation* is approximated. Explanation of this process is presented in three parts; approximation of linear terms, approximation and stability of convection terms, and approximation of friction terms.

Linear Terms:

The linear equation of motion in the x-direction is written as:

$$\frac{\partial M}{\partial t} + gD\frac{\partial \eta}{\partial x} = 0 \qquad \textbf{A12.11}$$

A central difference at the point (i+1/2, j, k) yields the following equation of an unknown $M_{i+1/2}^{k+1/2}, j$:

$$M_{i+1/2,j}^{k+1/2} = M_{i+1/2,j}^{k-1/2} - gD_{i+1/2,j}^{k}\frac{\Delta t}{\Delta x}\left[\eta_{i+1,j}^{k} - \eta_{i,j}^{k}\right] \qquad \textbf{A12.12}$$

where the total water depth $D_{i+1/2,j}^{k}$ is expressed as:

$$D_{i+1/2,j}^{k} = h_{i+1/2,j} + \eta_{i+1/2,j}^{k} = h_{i+1/2,j} + \frac{1}{2}\left[\eta_{i+1,j}^{k} + \eta_{i,j}^{k}\right] \qquad \textbf{A12.13}$$

Similar manipulation yields the following difference equation for the linear equation of motion in the y-direction.

$$N_{i,j+1/2}^{k+1/2} = N_{i,j-1/2}^{k-1/2} - gD_{i,j-1/2}^{k}\frac{\Delta t}{\Delta x}\left[\eta_{i,j+1}^{k} - \eta_{i,j}^{k}\right] \qquad \textbf{A12.14}$$

$$D_{i,j-1/2}^{k} = h_{i,j-1/2} + \eta_{i,j-1/2}^{k} = h_{i,j-1/2} + \frac{1}{2}\left[\eta_{i,j+1}^{k} + \eta_{i,j}^{k}\right] \qquad \textbf{A12.15}$$

The linear long wave solution is obtained by solving equations A12.10, A12.12, and A12.14 simultaneously. Note that this linear computation may become unstable if h is smaller than η.

Convection Terms:

An upwind difference scheme is applied to the convection terms in order to make the computation stable i.e. the difference is taken in the direction of flow; positive propagation velocity = backward difference, negative propagation velocity = forward difference. Truncation error for convective terms is in the order of Δx. The convection terms in Equation All.6 are expressed as the following if an upwind scheme is applied:

$$\frac{\partial}{\partial x}\left(\frac{M^2}{D}\right)=\frac{1}{\Delta x}\left[\lambda_{11}\frac{\left(M_{i+3/2,j}^{k-1/2}\right)^2}{D_{i+3/2,j}^{k-1/2}}+\lambda_{21}\frac{\left(M_{i+1/2,j}^{k-1/2}\right)^2}{D_{i+1/2,j}^{k-1/2}}+\lambda_{31}\frac{\left(M_{i-1/2,j}^{k-1/2}\right)^2}{D_{i-1/2,j}^{k-1/2}}\right]$$

$$\frac{\partial}{\partial y}\left(\frac{MN}{D}\right)=\frac{1}{\Delta y}\left[\nu_{11}\frac{M_{i+1/2,j+1}^{k-1/2}N_{i+1/2,j+1}^{k-1/2}}{D_{i+1/2,j+1}^{k-1/2}}+\nu_{21}\frac{M_{i+1/2,j}^{k-1/2}N_{i+1/2,j}^{k-1/2}}{D_{i+1/2,j}^{k-1/2}}+\nu_{31}\frac{M_{i+1/2,j-1}^{k-1/2}N_{i+1/2,j-1}^{k-1/2}}{D_{i+1/2,j-1}^{k-1/2}}\right]$$

$$\frac{\partial}{\partial x}\left(\frac{MN}{D}\right)=\frac{1}{\Delta x}\left[\lambda_{12}\frac{M_{i+1,j+1/2}^{k-1/2}N_{i+1,j+1/2}^{k-1/2}}{D_{i+1,j+1/2}^{k-1/2}}+\lambda_{22}\frac{M_{i,j+1/2}^{k-1/2}N_{i,j+1/2}^{k-1/2}}{D_{i,j+1/2}^{k-1/2}}+\lambda_{32}\frac{M_{i-1,j+1/2}^{k-1/2}N_{i-1,j+1/2}^{k-1/2}}{D_{i-1,j+1/2}^{k-1/2}}\right]$$

$$\frac{\partial}{\partial y}\left(\frac{N^2}{D}\right)=\frac{1}{\Delta y}\left[\nu_{12}\frac{\left(N_{i,j+3/2}^{k-1/2}\right)^2}{D_{i,j+3/2}^{k-1/2}}+\nu_{22}\frac{\left(N_{i,j+1/2}^{k-1/2}\right)^2}{D_{i,j+1/2}^{k-1/2}}+\nu_{32}\frac{\left(N_{i,j-1/2}^{k-1/2}\right)^2}{D_{i,j-1/2}^{k-1/2}}\right]$$

where

$$\begin{aligned}
M_{i+1/2,j}^{k-1/2} \geq 0, &\quad \lambda_{11}=0, &\quad \lambda_{21}=1, &\quad \lambda_{31}=-1\\
< 0, &\quad \lambda_{11}=1, &\quad \lambda_{21}=-1, &\quad \lambda_{31}=0\\
N_{i+1/2,j}^{k-1/2} \geq 0, &\quad \nu_{11}=0, &\quad \nu_{21}=1, &\quad \nu_{31}=-1\\
< 0, &\quad \nu_{11}=1, &\quad \nu_{21}=-1, &\quad \nu_{31}=0\\
M_{i,j+1/2}^{k-1/2} \geq 0, &\quad \lambda_{12}=0, &\quad \lambda_{22}=1, &\quad \lambda_{32}=-1\\
< 0, &\quad \lambda_{12}=1, &\quad \lambda_{22}=-1, &\quad \lambda_{32}=0\\
N_{i,j+1/2}^{k-1/2} \geq 0, &\quad \nu_{12}=0, &\quad \nu_{22}=1, &\quad \nu_{32}=-1\\
< 0, &\quad \nu_{12}=1, &\quad \nu_{22}=-1, &\quad \nu_{32}=0
\end{aligned}$$

Friction Terms:

The friction term is discretised using an implicit scheme in order to prevent instability, associated with explicit discretisation.

$$\frac{gn^2}{D^{7/3}} M\sqrt{M^2+N^2} = \frac{gn^2}{\left(D_{i+1/2,j}^{k-1/2}\right)^{\frac{7}{3}}} \frac{1}{2}\left(M_{i+1/2,j}^{k+1/2} + M_{i+1/2,j}^{k-1/2}\right)\sqrt{\left(M_{i+1/2,j}^{k-1/2}\right)^2 + \left(N_{i+1/2,j}^{k-1/2}\right)^2}$$

$$\frac{gn^2}{D^{7/3}} N\sqrt{M^2+N^2} = \frac{gn^2}{\left(D_{i,j+1/2}^{k-1/2}\right)^{\frac{7}{3}}} \frac{1}{2}\left(N_{i,j+1/2}^{k+1/2} + N_{i,j+1/2}^{k-1/2}\right)\sqrt{\left(M_{i,j+1/2}^{k-1/2}\right)^2 + \left(N_{i,j+1/2}^{k-1/2}\right)^2}$$

A12.5 REFERENCES

Dean, R.G., and Dalrymple, R.A., 1991. *Water Wave Mechanics for Engineers and Scientists*, Prentice Hall, Inc., Singapore, 345 p.

de Lange, W.P., 1983. *Tsunami Hazard, an investigation into the potential tsunami hazards of the Bay of Plenty region using numerical models*; Unpublished M.Sc. Thesis, Department of Earth Sciences, The University of Waikato.

Goto, C., and Ogawa, Y., 1995. *Numerical Method of Tsunami Simulation with the Leap-Frog Scheme, Part 1: Shallow water theory and its difference scheme*, IUGG/IOC TIME project Manuals, 66 p.

Komar, P.D., 1976, *Beach Processes and Sedimentation,* Prentice-Hall Inc., Englewood Cliffs, New Jersey, U.S.A., p. 172.

Prasetya, G.S., 1998, Modelling Volcanic Tsunamis, M.Sc. Thesis, University of Waikato, Hamilton, 108 p.

Ramming, H.G., and Kowalik, Z., 1980. *Numerical Modelling of Marine Hydrodynamics: applications to dynamic physical processes*, Elsevier Scientific Publishing Company, Amsterdam, The Netherlands, 368 p.